REPORT DOCUMENTATION PAGE

Form Approved OMB NO. 0704-0188

The public reporting burden for this collection of information is estimated to average 1 hour per response, including the time for reviewing instructions, searching existing data sources, gathering and maintaining the data needed, and completing and reviewing the collection of information. Send comments regarding this burden estimate or any other aspect of this collection of information, including suggesstions for reducing this burden, to Washington Headquarters Services, Directorate for Information Operations and Reports, 1215 Jefferson Davis Highway, Suite 1204, Arlington VA, 22202-4302. Respondents should be aware that notwithstanding any other provision of law, no person shall be subject to any oenalty for failing to comply with a collection of information if it does not display a currently valid OMB control number.
PLEASE DO NOT RETURN YOUR FORM TO THE ABOVE ADDRESS.

1. REPORT DATE (DD-MM-YYYY)	2. REPORT TYPE	3. DATES COVERED (From - To)
13-03-2016	Ph.D. Dissertation	-

4. TITLE AND SUBTITLE
COHERENT OPERATIONS, ENTANGLEMENT, AND PROGRESS TOWARDQUANTUM SEARCH IN A LARGE 2D ARRAY OF NEUTRAL ATOM QUBITS

5a. CONTRACT NUMBER
W911NF-10-1-0347

5b. GRANT NUMBER

5c. PROGRAM ELEMENT NUMBER
411359

6. AUTHORS
Martin Lichtman

5d. PROJECT NUMBER

5e. TASK NUMBER

5f. WORK UNIT NUMBER

7. PERFORMING ORGANIZATION NAMES AND ADDRESSES
University of Wisconsin - Madison 1.00
Suite 6401
21 N Park St
Madison, WI 53715 -1218

8. PERFORMING ORGANIZATION REPORT NUMBER

9. SPONSORING/MONITORING AGENCY NAME(S) AND ADDRESS (ES)
U.S. Army Research Office
P.O. Box 12211
Research Triangle Park, NC 27709-2211

10. SPONSOR/MONITOR'S ACRONYM(S)
ARO

11. SPONSOR/MONITOR'S REPORT NUMBER(S)
58107-PH-MOC.29

12. DISTRIBUTION AVAILIBILITY STATEMENT
Distribution authorized to U.S. Government Agencies Only, Contains Proprietary information

13. SUPPLEMENTARY NOTES
The views, opinions and/or findings contained in this report are those of the author(s) and should not contrued as an official Department of the Army position, policy or decision, unless so designated by other documentation.

14. ABSTRACT
We have created a stable, inherently 2D array of neutral cesium atom qubits. Novel trapping schemes based first on projected arrays of Gaussian beams, and later on projected line grids, have been implemented. An atomic qubit array with 49 trapping sites and a loading fraction of 0.61 has been demonstrated, with progress toward an 121 site trap array. Single atom qubits in this array are individually addressable. Single qubit gates have been demonstrated with a fidelity of 0.9983(14) for global operations and 0.9923(7) for site specific operations.

15. SUBJECT TERMS
quantum computing, neutral atoms, quantum search

16. SECURITY CLASSIFICATION OF:			17. LIMITATION OF ABSTRACT	15. NUMBER OF PAGES	19a. NAME OF RESPONSIBLE PERSON
a. REPORT	b. ABSTRACT	c. THIS PAGE			MARK SAFFMAN
UL	UL	UL	UL		19b. TELEPHONE NUMBER 608-265-5601

Report Title

COHERENT OPERATIONS, ENTANGLEMENT, AND PROGRESS TOWARDQUANTUM SEARCH IN A LARGE 2D ARRAY OF NEUTRAL ATOM QUBITS

ABSTRACT

We have created a stable, inherently 2D array of neutral cesium atom qubits. Novel trapping schemes based first on projected arrays of Gaussian beams, and later on projected line grids, have been implemented. An atomic qubit array with 49 trapping sites and a loading fraction of 0.61 has been demonstrated, with progress toward an 121 site trap array. Single atom qubits in this array are individually addressable. Single qubit gates have been demonstrated with a fidelity of 0.9983(14) for global operations and 0.9923(7) for site specific operations. Two-qubit C-NOT gates have been implemented, and the non-classical result of 0.73(5) entanglement fidelity has been measured by Bell state parity oscillation. The system performance has been tuned using closed-loop optimization via original control software. Progress has been made toward implementing Grover's quantum search algorithm in the atomic qubit array.

COHERENT OPERATIONS, ENTANGLEMENT, AND PROGRESS TOWARD QUANTUM SEARCH IN A LARGE 2D ARRAY OF NEUTRAL ATOM QUBITS

by

Martin Tom Lichtman

A dissertation submitted in partial fulfillment of
the requirements for the degree of

Doctor of Philosophy

(Physics)

at the

UNIVERSITY OF WISCONSIN–MADISON

2015

Date of final oral examination: 2015-08-18

The dissertation is approved by the following members of the Final Oral Committee:
Mark Saffman, Professor, Physics
Thad Walker, Professor, Physics
Deniz Yavuz, Professor, Physics
Robert McDermott, Professor, Physics
Dieter van Melkebeek, Professor, Computer Sciences

© Copyright by Martin Tom Lichtman 2015
All Rights Reserved

For the colors in my life.

Acknowledgments

Thank you to my wife Dr. Hilary Barbra Gerstein for being my loudest cheering section, and loving me to pieces. Thank you to my daughter Winifred Rosetta Lichtman for the future. Thank you to my parents Diane and Harvey Lichtman for feeding and watering me. Thank you to my grandfather Arthur Phineas Weber for being an inspiration. Thank you to my advisor Dr. Mark Saffman for his wisdom and guidance. Thank you to the people of the United States of America for supporting this work through the IARPA Multi-Qubit Coherent Operations program. Thank you to my cohort of the UW-Madison Physics graduate program for being the most perfect friends through many beautiful summers and severe winters between these two lakes. And thank you to the great state of Wisconsin for being my home.

Forward.

— Martin Tom Lichtman
(Madison, WI. 2015)

Contents

Contents **iii**

Abstract **ix**

1 Introduction **1**
1.1 Quantum Computing in Neutral Alkali Atoms 1
1.2 AQuA: Atomic Qubit Array 2

I Background and Theory **3**

2 Quantum Information in Neutral Atoms **4**
2.1 Spin Qubits 4
2.2 Neutral Atoms 5
2.3 Single Qubit Gates 5
2.4 Rydberg Atoms 6
2.5 Rydberg Blockade 7
2.6 Rydberg Blockade Phase Gate 8
2.7 Universal Quantum Computing 9

3 Quantum Search Algorithm **11**
3.1 Algorithm 12
3.2 Number of Iterations 13
3.3 Fidelity of Result 15

4 Undecidable Propositions of Quantum Logic **17**
4.1 Introduction 17
4.2 Gödel's Incompleteness Theorem, Briefly 18
4.2.1 Mapping Statements to Gödel Numbers 19
4.2.2 Clever Substitution 20
4.2.3 Self-reference to Unprovability 20
4.2.4 Consequences of G on PM 21
4.2.5 PM is Unrepairable 21
4.3 Mapping Statements to Quantum States 22

4.3.1 Discretized Mapping . . . 23
4.3.2 Superposition Preserving Mapping . . . 24
4.4 Gödelizing QM . . . 24
4.4.1 QM is Incomplete . . . 24
4.4.2 Extending QM . . . 25
4.4.2.1 Superpositions of True and False . . . 25
4.4.2.2 Supernatural Numbers . . . 25
4.4.2.3 $|G\rangle \oplus \sim |G\rangle$ as an Axiom . . . 26
4.5 Encoding Operators and Density Matrices . . . 27
4.6 Conclusions . . . 28

II Methods **29**

5 System Layout **30**
5.1 Two Stage Cooling . . . 30
5.2 Single Atom Addressing . . . 36
5.3 Imaging . . . 39
5.4 Experiment Temperature Stabilization . . . 39

6 Magneto-Optical Trap Design **41**
6.1 Magneto-Optical Trap Design . . . 41
6.1.1 Magnetic Field Due to Coils . . . 41
6.1.2 Single Circular Coil . . . 42
6.1.3 Helmholtz Shim Coils . . . 42
6.1.4 Anti-Helmholtz Gradient Coils . . . 43
6.1.5 Choosing Wire Gauge . . . 44
6.2 3D MOT Coil Specifications . . . 45
6.3 Use of 3D Printing . . . 46

7 Single-Atom Laser Confinement Grids **48**
7.1 Optical Dipole Traps . . . 49
7.1.1 Red Traps and Blue Traps . . . 52
7.2 Trap Array Geometry Analysis . . . 55
7.2.1 Gaussian Beam Array . . . 55
7.2.1.1 Half-Incoherent Array . . . 57

7.2.1.2 Full-Incoherent Array . . . 62
7.2.2 Line Grid Array . . . 65
7.2.2.1 Unit Cell Analysis . . . 67
7.2.2.2 Infinite Grid Analysis . . . 70
7.2.2.3 Comparison to Gaussian Beam Array . . . 74
7.2.3 Gaussian Line Array . . . 76
7.3 Trap Array Implementations . . . 80
7.3.1 6 Site Half-Incoherent Gaussian Beam Array . . . 80
7.3.2 49 Site Full-Incoherent Gaussian Beam Array . . . 83
7.3.3 121 Site Full-Incoherent Line Grid Array . . . 92

8 Laser Systems **98**
8.1 High Power 780 nm Trapping Lasers . . . 98
8.1.1 1560 nm Second Harmonic Generation System . . . 98
8.1.1.1 Temperature Phase Matching . . . 99
8.1.1.2 Boyd-Kleinman Theory . . . 101
8.1.1.3 Measurement of d_{eff} and L_{eff} . . . 102
8.1.1.4 High Power Predictions . . . 103
8.1.1.5 Implementation of 10.4 W 780 nm Laser . . . 103
8.1.1.6 Phase Shift Problem in AR Coating . . . 105
8.1.2 Ti:Sapphire Laser . . . 107
8.2 852 nm Laser Cooling and Readout, 894 nm Optical Pumping . . . 109
8.2.1 2D MOT . . . 109
8.2.2 3D MOT . . . 111
8.2.3 Repump . . . 111
8.2.4 Optical Pumping . . . 112
8.2.5 Blowaway . . . 113
8.3 459 nm and 1038 nm Rydberg Lasers . . . 115
8.3.1 459 nm Rydberg Laser . . . 115
8.3.2 1038 nm Rydberg laser . . . 119
8.4 459 nm and 9.2 GHz Ground State Rotations . . . 119
8.4.1 9.2 GHz Microwave Horn . . . 120
8.5 459 nm Raman Lasers . . . 122
8.6 459 nm Stark Shifting Laser and 9.2 GHz Microwaves . . . 123

8.7 Frequency Comb . . . 126

9 Experiment Control Software **129**
9.1 Architecture . . . 130
9.2 Experiments, Iterations, Measurements and Shots . . . 131
9.3 Modularity, Maintainability, and Extensibility . . . 132
9.4 Implementation . . . 133
9.4.1 High-level Sequencing in Python . . . 133
9.4.2 Functional Waveforms . . . 134
9.4.3 Low-level Execution in Python, LabVIEW and C# . . . 135
9.4.4 Object-Oriented Programming . . . 136
9.4.5 GUI . . . 138
9.4.6 TCP/IP Networking . . . 138
9.4.7 Data Storage in HDF5 . . . 140
9.4.8 Variables . . . 141
9.4.8.1 Constants . . . 141
9.4.8.2 Independent Variables . . . 142
9.4.8.3 Dependent Variables . . . 142
9.5 Optimization . . . 142
9.5.1 Optimizer Methods . . . 144
9.5.1.1 Gradient Descent . . . 144
9.5.1.2 Genetic Algorithm . . . 145
9.5.1.3 Nelder-Mead Simplex . . . 147
9.5.1.4 Weighted Simplex . . . 148
9.5.2 Designing a Cost Function . . . 150
9.5.3 Machine Learning as a Teacher . . . 150

10 Analysis **151**
10.1 Region of Interest Determination . . . 151
10.1.1 Grid of Gaussian Regions . . . 151
10.1.2 Independent Component Analysis . . . 152
10.2 Analytical Threshold of Two Gaussians . . . 155
10.3 Analytical Overlap of Two Gaussians . . . 158
10.4 Optimal Selection of Test Points . . . 159

III Experiment **163**

11 Experimental Sequence **164**
11.1 Before Gate Operation . . . 164
11.2 Gate Operation . . . 165
11.3 After Gate Operation . . . 165
11.4 Magnetic Fields . . . 166

12 Catalysis Loading **168**
12.1 Calculation of Molecular Potentials . . . 169
12.2 Detuning Scan . . . 171

13 Single Qubit Operations **175**
13.1 Optical Pumping and Depumping . . . 175
13.2 Microwave Rabi Flopping Experiments . . . 177
13.2.1 Global Operations . . . 177
13.3 Site-selective Operations . . . 181
13.4 Randomized Benchmarking . . . 184
13.5 Coherence Measures . . . 187
13.5.1 Spin-Echo Techniques . . . 188
13.6 459 Alignment and Ground Ramsey . . . 191
13.7 Rydberg spectroscopy . . . 191
13.8 Rydberg Ramsey . . . 192

14 Two Qubit Experiments **196**
14.1 State Preparation . . . 196
14.2 Eye Diagram . . . 197
14.3 C_{NOT} Population . . . 198
14.4 Bell State Preparation . . . 200
14.5 Parity Measurement . . . 201

15 Grover Quantum Search **204**
15.1 Measurement of Gate Phases . . . 205
15.2 Correcting Gate Phases . . . 208
15.3 Two Qubit Grover Search . . . 209

16 Optimization **211**
16.1 Readout 211
16.2 Loading and Retention 214
16.3 Atom Temperature 218
16.4 Optical Pumping 219
16.5 Two-level Optimization 220
16.6 Rydberg 222
16.7 Single Site vs. Mean vs. Max Statistics 223

IV Coda **225**

17 Summary and Future Directions **226**

References **228**

Abstract

We have created a stable, inherently 2D array of neutral cesium atom qubits. Novel trapping schemes based first on projected arrays of Gaussian beams, and later on projected line grids, have been implemented. An atomic qubit array with 49 trapping sites and a loading fraction of 0.61 has been demonstrated, with progress toward an 121 site trap array. Single atom qubits in this array are individually addressable. Single qubit gates have been demonstrated with a fidelity of 0.9983(14) for global operations and 0.9923(7) for site specific operations. Two-qubit C-NOT gates have been implemented, and the non-classical result of 0.73(5) entanglement fidelity has been measured by Bell state parity oscillation. The system performance has been tuned using closed-loop optimization via original control software. Progress has been made toward implementing Grover's quantum search algorithm in the atomic qubit array.

1 Introduction

Quantum computing is the synthesis of information science and quantum physics. As such, its experimental implementation promises a revolution in computational capability, and heralds the realization of exquisite control over small engineered systems. This work represents a contribution toward that goal. Herein the techniques of atomic physics are applied to the field of quantum information. Atomic physics is the playground of quantum mechanics. The weird laws that define quantum mechanics are both necessary and most obvious at the atomic scale, as so it is at this level that those laws may be most well harnessed. The challenge in using atomic systems as a platform for computation is that to build a useful computing system it must have a large amount of processing capacity, and this inherently means extending the size of the system beyond the atomic scale. The work presented here attempts to bridge that gap by demonstrating computation using atomic qubits in an array of up to 49 trapped single atoms.

1.1 Quantum Computing in Neutral Alkali Atoms

The implementation of a quantum computer requires first and foremost a two-level system. These two levels represent the $|0\rangle$ and $|1\rangle$ states of the computational basis. This system is referred to as a quantum bit, or most commonly and with some humor: a qubit[1]. This system must be well isolated from the natural environment to protect the information stored within. However, it also must be easily controllable and accessible to be usable.

Alkali atoms present an excellent candidate qubit. Alkali elements, which are catalogued on the left-hand side of the periodic table, are defined by completely filled electron shells, save for one valence electron alone in the outermost shell. Laser interactions with these atoms can then easily manipulate just the state of the outermost electron, as the electrons in the filled shells are in highly stable states. The state of just the valence electron is a much simpler system than the whole atom, and it provides an opportunity to map an idealized two-level system to a real world system. The atom holds onto the electron, and to control the electron, only the much larger atom needs to be manipulated. The salient features of these atomic qubits are detailed in Part I.

[1] The ancient Egyptian *cubit* was the first standard unit of length: the distance from the elbow to the tip of the middle finger.

In Part II we discuss our implementation of the atomic qubit. Using atoms in their neutral state, with zero net charge, removes coupling to static external electric fields. However, it also removes such coupling as a tool for atom trapping. The techniques to trap neutral atoms therefore represent a major part of this effort, addressed in Chapter 7.

1.2 AQuA: Atomic Qubit Array

In Part III we will present the experiment results realized in our quantum computing system. Previous works have demonstrated the feasibility of quantum computing using neutral atoms. In particular, Isenhower et al. [1] and Wilk et al. [2] demonstrated two qubit entangling operations using the Rydberg blockade. The number of addressable qubits was increased from two to five by Knoernschild et al. [3]. As we will discuss in Chapter 2, despite the powerful quadratic or exponential scaling, a quantum computer capable of outperforming classical supercomputers will require thousands of qubits. The Atomic Qubit Array (*AQuA*) project aims to progress toward that goal with increasingly larger grids of addressable trapped single neutral atoms. By implementing new atom trapping techniques, we are able to create 6, 49, and 121 site trap arrays, discussed in Chapter 7. In Chapter 13 we discuss performing single-site addressed operations with high fidelity in these trap arrays.

At the same time, the quality of the qubit operations is equally as important as the quantity of qubits. The quantum computing speedup will only be realized if the individual quantum gates are reliable enough that error correction techniques may be applied. Isenhower et al. [1] and Wilk et al. [2] showed two-qubit entanglement fidelity just under the threshold for entanglement (0.46 and 0.48, respectively), but which can be inferred to give entanglement fidelities of 0.58 and 0.75, respectively, when *a posteriori* selection techniques are applied to account for atom loss. Zhang et al. [4] improved this result to 0.58 without any post-selection. In this work we show improvement to an entanglement fidelity of 0.73 without any post selection, as discussed in Chapter 14.

By improving both the number of qubits, and the fidelity of operations that we can perform with those qubits, *AQuA* has helped progress toward realizing quantum computing in neutral atoms. In Chapter 15 we explain our work toward a demonstration of the quantum search algorithm in the atomic qubit array.

Part I

Background and Theory

2 Quantum Information in Neutral Atoms

2.1 Spin Qubits

The fundamental building block of a quantum computer is the qubit, which can be any two level quantum mechanical system. A good choice of system will have these levels well defined, easily controllable, and also well-isolated from the environment. The spin of an electron is an excellent candidate because it is a very small magnetic moment with weak coupling to the environment, and yet because of its close proximity to the atomic nucleus, a strong spin-spin hyperfine interaction makes the spin state very well defined.

In our platform, we choose the $m_F = 0$ ground hyperfine states of cesium-133. Cesium is an alkali element, with 5 fully filled electron shells and one valence electron in the outer shell with a ground state of $6s_{1/2}$. ^{133}Cs has a nuclear spin of $I = 7/2$ and so the interaction with the spin-$1/2$ valence electron gives $F = 3$ and $F = 4$ hyperfine levels. We choose the $m_F = 0$ magnetic sub-levels because of their lower sensitivity to external fields. We arbitrarily label $\left|6s_{1/2}, F = 3, m_F = 0\right\rangle$ and $\left|6s_{1/2}, F = 4, m_F = 0\right\rangle$, as $|0\rangle$ and $|1\rangle$ respectively, as shown in Figure 2.1. These states have an energy splitting of $9.192\,631\,770$ GHz, which is the cesium clock transition used as the exact S.I. definition of the second.

The cesium atom is of course not a truly two level system, and in fact we will make use of many other levels, particularly the Rydberg levels, in this implementation. However, even at room temperature the clock transition is well isolated, and in our cold atoms in the absence of incident laser radiation, the two level approximation is a good model.

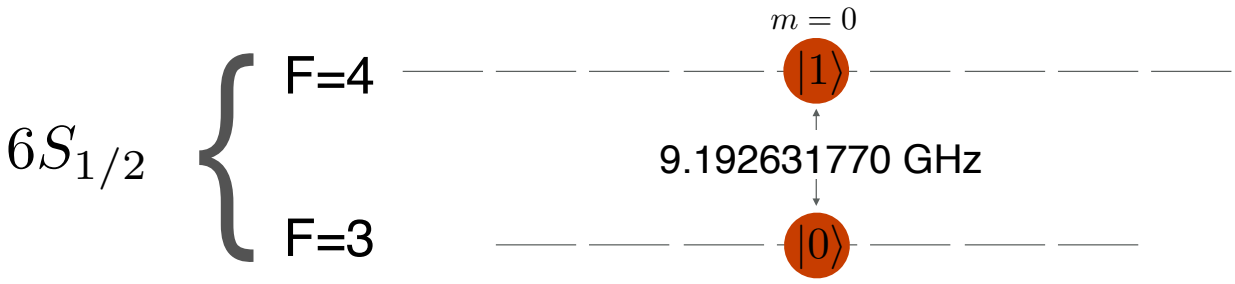


Figure 2.1: The $m = 0$ hyperfine ground states of ^{133}Cs are used as the qubit $|0\rangle$ and $|1\rangle$ in our quantum computing platform.

2.2 Neutral Atoms

Advancements in manipulating single neutral atoms have made them a viable candidate for creating a quantum register (Meschede and Rauschenbeutel [5]). The lack of net charge means there are minimal inter-atomic forces in the ground state (Saffman, Walker, and Mølmer [6]). The net zero charge also gives a low sensitivity to external electric fields in their ground state.

In a vacuum cell, we isolate single atoms from a vapor. There is no substrate, as the atoms are levitated by photon pressure from trapping light. The lack of charge makes trapping harder than with ion qubits. It is, however, a solvable problem, and the techniques we use are covered in Chapter 7.

Neutral atoms, particularly the alkali elements, can be laser cooled extremely well (Adams and Riis [7]). Interaction with the hot environment is the fundamental source of decoherence in macroscopic systems. We can use the techniques of magneto-optical trapping and optical molasses to cool our atoms to below $10\,\mu$K (see Chapters 6 and 8.2). This low temperature is a measure of how well we are able to effectively isolate the atoms from the environment.

2.3 Single Qubit Gates

The state of a single qubit is visualized as 2D vector on the Bloch sphere in a 3D (XYZ) space. We can perform rotations of the qubit state using microwaves resonant with the $9.2\,$GHz transition. The phase of the qubit precesses at this frequency, but our pulses are long compared to the precession period. So by tuning our RF generators to be resonant with the atoms we effectively put our apparatus in the rotating frame of the qubit. We define the X axis by the nominal phase of the RF generators. A rotation about the Y axis, or any axis on the XY plane, can be performed by shifting the phase of the microwave radiation.

The operations can be performed globally, or in a site-specific manner as addressed in Sections 8.6 and 13.3.

Rotations about the Z axis can be performed by combining X and Y rotations. We can also implement Z rotations directly. Using a laser detuned from the $6s_{1/2} \leftrightarrow 7p_{1/2}$ transition we can apply a differential Stark shift to the $|0\rangle$ and $|1\rangle$ states, causing a phase shift between the two.

2.4 Rydberg Atoms

When a single electron is excited to a high principle quantum number, the atom behaves very much like a hydrogen atom because the remaining nucleus and core electrons present a net $+1$ charge. At these highly excited states the energy levels go as

$$E = -\frac{R_y}{(n - \delta_{nlj})^2} \tag{2.1}$$

where $R_y = 13.60569253$ eV is the Rydberg constant. δ_{nlj} is the quantum defect, a function of species and quantum state, which accounts for the deviation from the hydrogenic energy levels due to penetration of the valence electron's wavefunction into the core electron shells. There is no strict boundary for the Rydberg states, but often above $n = 25$ is a common definition. Alkali atoms are particularly well suited for working with Rydberg states because of their single valence electron is easily manipulated, while the remaining electrons are stable in their completely filled shells. The properties of Rydberg atoms are reviewed in Gallagher [8].

The Rydberg states are extremely large. The orbital radius of the valence electron is, in the Bohr model,

$$r = \frac{4\pi\epsilon_0\hbar^2}{m_e e^2}\frac{n^2}{Z} = a_0\frac{n^2}{Z} \tag{2.2}$$

where ϵ_0 is the vacuum electric permittivity, $2\pi\hbar$ is the Plank constant, Z is the proton number, e is the elementary charge, m_e is the electron mass, and n is the excitation state. More accurately, for hydrogen the expectation value of the radius is

$$\langle r \rangle_H = \frac{a_0}{2}\left[3n^2 - \ell\left(\ell + 1\right)\right] \tag{2.3}$$

Normally atomic sizes are measured in Å (10^{-10} m), but in hydrogen for $n = 112$ we find $r = 1$ µm, which is quite enormous (Figure 2.2). The Rydberg states are on the same length scale as a biological cell.

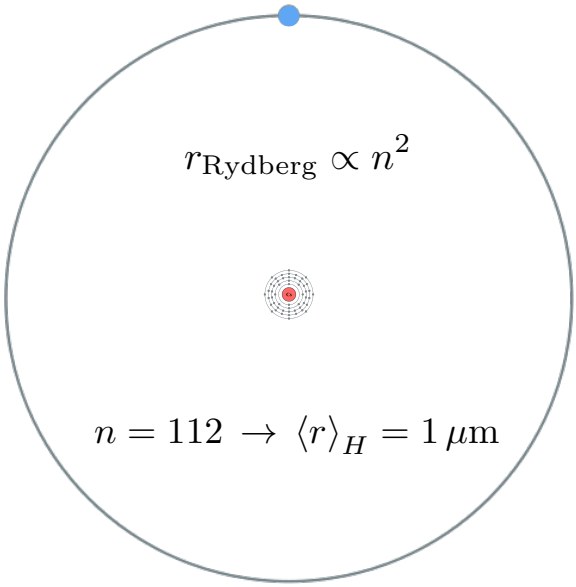


Figure 2.2: The orbital radius of the Rydberg states scale as n^2, giving very large atoms.

2.5 Rydberg Blockade

The large separation between the negatively charged electron and the positively charged core gives rise to a large dipole moment. When two Rydberg excited atoms are in proximity to each other, there is a dipole-dipole interaction which increases the energy of the doubly-excited state. This interaction has van der Waals character and the interaction energy scales with inter-atomic distance as (Saffman, Walker, and Mølmer [6])

$$B \propto \frac{1}{R^6} \tag{2.4}$$

The usefulness of this effect is such that if one atom is resonantly excited to a Rydberg state, then the energy necessary to excite a second nearby atom to the Rydberg state is shifted, and it will not be excited by the same laser frequency. The probability of a double excitation is

$$P = \frac{1}{2}\frac{\Omega^2}{B^2} \tag{2.5}$$

and the optimal Rabi frequency is $\Omega_{opt} \simeq (2\pi)^{1/3}\frac{B^{2/3}}{\tau^{1/3}}$ where τ is the radiative lifetime of the

Rydberg state which scales as $\sim n^3$ for alkali atoms (Saffman and Walker [9]).

2.6 Rydberg Blockade Phase Gate

We can use the Rydberg blockade to implement conditional logic. The fundamental Rydberg conditional phase gate uses a three pulse sequence, with one laser tuned to be resonant between the $|1\rangle$ state and the Rydberg state $|n\rangle$. We refer to the two atoms as *control* and *target*. The pulse sequence is a π pulse on the control, followed by a 2π pulse on the target, followed by a π pulse on the control as shown in Figure 2.3a.

If both atoms are in $|0\rangle$ then neither couples to the Rydberg state and the final state remains unchanged. If the control atom is in $|0\rangle$ and the target in $|1\rangle$, then the target atom makes a 2π round-trip to the Rydberg state, and acquires a π phase shift. If the control atom is in $|1\rangle$ and the target in $|0\rangle$, then the control atom will acquire the π phase shift. If both atoms are in $|1\rangle$, then the control atom excites to the Rydberg state, but the target atom is blockaded and cannot be excited. In this case the two atom state acquires a π phase shift from the control, and none from the target. See Figure 2.3b for illustration. The gate matrix is therefore:

$$C_{z_{\text{Rydberg}}} = \begin{pmatrix} 1 & 0 & 0 & 0 \\ 0 & -1 & 0 & 0 \\ 0 & 0 & -1 & 0 \\ 0 & 0 & 0 & -1 \end{pmatrix} \tag{2.6}$$

The `if` statements in the preceding paragraph mean that after the gate operation, the state of the target atom depends on the state of the control, and they are therefore entangled. It is important to note that the sequence of laser pulses is the same no matter what the qubit states are. Therefore we can implement this without any measurements which would destroy superposition states. A superposition of states on the control leads to a superposition of the target having its phase both flipped and not-flipped. This conditional logic gives our system the power to implement coherent operations between qubits.

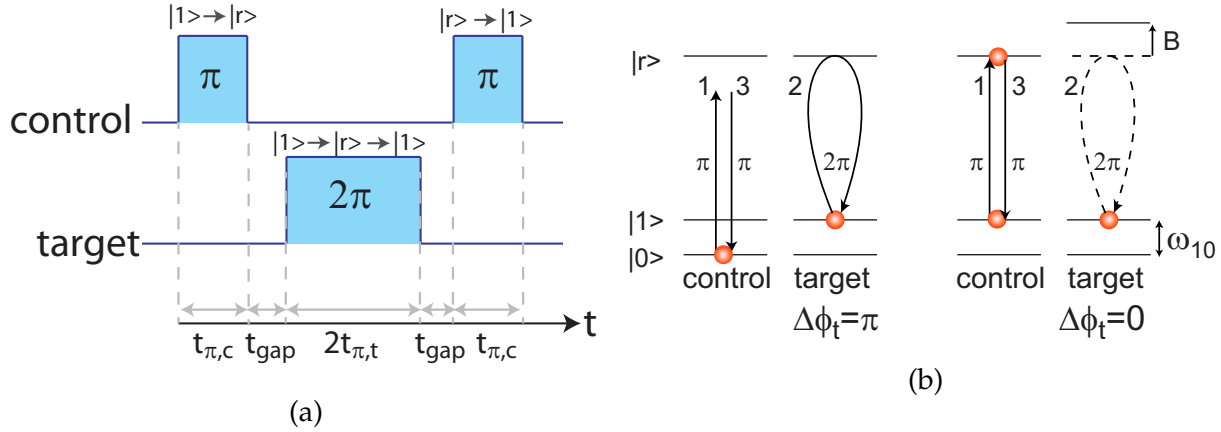


Figure 2.3: The Rydberg phase gate. (a) The three Rydberg pulse sequence that we use to implement a neutral atom qubit C_z gate. (b) Left: The control atom is not resonant with the transition to the Rydberg state, and so there is no blockade, allowing the target to acquire a π phase shift. Right: The control atom is resonant with the transition to the Rydberg state, and so the target atom is blockaded.

2.7 Universal Quantum Computing

A universal quantum computing architecture must satisfy five criteria as identified by DiVincenzo [10]. Our system satisfies these criteria as follows:

1. *A scalable physical system with well characterized qubits*:
   The lack of interaction between the neutral atoms makes it very straightforward to build an array of many thousands of qubits. We detail efforts to create large arrays of qubits in Chapter 7.

2. *The ability to initialize the state of the qubits to a simple fiducial state*:
   We use optical pumping to prepare the qubits into $|1\rangle$ as detailed in Section 8.2.4.

3. *Long relevant decoherence times, much longer than gate operation time*:
   Our T_2^* coherence time is ~ 14 ms, as discussed in Section 13.5, while the Rydberg gate times are ~ 1 µs and microwave gate times are ~ 50 µs.

4. *A "universal" set of quantum gates*:
   We can implement single qubit rotations using microwaves and Stark shifting lasers, and we implement a C_z gate using the Rydberg interaction, giving a universal set.

5. *A qubit-specific measurement capability*: We readout the qubit state using a state-selective blowaway and D2 fluorescence, as described in Section 8.2.

We might add the further goal of reaching the fault-tolerant threshold for error-correction, such that the quantum state of a logical qubit can be protected indefinitely [11, 12, 13, 14, 15]. The number of ancillary qubits necessary and the fidelity threshold necessary to realize this goal varies with different error correction codes [16, 17, 18, 19].

Such a system will have a powerful quadratic [20] or even exponential [21] speedup over classical computers. However, reaching the point where we can demonstrate empirically that capabilities beyond classical computation have been achieved, will require thousands of qubits. For example, 1154 qubits are required by Shor's algorithm to factor RSA-768, the largest number that has been factored on a classical computer [22, 23]. When implementing this along with an error correcting code, we would require several thousand qubits for such a demonstration. In this work we demonstrate an array of up to 49 qubits, and progress towards 121 qubits. Much advancement will be needed between the achievements presented here and a verifiable demonstration of computation beyond the power of classical computing, but we hope we have contributed toward that progress.

3 Quantum Search Algorithm

The quantum search algorithm developed by Lov Grover [20, 24] is a general algorithm for finding one or more "correct" answers in an unsorted database. The canonical example of a general search problem is a reverse phone book lookup. For a standard alphabetized "white pages" phonebook, it is trivial to look up a name and find the corresponding number. However, if given a phone number one must check on average $\frac{n}{2}$ entries before finding the corresponding name (for one correct answer in a database of size n). Any NP-complete problem can be described in this way, such that we could use a "brute force" search to find the right answer, but for any given query we can easily check if it is correct.

Grover's quantum search algorithm allows us to speed up this search. The algorithm requires an "oracle" which can be passed a quantum register, and which tags the correct state by inverting the phase of just that component (which is spread across all the qubits). Grover's algorithm speeds up the search process, such that it only takes $\mathcal{O}\left(\sqrt{n}\right)$ oracle calls to find the right answer.

Constructing such an oracle is not necessarily trivial, and there is no known algorithmic way to do so in general. For the phone book problem, the task of creating an oracle seems to require already knowing the correct answer, and so it defeats the utility of the algorithm. It is easier to understand the utility of Grover's algorithm in terms of an oracle defined as a function. For example, one could apply Grover's algorithm to factoring. The oracle would have stored a large composite number, and be passed a qubit register representing possible prime factors. It is trivial to test if a given query is a factor by dividing into the composite number. In this way, the oracle can test for correctness without having prior knowledge of the right answer. The same methodology could be applied to testing for correct solutions to a set of equations, or for testing for solutions that optimize some function to below a certain threshold.

Of course with Shor's algorithm [21, 25] we can achieve a much better exponential speedup for this particular problem, while Grover's algorithm only gives a quadratic speedup. The factoring problem admits this speedup due to the periodic structure. However, while it is believed by many to be impossible, it has not been proven that such a speedup is not possible on a classical computer. It has, however, been shown by Zalka [26] that for unstructured problems the quadratic speedup provided by Grover's algorithm is not possible classically, and is optimal.

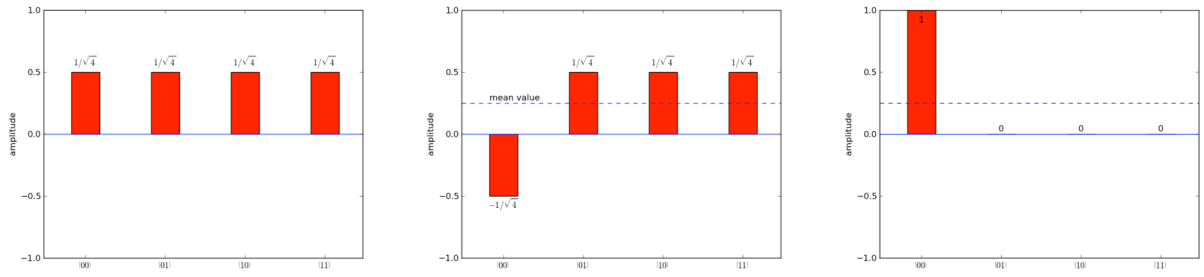
3.1 Algorithm

Grover's algorithm proceeds as follows,

1. Prepare a superposition with equal amplitude in all states.
2. Repeat $\sim \frac{\pi}{4}\sqrt{n}$ times.
   a) Consult the oracle, which tags the correct state by inverting its phase.
   b) Invert the amplitude of every state about the mean amplitude of the register.
3. Read out the qubit register to reveal the correct answer.

Let us illustrate this with an example for $N = 2$ qubits which permits a database size of $2^N = n = 4$. In this case $\frac{\pi}{4}\sqrt{2} \simeq 1$ and only one repeat is required. Suppose the correct answer that we are searching for is $|00\rangle$, then the sequence of states, shown also in Figure 3.1, is:

1. Equal amplitude in all states:
   $\frac{1}{\sqrt{4}}\left(|00\rangle + |01\rangle + |10\rangle + |11\rangle\right)$
2. Repeat once:
   a) Consult the oracle:
   $\frac{1}{\sqrt{4}}\left(-|00\rangle + |01\rangle + |10\rangle + |11\rangle\right)$
   b) Invert the amplitude of every state about the mean amplitude $(\frac{1}{4}\left(-\frac{1}{\sqrt{4}} + \frac{1}{\sqrt{4}} + \frac{1}{\sqrt{4}} + \frac{1}{\sqrt{4}}\right) = \frac{1}{4})$ of the register:
   $(1 \times |00\rangle + 0 \times |01\rangle + 0 \times |10\rangle + 0 \times |11\rangle)$
3. Read out: $|00\rangle$



(a) (b) (c)

Figure 3.1: An example of the sequence of states in Grover's algorithm for 2 qubits with the correct state $|00\rangle$. (a) Equal superposition of all states. (b) After the oracle call. (c) After inversion about the mean.

3.2 Number of Iterations

The 2 qubit example finds the correct answer with only one oracle call. Classically we expect that with only one call we have only a 25% chance of finding the correct answer, and so any performance above this level demonstrates non-classical behavior, as discussed in Chapter 15.

In Figure 3.2 we show how the quadratic speedup is determined for general N. Consider the state of the qubit register as a vector on a plane. Let the plane's axes be defined by the vector of all wrong answers $|wrong\rangle$, and the vector of all right answers $|right\rangle$. We allow for multiple right answers m, out of a total database size n. As the algorithm proceeds the state of the qubit register will stay in this plane. Let O be the oracle call operator, and M be the operator that inverts about the mean. We begin in the state $|\psi\rangle$ which is the equal superposition of all states. If $m \ll n$ then $|\psi\rangle$ is close to $|wrong\rangle$.

Figure 3.2a shows the first Grover iteration. The oracle call inverts only the component of $|\psi\rangle$ that is in the direction of $|right\rangle$, which has the effect of reflecting the state across $|wrong\rangle$ to the state $O|\psi\rangle$. Define the angle moved as θ. The mean state is now the component of $O|\psi\rangle$ in the direction of $|\psi\rangle$, and therefore inversion about the mean reflects $O|\psi\rangle$ across $|\psi\rangle$ by an angle 2θ to the state $MO|\psi\rangle$. The total angle moved in this iteration is θ toward $|right\rangle$.

Figure 3.2b shows the second Grover iteration. The oracle call and inversion about the mean are repeated again, which again moves the state by an angle θ toward $|right\rangle$.

To achieve the highest fidelity readout at the end of the algorithm, we want to repeat the Grover iteration however many times will bring the state vector as close as possible

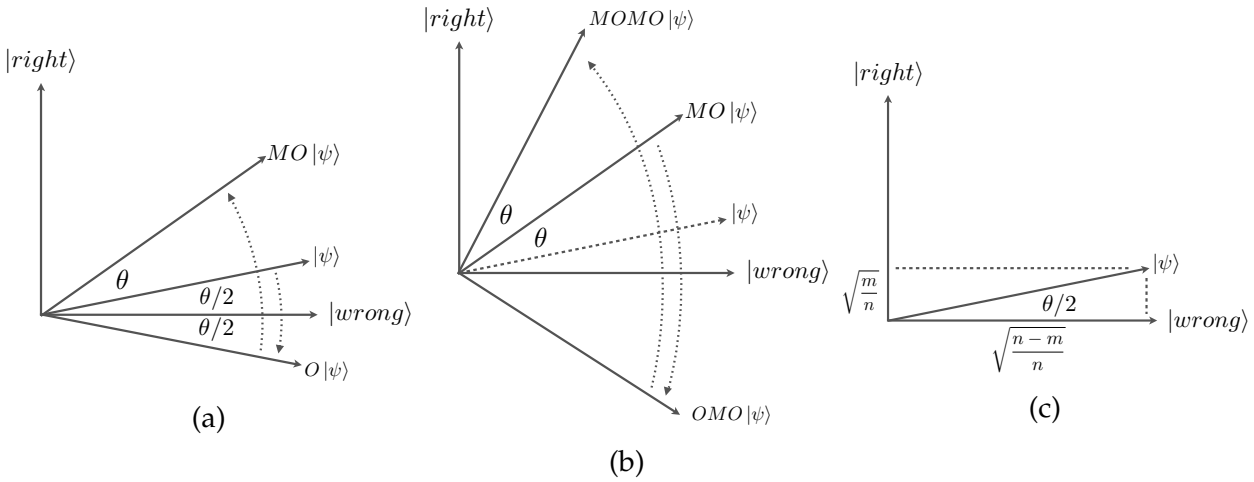


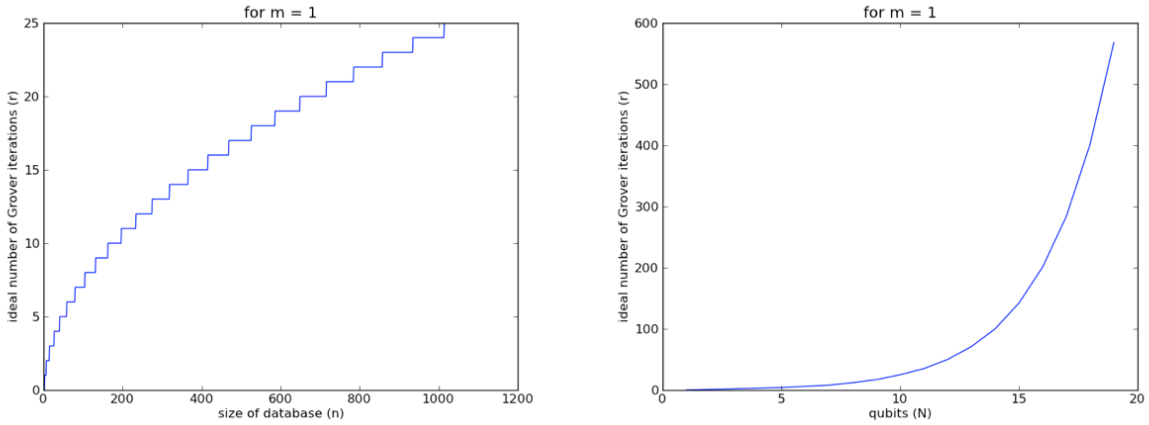
Figure 3.2: The Grover algorithm visualized as rotation of a state vector in a plane. Adapted from Nielsen and Chuang [27]. (a) The first Grover iteration, consisting of an oracle call and inversion about the mean, rotates by an angle θ. (b) The second and every successive Grover iteration rotates by θ again. (c) The optimal number of iterations is a function of the number of right answers m, and the database size n.

to $|right\rangle$. Figure 3.2c shows how the angle θ is determined as a function of the number of right answers m, the database size n, and the number of wrong answers $n - m$. We then find the optimal number of iterations by dividing the distance-to-be-rotated by the rotation-per-iteration:

$$
\begin{aligned}
iterations =& \frac{\arccos \langle right|\psi\rangle}{\theta} && (3.1)\\
=& \frac{\arccos \sqrt{\frac{m}{n}}}{2 \arccos \sqrt{\frac{n-m}{m}}} && (3.2)\\
=& \frac{\sim \frac{\pi}{2}}{\sim 2\sqrt{\frac{m}{n}}} && (3.3)\\
=& \frac{\pi}{4}\sqrt{\frac{n}{m}} && (3.4)\\
=& \mathcal{O}\left(\sqrt{n}\right) && (3.5)
\end{aligned}
$$

where we have simplified by assuming $m \ll n$.

And so we see the quadratic speedup, where the number of iterations scales as $\sqrt{n}$ in the database size, shown in Figure 3.3a. Plotted instead as a function of number of qubits in Figure 3.3b, we see that the iterations still increase exponentially as $2^{N/2}$.



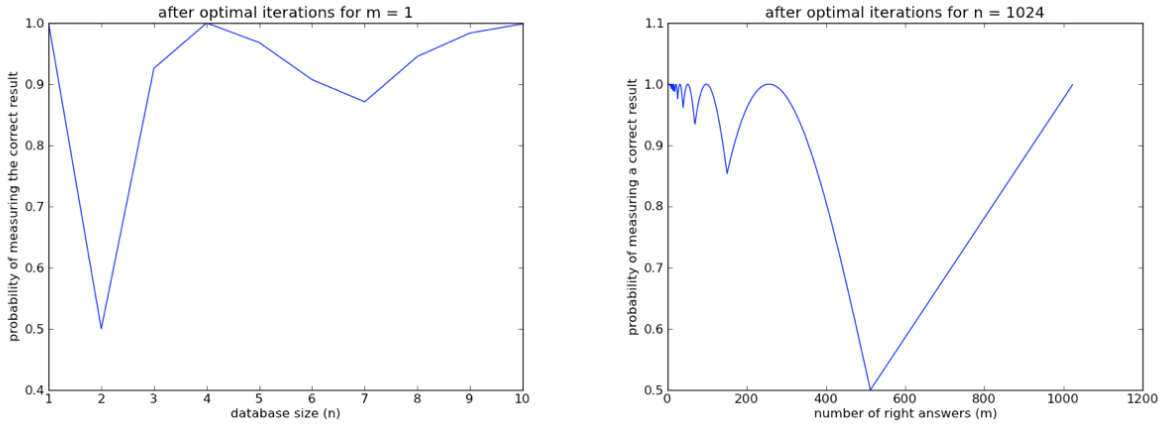
(a) (b)

Figure 3.3: The number of Grover iterations required (for $m = 1$) as a function of (a) database size and (b) number of qubits.

3.3 Fidelity of Result

The two qubit example gave the right answer with probability 1. In general the Grover rotation does not always exactly hit $|right\rangle$, and the probability of success is plotted in Figures 3.4a and 3.4b as a function of database size, and number of right answers, respectively. It is possible to modify the Grover algorithm as reported by Long [28], such that the oracle does not apply a π phase inversion, but rather a different phase that takes the rotation out of this plane, such that the final result is always identically $|right\rangle$.

We choose to focus on implementing Grover's algorithm because of its generality, and also because in a Rydberg blockade based computer we can achieve an order of magnitude improvement by using a native multi-qubit gate, as described by Mølmer, Isenhower, and Saffman [29]. The implementation of the algorithm in our system and results of attempted Grover algorithm experiments are given in Chapter 15.



(a) (b)

Figure 3.4: The probability of success for the Grover algorithm as a function of (a) database size (for $m = 1$) and (b) number of right answers (for $n = 1024$).

4 Undecidable Propositions of Quantum Logic

Before we describe the nuts-and-bolts experimental work of our project, let us in this chapter take the time to consider some of the theoretical underpinnings of quantum information. The universality of the quantum computer was addressed by Deutsch [30] and allows us to abstract the functionality of a quantum mechanical system as a purely logical device. However, as the quantum speedup is the raison d'être for our work in quantum computing, it is worthwhile to consider what aspects of the quantum computing platform are inherently different from classical computing. Here we consider the question of *incompleteness*.

4.1 Introduction

In this chapter we seek to extend the methods of Gödel's Incompleteness Theorems, which are statements on systems of natural numbers, to quantum logic. We will see what conclusions we can draw on systems of quantum states.

In 1930, Kurt Gödel proved that any formal system of arithmetic which is sufficiently powerful to express addition and multiplication, that is to say what we consider to be the bare minimum for computation, has a fatal flaw. Gödel devised a particular true statement that he could show was not provable in the system, and therefore showed the system to be incomplete. He also showed that if the statement were provable, its negation would also be provable, and so we are forced to choose between an incomplete mathematics, and an inconsistent one. The former is presumed to be less insidious, and so we choose incompleteness over inconsistency. We will summarize the proof in Section 4.2 below.

As Gödel's proof shows that there are true statements which cannot be proved, it puts fundamental limits on computation. The process of deriving a proof, starting from axioms and using rules of inference, is identical to the process of computing a solution, where we start from an initial condition and use logic gates to reach our goal. The statements which are undecidable are not only ones of interest to the logical trickster or philosopher. They have been shown to include for example, deciding whether a Diophantine equation (an equation of the form $\alpha x^a + \beta y^b + \gamma z^c + \cdots = 0 \, for \, (\alpha, a, \beta, b, \gamma, c, \dots) \in \mathbb{N}$, of which Fermat's Last Theorem is a specific example) has a solution, and also statements about prime numbers, to name a couple. As quantum computer scientists, where the whole value of the field hinges on what is (tractably) computable in different models of computation (including issues of complexity class and whether $P = NP$), we ought to be keenly interested in what

is, and what is not, computable.

We see an irresistible similarity between Gödel's Incompleteness Theorem and Heisenberg's Uncertainty Principle. Both tell us there are limits on what is knowable. This draws us to explore the application of Gödel's theorem to quantum mechanics.

Gödel's proof applies however only to natural numbers. To apply his results blindly to computation on real or complex numbers is not valid. In classical computing however, all computations be they on `ints` or `floats`, are done using integer math, and so they will be subject to incompleteness. Whether Gödel's results would hold in a truly analog system, where the full breadth of real numbers are available, is an open question. In quantum logic, however, as in the physical universe, information is held not in discrete integers, but in wavefunctions which can be expressed as weighted sums of discrete basis states, with those weights being (truly) complex valued. We have a hybrid system, with some aspects of natural numbers, and some of complex numbers. Leopold Kronecker famously said *"God, made integers; everything else is the work of man."*, but we physicists believe God works using quantum states, so then integers must then be the work of man.

Given sufficient resources, a quantum mechanical system can be simulated to arbitrary precision on a classical computer. Because of this, we expect that incompleteness will hold for the quantum logic system. Nevertheless, it is an interesting problem to attempt to directly apply Gödel's proof to a quantum mechanical system. It is not immediately obvious that the procedure is applicable, and exploring this direction will raise interesting new questions.

In Section 4.3 we propose a mapping of the symbols of propositional logic to quantum states, echoing Gödel's mapping of symbols to natural numbers. In Section 4.4 we evaluate the consequences of that mapping to discuss the applicability of the Incompleteness Theorem to quantum mechanics. The main conclusion of this paper is given in Section 4.4.1. In Section 4.5 we propose an alternate mapping to density matrices to include mixed states in the applicability of our results.

4.2 Gödel's Incompleteness Theorem, Briefly

In *On Formally Undecidable Propositions of Principia Mathematica and Related Systems, I.* [31], Kurt Gödel presents a rigorous mathematical proof of the incompleteness of our most basic mathematical systems. He furthermore shows that any attempt to patch this vulnerability with a more complicated system is doomed to create a new vulnerability. In this section

we give a very non-rigorous summary of the proof.

Gödel's proof deals with the system *Principia Mathematica* [32] (PM), one version of symbolic logic as formalized by Whitehead and Russell, which contains the basic rules that we usually simply call "logic", and the foundations of mathematics on the natural numbers (non-negative integers including zero). Whitehead and Russell presumed that their system of axioms and rules of inference could be used to derive all truths about natural numbers. Gödel showed this not to be the case.

Our notation here mostly echoes that of Gödel [31], but borrows from Hofstadter [33] as well.

4.2.1 Mapping Statements to Gödel Numbers

Gödel starts by creating a mapping of the typographical symbols of PM to natural numbers, similar to how a modern computer might encode characters into ASCII code. The mapping is as follows:

$$\begin{array}{ccc} 0 & \rightarrow & 1 \\ f\,(succession) & \rightarrow & 3 \\ \sim\,(negation) & \rightarrow & 5 \\ \vee\,(or) & \rightarrow & 7 \\ \Pi\,(for\,all) & \rightarrow & 9 \\ (& \rightarrow & 11 \\ ) & \rightarrow & 13 \\ x\,(a\,variable\,of\,rank\,n) & \rightarrow & p^{n+1} \text{ where p is a prime } > 13 \end{array} \tag{4.1}$$

And so for any statement, we can map that statement (one-to-one) to a finite series of natural numbers. Then a series of numbers $(n_1, n_2, ...)$ is mapped (one-to-one) to one number $2^{n_1}3^{n_2}5^{n_3}...p_k^{n_k}$ where p_k is the k^{th} prime. These mappings are unique, and so we can always convert a number back into a statement. These symbols seem like a limited vocabulary, but in *Principia Mathematica* these are used to derive all the familiar relations such as $=, \exists, +, *$, etc., so all statements can be expressed in terms of this basic alphabet. However, if we wish we can simply add more symbols to our mapping. For example if for convenience we also map $=\rightarrow 17$, and $+ \rightarrow 19$ (and remap the x variables accordingly), then we could map the (false) statement $1 + 2 = 4$ to $f0 + ff0 = fffff0 \rightarrow (3, 1, 19, 3, 3, 1, 17, 3, 3, 3, 3, 1) \rightarrow 2^3 3^1 5^{19} 7^3 11^3 13^1 17^{17} 19^3 23^3 29^3 31^3 37^1$ which is the natural number:

$$50421252020354593878163878814896254400762206666564941406250000$$

Furthermore, we can also take a list of statements to be a list of natural numbers. A proof, which is just a list of statements whereby rules of inference are used to go from one line to the next, can then be mapped to a list of numbers where certain mathematical rules allow us to go from one true statement to the next. By the same rules as above, an entire proof can then be uniquely mapped to one natural number. Note that while all natural numbers can be mapped to string of symbols, they do not all make grammatically correct statements in PM.

By making these mappings, Gödel defines all logical statements within PM as natural numbers, but since PM expresses statements about natural numbers, this simple mapping gives the system the power of introspection, and can now make statements about itself. These mappings are typically called Gödel numbers. The symbol $R(n)$ refers to the statement corresponding to the Gödel number n, a relationship which is definable in PM.

We may from here on out, speak of "proving" numbers and other such concepts that we heretofore applied only to statements.

4.2.2 Clever Substitution

Next we use the notation $[\alpha; n]$ to mean the following method of substitution: take the statement α which has one free variable, replace that free variable with the number n, and return the Gödel number of the resulting statement. This method is definable in PM, and so the method itself has a Gödel number.

Then if we write $[R(n); n]$, we are asking for a clever self-substitution: take the statement of one free variable which is encoded for by the Gödel number n, and replace the free variable with that Gödel number which codes for the statement itself, then return the Gödel number of the resulting statement. Gödel's genius is evident in this step, as here he tricks the system into making an indirect self-reference to itself. Again, as this is all definable in PM, and so the schema $[R(n); n]$ has a Gödel number.

4.2.3 Self-reference to Unprovability

Gödel then gives the statement $n \in K \equiv \overline{Provable([R(n); n])}$ which means that: n is in the set K `iff` (some X is the Gödel number returned by doing a self-substitution of n into the statement $R(n)$ that it codes for) AND (X is not provable in PM). Again provable means

that number could be reached from axioms by the allowed rules of inference. Gödel calls this statement q. We are now armed with all the tools we need to make the final stroke.

Consider $[R(q); q]$. This is the Gödel number we get by taking this statement q about the set of unprovable Gödel numbers, and asking whether or not the statement itself is in the set that it defines. Following the lead of Hofstadter [33], we show our admiration by calling Gödel's master statement: G.

4.2.4 Consequences of G on PM

If G is a theorem of PM, that is if it were provable by starting with axioms and using rules of inference to end up at G, then it must be true. However, G says that G itself is in the set of unprovable numbers, which means G is false. So we have a contradiction. If G is a theorem of PM, then PM is inconsistent, and that is most unacceptable for a mathematical system.

The alternative is for G not to be a theorem of PM. That is, G is unprovable. But G says that it is unprovable. So if G is not a theorem, then it is true. There are then true statements about numbers that are not provable in PM. PM is incomplete, despite Whitehead and Russell's best efforts to the contrary. There are mathematical truths that PM cannot decide. It cannot through any finite calculation arrive at either the number G or $\sim$G.

4.2.5 PM is Unrepairable

One may attempt to fix PM by simply adding G as an axiom, defining it to be manifestly true. However, the new system PM+G is just as expressive as before, and it also has a statement about sets of unprovable numbers. Albeit that statement G' has a different Gödel number than G before, but we nevertheless can perform self-substitution on this statement, and arrive at incompleteness yet again.

This process is the same as that of Cantor diagonalization, which is used to show that real numbers are uncountably infinite. Take a set of real numbers, let us use an example in base 2 for clarity:

$$\begin{array}{ccccc} 1 & . & 0 & 1 & 1 \\ 0 & . & 1 & 1 & 0 \\ 0 & . & 0 & 0 & 1 \\ 1 & . & 1 & 1 & 1 \end{array} \tag{4.2}$$

These numbers can have any number of decimal places, so we need not worry about making this list square. Take the diagonal elements: $(1, 1, 0, 1)$, then take the negation of that: $(0, 0, 1, 0)$. The resulting number: 0.010, is guaranteed not to be on the list, because it has at least one digit different from every number already on the list.

Similarly, no matter how many times we add G, G′, G″,... to the axioms of PM, there are still unprovable statements not on the list of calculable Gödel numbers.

4.3 Mapping Statements to Quantum States

Our goal is now clear. To explore whether a formal system of logic based on quantum mechanics (QM) presents us with the ability to do calculations which would not terminate on a classical computer. We do this by repeating Gödel's method, but on a system of quantum states, rather than a system of real numbers. As stated in the introduction, our motivation is that while probability amplitudes are continuously valued complex numbers, the basis states are discrete. The common practice in quantum computing of labelling product states on multiple qubits as $|0\rangle$,$|1\rangle$,$|2\rangle$,... makes the comparison to natural numbers obvious.

We begin as Gödel did, by mapping the basic logical symbols of QM. The mapping is arbitrary, so long as it is one-to-one, but if incompleteness is shown for any mapping, then it is a property of the system. The mapping need not be "onto" since not all strings of characters are grammatically correct statements of QM. We will need all the same logical expressiveness as PM, but we can allow ourselves to take a shortcut and at least include an equals sign:

$$\begin{array}{rcl} |0\rangle & \rightarrow & |1\rangle \\ a^{\dagger}\,(succession,\, creation) & \rightarrow & |3\rangle \\ \sim\,(negation) & \rightarrow & |5\rangle \\ =\,(equality) & \rightarrow & |7\rangle \\ & etc... & \end{array} \tag{4.3}$$

Note particularly that just as Gödel leverages the succession function f so the natural numbers themselves could be encoded using only a few symbols (thereby freeing up room in the alphabet for other symbols), we have done the same with the creation operator $a^{\dagger}$. For any statement we then have a list of states $(|n_1\rangle, |n_2\rangle, |n_3\rangle, \dots)$, and we will combine those into just one state with the mapping $(|2^{n_1}\rangle \otimes |3^{n_2}\rangle \otimes |5^{n_3}\rangle \otimes \dots \otimes |p_k^{n_k}\rangle)$ where p_k is the k^{th} prime. So then the k^{th} qubit register is in the $p_k^{n_k}$th state. This may require a tremendous

number of qubits, just as storing Gödel's numbers may require a tremendous number of bits, but as this is an exercise in theory, we have that liberty.

We have not yet dealt with superpositions, operators, or probability amplitudes.

4.3.1 Discretized Mapping

As a first attempt let us take the easy road and deal with only a finite set of operators. One way to map the operators is:

$$\begin{array}{rcc} X \text{ on qubit n} & \rightarrow & |11^n\rangle \\ Y \text{ on qubit n} & \rightarrow & |13^n\rangle \\ Z \text{ on qubit n} & \rightarrow & |17^n\rangle \\ C_{\text{NOT}} \text{ control qubit m, target qubit n} & \rightarrow & |19^m 23^n\rangle \\ & etc... & \end{array} \tag{4.4}$$

We can now encode statements about quantum states, using quantum states. For example, the (false) statement $X_1 |00\rangle = |11\rangle$ becomes $(|11^1\rangle, |1\rangle, |1\rangle, |7\rangle, |3\rangle, |1\rangle, |3\rangle, |1\rangle)$ $\rightarrow |2^{11}\rangle |3^1\rangle |5^1\rangle |7^7\rangle |11^3\rangle |13^1\rangle |17^3\rangle |19^1\rangle$.

To address the problem of how to encode superpositions of basis states, with non-integer probability amplitudes, let us say that we will discretize the phase space into a finite number of points. Each of these coefficients can then be mapped to a unique state. This is not an unrealistic assumption from an experimental standpoint, where detectors of any kind only have a certain number of bits of resolution. However, it is clearly an unsatisfying assumption, and we will remove this assumption in the next subsection.

First let us discuss the consequences of this assumption. By reducing all probability amplitudes to a finite set, all of our symbols are now effectively mapped to natural numbers. The basis states were already discretized, and now we add in more discretized numbers, so now although we have written everything in Dirac notation, the mapping is still to natural numbers.

The conclusions of Gödel's proof then hold in full for this system. We have simplified the system until it is isomorphic to the natural numbers, and so there will be no difference in what is computable.

4.3.2 Superposition Preserving Mapping

In the mapping proposed in Section 4.3.1, we eliminated everything which makes quantum mechanics special, and so it is not surprising that the results were lackluster. Even if our experimental apparatus can only record results to a finite precision, the evolution of a quantum system still samples the states continuously. Let us find a more complete way to handle superpositions. The most straightforward way seems to be to simply preserve the probability amplitudes and superpositions as we make the encodings. So let:

$$\frac{1}{\sqrt{2}}|0\rangle - \frac{i}{\sqrt{2}}|1\rangle \rightarrow \frac{1}{\sqrt{2}}|1\rangle - \frac{i}{\sqrt{2}}|31\rangle \tag{4.5}$$

We have suddenly abandoned a system of strictly natural numbers, but that is our aim here, to establish a system of logic on quantum states which can make statements about itself. We only need to ensure that this mapping is unique. To concatenate a list of characters, we maintain our previous rule of using primes to make sure the ordering is preserved, and use the same base for all kets in a given state. For example the (non-theorem) statement:

$$Z_1(\frac{1}{\sqrt{2}}|0\rangle - \frac{i}{\sqrt{2}}|1\rangle) \rightarrow (\left|17^1\right\rangle, \frac{1}{\sqrt{2}}|1\rangle - \frac{i}{\sqrt{2}}|31\rangle) \rightarrow \left|2^{17}\right\rangle \otimes (\frac{1}{\sqrt{2}}\left|3^1\right\rangle - \frac{i}{\sqrt{2}}\left|3^{31}\right\rangle) \tag{4.6}$$

And so we can make a one-to-one map between statements of QM and quantum states. We have not yet dealt with arbitrary operators. This will be attempted in Section 4.5. This is less of a serious simplification, because most quantum algorithms are built from a finite set of gates.

4.4 Gödelizing QM

4.4.1 QM is Incomplete

Now that we have a way to express statements about QM within QM, let us explore the consequences. We have all the same symbolic logic available as in PM, and so we can write the statement q, which was $n \in K \equiv \overline{Provable([R(n); n])}$, except now we use quantum states and write $\psi \in K \equiv \overline{Provable([R(\psi); \psi])}$. This statement itself, as before, can be Gödelized to give $R(q)$, which is now a Gödel state, rather than a Gödel number. Then we consider the statement$[R(q); q]$ which self-substitutes q into itself to give us the master statement, whose Gödel state we call $|G\rangle$.

But if we are able to write the state $|G\rangle$, that is all that it takes to be subject to the consequences of Gödel's proof. Despite the analog nature of the probability amplitudes, the discrete nature of the basis states has dominated and allowed us to create a mapping for the alphabet of QM to the very states it discusses. From there it is unavoidable that there will be unprovable statements.

This result is a direct refutation of the conclusions of Panković and Predojević [34]. Simply put, incompleteness does in fact apply to quantum logic.

This is the expected result, because quantum mechanics can be simulated, albeit inefficiently, on classical computers. The situation we have examined is similar to that of probabilistic computation. We have, however, taken a new approach to arrive at this conclusion, which gives a fresh perspective on the problem.

4.4.2 Extending QM

4.4.2.1 Superpositions of True and False

This is not the end of interesting behavior for QM however. In PM, we could evaluate a statement like $Provable(a\wedge \sim a)$ and this will always be false. However in QM we can create the statement $Provable(\psi\oplus \sim \psi)$, where we explicitly write the direct sum to emphasize that this is a quantum superposition. Through the linearity of quantum mechanics, this is $Provable(\psi) \oplus Provable(\sim \psi)$. How exactly to interpret $|true\rangle \oplus |false\rangle$ (where $|true\rangle$ is the Gödel state of some true statement, and $|false\rangle$ is the Gödel state of some false statement) is not clear. On their own, $|true\rangle$ encodes for a theorem, while $|false\rangle$ encodes for a non-theorem. Together it seems as if $|true\rangle \oplus |false\rangle$ codes for a theorem, as it was reachable via the simple substitution operation into a statement of QM. However, interpreted as to content we must cede that is both true and false at the same time, a quantum superposition of theorem and non-theorem.

The implications of this are not clear. We could accept the (usually rejected) consequence of Gödel's theorem that the system is inconsistent. Mathematicians routinely reject this in favor of incompleteness, but perhaps we as physicists could embrace this conclusion by interpreting it as quantum superposition.

4.4.2.2 Supernatural Numbers

In the Section 4.2.5, we discussed attempting to patch PM by adding G as an axiom. Attempting to patch QM by adding $|G\rangle$ as an axiom would similarly fail to remove the

incompleteness. However, there are other options.

Hofstadter [33] suggests extending PM by adding ∼G as an axiom. This is awkward, because we consider G to be manifestly true. However, that is a matter of interpretation, guided by assumptions outside the system, and we can define it to be true inside the system without a second thought. The result is that we assert G is a theorem. However, we can also recursively step through the natural numbers, and it can be shown (not here) that for any natural number tested, that number is not G. But if G is a theorem, that number must exist, so where then does it lie? Hofstadter's claim is that G is a "supernatural number".

Supernatural numbers are an extension of the natural numbers [35, 36, 37]. Any natural number is definable by its prime factorization $n = \Pi_p p^{n_p}$ where p are prime numbers and n_p are natural numbers (of no relation to complexity classes P and NP). Supernatural numbers relax the requirement that they can all be reached by successive addition of $+1$ by allowing allowing $n_p = \infty$. We now have numbers higher than all natural numbers, but that are quite distinct from each other. In other words not all infinities are equivalent. For example, in supernatural arithmetic $2^\infty \neq 3^\infty$. These numbers are still countable, however. Hofstadter suggests without elaboration that the supernaturals can be indexed via a triplet. We suggest one possible such indexing of all supernaturals using 3 natural indices as $(naturals(n), \infty(n), 0(n))$ where $naturals(n) = \Pi_p p^{n_p}$ for $n_p \in naturals$ gives a unique number encoding for the factors with finite non-zero exponents, $\infty(n) = \Pi_p p^1$ for p with $n_p = \infty$, and $0(n) = \Pi_p p^1$ for p with $n_p = 0$ and $p < max(p : n_p \in naturals)$ (to ensure that $0(n)$ is finite). With this indexing, multiplication is trivial, as $naturals(m * n) = \Pi_p p^{m_p + n_p}$, $\infty(m * n) = \infty(m) \cup \infty(n)$, and $0(m * n) = 0(m) \cap 0(n)$.

With all this in mind, we can consider the analogous concept for our system QM. Quantum numbers come to mind, as in the triplet (n, l, m) for atomic states. But there we have the restrictions $l < n$, $-l < m < l$ which do not have a counterpart in the supernatural numbers. Looking at our mapping scheme for QM, we see that we have identified the k^{th} qubit register as being in the $p_k^{n_k}$ state, and so we can perhaps identify supernatural states as encoding for some qubit register to be in the $n = \infty$ state. This corresponds to the continuum, a free particle, and perhaps then an open system.

4.4.2.3 $|G\rangle \oplus \sim |G\rangle$ as an Axiom

If we can discuss superpositions of $|true\rangle \oplus |false\rangle$ as we did in Section 4.4.2.1, then we can take the bold step of extending QM by adding $|G\rangle \oplus \sim |G\rangle$ as an axiom. By the linearity of all quantum operations, all derivations that utilize this axiom then give us superpositions

of the results from each. So we get states both incomplete and supernatural at the same time. How to interpret this is far beyond the scope of this chapter.

We should look in particular at the effect on one state, however, and that is $|G'\rangle$, the Gödel state in the system repaired by axiom $|G\rangle$. In the new system patched with $|G\rangle \oplus \sim |G\rangle$, $|G'\rangle$ no longer exists on its own, but instead is a quantum superposition of the special incompleteness inducing statement, and simultaneously a statement that is not at all special in this new system. What then, is its interpretation. . . ?

4.5 Encoding Operators and Density Matrices

In this final section we expand the generality of this discussion by relaxing the requirement for a finite set of operators, and also the requirement for pure states. We propose a method of mapping of statements that include arbitrary operators and density matrices.

For all these various mappings, we must make room for the logical symbols and statements by mapping naturals (or pure states) using only a subset of the code space. Gödel uses the succession function f to achieve this, and we echoed him by using the creation operator $a^\dagger$.

Our way of mapping both operators and density matrices, while still leaving some room for symbols and statements, will be to write the matrices out in long form using projection operators. For a density matrix we have:

$$\hat{\rho} = \sum_i p_i \, |\psi_i\rangle \, \langle\psi_i| \tag{4.7}$$

We already have notation for $|kets\rangle$ and variables. The summation could be written out as a long sum, derived from the more basic logical symbols or defined explicitly as a symbol in the alphabet. We lack a way to distinguish between $\langle bras|$ and their dual $|kets\rangle$, however. Our solution to this will be to add explicit signifiers $BRA(bra) = \langle bra|$ and $KET(ket) = |ket\rangle$ which can be added to the symbolic alphabet. Any density matrix can now be broken down into a statement on bras and kets, which allows it to be expressed as a quantum state using our mapping from Section 4.3.

Operators are more general than density matrices, but can also be defined in terms of projection operators:

$$A = \sum_{i,j} a_{ij} \, |\psi_i\rangle \, \langle\psi_j| \tag{4.8}$$

Operators therefore will yield to the same mapping scheme.

We have then defined how to make a one-to-one mapping for statements in QM that include operators and density matrices. By the same logic as in Section 4.4 then, these complete and unrestricted statements can be self-referential, and will ultimately yield to the methods of Gödel's proof. We then find QM to be inconsistent or incomplete, even in the absence of any simplifying assumptions.

4.6 Conclusions

We have shown that by using the methods of Gödel's Incompleteness Theorems, we find that a formal system of logic which makes statements about quantum states, and uses the laws of quantum mechanics for its rules of inference, will be either inconsistent or incomplete.

Although implied, we have not proven rigorously that the mappings presented here are one-to-one, and this is a potential source of error, and also a direction for future work.

Part II

Methods

5 System Layout

The AQuA experiment requires two full optical tables of lasers to create the colors of light necessary for cooling, trapping and manipulating the atomic qubits. The actual atomic qubit array, however is composed inside a small vacuum chamber. Fiber optics are used to transport light from the various lasers to the vacuum chamber. Supporting optics around the vacuum chamber are used to steer the beams, focus the light onto single atoms, and relay atom fluorescence onto a camera. This chapter covers the design of the vacuum chamber and supporting optics.

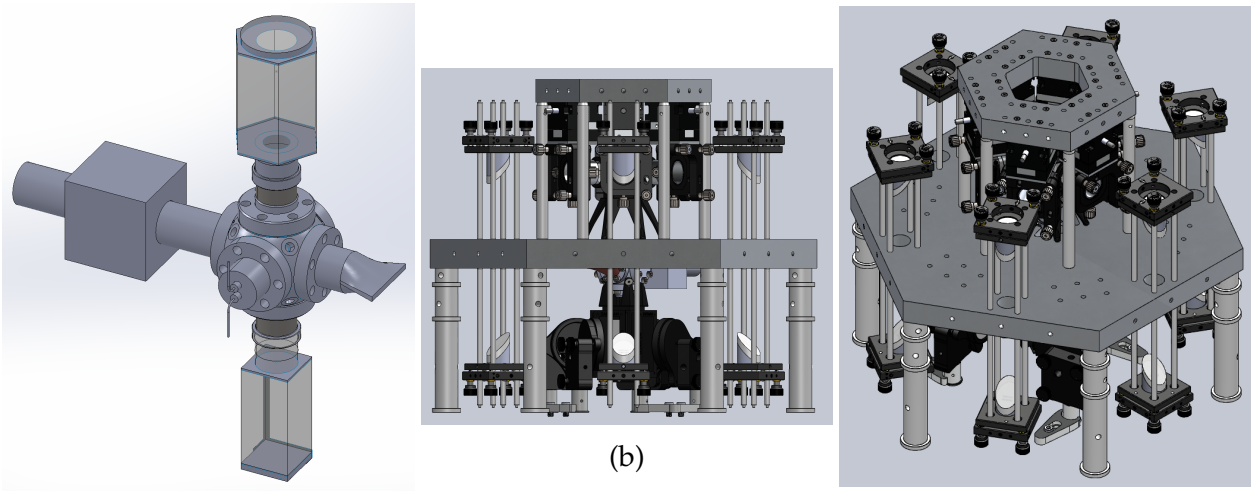
5.1 Two Stage Cooling

The atomic qubit array is composed inside a two cell vacuum chamber, built by ColdQuanta, and shown in Figure 5.1a. The lower chamber contains a 2D MOT and the upper chamber contains a 3D MOT and the trap array. A small aperture separates the two chambers. Atoms are pushed from the 2D MOT to the 3D MOT. By separating the chambers, we can achieve fast loading while still having low background pressure. An ion pump is connected to the upper chamber, and keeps the experiment at 10^{-11} Torr. The lifetime of the cold atoms in our trap array is limited by collisions with hot background atoms. The background atoms are ~ 300 K due to collisions with the room temperature walls of the chamber. As such, any collision will remove an atom from the array. We find a background limited trap lifetime of up to 25 s in a single red-detuned dipole trap in the upper chamber.

To support this double cell, and the focusing optics that surround it, we have created a two-level structure. Because of the appearance, as shown in Figure 5.1b and 5.1c, we have named this structure the *wedding cake*.

The lower chamber is an all glass cell with a square profile. Inside, a small cesium source provides ^{133}Cs atom vapor when a 2.5 A current is used to heat the emitter. A "2D" MOT is created using two pairs of large (~ 2 cm) retro-reflected beams in the horizontal plane to cool the atoms, as shown in Figure 5.2a. Two pairs of orthogonal horizontal anti-Helmholtz electromagnet coils provide spatial confinement. The resulting atoms are trapped in a 1D vertical line. The position of the line can be aligned with the inter-chamber aperture by adjusting the relative currents in each coil.

The upper chamber, shown in detail in Figure 5.2b is a hexagonal pyrex cell, with silicon end plates attached by anodic bonding. The hexagonal shape gives excellent optical

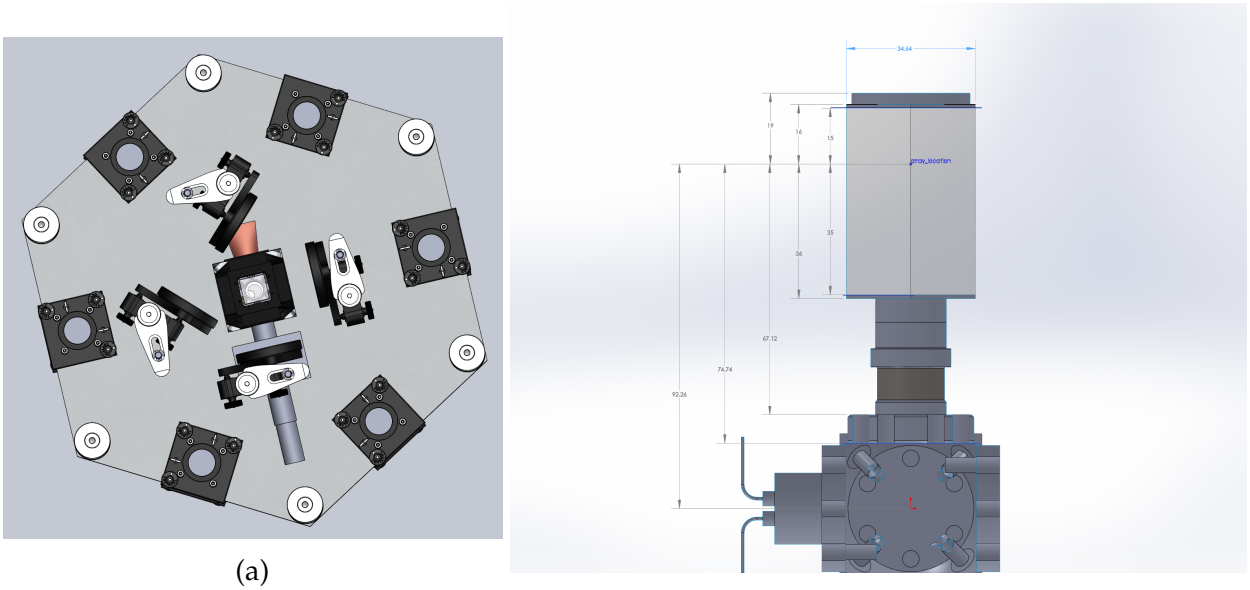


(a) (b) (c)

Figure 5.1: The double vacuum chamber. (a) A 2D MOT is formed in the lower square cell, and a 3D MOT and trap array is formed in the upper hexagonal cell. The central stainless steel spherical cube attaches the two cells to the ion pump. (b) and (c) The so-called *wedding cake* structure that supports the double-cell.

access, allowing us to bring in many independent beams to the experiment. A "3D" MOT is formed within this cell using three pairs of retro-reflected beams. Two pairs of (~ 2 mm) beams are brought in horizontally and retro-reflect through opposing windows. The third pair comes in nearly vertically, and reflects off a mirror on the bottom of the hex cell. This mirror has a low reflectance, probably due to damage during bake-out of the vacuum chamber, which would otherwise lead to a large power imbalance between the incoming and retro-reflected vertical beams. To combat this, the beam off the internal mirror is taken as the primary beam, which is then retro-reflected off a better mirror outside the cell. A pair of anti-Helmholtz electromagnet coils is arranged vertically and provides spatial confinement. The resulting atoms are trapped near a 0D point. The location of this trap can be adjusted using 4 pairs of Helmholtz magnetic shim coils. One shim coil pair is vertical, and the other three are horizontal, arranged at 60° spacing, parallel to the hex cell faces. One horizontal coil that is normal to the trap array, and concentric with the trap array and Rydberg beams, is reserved as the magnetic *bias* field. The bias coils are used to provide a $1.5\,\mathrm{G}$ magnetic field that gives a well defined quantization axis for the qubit state, optical pumping, and microwave operations.

Beams are tightly focused onto the atoms using $f = 23.125$ mm lenses with a numerical aperture of 0.4. These lenses are custom designed by JenOptik with anti-reflective (AR)

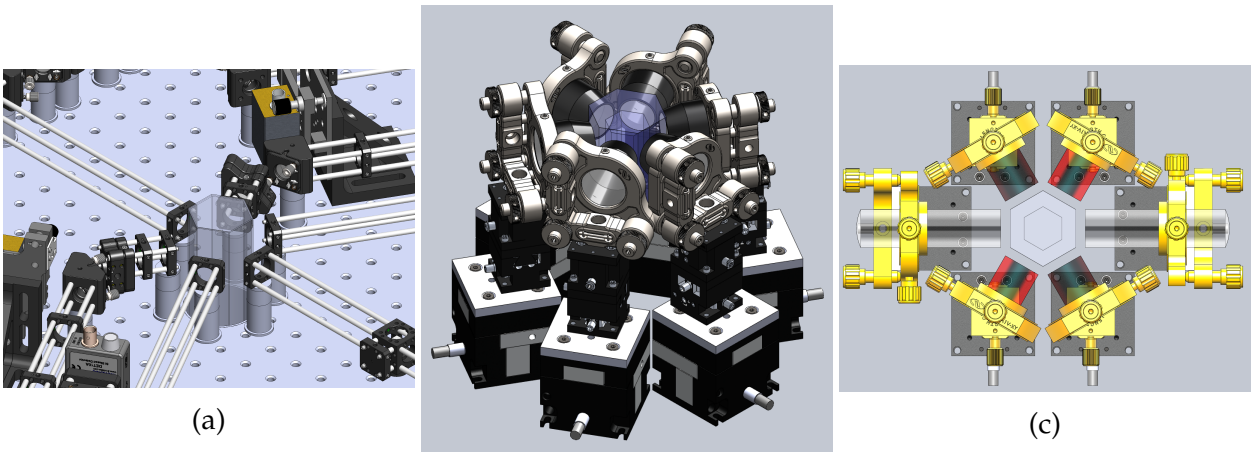


(a) (b)

Figure 5.2: (a) The 2D MOT cell and retro-reflection optics, as viewed from below the *wedding cake* structure. (b) The hexagonal pyrex vacuum cell, which contains the 3D MOT and the trap array. Dimensions in mm.

coatings, the same focal point, and low aberration, for 459, 780, 852, 894, 918 and 1038 nm. Effectively they are broadband AR coated across the visible and NIR. The positioning of these lenses is critical to the alignment of our systems. We require manual adjustment for rough alignment, plus piezo stages for fine alignment. We use the Physik Instrumente P-611.3 NanoCube XYZ three axis piezo stages, which give 100 nm range, and have closed-loop feedback to give sub-nm resolution and repeatability.

Our system was designed to have six of these setups, one on each face of the hex cell. This results in rather tight confines, and posed a difficult layout challenge. Initial designs called for the vacuum system to occupy a hole in a lofted optical breadboard, with the 2D chamber protruding below, and the 3D chamber protruding above, as shown in Figure 5.3a. The final design of the vacuum chamber however was not compatible with the hole already machined in the breadboard, so the wedding cake structure was devised to compensate for this. The stainless steel spherical cube between the two glass cells is mounted to the middle plate, as shown in Figure 5.5a. Figure 5.5b shows the hex cell on the support structure, without the eventual surrounding optics. To position the six lenses, we experimented with many layouts. The necessity to stack the rough and fine positioning stages led most designs to be too tall, as shown for example in Figure 5.3b. Efforts were also made to bring the



(a) (b) (c)

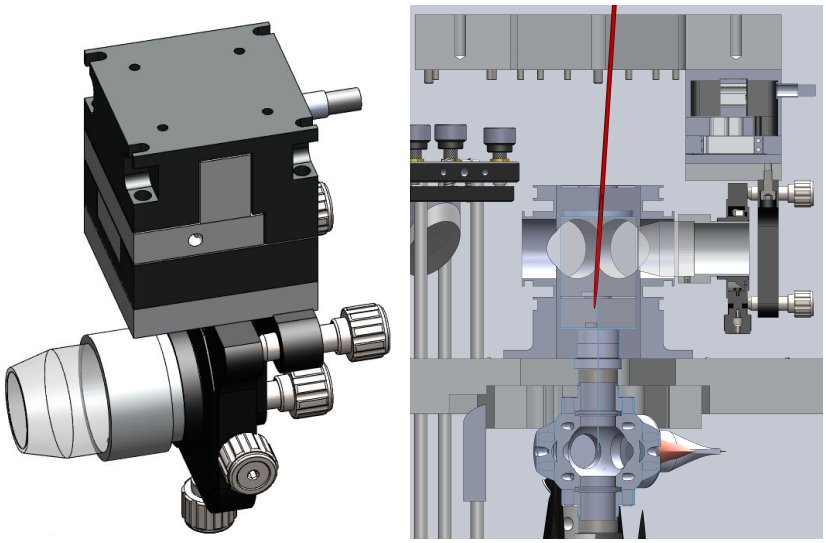
Figure 5.3: The system layout went through many iterations. Shown here are several superseded designs. (a) The hex cell protruding from a hole in a lofted optical breadboard. The 2D square cell protrudes below (unseen). (b) The need to stack rough and fine alignment stages made some designs too tall. (c) An attempt to bring the piezo stages closer to the hex cell by using a rectilinear layout.

piezo stages as close to the cell as possible by experimenting with different layouts, such as the rectilinear design shown in Figure 5.3c.

Ultimately it was deemed necessary to hang the piezo stages upside down in order to create enough room, both vertical and horizontal, to place the stages around the hex cell while clearing the vacuum connection hardware. The top level of the wedding cake is necessary because it provides the support from which the piezo stages hang. The JenOptik lenses themselves are mounted in a 5-axis manual Newport LPV-1 stage, which because of its concentric design around the lens provides a shorter setup than some possible designs. The resulting motion stage stack, hung upside down, is shown in Figure 5.4a, and the integration into the wedding cake is shown in cutaway in Figure 5.4b, as well as in Figures 5.1b and 5.1c.

In this setup, the 2D MOT square cell is at the level of the breadboard, but the 3D MOT hex cell is elevated. Periscopes are required to bring the various beams up to the height of the hex cell. These have been integrated into the wedding cake as is visible also in Figures 5.1b and 5.1c.

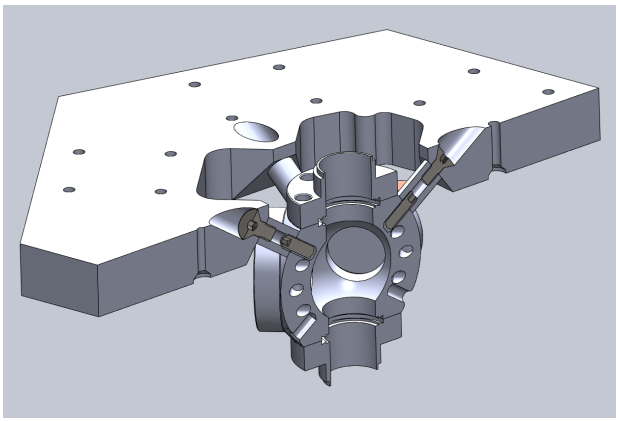
Finally, the complete structure is placed on an Invar (low-thermal expansion, high-nickel stainless steel) optical breadboard. This is surrounded by optics for trap array creation, atom addressing, and imaging. The complete setup is shown as designed in Figure 5.6a,



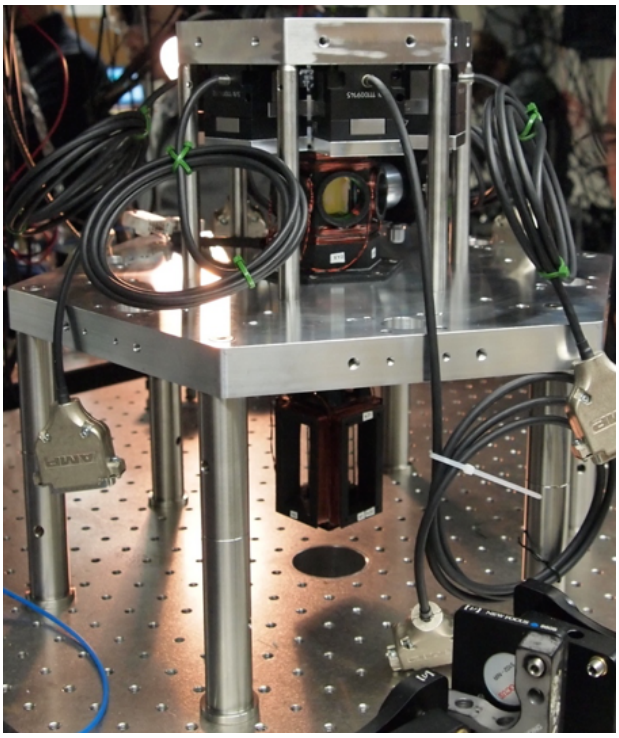
(a) (b)

Figure 5.4: The manual and piezo positioning stages are stacked and hung upside down in order to get close enough to the hex cell without interfering with the vacuum hardware. (a) Alignment stack with JenOptik lens. (b) Spacing of the stack and lens when integrated into the wedding cake, magnet coils, and hex cell. Red beam shows the location of the vertical MOT beam in the hex cell.

and implemented in Figure 5.6b.

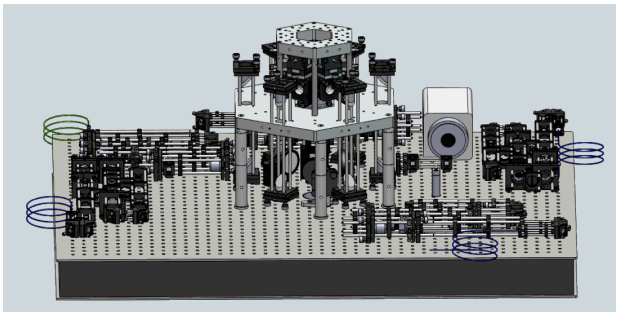


(a)

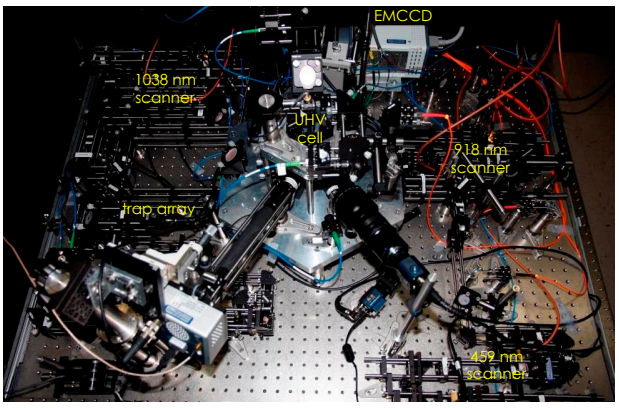


(b)

Figure 5.5: (a) The central stainless spherical cube that connects the 2D square and 3D hex vacuum cells is mounted to the middle plate of the wedding cake structure. Shown here in cutaway. (b) The hex cell mounted on the wedding cake structure.



(a)



(b)

Figure 5.6: The complete layout of the experimental optical breadboard, shown as: (a) CAD model (b) actual image.

5.2 Single Atom Addressing

The JenOptik lenses are capable of focusing beams down to ~ 1 µm, which gives us the ability to target a single atom. However, we must be able to rapidly select different atoms during the course of an experiment. This functionality is provided by two beam addressing systems. Each system is composed of two acousto-optic modulators (AOMs), one that deflects the beam vertically and one that deflects the beam horizontally. A beam addressing system for the 1038 nm light is located on the same side of the hex cell as the 780 nm trapping light and the imaging optics, while the 459 nm beam addressing system is located on the opposite side.

Several wavelengths of light are combined using dichroic beamsplitters so that they may enter the same side of the hex cell. In particular, the 1038 nm Rydberg light is combined with the 780 nm trapping light. This side of the hex cell is also used for fluorescence imaging at 852 nm because it will be the direction most immune to 780 nm background. A second dichroic separates the outgoing images from the incoming light. A schematic of the various laser wavelengths entering the hex cell is shown in Figure 5.7.

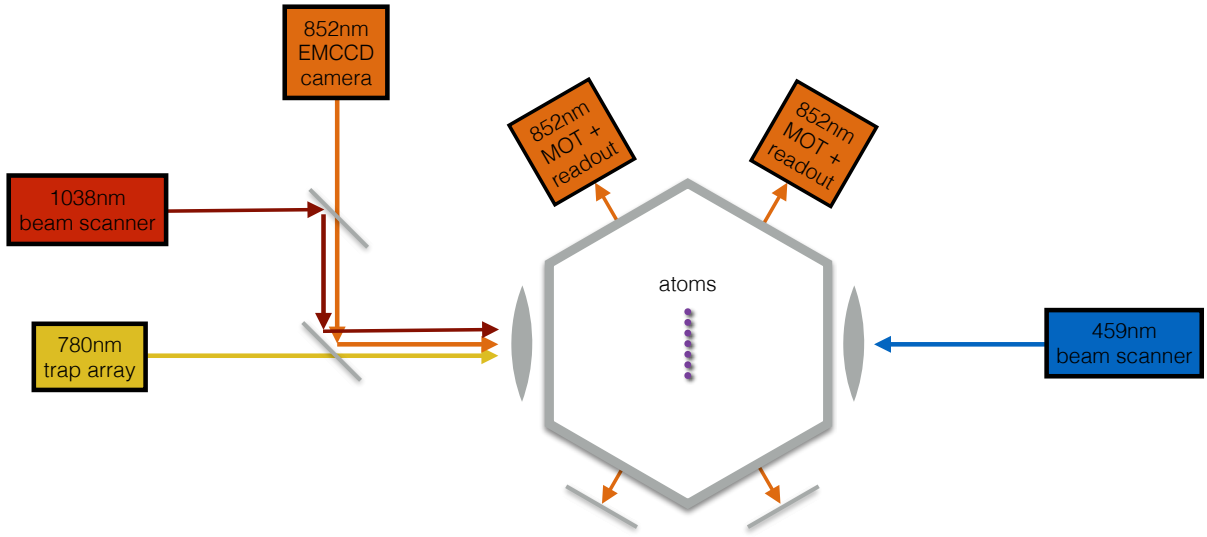
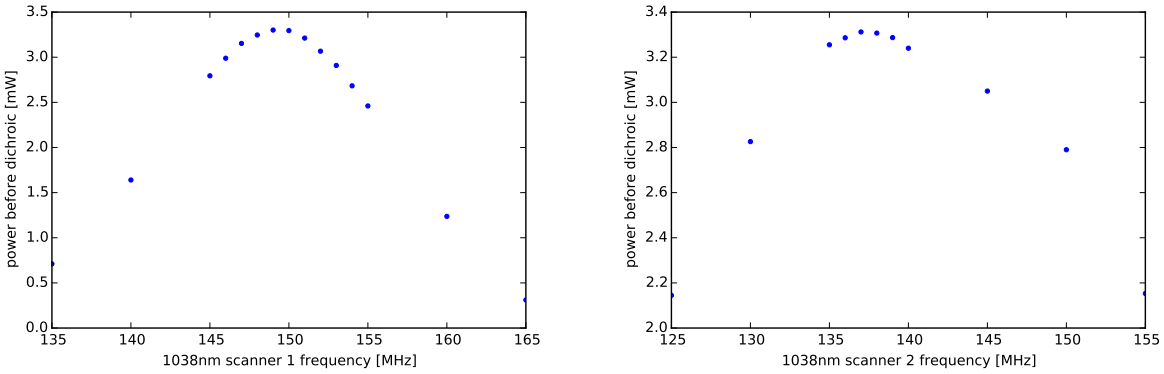


Figure 5.7: A schematic of the various wavelengths to enter the hex cell. Dichroic beamsplitters are used to join the 1038 nm and 780 nm light, as well as to separate that light from the 852 nm fluorescence.

As the scanners are shifted in frequency to point the beam at various sites across the array, the efficiency falls off as the beam deviates from the Bragg angle. Plots of output

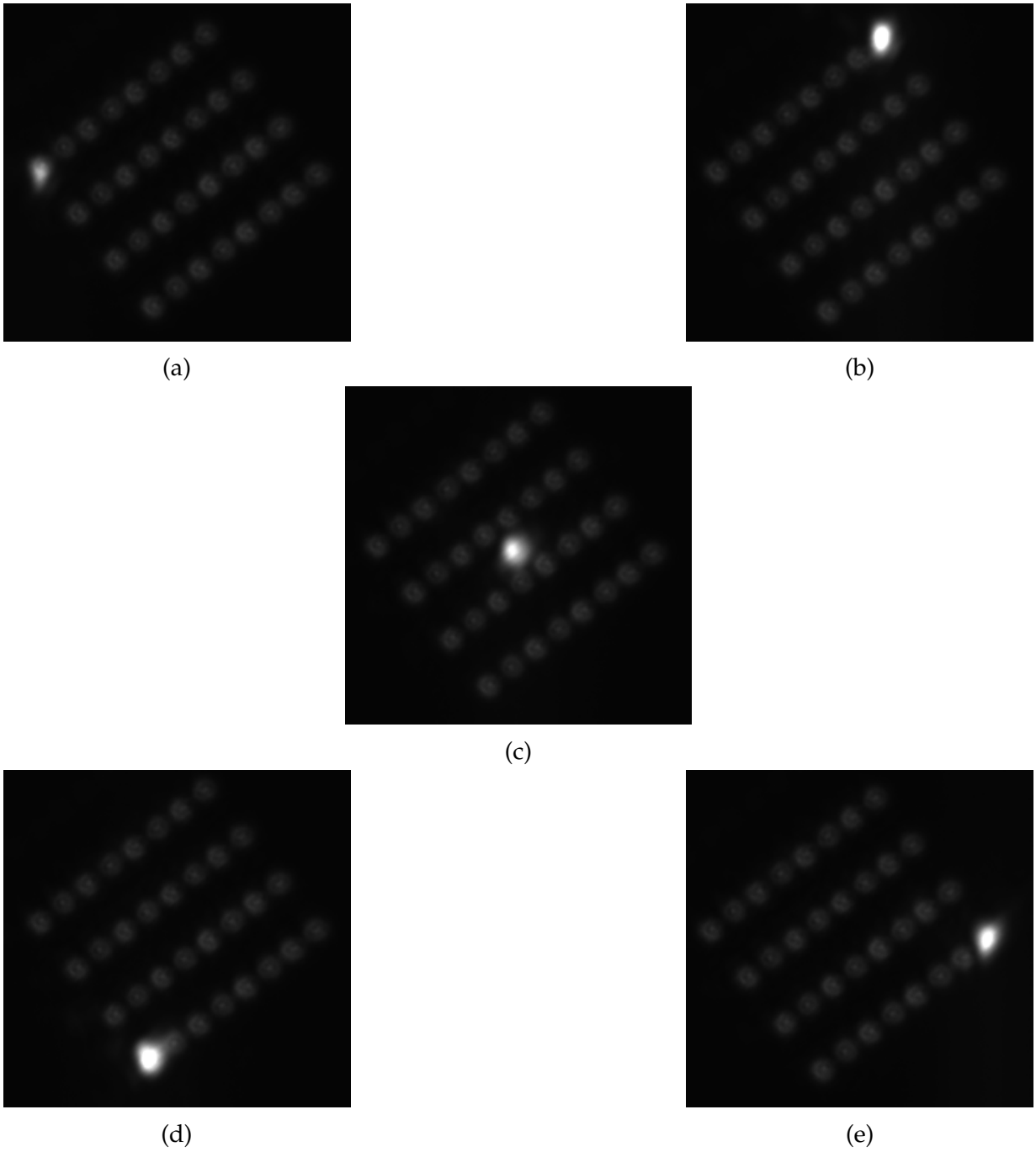


(a) (b)

Figure 5.8: The power transmission of the 1038 nm beam scanners as a function of AOM frequency. Data from 2015-07-27.

power versus AOM frequency for the 1038 nm scanners are given in Figure 5.8. The scanners are capable of electronically moving the beams across the whole array, while maintaining good beam shape, as shown in Figure 5.9. As the beam power falls off at the edges of the array, longer laser pulse times will be necessary to perform Rydberg operations.

The beam scanners are capable of addressing the entire 7x7 array. Results of single site addressed operations are presented in Chapter 13.



(a) (b) (c) (d) (e)

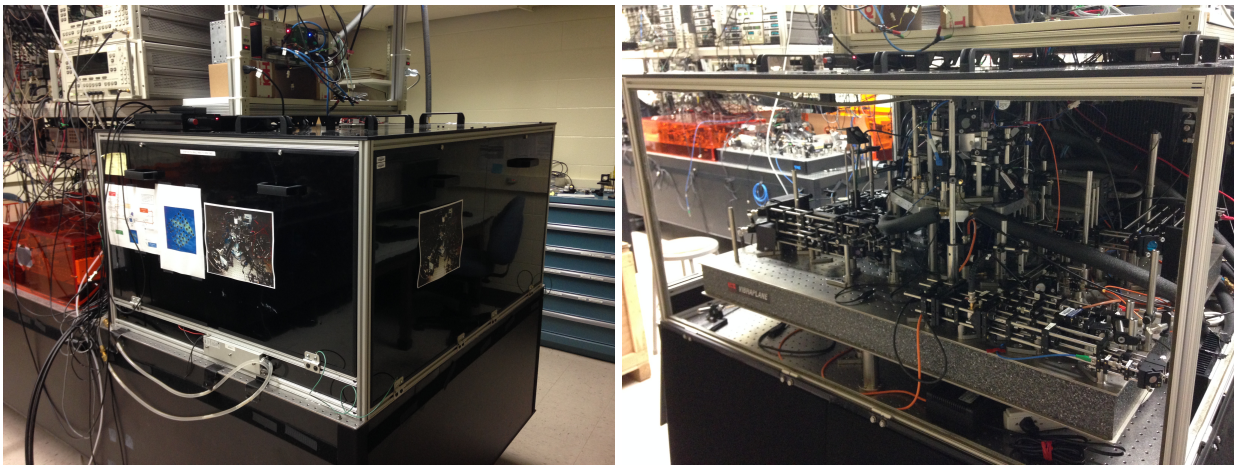
Figure 5.9: The 1038 nm beam scanner, shown on the same camera as the 780 nm trapping light (SHG only, Ti:S off). These images were taken by changing the beam scanner frequency only, with no manual realignment. The beam is shown (c) centered and (a,b,d,e) at the corners of the array. Data from 2015-07-27.

5.3 Imaging

Readout is done on all the qubits at the same time using camera imaging. The 3D MOT beams are used to fluoresce the atoms with a large detuning (see Section 8.2.2). A Hamamatsu C9100-13 EMCCD camera is used to image the atoms. Relay optics magnify the atoms such that at the focal plane we have 0.63 µm per pixel. The EMCCD has a quantum efficiency of 70%. The light collection efficiency is given by $\frac{\pi \arcsin(\text{N.A.})^2}{4\pi}$ which for our numerical aperture of 0.4 is 4.2%. The overall transmission efficiency of the JenOptik lenses and the relay optics is 80%, giving an overall readout efficiency of 2.4%.

5.4 Experiment Temperature Stabilization

Temperature changes in the lab air are a major source of instability in the experiment. To combat this, we have enclosed the entire Invar breadboard in a temperature controlled box, shown in Figure 5.10. Water cooled cold plates made by Laird and stabilized by PID servo controllers are built into the walls of the box, with TECs leading to radiators on the inside. This setup is able to control the temperature inside the box to ± 50 mK, as shown in the temperature log trace in Figure 5.11.



(a) (b)

Figure 5.10: A temperature controlled box uses PID servo'd cold plates on the walls to stabilize the experiment temperature to ± 50 mK. (a) Closed. (b) Open.

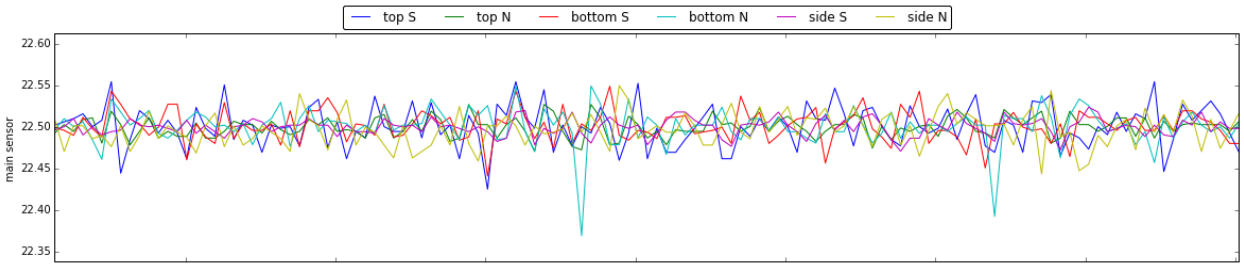


Figure 5.11: A log of the temperature readings in the experiment box over the course of 1 day.

6 Magneto-Optical Trap Design

The 2D and 3D magneto-optical traps (MOT) (see e.g. [38, 39, 40, 41, 42]) are used to load atoms into the trap array as described in Chapters 5, 7 and 11. This chapter is concerned with the design of the magnetic coils used to create the magneto-optical trap. We address optimal coil geometry, and the geometry we have chosen for our implementation. The cloud of atoms cooled and trapped by the 3D MOT is shown in Figure 6.1.

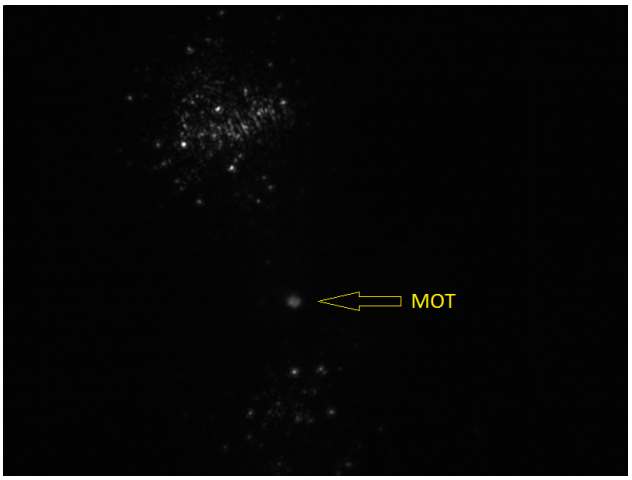


Figure 6.1: An image of the 3D MOT, along with light scattered off the surface of the hex cell.

6.1 Magneto-Optical Trap Design

6.1.1 Magnetic Field Due to Coils

The differential magnetic field due to a single current carrying wire element is given by the Biot-Savart Law as

$$dB = \frac{\mu_0 I \sin\theta}{4\pi r^2} dl \tag{6.1}$$

Where μ_0 is the magnetic permeability of free space, $\vec{r}$ is vector from the element to the test point, I is the current, θ is the angle between the current element and $\vec{r}$, and dl is the differential length of the wire element.

6.1.2 Single Circular Coil

In general in MOT design we are concerned with the magnetic field on the axis of a circular coil. For a single circular coil of radius R, concentric with the z axis, for test points on-axis only, we have $r = \sqrt{R^2 + z^2}$ and $\sin\theta = 1$. Due to opposing elements on the coil, the x and y components of the field will be canceled, leaving only the z component with strength $dB_z = \sin\phi\, dB$, where $\sin\phi = R/r$. The magnetic field at a test point is then found by integrating the contribution to the z field around the circle, which is

$$B(z) = \int_0^{2\pi R} \frac{R}{r} \frac{\mu_0 I}{4\pi (R^2 + z^2)} dl = \frac{\mu_0 I R^2}{2 (R^2 + z^2)^{3/2}} \tag{6.2}$$

As expected this gives a maximum field when $z = 0$ at the coil center. Away from the center we see the competing effects of R^2 in the numerator indicating that increased coil radius gives more integrated current that contributes to the B-field, while $(R^2 + z^2)$ in the denominator shows that increased coil radius takes the wire farther from the test point. We find that for a fixed distance z there is an optimal coil radius $R = \sqrt{2}z$ that gives a maximum $B = \frac{\mu_0 I}{\sqrt{27}z}$.

There are two possible geometries of coil pairs that concern us. To create a MOT, we use a pair of anti-Helmholtz coils, with current rotating in opposite directions, which gives us a quadrupole field with a zero magnetic field halfway between the two coils. To adjust the MOT with magnetic *shims*, we use pairs of Helmholtz coils, with the current rotating in the same direction, to add a constant offset to the field. Using several orthogonal shim coils allows us to cancel Earth's magnetic field, or move the $B = 0$ location to coincide best with the MOT lasers.

6.1.3 Helmholtz Shim Coils

For a pair of Helmholtz coils the on-axis contribution from both coils gives

$$B(z) = \frac{\mu_0 I R^2}{2\left(R^2 + \left(\frac{d}{2} - z\right)^2\right)^{3/2}} + \frac{\mu_0 I R^2}{2\left(R^2 + \left(\frac{d}{2} + z\right)^2\right)^{3/2}} \tag{6.3}$$

where d is the distance between coil centers. The on-axis field strength is plotted in Figure 6.2. Evaluating the field at the origin we have

$$B\left(0\right)=\frac{\mu_0 I R^2}{\left(R^2+\left(\frac{d}{2}\right)^2\right)^{3/2}} \tag{6.4}$$

Once again we can identify an optimal coil size at $R=\frac{d}{\sqrt{2}}$ with

$$B_{max}\left(0\right)=\frac{4\mu_0 I}{\sqrt{27}d} \tag{6.5}$$

Around the optimal point, the change in B is flat with regard to R (by definition), but an advantage can always be gained by decreasing d, so it is desirable to bring the coils in closer.

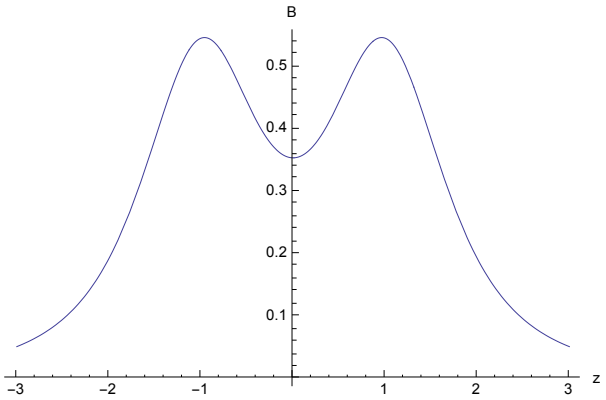


Figure 6.2: The on-axis magnetic field due to two co-rotating coils, at different locations along the axis. Maxima correspond to the coil centers.

6.1.4 Anti-Helmholtz Gradient Coils

The anti-Helmholtz coils give a magnetic field gradient with a zero between the two coils. The field due to two counter-rotating coils separated by a distance d is

$$B\left(z\right)=-\frac{\mu_0 I R^2}{2\left(R^2+\left(\frac{d}{2}-z\right)^2\right)^{3/2}}+\frac{\mu_0 I R^2}{2\left(R^2+\left(\frac{d}{2}+z\right)^2\right)^{3/2}} \tag{6.6}$$

The on-axis field strength is plotted in Figure 6.3. For anti-Helmholtz coils, we are not interested in maximizing the field (because the $B = 0$ point is necessary for stable atom trapping), however we do want to maximize the field gradient at this location. The field gradient is

$$\frac{dB}{dz} = -\frac{3\mu_0 I R^2 \left(\frac{d}{2} - z\right)}{2\left(R^2 + \left(\frac{d}{2} - z\right)^2\right)^{5/2}} + \frac{3\mu_0 I R^2 \left(\frac{d}{2} + z\right)}{2\left(R^2 + \left(\frac{d}{2} + z\right)^2\right)^{5/2}} \tag{6.7}$$

And the gradient at $z = 0$ is maximized at $R = d/\sqrt{6}$ giving

$$\frac{dB}{dz}_{max} = -72\sqrt{3}\mu_0 I d^2 \left(\frac{\frac{d}{2} - z}{(5d^2 - 12dz + 12z^2)^{5/2}} + \frac{\frac{d}{2} + z}{(5d^2 - 12dz + 12z^2)^{5/2}}\right) \tag{6.8}$$

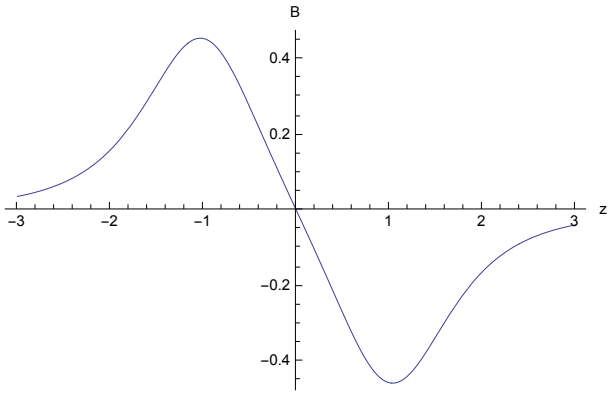


Figure 6.3: The on-axis magnetic field due to two counter-rotating coils, at different locations along the axis. The zero field is halfway between the coils. It is desirable to maximize the gradient at this location.

6.1.5 Choosing Wire Gauge

The choice of wire gauge depends on the constraints imposed. The power consumption is found from

$$P = IV,\ V = IR \tag{6.9}$$

$$R = \frac{2\pi r \rho N}{\pi d^2/4} \propto \frac{N}{d^2} \tag{6.10}$$

where P is power consumption, I, V and R are current, voltage and resistance, r is the radius of the coil, d is the wire gauge diameter, ρ is the resistivity of the material and N is

the number of turns of wire. For a fixed geometry, $B \propto NI$, and so

$$P = I^2 R \propto I^2 \frac{N}{d^2} \propto \frac{B^2}{N d^2} \tag{6.11}$$

So in general we want to maximize the number of turns and also use the largest gauge wire possible, to get a given B-field with minimum power consumption.

However, if we have space constraints, we can relate the wire diameter d to the number of possible coils N. For a single layer of wire wrapping in a fixed width, we have $N \propto 1/d$, and so

$$P \propto B^2/d \tag{6.12}$$

So for a single layer of wire wrapping with a fixed coil width, it is still advantageous to use the largest diameter of wire.

If we have space constraints with a cross sectional area envelope, but allow multiple layers of wire wrapping, then $N \propto 1/d^2$, and so

$$P \propto B^2 \tag{6.13}$$

For multiple layers of wire wrapping within a fixed envelope, the trade-off between wire gauge and number of wraps has no effect on power consumption. Because of the tight confines imposed on our MOT coil design by the optics, this is the regime we find ourselves in, and so we are free to choose wire gauge by other constraints.

We find that for most reasonable gauges of wire, the safe amperage limits put a maximum on the current we can deliver through the wire. Operating at maximum safe current levels therefore defines how many coil turns N we must use. Analyzing several engineering tables of wire amperage limits, we find 22 gauge wire to have an anomalously high limit. This is most likely an empirical error, however having a large amount of 22 gauge enameled wire on hand we have chosen to make all of our MOT gradient and shim coils using 22 gauge.

6.2 3D MOT Coil Specifications

The MOT coils went through several iterations, shown in Figure 6.4 for the 3D MOT and Figure 6.5 for the 2D MOT.

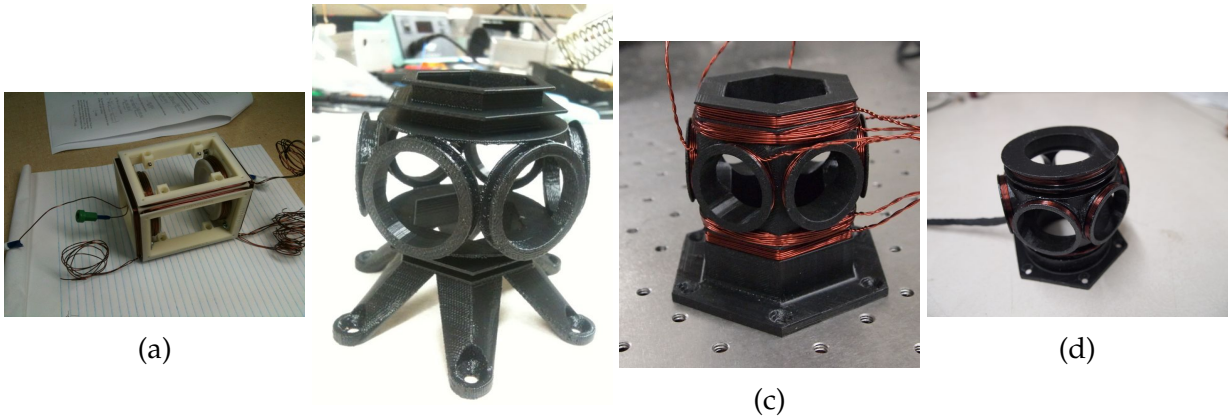
The final design has 100 turns of the anti-Helmholtz coils giving a field gradient of

17.8 G/cm/A, which we operate at 1.5 A to get 26 G/cm.

The shim coils all have 10 wraps. The vertical shim coils give 1.8 G/A, while the three pairs of horizontal shims provide 0.6 G/A due to a farther from optimal diameter-to-separation ratio. During the MOT loading phase, we have optimized the horizontal shim coils at 0 mA, 725 mA, and 419 mA, while the vertical shim is optimized at 152 mA. This gives a combined field magnitude of 0.6 G, whereas we expect to require a shim field on the order of 1 G to counter Earth's magnetic field.

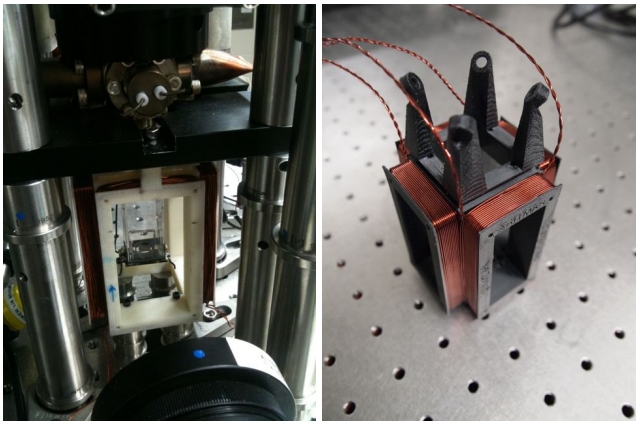
6.3 Use of 3D Printing

We used 3D printing to enable the creation of complicated coil holder designs at a fraction of the cost that it would take to manufacture these without 3D printing. The evolution of these designs is shown in Figures 6.4 and 6.5. The major concern with 3D printed materials is their properties when exposed to the heat of the magnet coils. The black and cream colored 3D printed coil holders are made on an FDM machine from ABS plastic, which has a heat deflection temperature of 98 C at 0.46 MPa and 88 C at 1.8 MPa. Not shown here, we have also produced clear 3D printed parts, made on an SLA machine from Accura 60, which has a heat deflection temperature of 54 C at 0.46 MPa and 49 C at 1.8 MPa. We have not had any problems with heat deformation of the magnetic coil holders.



(a) (b) (c) (d)

Figure 6.4: (a)-(d) Iterative design of the 3D MOT coil holders. Heavy use was made of the capabilities of 3D printing in later designs.



(a) (b)

Figure 6.5: (a)-(b) Iterative design of the 2D MOT coil holders. Heavy use was made of the capabilities of 3D printing in later designs.

7 Single-Atom Laser Confinement Grids

The Atomic Qubit Array consists of a 2D grid of trapped single cesium atoms. Particularly unique to this project is that we utilize an inherently 2D grid. By trapping atoms in a single plane, we avoid the possibility of crosstalk between atoms at different depths along the optical path when attempting to address or measure single atoms. To achieve this setup, we use techniques that were developed for the trapping of one single atom, and multiply them in novel ways that allow us to trap many single atoms in well defined locations in close proximity to each other.

Implementing the qubit array in 2D provides an easier road to making progress towards realizing quantum computation. In the long run, a 3D implementation such as that by pursued Nelson, Li, and Weiss [43] can provide higher volumetric qubit densities than a 2D grid. Even a 2D grid can support dozens of qubits within the Rydberg blockade radius, and so we use a planar design in our work. Once the challenges of neutral atom quantum computing in small arrays have been thoroughly worked out, moving toward a 3D implementation would be a logical future direction.

The positional stability of our trapping sites is extremely important. In order to perform extended algorithms on a qubit register, we must repeatedly address single atoms. This means that the location of the atoms must be stable over time. The trapping sites certainly cannot allow for motion over the timescale of a computation. However, even motion over longer time scales that would require active feedback to suppress is undesirable compared to an implementation with inherent positional stability. The most well-established technique for creating many atom trapping sites is an optical lattice, using interference between pairs of counter-propagating laser beams at the same frequency [44]. The optical lattice can be implemented as a 1D array of planar traps using two counter-propagating beams, a 2D array of linear traps using two orthogonal pairs of counter-propagating beams, or as a 3D array of point-like traps using three orthogonal pairs of counter-propagating beams. Furthermore, the trapping geometry can be effectively altered in dimension by intersecting with cooling beams of other dimensionality to load only part of the lattice volume, or by flattening a cooled atom cloud against evanescent waves on a surface, such as Gillen et al. [45]. This last technique has yielded great 2D single-atom trapping and imaging results in the quantum gas microscope developed by Sherson et al. [46]. If instead of using large beams, the source beams are narrowed, then two counter-propagating beams can create a 1D string of trap sites as in the work of Schrader et al. [47]. However, all these optical lattice

based techniques will suffer from movement of the trapping sites due to phase fluctuations.

In this work, we present techniques for creating a lattice of trap sites that is not an "optical lattice" in the sense traditionally referred to in the literature. The design we have pursued has no interferometric phase sensitivity. We do not use counter-propagating beams to create intensity maxima and minima in an interference pattern that define the trapping sites. Our trapping relies on the principle of the *optical dipole trap*, just as the optical lattice does. However, we use a combination of the pencil beam technique, diffractive optical elements, birefringent beam displacers, and beam splitters to create our 2D pattern of trapping light in such a way, as will be described in this chapter, as to avoid interferometric instability.

7.1 Optical Dipole Traps

The optical dipole trap can impart a force on a neutral atom when some separation of charge within the atom gives it a polarizability, which makes it act as a dipole in the presence of an external electric field. We begin by following the standard development of the potential due to an optical dipole (e.g. Grimm, Weidemüller, and Ovchinnikov [48]). Assume an external electric field oscillating in time, t, at angular frequency ω

$$\vec{E}(t) = E\hat{e}\left(e^{-i\omega t} + e^{i\omega t}\right) \tag{7.1}$$

where $\hat{e}$ is the unit vector of the polarization direction of the field, and E is the amplitude of the electric field oscillation. There is a frequency dependent polarizability, α, and the amplitude, p, of the dipole moment, $\vec{p}$, is then

$$p(\omega) = \alpha E \tag{7.2}$$

The intensity of the electric field is proportional to the square of the amplitude

$$I = 2\varepsilon_0 c\,|E|^2 \tag{7.3}$$

and the time-averaged potential due to the dipole is

$$U_{dip} = -\frac{1}{2}\left\langle \vec{p}\vec{E} \right\rangle = -\frac{1}{2\varepsilon_0 c}\mathrm{Re}\,(\alpha)\,I \tag{7.4}$$

The force on the atom, found by taking the gradient of the potential, is then proportional to the intensity gradient

$$\vec{F}_{dip}\left(\vec{r}\right) = -\nabla U_{dip}\left(\vec{r}\right) = \frac{1}{2\varepsilon_0 c}\mathrm{Re}\left(\alpha\right)\boldsymbol{\nabla} I\left(\vec{r}\right) \tag{7.5}$$

To find the value for the polarizability, first consider the classical equation of motion for an electron of mass m_e and charge $-e$

$$\ddot{x} + \Gamma_\omega \dot{x} + \omega_0^2 x = -\frac{eE(t)}{m_e} \tag{7.6}$$

For a free electron we have the polarizability (Saffman, Walker, and Mølmer [6])

$$\alpha = -\frac{e^2}{m_e \omega^2} \tag{7.7}$$

This value is of importance to the trapping of Rydberg states, and we shall return to it later. However for an electron bound to the atomic core (which includes the nucleus and the remaining inner shell electrons, making a net charge of $+1$)

$$\alpha = \frac{e^2}{m_e}\frac{1}{\omega_0^2 - \omega^2 - i\omega\Gamma_\omega} \tag{7.8}$$

The damping rate due to radiation from the classical charged oscillator is:

$$\Gamma_\omega = \frac{e^2\omega^2}{6\pi\varepsilon_0 m_e c^3} \tag{7.9}$$

Using this value to substitute for $\frac{e^2}{m_e}$ gives

$$\alpha = 6\pi\varepsilon_0 c^3 \frac{\Gamma/\omega_0}{\omega_0^2 - \omega^2 - i\left(\omega^3/\omega_0^2\right)\Gamma} \tag{7.10}$$

but in the semi-classical two-level model the energy loss rate is defined by the matrix element between the ground and excited states

$$\Gamma = \frac{\omega_0^3}{3\pi\varepsilon_0\hbar c^3}\left|\langle e|\,\mu\,|g\rangle\right|^2 \tag{7.11}$$

Taking the case of weak beams that do not saturate the excited state

$$U_{dip}\left(\vec{r}\right) = -\frac{3\pi c^2}{2\omega_0^3}\left(\frac{\Gamma}{\omega_0 - \omega} + \frac{\Gamma}{\omega_0 + \omega}\right) I\left(\vec{r}\right) \tag{7.12}$$

Define the detuning as $\Delta \equiv \omega - \omega_0$ and assume that for small detuning $|\Delta| \equiv \omega - \omega_0$ we may use the rotating wave approximation and discard the fast oscillating term. Then the dipole potential is given by

$$U_{dip}\left(\vec{r}\right) = \frac{3\pi c^2}{2\omega_0^3}\frac{\Gamma}{\Delta} I\left(\vec{r}\right) \tag{7.13}$$

We will make use of this idea of a trapping potential and discuss the trap depth of various implementations of dipole traps by comparing the maximum and minimum potentials. The trap depth can be expressed as a temperature by

$$T = \frac{2}{3k_B}\left(U_{max} - U_{min}\right) \tag{7.14}$$

where $k_B = 1.38064852(79) \times 10^{-23}\frac{J}{K}$ is the Boltzmann constant. For effective traps with long containment lifetimes we want our trap depth to be many (~ 50) times our atom temperature.

In addition to the trap depth, one must also consider the photon scattering rate, which goes as

$$\Gamma_{sc}\left(\vec{r}\right) = \frac{1}{\hbar\varepsilon_0 c}\mathrm{Im}\left(\alpha\right) I\left(\vec{r}\right) \tag{7.15}$$

which in the simplifying assumptions followed above reduces to

$$\Gamma_{sc}\left(\vec{r}\right) = \frac{3\pi c^2}{2\hbar\omega_0^3}\left(\frac{\Gamma}{\Delta}\right)^2 I\left(\vec{r}\right) \tag{7.16}$$

We note from Equations 7.13 and 7.16 that the trap potential scales as I/Δ while the scattering rate scales as I/Δ^2. This drives us toward the *far off-resonance dipole trap*, with a large detuning to get a low scattering rate, but a high intensity to maintain trap depth. In our application we use a wavelength of $780\,\mathrm{nm}$ which is over $32\,\mathrm{THz}$ detuned from the strong D2 line in cesium at $852\,\mathrm{nm}$ and $49\,\mathrm{THz}$ detuned from the D1 line at $894\,\mathrm{nm}$. This large detuning therefore requires powerful lasers, as described in Section 8.1.

7.1.1 Red Traps and Blue Traps

The optical dipole trap can function in two modes, depending on the sign of the detuning of the light relative to the nearby energy transitions in the atomic species that we wish to trap. The atom is attracted to an intensity minimum if the light is lower frequency than, i.e. "red" of, the strong nearby atomic transitions. The atom is repelled from regions of high intensity if the light is higher frequency than, i.e. "blue" of, the strong nearby atomic transitions. This is manifested in the sign of dipole potential, as we can see from Equation 7.13.

By focusing a laser beam to a small spot, an intensity maximum is created, which is useful as a red trap. A simple way to create this is by tightly focusing a Gaussian beam to a small waist. Because the trap depth increases with increasing intensity gradient, it also increases as we focus the beam to a smaller waist. As shown in Figure 7.1, a tightly focused Gaussian beam creates a high intensity spot, providing trapping in both the transverse and longitudinal directions.

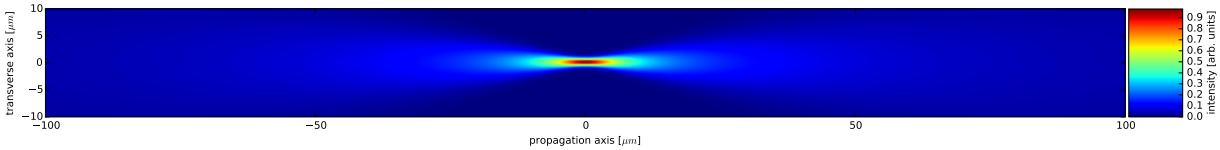


Figure 7.1: A tightly focused Gaussian beam, demonstrating the intensity maximum that allows such a pencil beam to act as a dipole trap when red-detuned. Example for $1\,\mu$m waist at $780\,$nm. Arbitrary normalized intensity units.

By using a sufficiently small waist, this technique can be used to trap single atoms, as demonstrated by Schlosser et al. [49]. In that implementation, an objective lens with numerical aperture 0.7 was used to create a diffraction limited spot size of 0.7 μm. While in a larger dipole trap, the number of atoms loaded follows a Poisson distribution, in this *collisional blockade* regime, the atoms are so tightly confined that spin-exchange collisions will tend to release one hyperfine photon, kicking both atoms in a pair out of the trap (Nesnidal and Walker [50] and Gensemer et al. [51]). For cesium with $f_{hf} = 9.192\,631\,770\,\text{GHz}$, this energy is equivalent to a trap depth of

$$T = \frac{2hf_{hf}}{3k_B} = 294\,\text{mK} \tag{7.17}$$

which is far larger than the available optical dipole trap depth. The result is that if the trap

site starts with an odd number of atoms, they pair collide down to one, and if the trap starts with an even number of atoms, they pair collide down to zero. All things being equal (i.e. in the limit of large vapor density) there is a 50% probability to load either zero or one atom.

For the red trap, the ground state has a negative Stark shift, while the excited state has a positive Stark shift. The assumption in the development above was that the ground-to-excited transition was not saturated, and the atom spends most of its time in the ground state, and so has an attractive potential. However, in the case of atoms that are kept in an excited state, such as a Rydberg state, for a significant amount of time, this is no longer a good assumption. Particularly so with the Rydberg state, which acts as a free electron and hence has polarizability $\alpha = -\frac{e^2}{m_e\omega^2}$ as in Eq. 7.7. This negative polarizability has no relation to the detuning, and causes a repulsive potential, regardless of whether the trap is red or blue detuned from any intermediate excited state. It is because of this that experiments with Rydberg atoms in red detuned dipole traps usually have the traps turned off momentarily while the atoms are excited to the Rydberg states, so as not to repel the atoms from their nominal location (e.g. Urban et al. [52, fig. 2]). The action of gravity and more-so of kinetic motion (i.e. temperature) will act to displace the atoms during this time and so it cannot typically be more than a few microseconds.

A blue trap will be repulsive to the ground state, because the positive detuning creates a convex potential via Eq. 7.13. However it will also be repulsive to the Rydberg states, because any trapping light usable for ground states is so far detuned from the Rydberg states that there is no resonant interaction to consider, and so only the free-electron polarizability is relevant. This means that a blue trap could be designed to trap both the ground and Rydberg states in our system, and so in our implementation we will be using blue-detuned dipole traps.

The trapping geometry for blue traps, however, is significantly more complicated. Because of the repulsive nature of the light, a simple (0th order) Gaussian beam will not work, because there is no intensity minimum except at $r \to \infty$. In the first trapping experiments with blue traps, Davidson et al. [53] used sheets of light to create walls to box in the atoms. This was simplified by Lee et al. [54] who used V-shaped intersections of sheets of light. The V opened upwards, and hence gravity provided the localization into the trap bottom. The sheets of light use a great deal of light at places away from the trap center, and so Kuga et al. [55] used a Laguerre-Gauss beam in an $LG_{0,l}$, $l \neq 0$ mode, which gives a hollow beam that could trap atoms in the dark center. The intensity profile for this

type of beam is shown in Figure 7.2. Because the core continues to be hollow as the beam propagates, there is no trapping in the longitudinal direction, and hence this technique requires the traps to be capped using orthogonal plugging beams, as shown in Figure 7.3a.

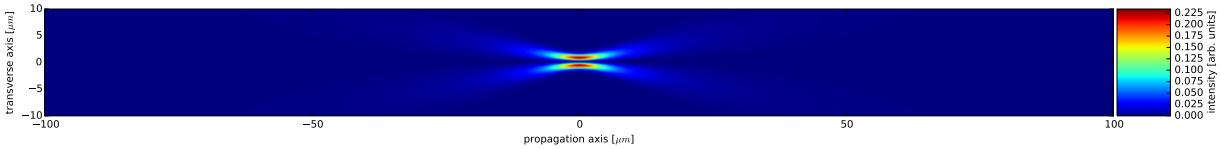
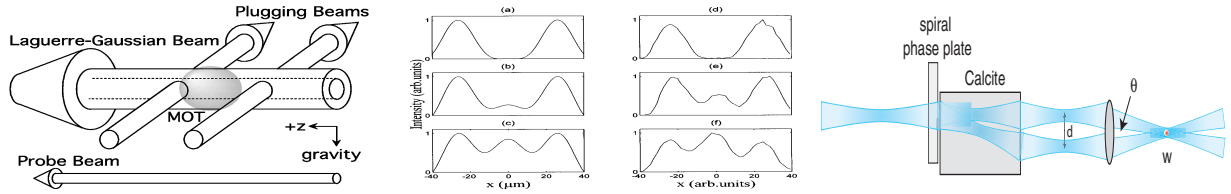


Figure 7.2: A tightly focused Laguerre-Gauss $n = 0$, $l = 1$ mode beam, showing the hollow core. This is the type of beam used by Kuga et al. [55] as a blue-detuned dipole trap. We can see from the lack of trapping in the longitudinal direction why extra plugging beams are required. Example for $1\,\mu$m waist at $780\,$nm. Arbitrary normalized intensity units.

An improvement on the hollow core blue-detuned trap was made by Ozeri, Khaykovich, and Davidson [56], whereby a phase plate was used to apply a π phase shift to the central region of a collimated beam. When focused, destructive interference between the regions causes a dark central spot, surrounded by a bright region. What is more, as the larger outer region and the smaller core propagate with different Rayleigh lengths, their convergence angles are different, causing a variation in the interference pattern in the longitudinal direction as shown in Figure 7.3b. This creates bright regions along the propagation axis away from the focus, which caps off the trap without the need for plugging beams. This type of single beam trap is one configuration of what is known as a *bottle beam trap*.

A variation on the bottle beam trap that we have used in prior single-atom trapping experiments is the crossed-vortex bottle beam trap described in Zhang, Robicheaux, and Saffman [57] and Li et al. [58] and shown in Figure 7.3c.

The shortcoming of these bottle beam trap geometries comes when we try to build an array of them. Bringing the bottle beams too close in the transverse direction would cause interference between the walls of the different bottles, compromising the integrity of each trap. However, placing the bottles far enough apart means there will be two walls between every pair of atoms, which wastes light power. The solution to this problem that we have pursued is to instead use an array of Gaussian beams, as presented in the next section.



(a) (b) (c)

Figure 7.3: Various configurations of the blue-detuned bottle beam trap. (a) The hollow core Laguerre-Gauss beam trap, with plugging beams to close the traps in the propagation direction. Figure from Kuga et al. [55, Fig. 2]. (b) Intensity profiles for a bottle beam trap constructed by applying a π phase shift to the core of a Gaussian beam, prior to focusing. Cross-sections at 0, 1 and 1.5 mm from the focal plane are shown as (subfigure a-c) calculated and (subfigure d-f) measured. Figure from Ozeri, Khaykovich, and Davidson [56, Fig. 2]. (c) A crossed vortex bottle beam trap, constructed using a spiral wave plate on two intersecting beams of opposite polarization. Figure from Zhang, Robicheaux, and Saffman [57, Fig. 2b].

7.2 Trap Array Geometry Analysis

The limitations with all the methods discussed above have guided us to a new kind of trapping geometry that we call the *Gaussian beam array*, and its successors the *line grid array* and *Gaussian line array*.

7.2.1 Gaussian Beam Array

The Gaussian beam array is a blue-detuned trap array created by multiple parallel Gaussian beams, all tightly focused at the same plane, as shown in Figure 7.4.

By positioning the beams in close proximity to one another, the N beams create a grid of N^2 bright spots and $(N-1)^2$ dark spots, as shown in Figure 7.5. The light is blue-detuned, and so the atoms are trapped at the dark spots. Away from the focus, the beams spread out, and as they do so, they merge together, capping off the trapping bottles in the longitudinal direction.

The advantage of such a construction, is that the position of the traps depends only on the stability of the generating optics, and not on the phase of those beams as with the optical lattice. To ensure, however, that the trapping bottles are "water tight", the beams must always add constructively. Any destructive interference between the neighboring beams might create holes in the trapping bottles. To this end, we design the Gaussian beam array so that the beams are incoherent with their neighbors. This allows the beam intensities to

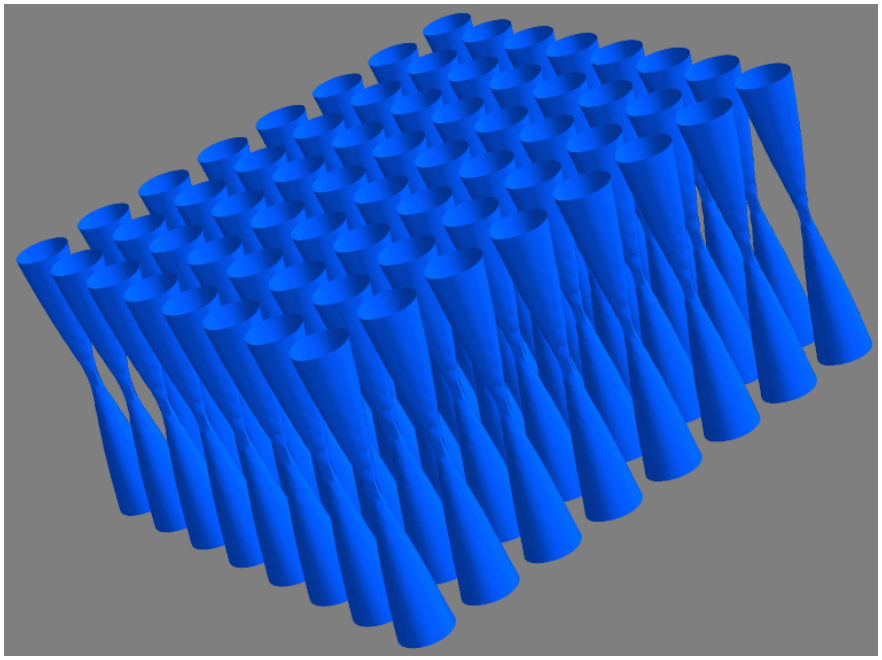


Figure 7.4: The Gaussian beam array is composed of a grid of many parallel Gaussian beams, all tightly focused in the same plane. The light is blue-detuned, and atoms are trapped in the dark spots between beams.

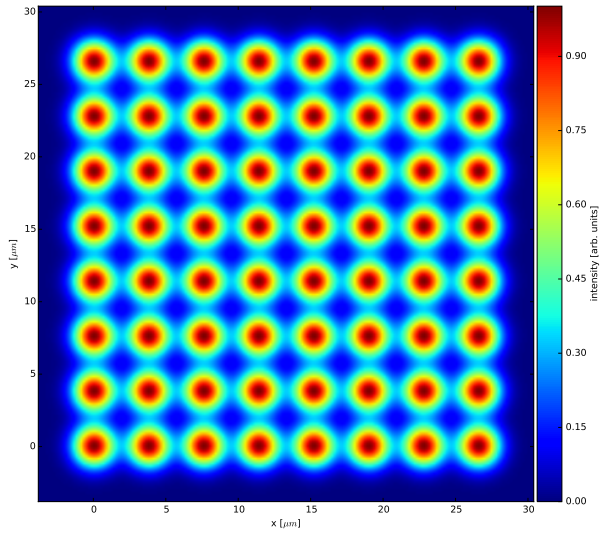


Figure 7.5: In the focal plane, the Gaussian beam array creates a grid of bright spots, where atoms can be trapped at the dark spots between the beams.

sum (which add as the square of the amplitude and therefore are always positive), rather than the beam amplitudes (which could add constructively or destructively). We have achieved this in two different ways, which call the *half-incoherent* and *full-incoherent* designs (Piotrowicz et al. [59]).

The Gaussian beam array is composed of weakly overlapping beams, each of which can be described by its waist parameter w_0 (the radius where the intensity is $1/e^2$ of the maximum) and the array periodicity d (the distance from one beam center to the next). The arrays are rectilinear, with the same spacing in both transverse directions. A very useful parameter for the discussion of these arrays is the *aspect ratio* which we define as $s = d/w_0$. The following analysis will show that the array is well characterized by this parameter. The Gaussian beams are *weakly overlapping* when $d > w_0$ but the spacing is approximately $s \sim 2$, such that neighboring beams overlap and form trapping walls, without filling in the trap centers. Furthermore, the weakly overlapping condition means that the overlap between beyond-nearest-neighbor beams is negligible.

Additionally, if the trapping light were coherent, this would lead to the Talbot effect, which would create periodicity along the longitudinal direction, and therefore create unwanted multiple trapping planes. This effect becomes enhanced for larger arrays, and as the size of the array goes towards infinity, the effect becomes perfect. The half-incoherent and full-incoherent designs both effectively suppress this effect to give just a single trapping plane as desired.

7.2.1.1 Half-Incoherent Array

In the half-incoherent design, we use one source laser beam, but design the array such that nearest 4-neighbor beams have orthogonal polarizations, as shown in Figure 7.6, which means they will add completely incoherently. The source laser will be far detuned from any atomic resonances, so that vector and tensor contributions to the ground-state polarizability are negligible. The remaining field interference term is therefore that of a diagonal neighbor, with a separation of $\sqrt{2}d$, where the separation between nearest neighbors is d. At the trap center, the field amplitude has fallen to $e^{-s^2/2}$, which for an aspect ratio of $s = 2$ is still 13.5%. And so although the interference along the diagonal is therefore strongly suppressed, this is still a remaining source of intensity fluctuation at the minimum, and it will be addressed by the *full-incoherent* array design.

To analyze the half-incoherent array design, consider the unit cell as shown in Figure 7.7 with neighboring beams having orthogonal polarization states. At the saddle point along

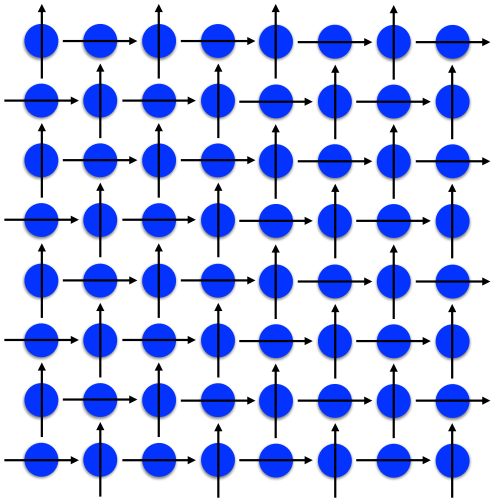


Figure 7.6: The beam layout of half-incoherent array design. Arrows indicate polarization. For every beam all of its 4-neighbors have a different polarization, and so they are incoherent. The diagonally situated beams still interfere coherently.

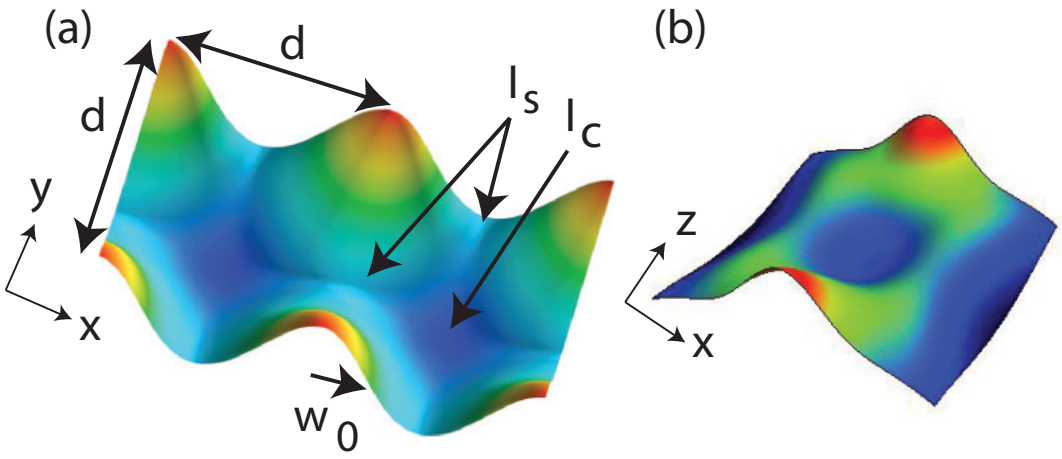


Figure 7.7: Intensity distribution of a the Gaussian beam array in the (a) x-y and (b) x-z planes.

each side of the unit cell, the intensity is

$$I_s = 2I_0 e^{-2(d/2)^2/w_0^2} = 2I_0 e^{-d^2/2w_0^2} \tag{7.18}$$

when considering in approximation only the contribution from the two nearest peaks, where I_0 is the peak intensity of one beam. We ignore the contribution from any more distant beams. Let us take the worst-case scenario of diagonally opposite beams being in-phase, which will give the lowest trapping potential. The intensity at the atom location at the center of the unit cell is then

$$I_c = 2I_0 \left(2e^{-\left(d/\sqrt{2}\right)^2/w_0^2}\right)^2 = 8I_0 e^{-d^2/w_0^2} \tag{7.19}$$

The trap depth is then proportional to the difference between the saddle intensity I_s, and the center intensity I_c

$$I_t = I_s - I_c = I_0 2e^{-s^2/2}(1 - 4e^{-s^2/2}) \tag{7.20}$$

The trap depth as a function of the aspect ratio is plotted in Figure 7.8(a). Denoting the aspect ratio at the trapping plane as s_0, the trap depth has a maximum at $s_0 = (2\ln 8)^{1/2} \simeq 2.04$. At this parameter $I_s = I_0/4$, $I_c = I_0/8$, and $I_t = I_0/8$.

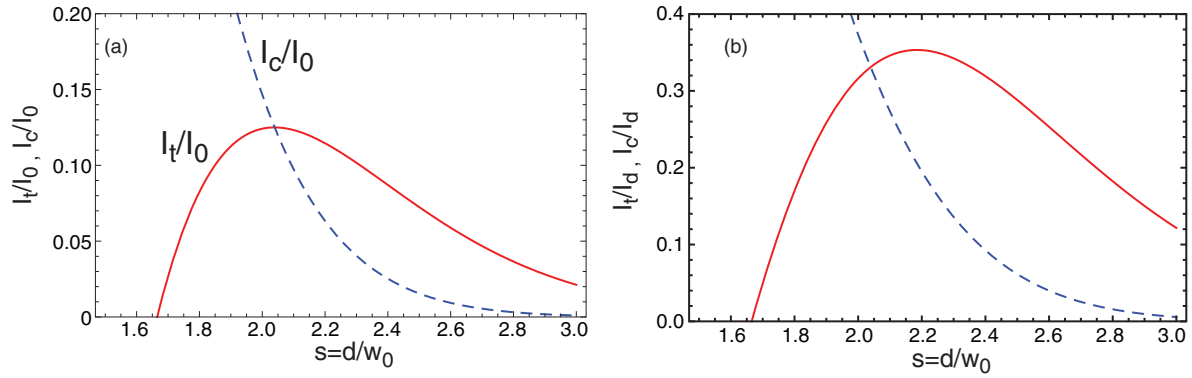


Figure 7.8: Normalized trap depth (solid red curve) and intensity at trap center (dashed blue curve) versus normalized array period for the half-incoherent array. Variation at (a) constant peak intensity I_0 and at (b) constant average intensity I_d.

In practice, we have a fixed optical power available, and a fixed atom-to-atom spacing. So it is convenient to define the trap depth as a function of w_0 for a fixed power and fixed

period d. Defining the average intensity in a unit cell of area d^2 as

$$I_d = \frac{P}{d^2} = \frac{\pi w_0^2 I_0}{2d^2} = \frac{\pi I_0}{2s^2} \tag{7.21}$$

then the trap intensity is

$$I_t = I_d \frac{4s^2 e^{-s^2/2}}{\pi}(1 - 4e^{-s^2/2}) \tag{7.22}$$

Figure 7.8b shows the trap depth as a function of unit cell intensity, and has a maximum of $I_t/I_d = 0.35$ at $s = 2.19$. Note that the calculated trap depth in Figure 7.8 was based on the worst-case phase assumption. If the diagonal beams were out of phase, we would get $I_c = 0$ and the peak trap depth would be about twice as large. Figure 7.8 also shows graphically how the contribution from more distant neighbors, which effectively at least doubles s, is negligible.

In addition to the trap depth, it is important to know the spatial localization and oscillation frequencies. These can be found by taking a Taylor expansion of the trapping potentials around the trap center, and comparing the quadratic term to a Hooke's Law spring potential to find the effective spring constants. Let us start by considering the intensity in three dimensions with the trap center at $(0, 0, 0)$, which when taking into account the four nearest neighbors is

$$\begin{aligned} I(x,y,z) = \frac{w_0^2}{w(z)^2}\frac{2I_d s^2}{\pi}\Bigg(&\left(e^{-\frac{\left(x-\frac{d}{2}\right)^2+\left(y-\frac{d}{2}\right)^2}{w^2}} + e^{-\frac{\left(x+\frac{d}{2}\right)^2+\left(y+\frac{d}{2}\right)^2}{w^2}}\right)^2 \\ &+ \left(e^{-\frac{\left(x+\frac{d}{2}\right)^2+\left(y-\frac{d}{2}\right)^2}{w^2}} + e^{-\frac{\left(x-\frac{d}{2}\right)^2+\left(y+\frac{d}{2}\right)^2}{w^2}}\right)^2\Bigg) \end{aligned} \tag{7.23}$$

where w_0 is the true waist at the focal plane, and $w(z) = w_0\sqrt{1 + z^2/z_R^2}$ is the diverging waist at longitudinal distance z, where the Rayleigh range $z_R = \frac{\pi n w_0^2}{\lambda}$.

Consider the trapping in the x direction, directed from the trap center toward a neighboring saddle, by setting $y = 0, z = 0$.

$$I(x) = \frac{4I_d s^2}{\pi}\left(e^{\frac{s^2\left(-\frac{d^2}{4}-\left(x-\frac{d}{2}\right)^2\right)}{d^2}} + e^{\frac{s^2\left(-\frac{d^2}{4}-\left(\frac{d}{2}+x\right)^2\right)}{d^2}}\right)^2 \tag{7.24}$$

Then take the Taylor expansion out to second order:

$$\begin{aligned} I(x) &\simeq I(0) + \left(\frac{\partial I}{\partial x}\right)_{x=0} x + \frac{1}{2!}\left(\frac{\partial^2 I}{\partial x^2}\right)_{x=0} x^2 \\ &= \frac{16 I_d e^{-s^2} s^2}{\pi}\left(\frac{2s^2}{d^2}\left(s^2-2\right)x^2 + 1\right) \end{aligned} \tag{7.25}$$

The second order term is compared to $\frac{1}{2}\kappa_x x^2$ to give

$$\kappa_x = \frac{32\left|U_d\right|}{\pi d^2} s^4 \left(s^2-2\right) e^{-s^2} \tag{7.26}$$

where the intensity has been converted to a potential using $U_d = \frac{\alpha}{2\epsilon_0 c} I_d$. By symmetry, we have

$$\kappa_y = \kappa_x \tag{7.27}$$

and repeating the analysis in z gives

$$\kappa_z = \frac{32\lambda^2\left|U_d\right|}{\pi^3 d^4 n^2} s^6 \left(s^2-1\right) e^{-s^2} \tag{7.28}$$

where λ, the wavelength of the trapping light, has entered the expression via the Rayleigh range. The corresponding oscillation frequencies are $\omega_j = \sqrt{\kappa_j / m_a}$ with m_a the atomic mass.

The time-averaged position variances are found from $\frac{1}{2}\kappa_j \sigma_j^2 = \frac{1}{2}\kappa_j \left\langle r_j^2 \right\rangle = \frac{1}{2} k_B T$ where T is the atom temperature. Using the spring constants above we have

$$\sigma_x^2 = \frac{\pi k_B T}{32\left|U_d\right|} \frac{e^{s^2}}{s^2(s^2-2)} w_o^2 = \sigma_{x0}^2 \frac{e^{s^2}}{s^4\left(s^2-2\right)} \tag{7.29}$$

$$\sigma_y^2 = \sigma_x^2 \tag{7.30}$$

$$\sigma_z^2 = \frac{\pi k_B T}{32\left|U_d\right|} \frac{e^{s^2}}{s^2(s^2-1)} z_R^2 = \sigma_{z0}^2 \frac{e^{s^3}}{s^6\left(s^2-1\right)} \tag{7.31}$$

Where the values $\sigma_{x0} = \sqrt{\frac{\pi d^2 k_B T}{32|U_d|}}$ and $\sigma_{z0} = \sqrt{\frac{\pi^3 d^4 n^2 k_B T}{32\lambda^2 |U_d|}}$ will be useful simplifications when comparing later to localization for the full-incoherent array. The maximal confinement is found at $\sigma_x = 1.31\sigma_{x0}$ and $\sigma_z = 0.53\sigma_{z0}$ at $s = \sqrt{\frac{5+\sqrt{13}}{2}} \simeq 2.07$. The dependency of the positional standard deviation on the aspect ratio is shown in Figure 7.9.

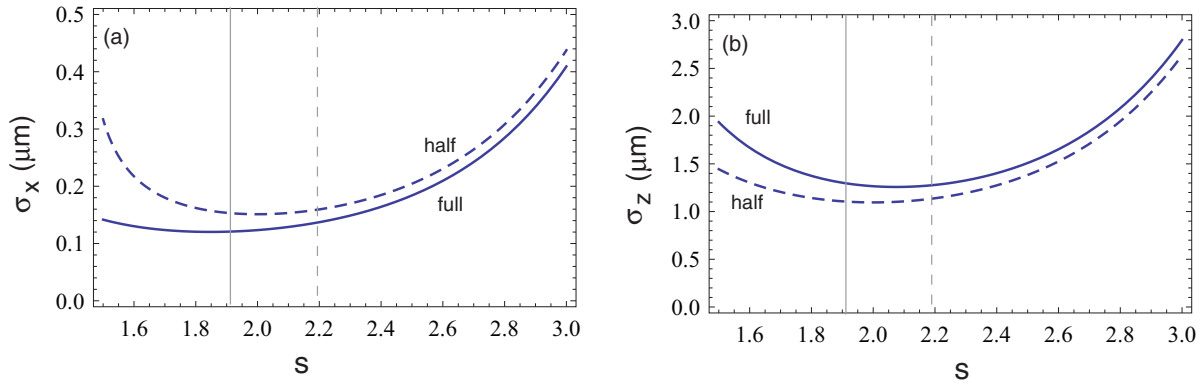


Figure 7.9: Standard deviation of (a) the x position and (b) z position, for the half-incoherent array [dashed curves] and full-incoherent array [solid curves]. Vertical lines are at the aspect ratio, s, for which the trap depths are maximized. Parameters are $\lambda = 780\,\text{nm}$, $d = 3.6\,\mu\text{m}$, $T = 10\,\mu\text{K}$, and $U_t = k_B \times 300\,\mu\text{K}$.

7.2.1.2 Full-Incoherent Array

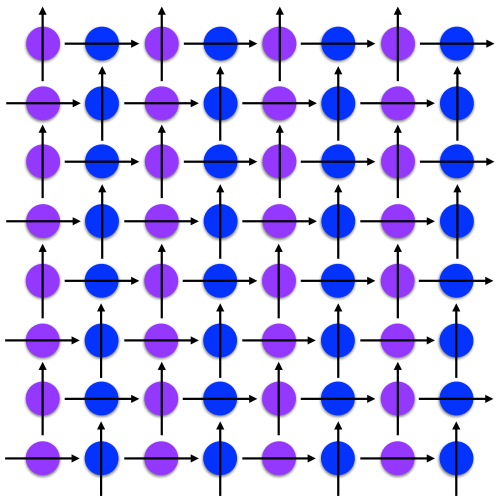


Figure 7.10: The beam layout of full-incoherent array design. Arrows indicate polarization, colors indicate different source lasers. For every beam all of its 8-neighbors have a different polarization, different frequency, or both, and so they are incoherent over this length scale.

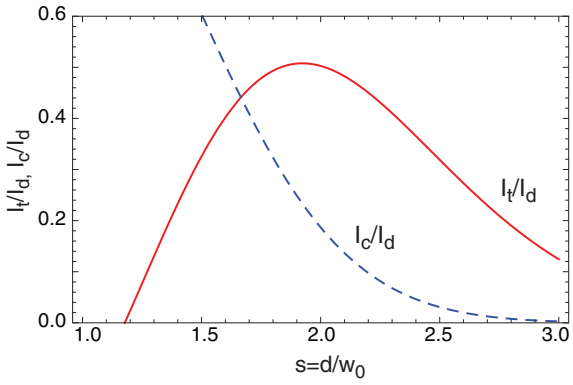


Figure 7.11: Trapping depth (solid curve) and intensity at trap center (dashed curve) versus normalized array period for the full-incoherent array. Values are normalized by the average intensity I_d.

The full-incoherent array design overcomes the remaining phase-dependence at the trap center by using two source lasers to create a pattern where all 8-neighbors of a given beam are either a) a different frequency, b) an orthogonal polarization, or c) both a different frequency and orthogonal polarization, as shown in Figure 7.10. The two source lasers can be similar in frequency, so long as they are incoherent over the length scale of the array. In our application, both source lasers are tuned close to $780\,\text{nm}$, but they are not phase locked together, and their wavelengths differ by approximately $0.1\,\text{nm}$. The interference has a length scale of

$$\frac{c}{\lambda_{\text{interference}}} = \left| \frac{c}{\lambda_1} - \frac{c}{\lambda_2} \right| \tag{7.32}$$

which for our application gives $\lambda_{\text{interference}} = 6\,\text{mm}$, which is far longer than the $\simeq 25\,\mu\text{m}$ extent of our trap array.

For this arrangement the saddle intensity is the same as for the half-incoherent array:

$$I_s = 2I_0 e^{-s^2/s} \tag{7.33}$$

but the center intensity is now instead the incoherent sum of four beams

$$I_c = 4I_0 e^{-2\left(d/\sqrt{2}\right)^2/w_0^2} = 4I_0 e^{-s^2} \tag{7.34}$$

The center intensity is reduced by a factor of two compared to the half-incoherent design because of the eliminated phase dependence. Eliminating the phase dependence is inherently beneficial for stability and simplification of the trap structure, but it also increases

the trap depth. The trap depth is now

$$I_t = I_0 \times 2e^{-s^2/2}\left(1 - 2e^{-s^2/2}\right) = I_d \times \frac{4s^2 e^{-s^2/2}}{\pi}\left(1 - 2e^{-s^2/2}\right) \tag{7.35}$$

where I_d is again the average intensity over a unit cell. Figure 7.11 shows the trap depth as a function of s. The maximum trap depth of $I_t/I_d = 0.51$ occurs at $s = 1.92$.

We can analyze the spring constants and localization as we did for the half-incoherent design. Again we approximate by taking into account the effect of only the 4 nearest beams, and Taylor expand at the trap center

$$\begin{aligned} I(x,y,z) = \frac{2I_d s^2}{\pi}\frac{w_0^2}{w^2}\Bigg(\Bigg(&e^{-\frac{2\left(\left(x-\frac{d}{2}\right)^2+\left(y-\frac{d}{2}\right)^2\right)}{w^2}} + e^{-\frac{2\left(\left(x-\frac{d}{2}\right)^2+\left(\frac{d}{2}+y\right)^2\right)}{w^2}}\Bigg) \\ &+ \Bigg(e^{-\frac{2\left(\left(\frac{d}{2}+x\right)^2+\left(y-\frac{d}{2}\right)^2\right)}{w^2}} + e^{-\frac{2\left(\left(\frac{d}{2}+x\right)^2+\left(\frac{d}{2}+y\right)^2\right)}{w^2}}\Bigg)\Bigg) \end{aligned} \tag{7.36}$$

$$I(x,0,0) = \frac{2I_d s^2}{\pi}\left(2e^{-2\frac{s^2}{d^2}\left(\frac{d^2}{4}+\left(x-\frac{d}{2}\right)^2\right)} + 2e^{-2\frac{s^2}{d^2}\left(\frac{d^2}{4}+\left(x+\frac{d}{2}\right)^2\right)}\right) \tag{7.37}$$

$$\begin{aligned} I(x) &\simeq I(0) + \left(\frac{\partial I}{\partial x}\right)_{x=0} x + \frac{1}{2!}\left(\frac{\partial^2 I}{\partial x^2}\right)_{x=0} x^2 \\ &= \frac{8I_d}{\pi d^2} e^{-s^2} s^2\left(d^2 + 2s^2\left(s^2-1\right)x^2\right) \end{aligned} \tag{7.38}$$

$$I(0,0,z) = \frac{8I_d}{\pi\left(\frac{\lambda^2 s^4 z^2}{\pi^2 d^4 n^2}+1\right)} s^2 e^{-\frac{s^2}{\frac{\lambda^2 s^4 z^2}{\pi^2 d^4 n^2}+1}} \tag{7.39}$$

$$\begin{aligned} I(x) &\simeq I(0) + \left(\frac{\partial I}{\partial x}\right)_{x=0} x + \frac{1}{2!}\left(\frac{\partial^2 I}{\partial x^2}\right)_{x=0} x^2 \\ &= \frac{8I_d}{\pi^3 d^4 n^2} e^{-s^2} s^2\left(\pi^2 d^4 n^2 + \lambda^2 s^4\left(s^2-1\right)z^2\right) \end{aligned} \tag{7.40}$$

Again taking the quadratic term gives the spring constants

$$\kappa_x = \frac{32\left|U_d\right|}{\pi d^2} s^4\left(s^2-1\right)e^{-s^2} \tag{7.41}$$

$$\kappa_y = \kappa_x \tag{7.42}$$

$$\kappa_z = \frac{16\lambda^2\left|U_d\right|}{\pi^3 d^4 n^2} s^6\left(s^2-1\right)e^{-s^2} \tag{7.43}$$

And the positional variances, in terms of σ_{x0}^2 and σ_{z0}^2 as given for the half-incoherent design, are

$$\sigma_x^2 = \sigma_{x0}^2 \frac{e^{s^2}}{s^4\left(s^2-1\right)} \tag{7.44}$$

$$\sigma_y^2 = \sigma_x^2 \tag{7.45}$$

$$\sigma_z^2 = \sigma_{z0}^2 \frac{2e^{s^2}}{s^6\left(s^2-1\right)} \tag{7.46}$$

The maximum confinement is found to be $\sigma_x = 1.04\sigma_{x0}$ at $s = \sqrt{2+\sqrt{2}} \simeq 1.85$ and $\sigma_z = 0.65\sigma_{z0}$ at $s = 2$. Thus the full-incoherent design not only has better trap depth for the same power, but also has better transverse localization. The axial localization is worse, but this is less important because the addressing beams propagate along the z axis. The full-incoherent array should therefore give better performance for both qubit control and also be less sensitive to parasitic light scattering and optical imperfections.

7.2.2 Line Grid Array

The shortcoming of the Gaussian beam array design is that the trapping potential is not defined by the peak intensity, but rather by the much lower saddle height. There is an optimal aspect ratio for the Gaussian beam array because if the beams are too narrow the saddles will open up, however if the beams are too wide then the trap centers will fill in. This optimal aspect ratio is shown in Figures 7.8 and 7.11. This geometry means that we are wasting light power at the beam peaks which does not contribute to the trap depth. For a given amount of available source laser power, a more efficient design would allow us to either make deeper traps for the same number of sites, or to make more trapping sites at the same trap depth. As an advancement on the Gaussian beam array, we instead create a design formed by *lines* instead of *spots* (Saffman and Lichtman [60]). The advantage of this is demonstrated in Figure 7.12 which shows that while the Gaussian beam array has most of its light power wasted at the peaks (Fig. 7.12a), the *line grid array* redistributes the power to fill in the saddles (Fig. 7.12b). The *Gaussian line array* shown in (Fig. 7.12c) is a further variant discussed in the next section.

The basic geometry of the *line grid array* is a square grid of lines projected onto the atoms. The functionality is the same as the Gaussian beam array, except the beams are replaced by lines. This makes the transverse saddle points higher, giving better trap depth, while

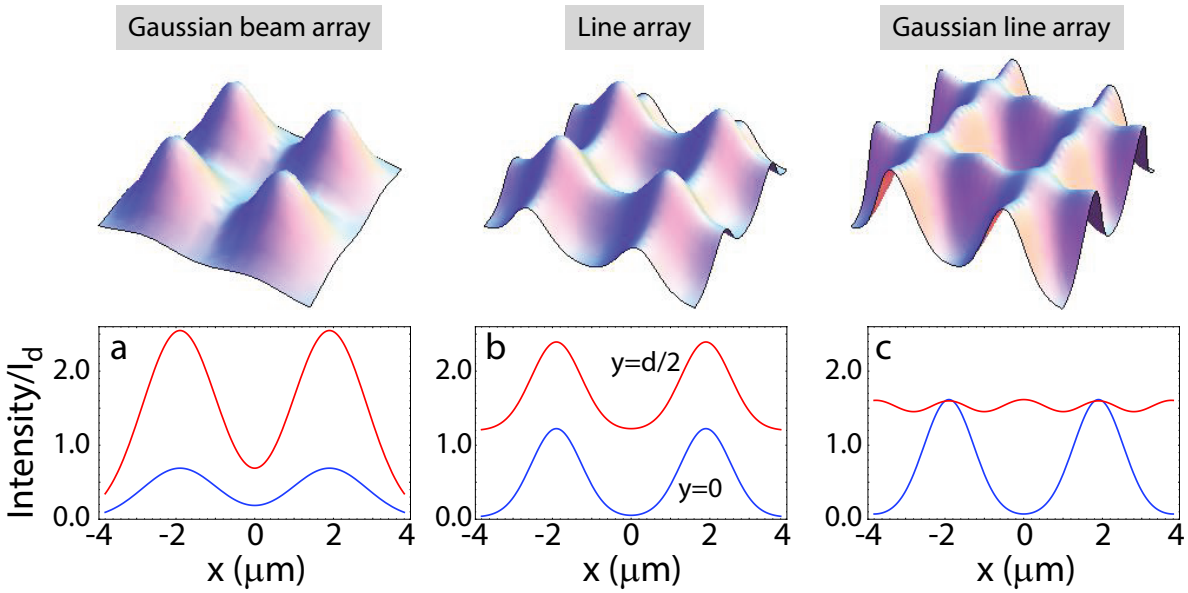


Figure 7.12: Intensity profiles in the focal plane $z = 0$ for (a) Gaussian beam array with $s = 2$, (b) line grid array with $s = 3$, and (c) Gaussian line array with $s_{\parallel} = 1.66$, $s_{\perp} = 3$.

z confinement is provided by the diffraction. As with the Gaussian beam array, we have to be careful about the Talbot effect giving multiple trapping planes. This is suppressed using combinations of mutually incoherent fields, which also removes phase dependence of the intensity structure at the trap center. Various configurations for creating the light fields are shown in Figure 7.13. We may have fully coherent, partially incoherent, or fully incoherent setups. Figure 7.13c demonstrates how we can combine two laser sources and orthogonal polarizations to create a completely incoherent implementation, in the same manner as with the full-incoherent Gaussian beam array.

We will proceed with analyzing the fully incoherent implementation of the line grid array. Each line is a 1D Gaussian beam, which is to say that it has a Gaussian intensity profile $I(\rho) = I_0 e^{-2\rho^2/w_0^2}$ in one transverse dimension where ρ is the perpendicular coordinate. The intensity is constant in the parallel transverse dimension, at least over some length. Such "flat-top" Gaussian beams can be created using diffractive or refractive optical elements. The power per unit length of the 1D Gaussian is $P_{\parallel} = \sqrt{\pi/2} w_0 I_0$ with I_0 the intensity at the peak. In the limit of an infinite array, the light per unit cell is that of four half-beams of length d, equivalent to a contribution of length $2d$ from a single line. The power per trapping site is $P = 2dP_{\parallel} = \sqrt{2\pi} d w_0 I_0$ or $I_0 = \frac{P}{\sqrt{2\pi} d w_0}$. We will use the *aspect ratio* parameter $s = d/w_0$ again, where this time it refers only to the perpendicular spacing-to-width ratio.

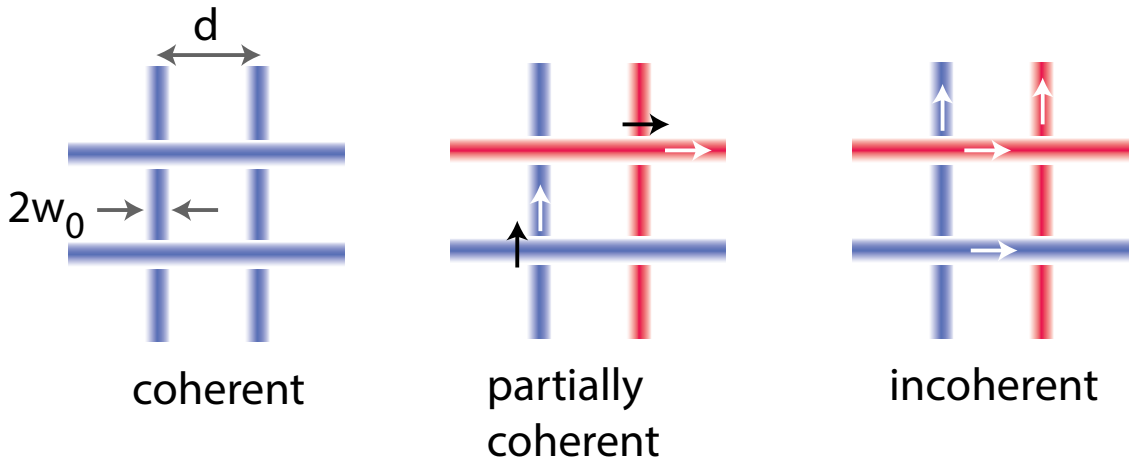


Figure 7.13: Various configurations of trap arrays based on a projected grid of lines. Each unit cell is $d \times d$. Different colors represent different frequencies that are separated by a detuning large compared to all other rates so they are effectively incoherent as concerns the atomic motion. The different cases from left to right are: fully coherent (one frequency and one polarization), partially coherent (two frequencies, each with one polarization), and fully incoherent (two frequencies, each with two polarizations).

In terms of this parameter

$$P_{\parallel} = \sqrt{\frac{\pi}{2}}\frac{d}{s} I_0 \tag{7.47}$$

$$P = \frac{\sqrt{2\pi} d^2}{s} I_0 \tag{7.48}$$

$$I_0 = \frac{s}{\sqrt{2\pi} d^2} P \tag{7.49}$$

7.2.2.1 Unit Cell Analysis

Considering only the contributions within one unit cell, with all beams in a unit cell fully incoherent, the intensity at the saddle is

$$I_s = I_0 \left(1 + 2e^{-s^2/2}\right) \tag{7.50}$$

The intensity at the trap center is

$$I_c = 4 I_0 e^{-s^2/2} \tag{7.51}$$

and the trapping intensity in the transverse plane is

$$I_{t,xy} = I_s - I_c = I_0\left(1 - 2e^{-s^2/2}\right) = I_d \times \frac{s}{\sqrt{2\pi}}\left(1 - 2e^{-s^2/2}\right) \tag{7.52}$$

with $I_d = \frac{P}{d^2} = \sqrt{2\pi} I_0/s$. The trapping intensity increases approximately linearly with s.

The intensity at trap center a distance z perpendicular to the trapping plane is

$$I_c(z) = 4\frac{I_0}{\sqrt{1+\frac{z^2}{z_R}}} e^{-\frac{s^2}{2}\frac{1}{1+z^2/z_R^2}} \tag{7.53}$$

where $z_R = \frac{\pi n w_0^2}{\lambda} = \frac{\pi d^2}{s^2 \lambda}$ is the Rayleigh range with λ the trapping light wavelength and n the index of refraction from hereon assumed to be $n = 1$. Here we have assumed that the lines have a constant parallel intensity over a sufficiently long length that we can neglect the parallel diffractive spreading. The out of plane trapping intensity is

$$I_{t,z}(z) = I_c(z) - I_c(0) \tag{7.54}$$

$$= 4I_0\left(\frac{e^{-\frac{s^2}{2}\frac{1}{1+z^2/z_R^2}}}{\sqrt{1+\frac{z^2}{z_R^2}}} - e^{-s^2/2}\right) \tag{7.55}$$

$$= I_d \times \frac{4s}{\sqrt{2\pi}}\left(\frac{1}{\sqrt{e}} - se^{-s^2/2}\right) \tag{7.56}$$

This has a maximum at $z_{max} = z_R\sqrt{s^2-1}$, where

$$I_{t,z}(z_{max}) = I_d \times \frac{4}{\sqrt{2\pi}}\left(\frac{1}{\sqrt{e}} - se^{-s^2/2}\right) \tag{7.57}$$

As $s \to \infty$ the trapping intensity asymptotes to

$$I_{t,z,max} = I_d \times \frac{4}{\sqrt{2\pi e}} \tag{7.58}$$

The trapping intensity as a function of s is shown in Figure 7.14. We see that for small s the out of plane trap depth is largest, and for large s the transverse trap depth is largest. In other words, for wide beams the transverse trapping is limiting, but for narrow beams the longitudinal trapping is limiting. Taking the minimum of these trap walls to be the more important factor, there is a cross-over at $s = 1.32$. When $s < 1.32$ the the 3D trap depth is

given by Eq. 7.52, and for $s > 1.32$ the 3D trap depth is given by Eq. 7.54. In general it will be the high aspect ratio condition that we wish to operate at, because that is where we see the best trap depth. Taking the $s > 1.32$ high aspect ratio condition, the trapping potential is then

$$U_t = -\frac{\alpha}{2\epsilon_0 c} I_t = U_d \frac{4}{\sqrt{2\pi}} \left(\frac{1}{\sqrt{e}} - s e^{-s^2/2} \right) \tag{7.59}$$

with $U_d = -\frac{\alpha I_d}{2\epsilon_0 c}$ and α the atomic polarizability. Since $I_d = P/d^2$ we recognize U_d as the characteristic optical potential per unit cell.

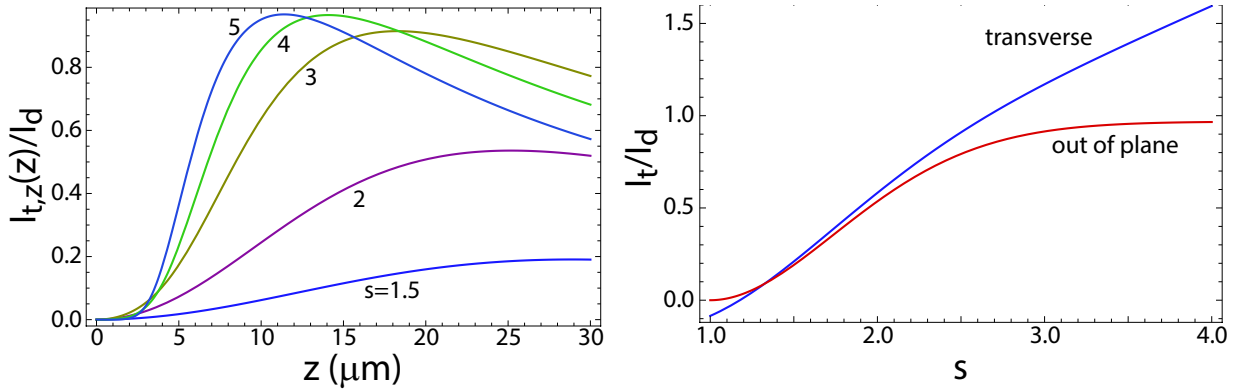


Figure 7.14: Line grid array trapping intensity for different beam parameters. The left panel shows $I_{t,z}$ versus the out of plane coordinate z for $d = 3.8\,\mu\text{m}$, $\lambda = 780\,\text{nm}$, and several values of s. The right panel shows the transverse (blue curve) and out of plane (red curve) trapping intensities versus s. The curves are normalized to $I_d = P/d^2$.

The atomic localization is found from the 2nd order trap curvature at the origin, as was done for the Gaussian beam array. Considering still just one unit cell, an atom at position $\vec{r} = (x, y, z)$ relative to the origin of that unit cell sees an optical potential

$$U(\vec{r}) = -\frac{\alpha}{2\epsilon_0 c} I(\vec{r}) \tag{7.60}$$

$$= U_d \frac{s}{\sqrt{2\pi}} \frac{w_0^2}{w^2} \left(e^{-2(x+d/2)^2/w^2} + e^{-2(x-d/2)^2/w^2} + e^{-2(y+d/2)^2/w^2} + e^{-2(y-d/2)^2/w^2} \right) \tag{7.61}$$

$$= U_d \frac{s}{\sqrt{2\pi\left(1 + z^2/z_R^2\right)}} \left(e^{-\frac{2s^2(x-d/2)^2}{d^2\left(1+z^2/z_R^2\right)}} + e^{-\frac{2s^2(x+d/2)^2}{d^2\left(1+z^2/z_R^2\right)}} + e^{-\frac{2s^2(y+d/2)^2}{d^2\left(1+z^2/z_R^2\right)}} + e^{-\frac{2s^2(y-d/2)^2}{d^2\left(1+z^2/z_R^2\right)}} \right) \tag{7.62}$$

Taking a Taylor expansion about the origin, up to second order, gives

$$U\left(\vec{r}\right) \simeq U\left(0\right) + \frac{U_d}{d^2}\sqrt{8/\pi}s^3\left(s^2-1\right)e^{-s^2/2}\left(x^2+y^2\right) + \frac{U_d}{d^2}\frac{\lambda^2}{d^2n^2}\sqrt{2/\pi^5}s^5\left(s^2-2\right)e^{-s^2/2}z^2 \tag{7.63}$$

The spring constants are then

$$\kappa_x = \frac{U_d}{d^2}\sqrt{32/\pi}s^3\left(s^2-1\right)e^{-s^2/2} \tag{7.64}$$

$$\kappa_y = \kappa_x \tag{7.65}$$

$$\kappa_z = \frac{U_d}{d^2}\frac{\lambda^2}{d^2n^2}\sqrt{8/\pi^5}s^5\left(s^2-2\right)e^{-s^2/2} \tag{7.66}$$

Because the curvature is symmetrical with respect to $r^2 = x^2 + y^2$, the spring constant is the same for motion in any direction in the xy plane. The spring constants are maximal for $s = \sqrt{3+\sqrt{6}} = 2.33$ for xy motion, and $s = \sqrt{\frac{9+\sqrt{41}}{2}} = 2.77$ for z motion. The oscillation frequencies are given by $\omega = \sqrt{\kappa/m_a}$ with m_a the atomic mass. The time-averaged position variances are, as previously, found from $\frac{1}{2}\kappa_j\sigma_j^2 = \frac{1}{2}\kappa_j\left\langle r_j^2\right\rangle = \frac{1}{2}k_BT$ with T the atomic temperature. The variances are:

$$\sigma_x^2 = \frac{\pi d^2 k_B T}{32\left|U_d\right|}\sqrt{\frac{32}{\pi}}\frac{e^{s^2/2}}{s^3\left(s^2-1\right)} = \sigma_{x0}^2\sqrt{\frac{32}{\pi}}\frac{e^{s^2/2}}{s^3\left(s^2-1\right)} \tag{7.67}$$

$$\sigma_y^2 = \sigma_x^2 \tag{7.68}$$

$$\sigma_z^2 = \frac{\pi^3 d^4 n^2 k_B T}{32\lambda^2\left|U_d\right|}\sqrt{\frac{128}{\pi}}\frac{e^{s^2/2}}{s^5\left(s^2-2\right)} = \sigma_{z0}^2\sqrt{\frac{128}{\pi}}\frac{e^{s^2/2}}{s^5\left(s^2-2\right)} \tag{7.69}$$

where as for the Gaussian beam array analysis $\sigma_{x0}^2 = \frac{\pi d^2 k_B T}{32|U_d|}$ and $\sigma_{x0}^2 = \frac{\pi^3 d^4 n^2 k_B T}{32\lambda^2|U_d|}$. Plots of the localization lengths σ_x and σ_z are shown in Figure 7.15 for nominal experimental parameters.

7.2.2.2 Infinite Grid Analysis

There are notable qualitative differences in the line grid array analysis that arise depending on how many terms are included. In the prior section, only a unit cell was analyzed, and so no light contribution beyond $d/2$ from the center was considered.

First let us see how this assumption affects the concavity of the traps. For the traps to hold atoms, the minimum intensity must be lower than the saddle intensity. As discussed

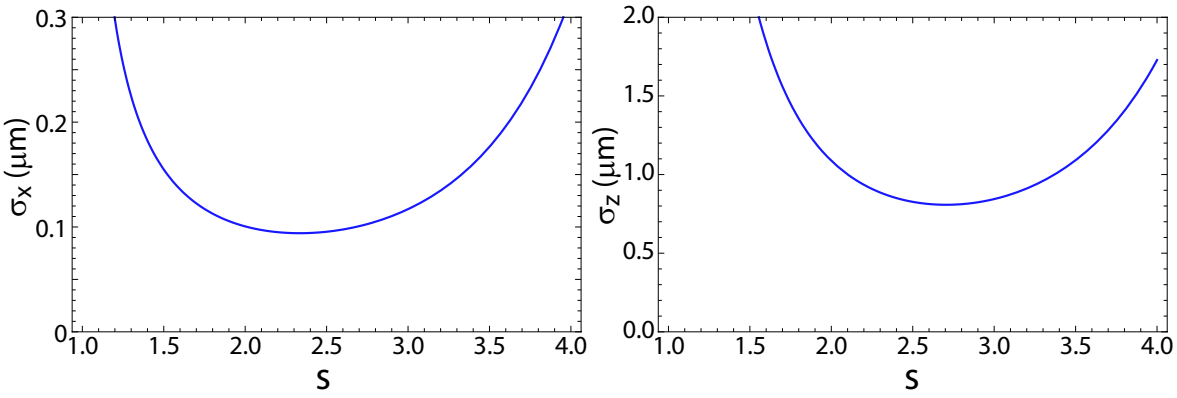
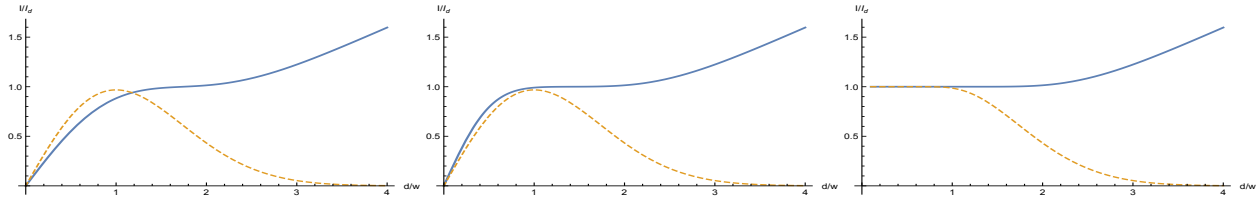


Figure 7.15: Localization lengths σ_x, σ_z as a function of s for Cs atoms with $P = 26\,\text{mW}$, $d = 3.8\,\mu\text{m}$, $\lambda = 780\,\text{nm}$, and $T = 5\,\mu\text{K}$. These parameters give a trap depth of $0.5\,\mu\text{K}$ at $s = 2.33$.



(a) (b) (c)

Figure 7.16: Analysis of the line grid array transverse concavity for three different analyses. Blue solid curves are trap saddle intensity I_s. Yellow dashed curves are trap center intensity I_c. There is transverse trapping when $I_s > I_c$. (a) Unit cell analysis considering contributions from lines up to $d/2$ from center. (b) Analysis considering contributions from lines up to d from center. (c) Analysis considering an array of infinite extent and all contributions.

above, in the unit cell analysis the intensity at the trap center and saddle are

$$I_c = I_d \frac{4}{\sqrt{2\pi}} s e^{-s^2/2} \quad I_s = I_d \frac{s}{\sqrt{2\pi}} \left(1 + 2e^{-s^2/2}\right) \tag{7.70}$$

Figure 7.16a demonstrates the concavity for this unit cell analysis. In this case, the traps are concave only when $s > \sqrt{2 \log 2} = 1.17$.

Now consider the analysis including contributions from lines up to d away. The intensity at the trap center and saddle are

$$I_c = I_d \frac{4}{\sqrt{2\pi}} s e^{-s^2/2} \quad I_s = I_d \frac{s}{\sqrt{2\pi}} \left(1 + 2e^{-s^2/2} + 2e^{-2s^2}\right) \tag{7.71}$$

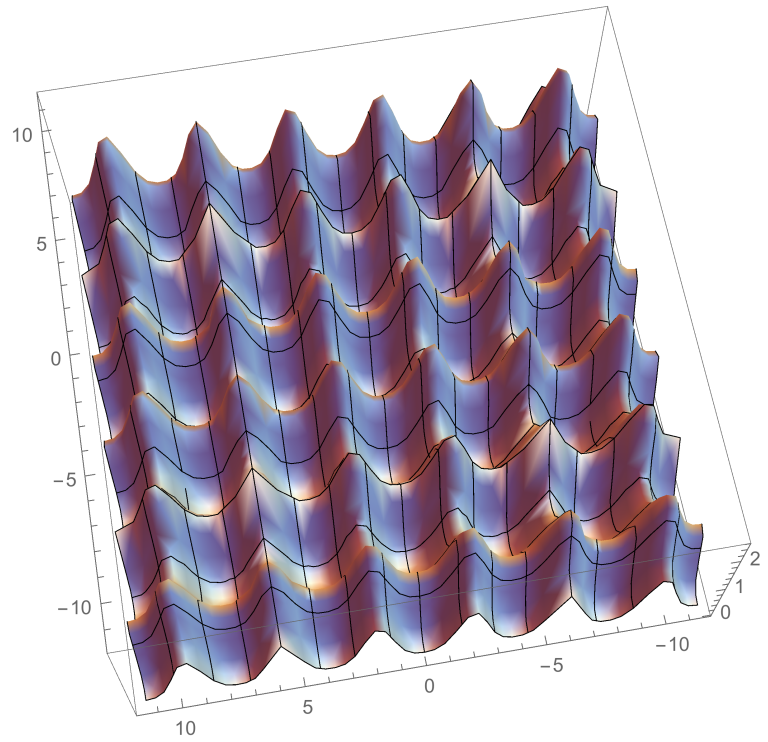


Figure 7.17: An example of a large line grid array (shown for $s = 3.2$, $d = 3.8\,\mu\text{m}$). The small contribution from an infinite number of distant lines qualitatively changes the trap properties.

Figure 7.16b shows that when the concavity is considered with this extra contribution, it is always the case that $I_s > I_c$. There is no cross-over and the traps will always hold atoms for any aspect ratio.

This motivates the further study of the contributions from the more distant lines. To make a useful quantum computer, we will need to implement a very large array of atom traps. We have seen that even the 2^{nd} row of lines should be considered in an analysis. Although the contribution from more distant lines is small, if we consider an infinite number of those lines their effect is non-negligible. We now consider an infinite incoherent line grid array, where all beam intensities sum. The full-incoherent design will have interference between sets of every-other beam, however that interference might be constructive or destructive, and so we take the incoherent case as illustrative.

In the unit cell analysis the peak intensity is the intersection of two lines, $I_{peak} = 2\frac{I_d s}{\sqrt{2\pi}}$.

However, if we consider the sum of an infinite number of contributing lines, we have

$$I_{peak} = 2\frac{I_d s}{\sqrt{2\pi}} + \sum_{j=1}^{\infty}\left(4\frac{I_d s}{\sqrt{2\pi}} e^{-2s^2((j*d)/d)^2}\right) \tag{7.72}$$

$$= I_d s\sqrt{\frac{2}{\pi}}\vartheta_3\left(0, e^{-2s^2}\right) \tag{7.73}$$

where ϑ_3 is an Elliptic Theta function of the third kind, defined as

$$\vartheta_3(u,q) = 2\sum_{n=1}^{\infty} q^{n^2}(\cos(2nu)) + 1 \tag{7.74}$$

These functions are useful because they have known analytical solutions for their derivatives, which makes it possible to analyze the line grid array trap properties for the case of infinite extent.

The trap center intensity is

$$I_c = \sum_{j=0}^{\infty}\left(4\frac{I_d s}{\sqrt{2\pi}} e^{-2s^2(((j+1/2)*d)/d)^2}\right) \tag{7.75}$$

$$= I_d s\sqrt{\frac{2}{\pi}}\vartheta_2\left(0, e^{-2s^2}\right) \tag{7.76}$$

with the Elliptic Theta function of the second kind

$$\vartheta_2(u,q) = 2\sqrt[4]{q}\sum_{n=0}^{\infty} q^{n(n+1)}\cos((2n+1)u) \tag{7.77}$$

The saddle intensity is

$$I_s = \frac{I_d s}{\sqrt{2\pi}} + \sum_{j=1}^{\infty}\left(2\frac{I_d s}{\sqrt{2\pi}} e^{-2s^2((j*d/2)/d)^2}\right) \tag{7.78}$$

$$= \frac{I_d s}{\sqrt{2\pi}}\vartheta_3\left(0, e^{-s^2/2}\right) \tag{7.79}$$

The transverse trapping intensity is then

$$I_{t,xy} = \frac{I_d s}{\sqrt{2\pi}}\left(\vartheta_3\left(0, e^{-s^2/2}\right) - \vartheta_2\left(0, e^{-2s^2}\right)\right) \tag{7.80}$$

If we look at the transverse concavity for the infinite extent, plotted in Figure 7.16c, we see a qualitatively different behavior, where at low s both the saddle and center intensity asymptote to I_d, but always $I_s > I_c$ so the traps hold atoms at any aspect ratio.

The intensity in the propagation direction is found by taking the intensity at the trap center and modifying the aspect ratio as a function of z

$$I_c(z) = \frac{I_d s \sqrt{\frac{2}{\pi}}}{\sqrt{1 + \frac{z^2\lambda^2}{n^2\pi^2 w_0^4}}} \vartheta_2\left(0, e^{-2s^2/\left(1+\frac{z^2\lambda^2}{n^2\pi^2 w_0^2}\right)}\right) \tag{7.81}$$

The intensity along the z axis has no peak, instead it asymptotes to I_d as $z \to \infty$ as shown in Figure 7.18. When this constant z trapping intensity is compared to the transverse saddle intensity, we see that the saddle intensity is always greater, as in Figure 7.19. Therefore in the infinite incoherent grid the trap depth is always defined by the longitudinal trapping. This can been seen explicitly in Figure 7.20 which shows the longitudinal and transverse trap depths. We see that the longitudinal depth is always lower, and that it asymptotes to I_d as the aspect ratio becomes large. The trap depth is $0.946 I_d$ at $s = 3$ and $0.998 I_d$ at $s = 4$. Therefore nearly all the benefit of a high aspect ratio has been achieved by $s = 3$ or 4 and there is little benefit to going higher.

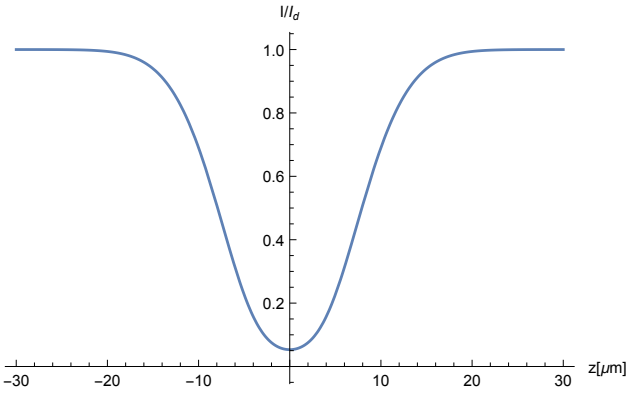


Figure 7.18: The trap center intensity along the z axis for the infinite incoherent line grid array. The intensity asymptotes to I_d as all the beams merge together. Parameters used were $\lambda = 780\,\text{nm}$, $d = 3.8\,\mu\text{m}$, and $s = 3$.

7.2.2.3 Comparison to Gaussian Beam Array

We saw that the best trap depth for the full-incoherent Gaussian beam array was achieved at $U_{t,GBA}/U_d = 0.51$ at $s = 1.92$, while the line array achieves a maximum of $U_{t,LA}/U_d \to 1$

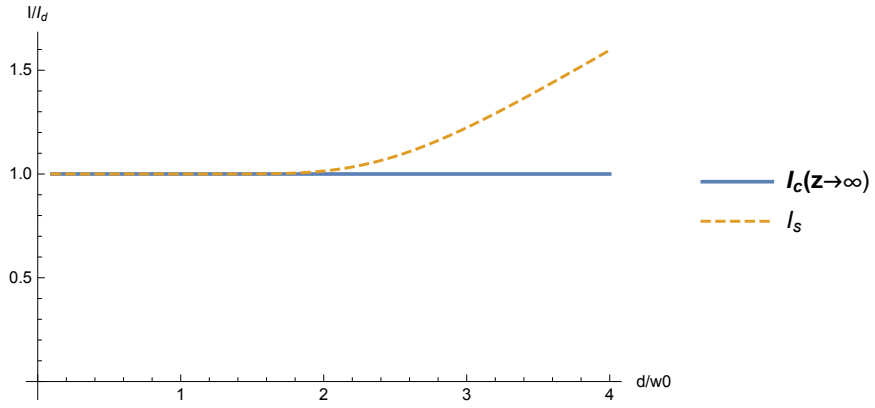


Figure 7.19: A comparison of the transverse saddle intensity (dashed yellow curve) and maximum longitudinal intensitiy (solid blue curve) for the infinite incoherent line grid array. The longitudinal intensity (solid blue line) is constant at I_d as the beams always merge to this average intensity at $z \to \infty$. In the analysis of the grid of infinite extent the transverse saddle intensity is always greater than the maximum longitudinal intensity for any aspect ratio s.

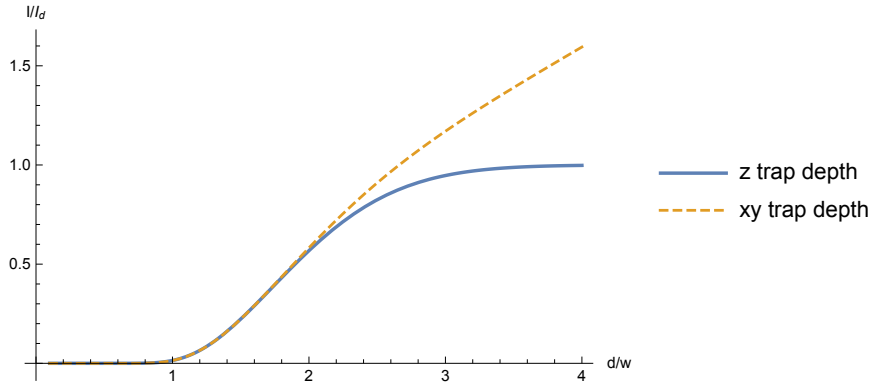


Figure 7.20: A comparison of the transverse and longitudinal trap intensities for the infinite incoherent line grid array. The longitudinal intensity (solid blue line) always asymptotes to I_d. In the analysis of the grid of infinite extent, the transverse saddle intensity (dashed yellow curve) is always greater than the longitudinal trap intensity for any aspect ratio s.

as $s \to \infty$. So the line array design is more efficient in optical power usage by a factor of $U_{t,LA}/U_{t,GBA} = 1/0.51 = 1.96$. It should be mentioned that the line array has poor atomic localization at $s \to \infty$, as was shown above. If instead we take the line array at $s = 3$ we have $U_{t,LA} = 0.95$ and the line array is still advantageous by a factor of $U_{t,LA}/U_{t,GBA} = 0.95/0.51 = 1.85$.

The localization for the Gaussian beam array at the best trap depth setting of $s = 1.92$ is $\sigma_x = 1.05\sigma_{x0}$ and $\sigma_z = 0.77\sigma_{z0}$, where σ_{x0} and σ_{z0} were defined in Section 7.2.1.1. The localization for the line grid array at $s = 3$ is $\sigma_x = 1.15\sigma_{x0}$ and $\sigma_z = 0.23\sigma_{z0}$. So for these parameters the line array has comparable but slightly worse transverse localization, while it has significantly better longitudinal localization. For reasonable experiment parameters of $s = 1.92$, $\lambda = 780\,\text{nm}$, $d = 3.8\,\mu\text{m}$, $T = 10\,\mu\text{K}$, and $\frac{U_d}{k_B} = 500\,\mu\text{K}$ the Gaussian beam array has localization of $\sigma_x = 0.18\,\mu\text{m}$ and $\sigma_z = 1.98\,\mu\text{m}$. At these same parameters, except $s = 3$, the line grid array has localization of $\sigma_x = 0.17\,\mu\text{m}$ and $\sigma_z = 0.98\,\mu\text{m}$.

The line array shows clear advantages in trap parameters. There is also a distinct advantage in alignment stability because of the increased symmetry of the line array. A misalignment of one set of lines (i.e. just the vertical lines) along the parallel direction (i.e. vertical misalignment) will have no effect on the trapping, except for the edge sites. Furthermore, a misalignment of one set of lines (i.e. just the vertical lines) along the perpendicular direction (i.e. horizontal misalignment) will only act to shift the location of the trapping sites, which is easily accounted for during initial calibration of the camera regions of interest. So it is expected that the line array will provide significantly increased stability.

7.2.3 Gaussian Line Array

One further modification explored, as an attempt to improve the efficiency of the trap array even further, is shown in Figure 7.12c. It is a mixture of the ideas of the Gaussian beam array and the line grid array, and we refer to it as the *Gaussian line array*. We use elliptical Gaussian beams to fill in the trap saddles, avoiding the low saddle height of the Gaussian beam array. However because the elliptical beams do not intersect, we do not create an extra doubling of light at the vertices as the line grid array does. This light pattern is created using the parquet pattern shown in Figure 7.21, where sets of beams are elliptical in orthogonal directions to most efficiently fill in the array.

Each side of the unit cell can be defined by a Gaussian beam propagating along z as

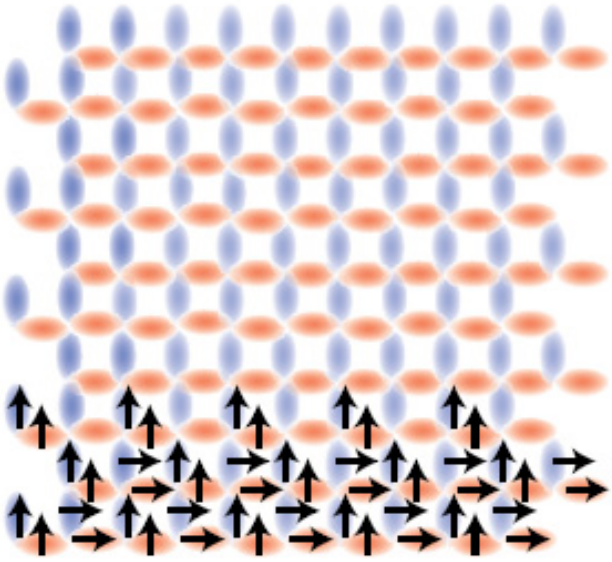


Figure 7.21: The parquet pattern of elliptical beams that create the Gaussian line array. Alternating orthogonal orientations provide filling of the trap light with minimal overlap. Arrows indicate polarization. However, despite the efficient appearance, the Gaussian line array is less advantageous than the line grid array.

before, but with transverse intensity profile

$$I\left(r_{\|}, r_{\perp}\right) = I_0 e^{-2r_{\|}^2/w_{\|}^2} e^{-2r_{\perp}^2/w_{\perp}^2} \tag{7.82}$$

Here $r_{\|}$ and $r_{\perp}$ are coordinates along/perpendicular to each line segment and we will introduce two different aspect ratios $s_{\|} = d/w_{\|}$ and $s_{\perp} = d/w_{\perp}$. For a fully incoherent arrangement the intensity at the unit cell corner is approximately

$$I_{corner} = 4I_0 e^{-s_{\|}^2/2} \tag{7.83}$$

while the intensity in the middle of the unit cell is

$$I_{side} = I_0 \left(1 + (2 \pm 2) e^{-2s_{\|}^2}\right) \tag{7.84}$$

where the $\pm$ sign depends on the fields from neighboring unit cells, which are mutually coherent, and if the interference is constructive or destructive. We have assumed $s_{\|} \ll s_{\|}$. Setting $I_{corner} = I_{side}$ with 2 ± 2 replaced by the average value of 2 gives $s_{\|} \simeq 1.66$. This value of $s_{\|}$ changes by less than one percent irrespective of the sign of the field interference

which provides only a small correction to the intensity profile. The light shift profile shown in Figure 7.12c uses the averaged condition.

In the following analysis of the Gaussian line array design we will keep $s_\parallel = 1.66$, take the average of the field interference from the neighboring cells (e.g. replace 2 ± 2 by 2), and vary $s_\perp$ to find optimal trap parameters. The power per unit cell in an extended array is simply the power of two sides or $P = 2\frac{\pi w_\parallel w_\perp}{2} I_0$ with I_0 the peak intensity of the elliptical Gaussian beam. We can write this relation as

$$I_0 = \frac{P}{\pi w_\parallel w_\perp} = \frac{P}{d^2}\frac{s_\parallel s_\perp}{\pi} = I_d \frac{s_\parallel s_\perp}{\pi} \tag{7.85}$$

The intensity at the trap center is

$$I_c = 4I_0 e^{-s^2/2} = I_d \times \frac{4 s_\parallel s_\perp}{\pi} e^{-s^2/2} \tag{7.86}$$

The transverse trapping intensity is thus

$$I_{t,xy} = I_0 - I_c = I_d \times \frac{s_\parallel s_\perp}{\pi}\left(1 - 4e^{-s_\perp^2/2}\right) \tag{7.87}$$

and the transverse trap depth is

$$U_{t,xy} = U_d \times \frac{s_\parallel s_\perp}{\pi}\left(1 - 4e^{-s_\perp^2/2}\right) \tag{7.88}$$

Taking $s_\parallel = 1.66$ and $s_\perp = 3.0$ we get $U_{t,xy}/U_d = 1.51$ which is 59% better than the value of 0.95 we found for the line grid array at $s = 3$. Unfortunately the out of plane trapping potential is similar to that found for the line grid array, so there is no significant improvement in trap depth. This can be seen in Figure 7.22 where it is seen that the maximum closed contour for the line grid array and the Gaussian line array both have a relative intensity of $0.95U_d$. Using this metric the line grid array and Gaussian line array both beat the Gaussian beam array, which has a maximum closed contour of 0.5.

To find the out of plane trapping, we take the intensity at trap center a distance z perpendicular to the trapping plane

$$I_c(z) = 4I_0 \frac{e^{-s_\perp^2/\left(2\left(1+z^2/z_{R\perp}^2\right)\right)}}{\sqrt{1 + z^2/z_{R\parallel}^2}\sqrt{1 + z^2/z_{R\perp}^2}} \tag{7.89}$$

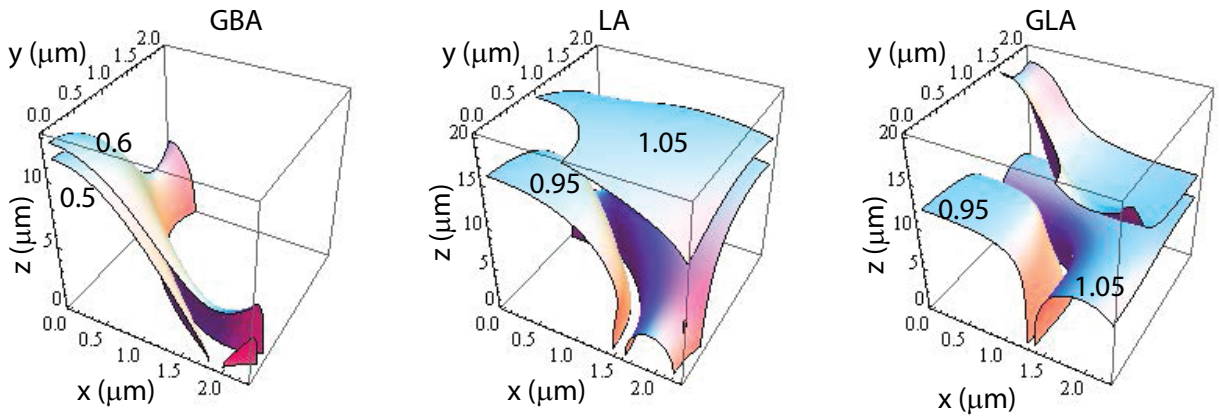


Figure 7.22: Contours of constant trap potential U_t/U_d in the positive octant for the (a) Gaussian beam array, (b) line grid array and (c) Gaussian line array with $d = 3.8\,\mu\text{m}$, $\lambda = 780\,\text{nm}$, $s_{GBA} = 2$, $s_{LA} = 3$, $s_\parallel = 1.66$ and $s_\perp = 3$. Contours are labeled with U_t/U_d and those that are concave towards the origin in the entire octant are stable traps.

with $z_{R\parallel} = \frac{\pi d^2}{s_\parallel^2 \lambda}$ and $z_{R\perp} = \frac{\pi d^2}{s_\perp^2 \lambda}$. The out of plane trapping intensity is

$$I_{t,z} = I_c(z) - I_c(0) \tag{7.90}$$

$$= I_d \times \frac{4 s_\parallel s_\perp}{\pi} \left(\frac{e^{-s_\perp^2/\left(2\left(1+z^2/z_{R\perp}^2\right)\right)}}{\sqrt{1+z^2/z_{R\parallel}^2}\sqrt{1+z^2/z_{R\perp}^2}} - e^{-s_\perp^2/2} \right) \tag{7.91}$$

This has a maximum intensity at

$$z = \frac{1}{2}\sqrt{\frac{\pi^2\sqrt{d^8\lambda^4 \mathrm{s}_\parallel^8\left(\mathrm{s}_\parallel^8\mathrm{s}_\perp^4 - 6\mathrm{s}_\parallel^8\mathrm{s}_\perp^2 + \mathrm{s}_\parallel^8 + 6\mathrm{s}_\parallel^4\mathrm{s}_\perp^6 - 2\mathrm{s}_\parallel^4\mathrm{s}_\perp^4 + \mathrm{s}_\perp^8\right)}}{\lambda^4\mathrm{s}_\parallel^4\mathrm{s}_\perp^8} - \frac{\pi^2 d^4}{\lambda^2\mathrm{s}_\parallel^4} - \frac{3\pi^2 d^4}{\lambda^2\mathrm{s}_\perp^4} + \frac{\pi^2 d^4}{\lambda^2\mathrm{s}_\perp^2}} \tag{7.92}$$

For $s_\parallel = 1.66$, $s_\perp = 3$, $d = 3.8\,\mu\text{m}$, $\lambda = 780\,\text{nm}$ this gives maximum out-of-plane trap intensity of $0.94 I_d$ at $z = 15.1\,\mu\text{m}$. As this is lower than the transverse trap intensity, this is the limiting figure.

Despite its apparent more efficient distribution of light, the Gaussian line array does not improve upon the line grid array because, just like the Gaussian beam array in s, it is subject to an optimal aspect ratio in $s_\parallel$, which ultimately limits the maximum achievable trap depth. Because it does not offer an improvement in trap depth over the line grid array, but suffers from the same sensitivity to misalignment as the Gaussian beam array, and is

yet more complicated to implement than either of those, we do not have plans to implement the Gaussian line array. The line grid array offers the most promise for making stable traps, and so that will be pursued for further large atomic qubit arrays.

7.3 Trap Array Implementations

We have implemented several versions of the single-atom laser confinement light. First the half-incoherent Gaussian beam array was implemented in a 6 site design, as will be discussed in Section 7.3.1, followed by the full-incoherent Gaussian beam array in a 49 site design as will be discussed in Section 7.3.2. Atom trapping and qubit operations have been demonstrated in both of these grids. Finally, the line grid array has been implemented for an 121 site design as will be discussed in Section 7.3.3, but has not yet been used for atom trapping. The design and construction of each of these trap arrays will be discussed below.

To implement these trapping arrays, it would be straightforward to create the entire pattern with a single diffractive optical element. However for our desired aspect ratios it turns out to be infeasible to do so. The diffractive spreading angle of a Gaussian beam of waist w_0 is $\theta_d = \frac{\lambda}{\pi w_0}$. The angular separation of the beams from a grating of period Λ is $\theta_g = \lambda/\Lambda$. In order to achieve $s = d/w_0 \simeq 2$, which we identified in the previous section as the optimal spacing for the full-incoherent array, we need $\theta_g/\theta_d \simeq 2$. However this implies that $\theta_g/\theta_d = \frac{\pi w_0}{\Lambda} \simeq 2$ or $\Lambda = \frac{\pi w_0}{2}$. In other words, the grating period is comparable to the waist of the Gaussian beam illuminating the grating. In this regime standard diffractive optical elements do not perform well and lead to large distortions of the diffracted spot array. Our tests show that the beam quality after the grating is good when $s \gtrsim 4$.

To satisfy this requirement of large spacing, we use a diffractive optical element with $s \sim 4$, followed by a birefringent calcite beam displacer to double the trap period to $s \sim 2$. The calcite beam displacement optics serve the additional function of giving neighboring beams orthogonal polarizations, which is necessary for our incoherent light field design.

7.3.1 6 Site Half-Incoherent Gaussian Beam Array

We have implemented a 6 site version of the half-incoherent Gaussian beam array, as described in Piotrowicz et al. [59]. The optics layout for this setup is given in Figure 7.23. All lenses specified in Figure 7.23 are positioned confocally. The high-power 780 nm source, which is detailed in Section 8.1, is coupled into a single-mode polarization maintaining fiber so that the array optics are provided with a very clean Gaussian TEM_{00} beam with linear

polarization. We used a Holo/Or MS-248-X-Y-A grating which has the effect of multiplying one beam into a 2-by-2 grid with a separation angle of $2.925°$. After appropriate collimation optics, the grid is doubled at $45°$ by a displacement of $d/\sqrt{2}$ in a birefringent calcite beam displacer (thickness 3.3 mm, 354 µm displacement). The resulting pattern has 8 beams, with two sets of 4 at orthogonal polarizations. The polarization is at $45°$ to the crystal ordinary and extraordinary axes, and so the resulting beams have equal intensity. The pattern is then doubled again in another calcite, this time at $-90°$ to the pattern by a displacement of $d/2$. Again all polarizations are at $45°$ to the calcite axes, and so the resulting beams have equal intensity. The final pattern after the second calcite has 16 beams, at two orthogonal polarizations. The beam pattern after each element is shown in Figure 7.25. The array produced using $\lambda = 780\,\text{nm}$ light has $d = 250\,\mu\text{m}$ and $w_0 = 120\,\mu\text{m}$, giving $s = 2.1$. The desired light pattern and the corresponding atom trapping locations are shown in Figure 7.24a. The actual pattern of light produced is shown in Figure 7.24b. This pattern is reduced down using two confocal telescopes to the atom trapping plane with $d = 3.8\,\mu\text{m}$ and $w_0 = 1.8\,\mu\text{m}$, while keeping the $s = 2.1$ aspect ratio.

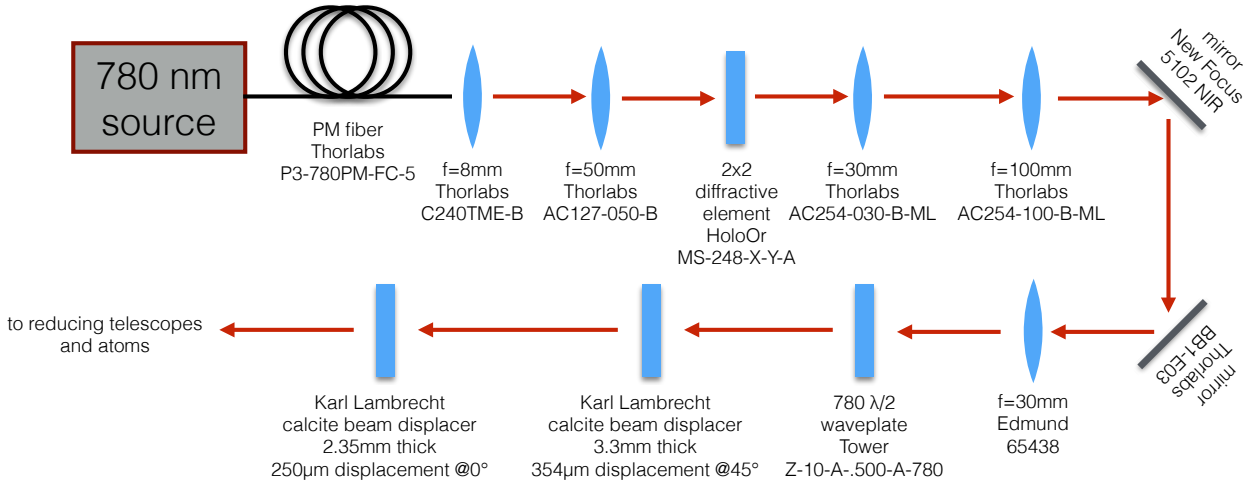


Figure 7.23: The optics layout for our 6 site half-incoherent Gaussian beam array implementation. Not to scale.

We have demonstrated atom loading into this six site array. The atom cooling and loading sequence is described in Chapter 11. We transmit $3\,\text{W}$ of $780\,\text{nm}$ light out of the fiber into the array optics. The array optics and subsequent telescoping optics have an efficiency of 50% giving $1.5\,\text{W}$ at the atoms divided into 16 beams and a trap depth of $\sim 830\,\mu\text{K}$. Figure 7.26a shows imaging of the trapped atoms. Figure 7.26a gives a loading histogram for one site. The loading rates vary from 50% to 60% depending on the site, with

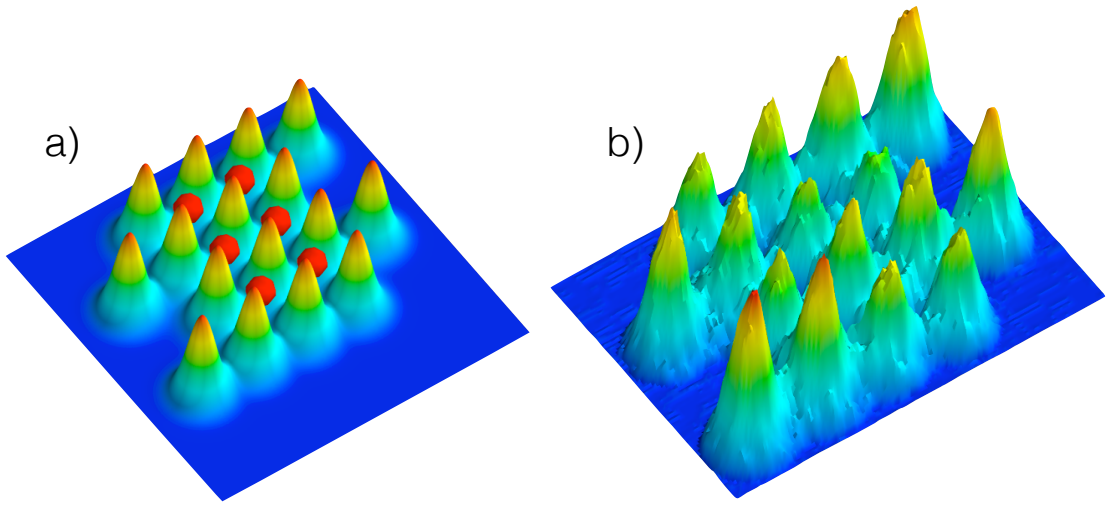


Figure 7.24: The light pattern for the 6 site half-incoherent Gaussian beam array. (a) Simulated light pattern with red balls showing the atom trapping locations. (b) Measured intensity map of the light field produced by the 6 site optics at $\lambda = 780\,\text{nm}$ with resulting $d = 250\,\mu\text{m}$, $w_0 = 120\,\mu\text{m}$ giving $s = 2.1$.

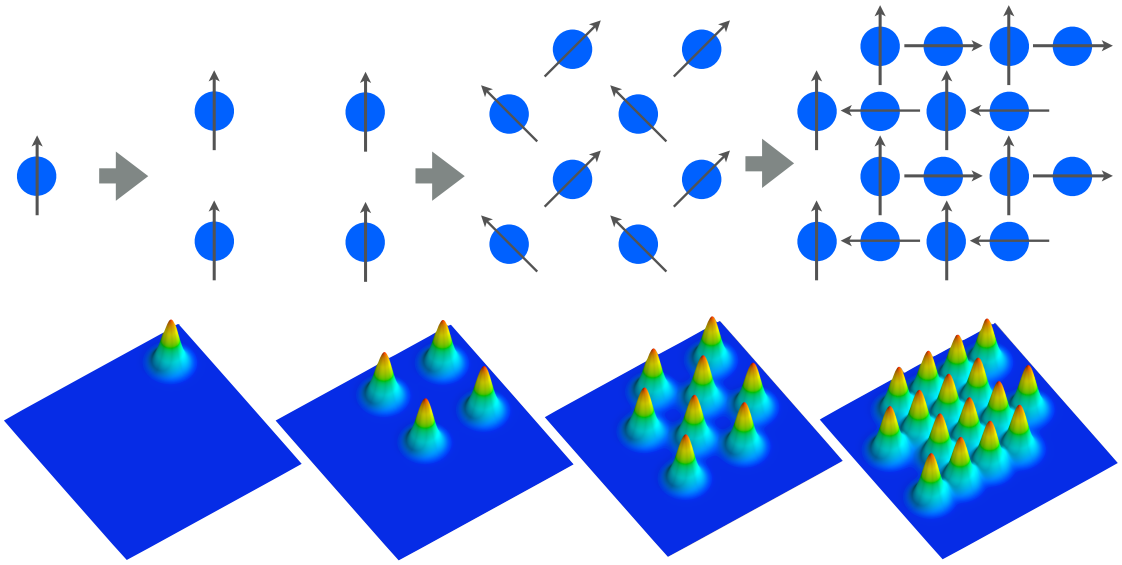


Figure 7.25: The sequence of beam manipulations for the 6 site half-incoherent Gaussian beam array. A single Gaussian beam is split into 2x2 using a diffractive optical element, followed by duplication at $45°$ in a calcite beam displacer, followed by duplication at $0°$ in another calcite beam displacer. Arrows indicate polarization of each beam. The resulting 16 beam pattern has 6 dark sites for atom trapping.

an average of 52.5%. The loading is sub-Poissonian because we see no two atom loading events.

We have measured the trap frequencies by modulating the trapping light and observing the atom retention as a function of the pulsation frequency. The modulation was applied for 100 ms for $f < 35$ kHz and 5 ms for $f > 35$ kHz. Results of 200 measurements at each frequency step are shown in Figure 7.27. When the frequency matches $\frac{2\omega_0}{2\pi}$ the atoms should be heated out of the traps and lost. The expected trap frequencies are $\omega_z = 2\pi \times 6.4$ kHz and $\omega_x = 2\pi \times 39$ kHz. The measured resonances are at 18 kHz and 90 kHz, corresponding to $\omega_z/2\pi = 9$kHz and $\omega_x/2\pi = 45$kHz respectively. The axial frequency is 40% higher than expected and the radial frequency is 15% higher than expected. We have observed that the individual focused beams in the array do not have an ideal Gaussian profile and diverge more rapidly than for a Gaussian with the same waist (i.e. the beam quality $M^2 > 1$). This fast divergence will have minimal effect on the radial frequency, but will increase the axial frequency, which explains the discrepancy between the calculated trap depth and the measured radial and the axial trap frequency measurements.

The trap lifetime was measured by turning off all light except the 780 nm trapping light after initial atom capture and imaging, and then re-imaging after some delay. The measured $1/e$ lifetimes range from 3.7 to 11 s for different sites. The lifetime was previously measured to be 20 s in a 1038 nm single-beam red-detuned trap with mK trap depth. This gives the trap lifetime limit due to collisions with untrapped hot background atoms in the imperfect vacuum. The shorter lifetime in the 6 site blue-detuned array is likely due to the smaller trap depth and imperfections in the trap shape.

7.3.2 49 Site Full-Incoherent Gaussian Beam Array

We have implemented a 49 site array using the full-incoherent Gaussian beam array design. The optics layout used to achieve this is shown in Figure 7.28. To satisfy the full-incoherent condition we had to take advantage of orthogonal polarizations as in the half-incoherent design, but also use two laser sources. One source was a 1560 nm source frequency-doubled by second harmonic generation, and the other a 532 nm pumped Ti:Sapphire laser. Both sources are described further in Section 8.1. The beams from each laser are split into a 4×4 grid by a diffractive optical element. These two 4×4 patterns are combined on a polarizing beam cube. Orthogonal polarizations are used for each source so that the patterns can be combined on the PBS with high efficiency. This forms a 4×8 pattern which is then

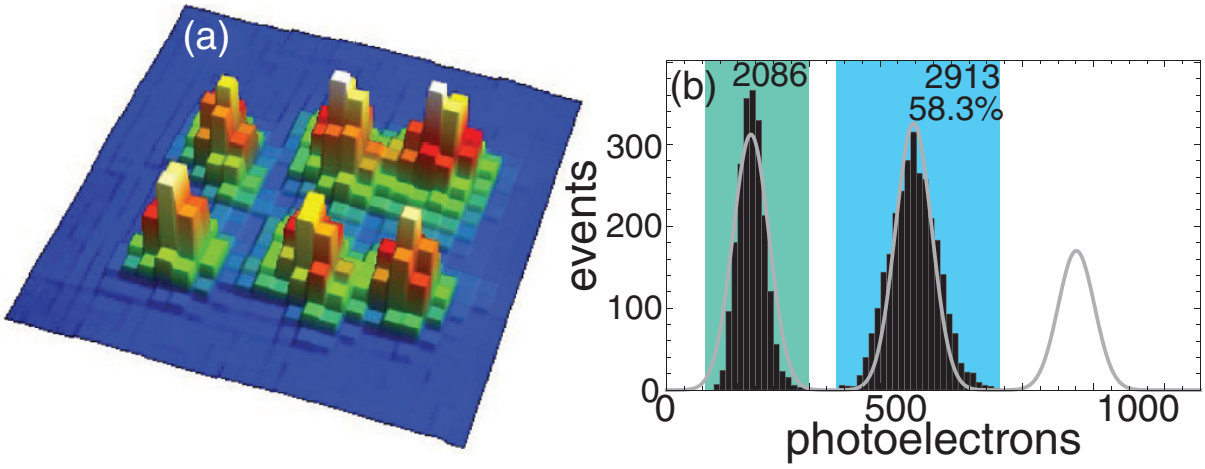


Figure 7.26: (a) Fluorescence image and (b) atom number histogram in the six-site half-incoherent array. The image is an average of 105 of 5000 events where all six sites loaded a single atom. Each pixel is $0.63 \times 0.63\,\mu m^2$. The atom number histogram shows the brightness distribution over 500 events for one of the six sites. It shows a clear separation of the zero-atom background from the one-atom peak. The solid line is a Poissonian model fitted to the one-atom peak. No two-atom loading is observed.

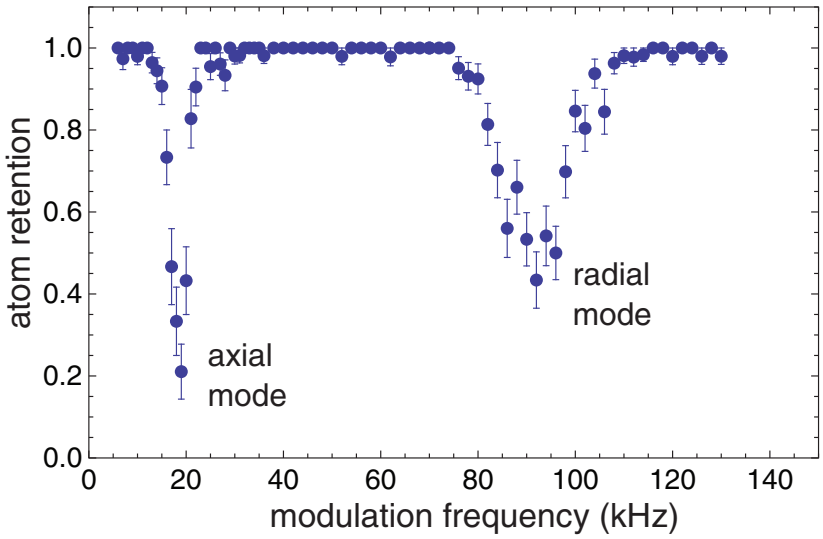


Figure 7.27: Parametric heating measurement of trap frequencies.

doubled to an 8×8 pattern by a calcite beam displacer with the crystal angle at $45°$ to either polarization. The sequence of beam manipulations is shown in Figure 7.29.

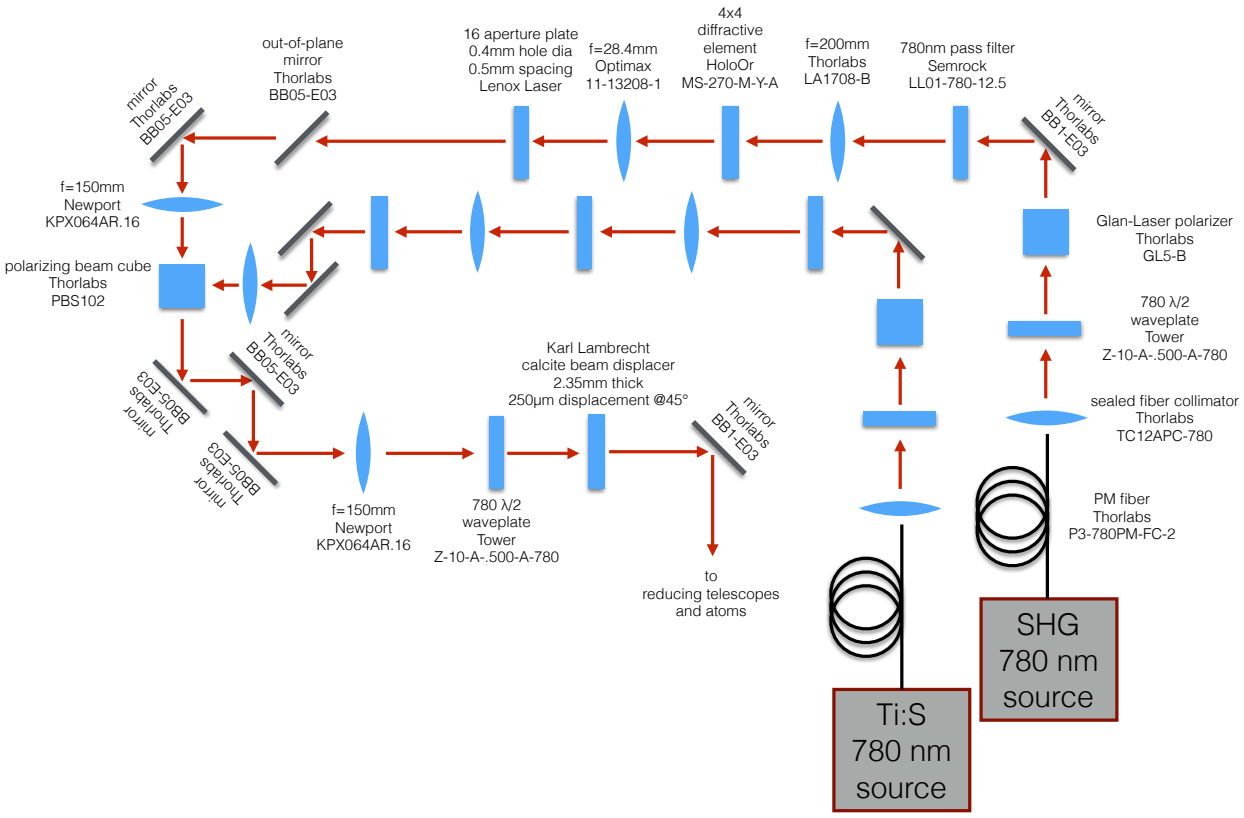


Figure 7.28: The optics layout for our 49 site full-incoherent Gaussian beam array implementation. Not to scale. The optics and path lengths from the two laser sources are identical up to the PBS. The unlabeled optics on the Ti:S path are identical to the corresponding optics on the SHG path.

The two laser systems were adjusted to have wavelengths approximately 0.1 nm apart. The source lasers were coupled into single-mode polarization maintaining fibers, and each laser was adjusted to provide 2.5 W out of the respective fiber. The full-incoherent optics and subsequent relay telescopes have a transmission efficiency of 60%, giving 3 W at the atoms, or 47 mW into each of 64 beams (an 8×8 grid) with $d = 3.8$ μm and $s = 2.1$. The atom trapping positions and the actual light field produced are shown in Figure 7.30.

This provides a trapping potential of 570 μK for 49 sites (a 7×7 grid). Atom trapping has been observed even with half this input power (~ 285 μK trap depth). Additionally, the atom trapping is very insensitive to a power imbalance between the two laser sources. The atom trapping is however very dependent on the mutual alignment of the two laser paths,

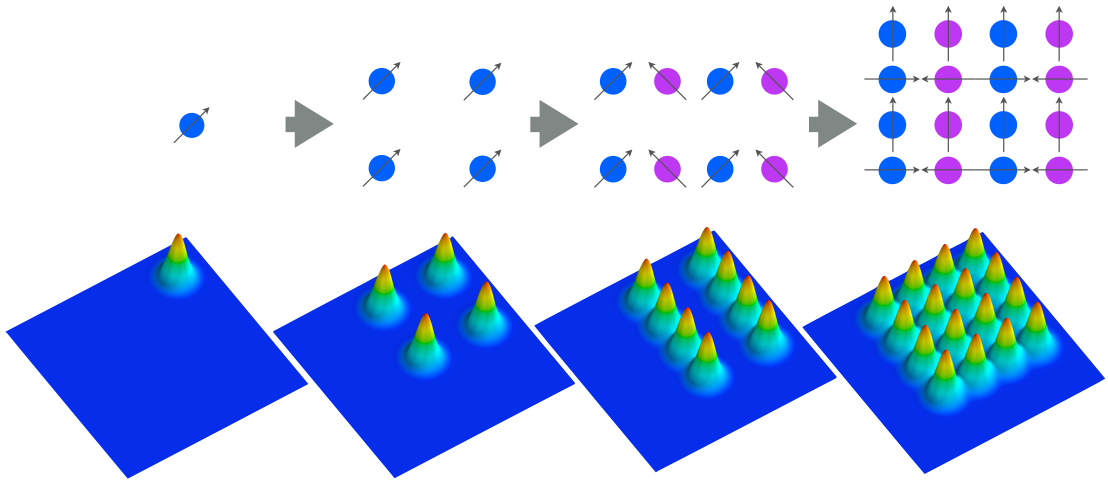


Figure 7.29: The sequence of beam manipulations for the 49 site full-incoherent Gaussian beam array. Shown here as a 16 beams for clarity, but implemented in the lab with 64 beams. A single Gaussian beam is split into 4x4 using a diffractive optical element. This is combined on a polarizing beam splitter with another 4x4 pattern from another laser source, making a 4x8 pattern with each laser at orthogonal polarizations. This is then doubled at 0° in a calcite beam displacer. Arrows indicate polarization of each beam. The resulting 64 beam pattern has 49 dark sites for atom trapping.

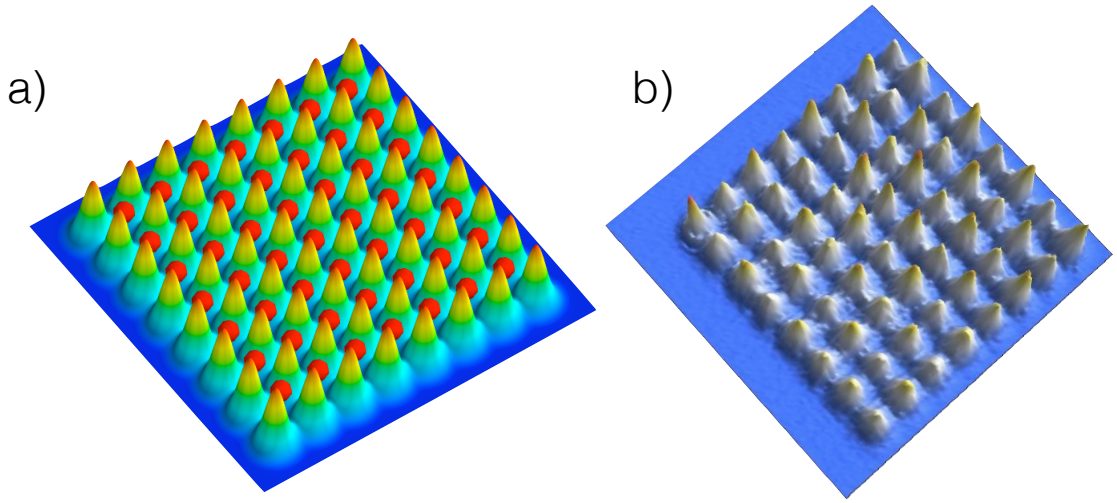


Figure 7.30: The light pattern for the 49 site full-incoherent Gaussian beam array. (a) Simulated light pattern with red balls showing the atom trapping locations. (b) Measured intensity map of the light field produced by the 49 site optics at $\lambda = 780\,\text{nm}$ with resulting $d = 250\,\mu\text{m}$, $w_0 = 120\,\mu\text{m}$ giving $s = 2.1$.

an 8 degree-of-freedom system. The successful alignment technique is to first individually align each 4×8 laser beam set to the optics cages. The beams will be overlapping. Then while leaving one 4×8 set fixed, offset the other by d using the first as a guide. It is necessary to view the resulting pattern in multiple planes to ensure that both sets are propagating parallel to each other.

Every experiment consists of two fluorescence pictures, with some qubit operation between them. Samples of individual raw camera pictures of the 49-site atom fluorescence (852 nm on $6s_{1/2}, f = 4 \leftrightarrow 6p_{3/2}, f = 5$) are shown in Figure 7.31.

Taking the mean of several shots reveals the atom array, as shown in Figure 7.32. The average deviation of the atomic centroids from a regular grid is seen to be 0.35 µm, which is half that observed for the 6 site half-coherent array implementation. A 3D visualization of the mean atom fluorescence is shown in Figure 7.33.

We identify a region of interest around each site as shown in Figure 7.34. The photoelectron counts are integrated over each region of interest to give a signal for each trapping site. A histogram of this region of interest signal is shown in Figure 7.35. The histograms show a zero-atom background peak, and a one-atom signal peak. A cutoff threshold is identified between these two peaks. After initial calibration, the threshold is used to identify if an atom is present or not.

With proper optimization (see Sections 9.5 and 16.2) we achieve an array averaged loading of up to 60.9%, giving an average of 29.8 atoms per shot. Individual sites have been observed to load as well as 70%. Loading histograms for each of the 49 sites are shown in Figure 7.36.

The array averaged $1/e$ trap lifetime is 17 s, and the array averaged retention between the 1^{st} and 2^{nd} camera pictures in an experiment with 50 ms between them is 99% (after optimization). The array loading and retention performance will typically degrade over the course of several weeks and require periodic realignment and optimization to maintain these best values. The array performance is characterized by loading (see Table 7.1), retention (see Table 7.2), and reloading (see Table 7.2). Tables 7.1, 7.2, and 7.3 show results of a typical experiment (data from 2015-07-03-12-18-41).

The trap array light induces a Stark shift in the atomic levels, and this can be measured by scanning the frequency of the readout fluorescence light using an AOM frequency shift. A histogram of the readout response versus the detuning of the readout light is given in Figure 7.37. The same measurement can also be done for blowaway light, as is shown inset in the same figure. It is found that the trapping light induces a -6.7 ± 0.8 MHz Stark shift

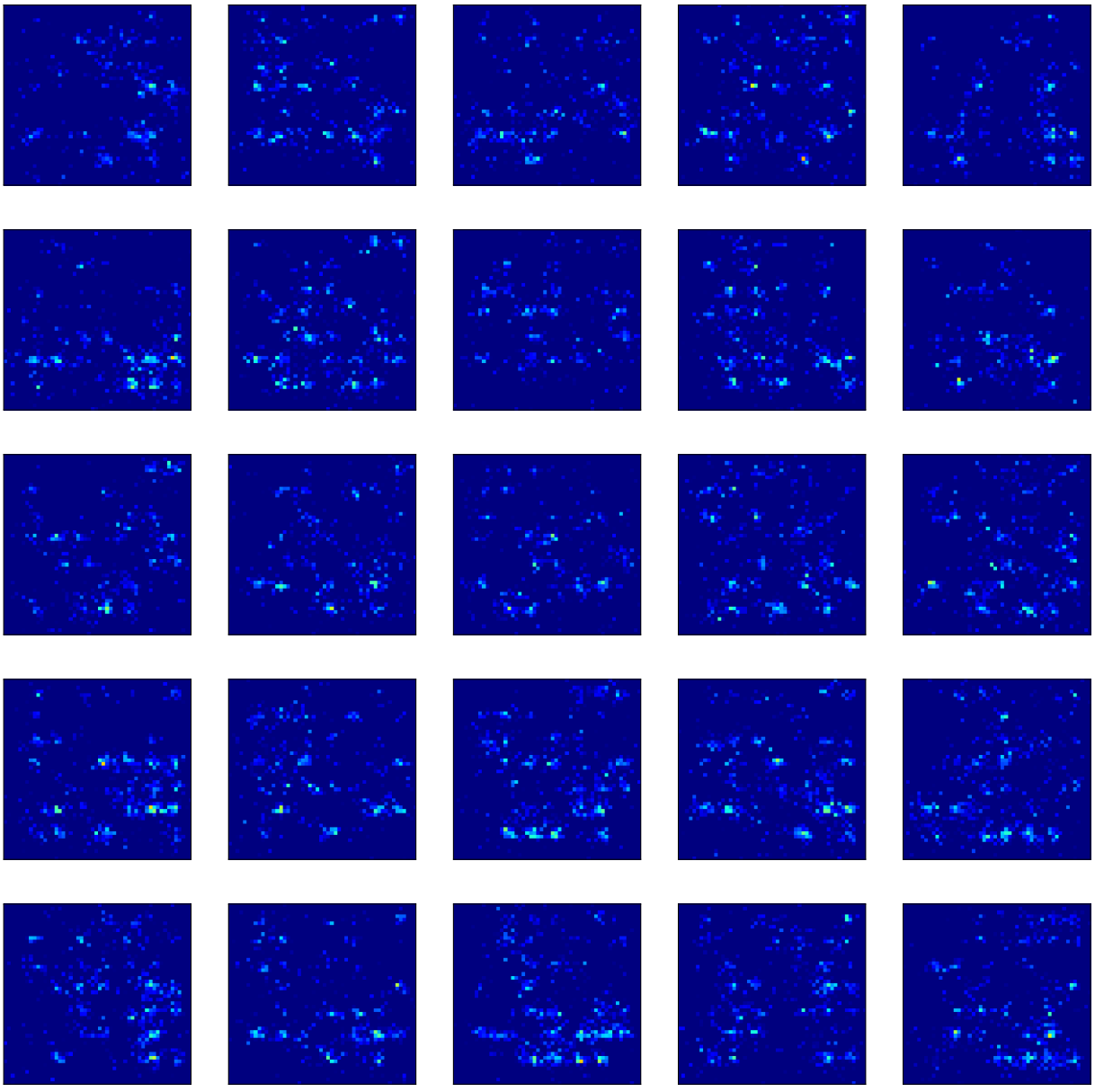


Figure 7.31: Sample raw images for atom fluorescence from the 49 site array. Bright spots indicate the presence of an atom. Data from 2015-03-06-08-00-54.

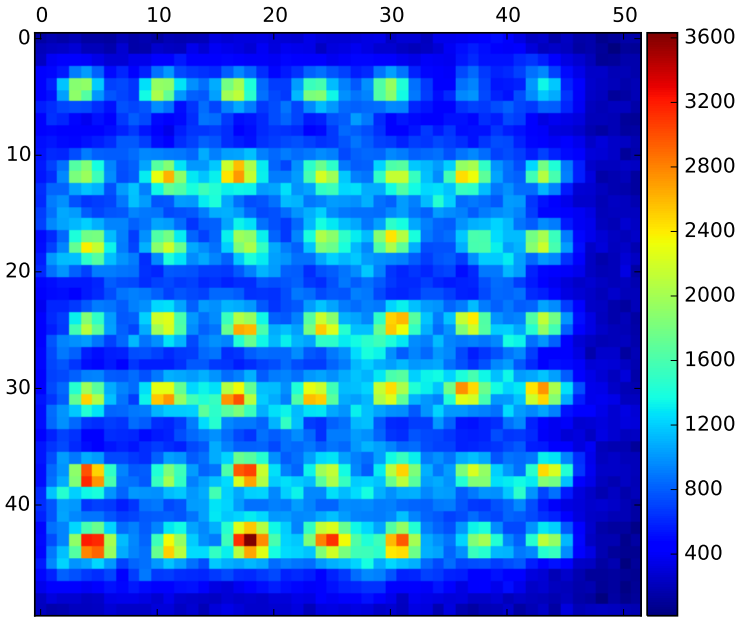


Figure 7.32: Mean image of atom fluorescence for 500 shots for the 49 site full-coherent Gaussian beam array. Intensity is photoelectron counts. Data from 2015-07-13-12-18-41.

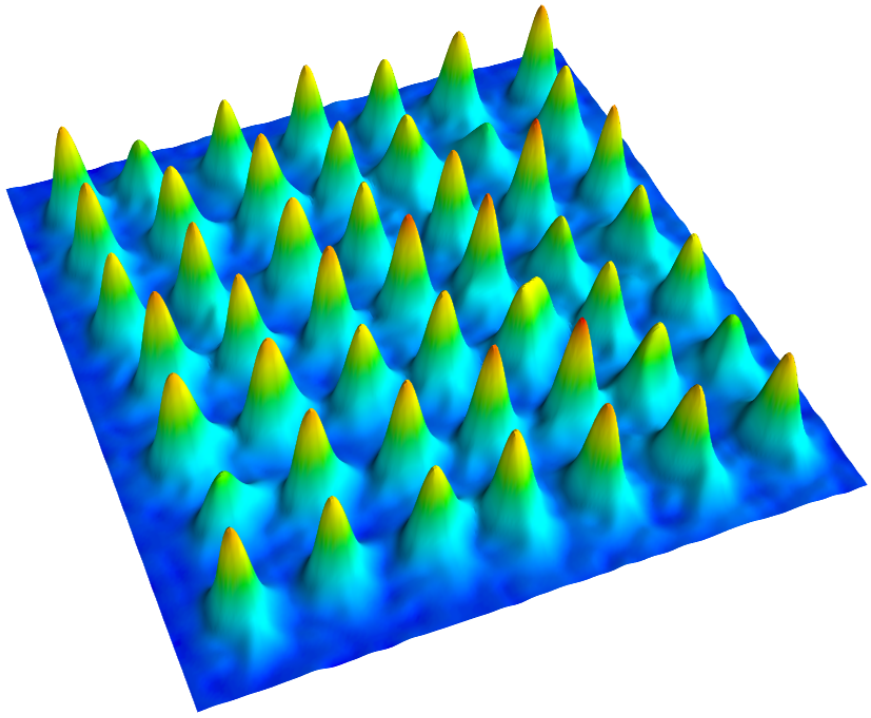


Figure 7.33: 3D visualization of the mean fluorescence image of the 49 site array. Peak heights correspond to a combination of readout intensity and atom loading. Data from 2013-11-14-15-18-54.

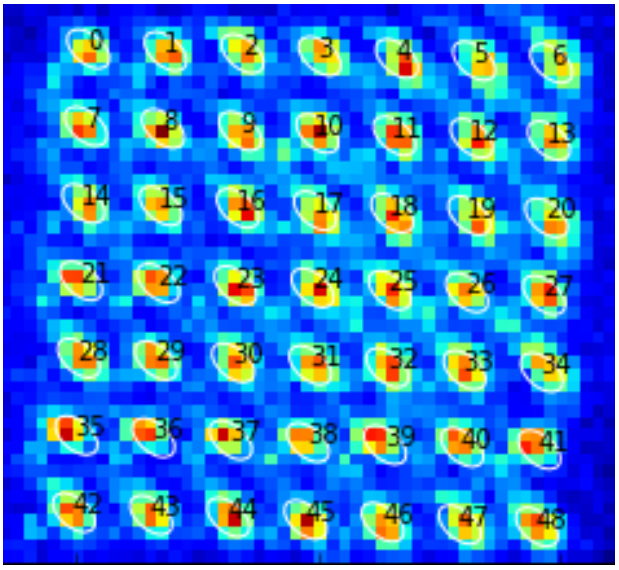


Figure 7.34: Identification of regions of interest around each atom loading site. Image is background subtracted and filtered using principal component analysis. White ellipses indicate 1σ contours of 2D Gaussian masks used as the regions of interest.

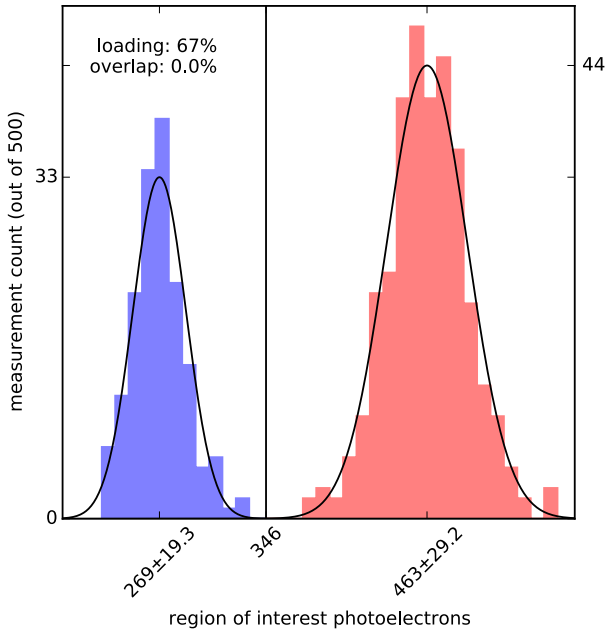


Figure 7.35: A loading histogram for one site in the 49 site array. The blue peak is the zero-atom background, and the red peak is the one-atom signal. The x-axis shows integrated region of interest photoelectrons, and the y-axis gives counts per 500 shots. Data from 2013-11-14-15-18-54.

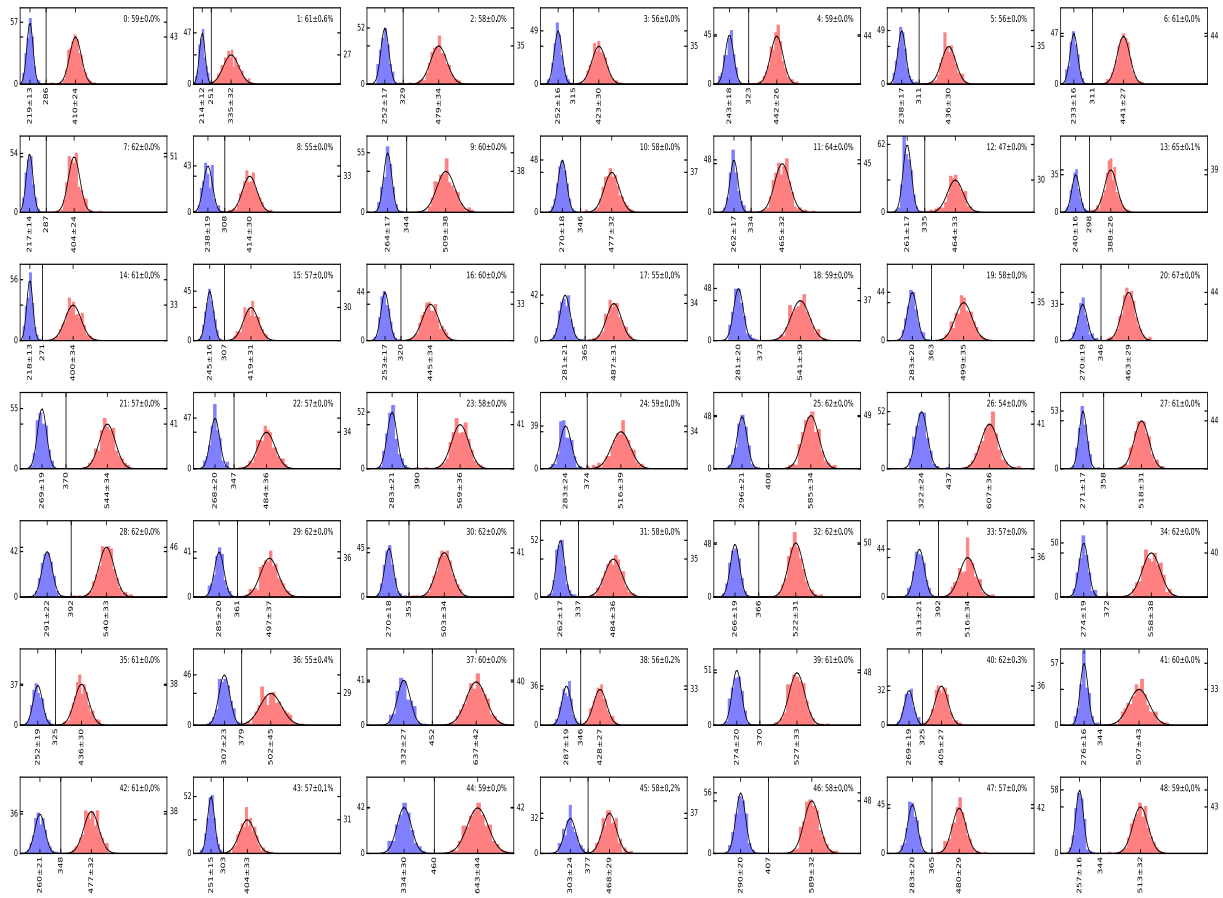


Figure 7.36: Loading histograms for each of the 49 trapping sites in the full-coherent Gaussian beam array. For each site, the blue peak is the zero-atom background, and the red peak is the one-atom signal. The x-axis shows integrated region of interest photoelectrons, and the y-axis gives counts per 500 shots. Data from 2015-07-04-02-19-16.

loading: $\left(\frac{\text{atoms in the } 1^{st} \text{ shot}}{\text{total measurements}}\right)$						
max 0.628, avg 0.499						
0.476	0.470	0.442	0.482	0.518	0.282	0.350
0.426	0.604	0.628	0.552	0.544	0.598	0.480
0.522	0.442	0.546	0.522	0.520	0.454	0.558
0.420	0.534	0.446	0.556	0.544	0.402	0.500
0.492	0.540	0.554	0.590	0.536	0.546	0.522
0.460	0.338	0.558	0.504	0.532	0.368	0.472
0.518	0.396	0.550	0.552	0.580	0.494	0.514

Table 7.1: A typical loading measurement. Data from 2015-07-03-12-18-41.

retention: $\left(\frac{\text{atoms in the } 2^{nd} \text{ shot, given that there was an atom in the } 1^{st} \text{ shot}}{\text{atoms in the } 1^{st} \text{ shot}}\right)$						
max 1.000, avg 0.982						
1.000	0.991	0.991	0.954	0.988	0.965	0.966
0.991	0.990	0.933	0.960	0.982	0.977	0.992
0.996	1.000	0.993	0.977	0.985	0.982	0.993
0.995	0.996	0.978	0.975	0.993	1.000	1.000
0.996	0.959	0.993	0.997	0.989	0.989	0.992
0.987	0.953	0.968	0.937	0.981	0.978	0.996
0.992	0.995	0.985	0.949	0.983	0.972	0.988

Table 7.2: A typical retention measurement over 50 ms. Data from 2015-07-03-12-18-41.

reloading: $\left(\frac{\text{atoms in the } 2^{nd} \text{ shot, given that there was no atom in the } 1^{st} \text{ shot}}{\text{total measurements} - \text{atoms in the } 1^{st} \text{ shot}}\right)$						
max 0.034, avg 0.004						
0.000	0.000	0.000	0.000	0.000	0.000	0.000
0.000	0.004	0.034	0.004	0.004	0.002	0.004
0.000	0.004	0.008	0.004	0.004	0.024	0.000
0.002	0.002	0.000	0.002	0.000	0.000	0.000
0.000	0.002	0.000	0.002	0.002	0.008	0.000
0.000	0.004	0.020	0.016	0.004	0.000	0.000
0.002	0.000	0.006	0.006	0.006	0.008	0.004

Table 7.3: A typical reloading measurement over 50 ms. Data from 2015-07-03-12-18-41.

relative to the value for an atom in free space. The deviation from site to site implies a difference in the light intensity at trap center, and hence this 12% fluctuation in Stark shift corresponds to a $.12 \times 570\,\mu K = 68\,\mu K$ fluctuation in trap depth.

These variations in Stark shift will manifest themselves as $\sim$60 Hz variations in the resonant hyperfine transition frequency. Because of this, to extend operations to long coherence times it will be necessary to keep track of individual site-specific shifts to be used for site-selective qubit rotations.

7.3.3 121 Site Full-Incoherent Line Grid Array

We have implemented an 121 site trapping array using the line grid array design. Due to other experiment priorities, atom trapping has not yet been performed in this array. The line grid array is constructed using a two laser system, similar to the full-incoherent Gaussian beam array. However, for the line grid array we require two diffractive optical elements on each beam path, as shown in Figure 7.38. The first diffractive element takes

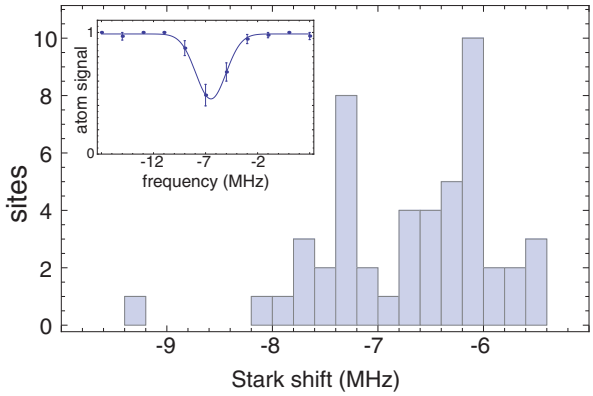


Figure 7.37: Stark shift of the $6s_{1/2}, f = 4 \leftrightarrow 6p_{3/2}, f = 5$ transition in the 49 site array. Inset: Atom blowaway curve as the laser frequency is scanned.

a Gaussian beam and spreads it into a top hat beam. A top hat is a line with (nearly) constant amplitude in the parallel (long) direction. The Gaussian profile is preserved in the perpendicular (short) direction. This is a distinctly different behavior from using a simple cylindrical lens to spread the beam, which would preserve a Gaussian profile in the parallel direction, causing trapping sites at the edges of the array to have lower trap depth. The second diffractive element is a multi-spot, which takes one line and multiplies it into 6 lines. Doing this for two laser sources, we create two sets of lines, six horizontal and six vertical, and then combine them on a polarizing beam splitter to create a grid. This grid is then doubled by a calcite beam displacer by shifting a distance $d/\sqrt{2}$ at 45° to the grid. This series of manipulations is shown in Figure 7.39.

For a finite sized grid, we must be concerned with how we align the horizontal and vertical beams to each other, because it has a big effect on the geometrical efficiency, defined as $\eta = \frac{N}{L}$, where N is the total number of trapping sites, and L is the total number of trapping sites that could be made with the same amount of light in an array of infinite extent. So $L = \frac{L_T}{2d}$ where L_T is the total length of line. This principle is demonstrated in Figure 7.40. We see for Figure 7.40a we start with sets of 4 lines, for a total length of 64, and make 49 trapping sites, for a geometric efficiency of $\eta = 0.76$. In Figure 7.40b 5 lines are used to make 81 sites, and $\eta = 0.81$. In Figure 7.40c the lines cross at their ends, instead of at a length d from the ends as with the first two examples. This results in again 81 sites, but starting with 6 lines makes the efficiency only 0.68. Instead, as in Figure 7.40d, if the 6 lines are $2d$ longer, but cross at d from the end, we make $N = 121$ sites $L = 144$ with for an efficiency of 0.84. It is this 121 site design that we will attempt to create.

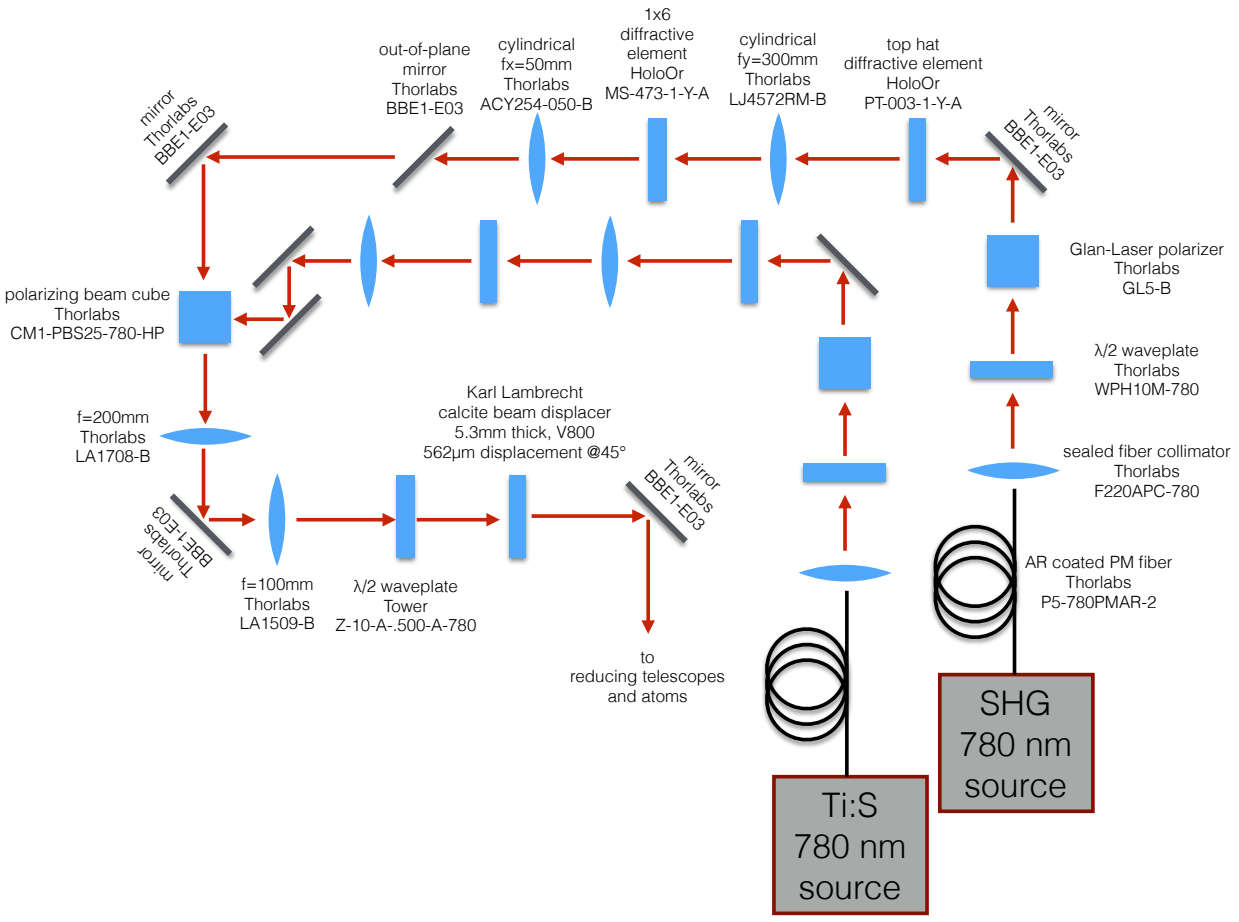


Figure 7.38: Optical implementation of the 121 site line grid array. Not to scale. All lenses are confocal, except for the $f_y = 300\,\text{mm}$ cylindrical lens which is placed close to the next element to compress the optics because the very large size of the vertical line has a very long Rayleigh range and is insensitive to this distance. The unlabeled elements and lengths on the Ti:S beam path are identical to the SHG beam path up to the polarizing beam cube.

The actual light pattern created is shown in Figure 7.41. The appearance of the light field is true to the desired pattern. The sites near the extremity are dimmer and may have lower trap depth. The regularity compared to the constructed Gaussian beam arrays is very good, and the trap centers are darker and therefore will have more uniform atomic transition frequencies.

The uniformity of the trap walls can be seen in Figure 7.42, which shows the intensity across the array, with columns averaged. The 12 vertical line intensities visible are uniform to within 10%. The rounded profile of the baseline is from the horizontal lines which have been averaged out, and indicates that the top-hat is not uniform, but instead has a variation

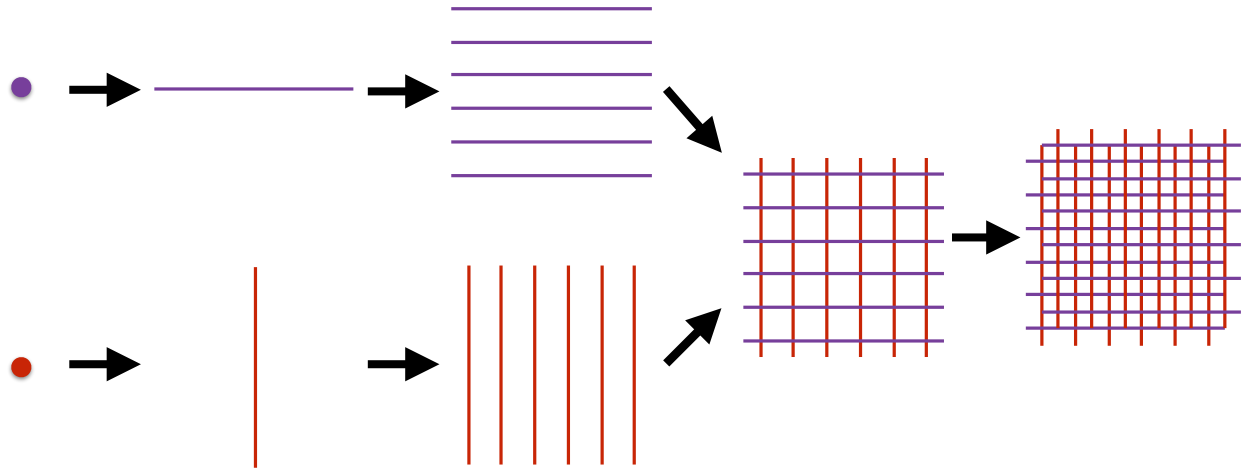


Figure 7.39: Steps to form an 121 site pattern. (a) Begin with two separate Gaussian beam sources at orthogonal polarizations. (b) Use a top-hat diffractive optical element to extend each point to a line, one horizontal and one vertical. (c) Use a multi-spot diffractive optical element to copy each line to 6 lines. (d) Combine the horizontal and vertical patterns on a polarizing beam cube. (e) Use a calcite beam displacer to shift the grid pattern by $d/\sqrt{2}$ at $45°$.

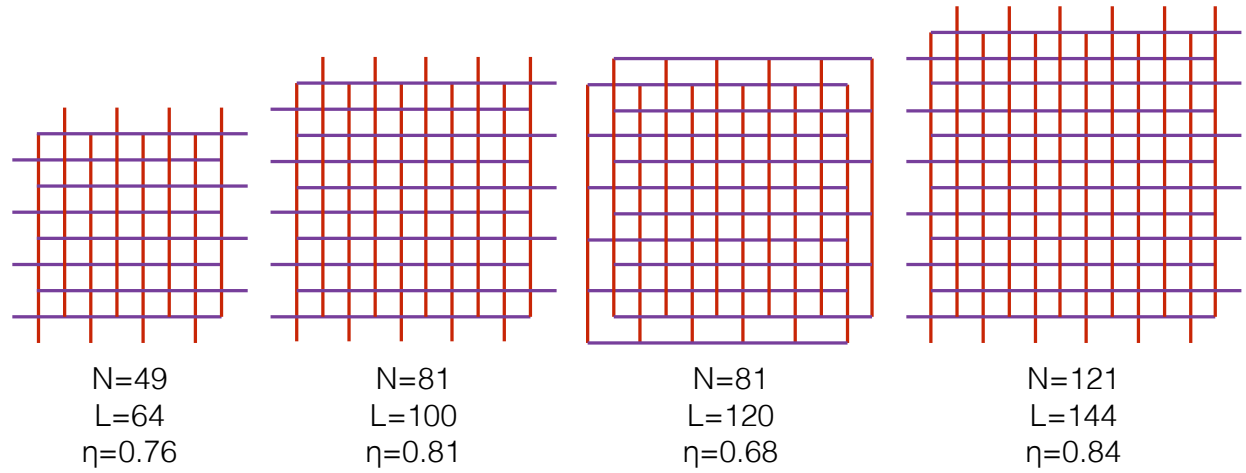


Figure 7.40: For a finite size line grid array, we must be concerned with the geometric efficiency. Above are presented geometric efficiency factors for various possible designs.

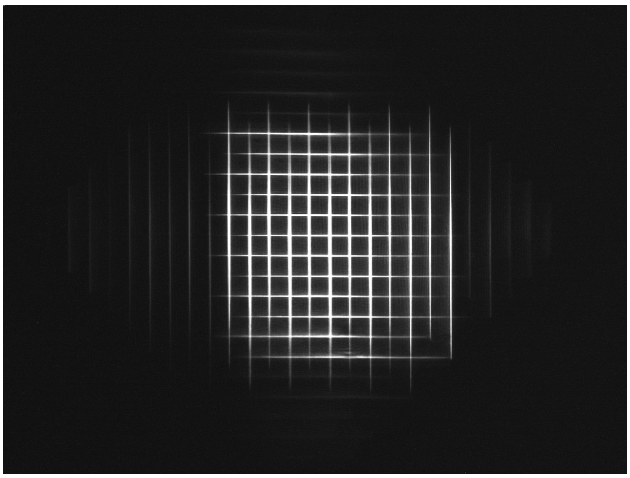


Figure 7.41: The light field created for the 121 site line grid array. All 121 grid boxes are visible, although some near the edges are dimmer and may have lower trap depth.

of almost 50% over the length of the line.

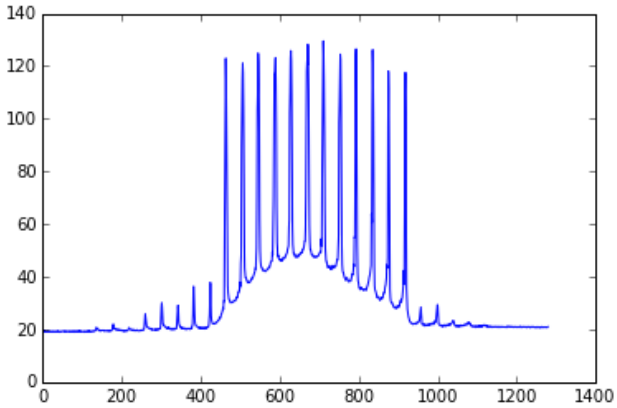


Figure 7.42: An intensity cross section of the line grid array light, created by averaging columns. The 12 vertical line intensities visible are uniform to within 10%. The rounded profile of the baseline is from the horizontal lines which have been averaged out, and indicates that the top-hat is not uniform, but instead has a variation of almost 50% over the length of the line.

To verify that the line grid array will trap in the longitudinal direction as well, we move the camera out of the trapping plane. We observe the blurring together of the lines which will form the longitudinal trap walls, as seen in Figure 7.43.

The 121 site implementation of the line grid array looks very promising, and it will be implemented in the near future. Currently experiments are still in progress using the 49

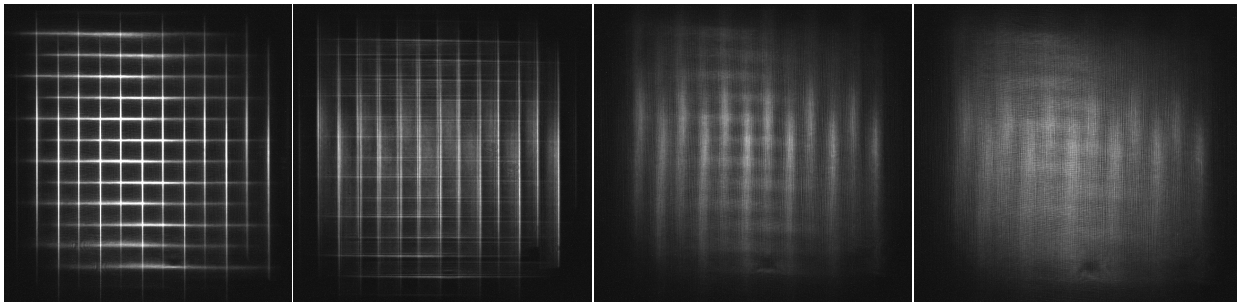


Figure 7.43: Imaging of the z trapping of the line grid array caused by out-of-plane spreading of the beams. (a) At the focal plane. (b)-(d) Progressively farther out of focal plane.

site Gaussian beam array, which will be replaced with the 121 site line grid array when the opportunity presents itself.

8 Laser Systems

8.1 High Power 780 nm Trapping Lasers

To maintain good atom trapping we desire a trap depth approximately 50 times larger than our atom temperature. As described above, this requires 2.5 W of power out of fibers from each of two separate systems. Although we have achieved fiber couplings as high as 80%, maintaining these high coupling efficiencies into single mode fibers at high power is very difficult. More commonly a coupling efficiency of 60% is achievable. The use of sealed fiber collimators, such as Thorlabs T06FC-780, has been invaluable in working with high power into fibers. The sealed collimator keeps the fiber tip isolated and clean, and it has prevented the accumulation of dust that leads to localized heating and then burning of the fiber. At an efficiency of 50% we require 4.1 W of power before each fiber. We generate this power using two different systems. The first is a system based off second harmonic generation of 1560 nm light from a fiber amplifier. The second is a Ti:Sapphire system. The reason for using two different methods is simply due to the equipment that was available; when the second laser was necessary for the switch from the 6 site half-coherent system to the 49 site full-coherent system, we were able to repurpose the Ti:Sapphire system from a decommissioned experiment.

The light of these two systems is combined in the Gaussian beam array configuration as shown in Figure 8.1.

8.1.1 1560 nm Second Harmonic Generation System

We have developed a high power, 10.4 W single frequency source at 780 nm. The 780 nm output is produced in periodically polled lithium niobate (PPLN) by second harmonic generation (SHG) of 1560 nm light from a 20 W fiber amplifier. This setup was chosen because 1560 nm is a telecom wavelength (high transmission efficiency through fiber optics) and therefore much investment has been made into technology at this wavelength. Therefore it is possible for us to get a high power amplifier at reasonable cost.

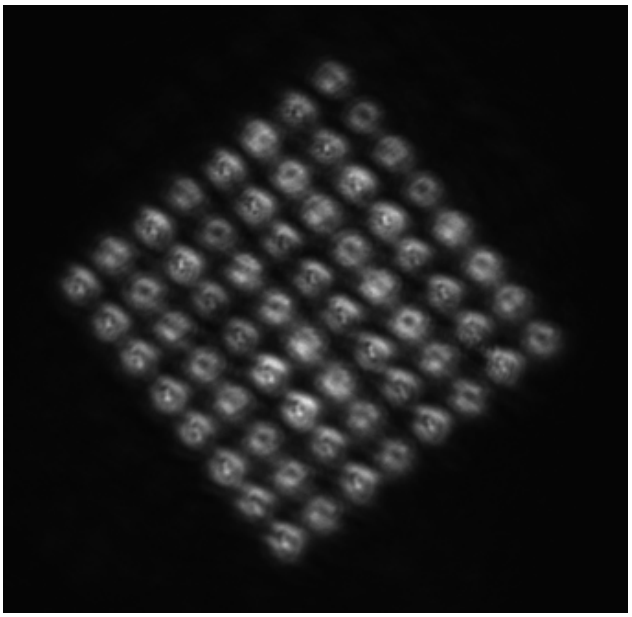


Figure 8.1: The combined light of the SHG and Ti:Sapph $780\,\text{nm}$ systems, forming the 64-beam, 49-site, Gaussian beam array. This image is taken at low power in the focal plane of a pickoff before the experiment cell. Airy rings due to the pinhole array are visible. Data from 2015-05-29.

8.1.1.1 Temperature Phase Matching

Second harmonic generation occurs when a non-linear atom-light interaction gives rise to polarization that depends on higher powers of the electric field

$$\vec{p} = \epsilon_0 \left(\chi_e \vec{E} + \frac{d}{2} \cdot \vec{E}\vec{E} + \dots \right) \tag{8.1}$$

where χ_e is the linear susceptibility, d is the 2^{nd} order non-linear susceptibility, and $\vec{E}$ is the electric field. The presence of terms that are quadratic or higher degree will result in $\vec{p}$ containing harmonics of the fundamental frequency, as first observed by Franken et al. [61]. In order for this to manifest, the crystal must not contain any point symmetries, because the quadratic term is linear in the symmetric tensor $\vec{E}\vec{E}$. While an isotropic material like glass does not satisfy this condition, lithium niobate ($LiNbO_3$) does, with the crystal structure shown in Figure 8.5b. The fundamental and second harmonic fields are coupled by the

equations

$$\frac{\partial \mathcal{E}_1}{\partial z} - \frac{i}{2k_1}\nabla_\perp^2 \mathcal{E}_1 = i\kappa_1 \mathcal{E}_1^* \mathcal{E}_2 e^{-i\Delta k z} \tag{8.2}$$

$$\frac{\partial \mathcal{E}_2}{\partial z} - \frac{i}{2k_2}\nabla_\perp^2 \mathcal{E}_2 = i\kappa_2 \mathcal{E}_1^2 e^{i\Delta k z} \tag{8.3}$$

where $\mathcal{E}_1$ and $\mathcal{E}_2$ are the fields for the fundamental and harmonic frequencies, respectively, and Δk is the wavenumber mismatch $2k_1 - k_2$.

In the plane-wave limit of weak focusing and no depletion of the pump light, the power output P_2 at the doubled frequency depends on the square of the input power P_1 as

$$P_2 = \left(\frac{P_1 \omega_1 d L}{w_{0,1}}\right)^2 \text{sinc}^2\left(\frac{\Delta k L}{2}\right) \tag{8.4}$$

where ω_1 is the pump angular frequency, d is the effective non-linear susceptibility which accounts for conversion efficiency, L is the length of the crystal over which conversion occurs, w_{01} is the pump beam waist, and Δk is the wavenumber mismatch. The frequency conversion is maximized at the phase matching condition $\Delta k = 0$. This condition can be controlled using temperature because the index of refraction is temperature dependent, and that temperature dependence is different for different wavelengths (Boyd, Bond, and Carter [62])

$$\Delta k = 2k_1 - k_2 = \frac{1}{c}\left(2\omega_1 n_1 - \omega_2 n_2\right) = \frac{2\pi}{\lambda_1}\left(n_1\left(T\right) - n_2\left(T\right)\right) \tag{8.5}$$

The Sellmeier equations give the index of refraction as a function of temperature

$$n\left(\lambda, T\right) = \sqrt{a_1 + b_1 f + \frac{a_2 + b_2 f}{\lambda^2 - \left(a_3 + b_3 f\right)^2} + \frac{a_4 + b_4 f}{\lambda^2 - a_5^2} - a_6 \lambda^2} \tag{8.6}$$

$$f\left(T\right) = \frac{T - 24.5}{T + 570.82} \tag{8.7}$$

for the temperature T in $^\circ C$, and the wavelength λ in µm. The coefficients a_{1-6} and b_{1-4} are empirically determined. We use magnesium-doped periodically-polled lithium niobate (PPLN) crystal as the SHG medium. The Sellmeier coefficients for $4.9\%\ Mg$ doped $LiNbO_3$ found by Gayer et al. [63] are given in Table 8.1.

The technique of periodic polling creates regions of alternating crystal orientation every polling period Λ, which results in the relative phase drift of the pump and output fields periodically reversing. This reduces the average phase mismatch by $1/\Lambda$. The polling

a_1	a_2	a_3	a_4
5.756×10^0	9.83×10^{-2}	2.020×10^{-1}	1.8932×10^2

b_1	b_2	b_3	b_4	b_5	b_6
1.252×10^1	1.32×10^{-2}	2.86×10^{-6}	4.7×10^{-8}	6.113×10^{-8}	1.516×10^{-4}

Table 8.1: Sellmeier coefficients for PPLN, from Gayer et al. [63].

period will be affected by material expansion as we modulate the temperature of the crystal, and the coefficient of thermal expansion of $LiNbO_3$ is given by Jundt [64] as

$$\frac{\Delta L}{L} = 1.54 \times 10^{-5} (T - 25) + 5.3 \times 10^{-9} (T - 25)^2 \tag{8.8}$$

where T is in $^\circ C$.

Used together, these equations can then determine the phase mismatch as a function of temperature

$$\Delta k = \frac{2\pi}{\lambda_1} (n(\lambda_1, T) - n(\lambda_2, T)) - \frac{1}{\Lambda \left(1 + \frac{\Delta L}{L}(T)\right)} \tag{8.9}$$

Conversely, for a given crystal length, the polling period can be chosen to give maximum conversion at a desired temperature.

8.1.1.2 Boyd-Kleinman Theory

Equation 8.4 gives the conversion efficiency for a plane wave. However because the conversion depends on the square of the intensity, it is advantageous to tightly focus the pump beam to create a region of higher intensity (Kleinman, Ashkin, and Boyd [65]). The solution for the coupling of the fields is then (Boyd and Kleinman [66])

$$A_2(z) = i\kappa_2 A_1^2 h(z) , \quad h(z) = \int_{z0}^{z} dz' \frac{e^{i\Delta k z'}}{1 + i\frac{z'}{z_{R_1}}} \tag{8.10}$$

where A_j are the pump and output fields, $z_{R_1}$is the Rayleigh range of the pump beam, and $h(z)$ converges to a sinc function as $z_{R_1} \to \infty$. For this coupling the optimal phase mismatch is *not* $\Delta k = 0$. It must be solved numerically, and for 1560 nm light focused to 45 µm in PPLN, in a double-pass configuration, we find the maximal conversion at $\Delta k = \frac{3.244}{L}$ with L the crystal length.

8.1.1.3 Measurement of d_{eff} and L_{eff}

PPLN is chosen because it has one of the highest non-linear susceptibilities available (Boyd et al. [67]). Our PPLN crystal is manufactured by Deltronics, and measures $0.5\,\text{mm} \times 5\,\text{mm} \times 50\,\text{mm}$, shown in Figure 8.5a. This $LiNbO_3$ congruent composition crystal is 5% MgO doped to increase the non-linear susceptibility. The polling period of $19.4\,\mu\text{m}$ was chosen to give phase matching at near $100°\text{C}$ because this further protects against photo-refractive damage, versus operating at room temperature.

The non-linear susceptibility for PPLN was measured to be $d = 15.8$ pm/V by Shoji et al. [68]. We measured the effective non-linear susceptibility d_{eff} for our crystal by performing SHG at a low power condition using the $28\,\text{mW}$ seed laser only. The results of this measurement are shown in Figure 8.2. The output power as a function of temperature was fit to Boyd-Kleinmann theory (Boyd and Kleinman [66]), giving values for our crystal of $L_{eff} = 45$ mm out of the full $50\,\text{mm}$ length, and $d_{eff} = 13.8$ pm/V (87% of the value from Shoji et al. [68]).

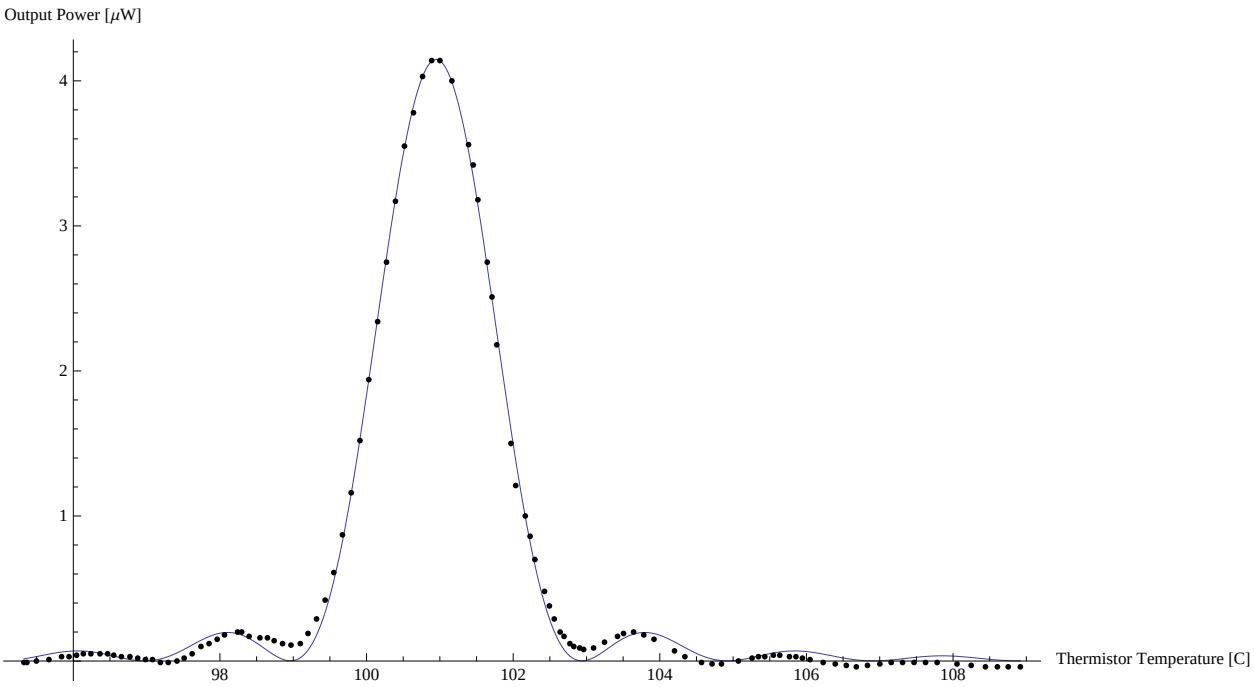
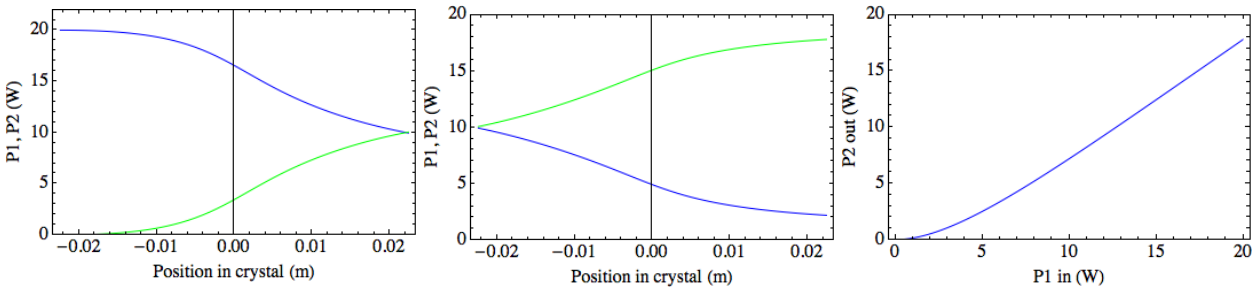


Figure 8.2: Output of $780\,\text{nm}$ light versus crystal temperature, for low power $28\,\text{mW}$ $1560\,\text{nm}$ pump light. The height of the peak is used to determine the non-linear susceptibility d_{eff}. The center temperature of the peak, along with the known value of the polling period, are used to determine the effective crystal length L_{eff}.



(a) (b) (c)

Figure 8.3: Theoretical predictions of high power SHG performance based on parameters measured at low power. (a) Single pass. Power conversion as a function of position in crystal. 1560 nm (blue curve) is depleted as 780 nm (green curve) is generated. (b) Double pass. Power conversion as a function of position in crystal on the second pass. (c) Total 780 nm power out after the second pass as a function of 1560 nm pump power.

8.1.1.4 High Power Predictions

Based on the parameters measured at low power, we can make predictions for the power achievable at high pump input power. We use the Boyd-Kleinman theory for SHG conversion with diffraction, as well as integrating the propagation through the crystal to account for depletion of pump power. The results are plotted in Figure 8.3, which shows that for an input power of 20 W of 1560 nm pump light, we should be able to achieve up to 17.8 W of 780 nm light output (89% efficiency). The optimal crystal temperature is predicted to be $96.26°C$.

8.1.1.5 Implementation of 10.4 W 780 nm Laser

SHG occurs in a 50 mm magnesium-doped periodically-polled lithium niobate (PPLN) crystal in a double-pass arrangement, as shown in Figure 8.4a. The seed laser is an Optilab DFB-B-20-1560 diode laser with 1560.20 ± 1 nm tunable output, at up to 13.84 dBm. We operate the seed at 1560.20 nm and 6.7 dBm. This light is amplified in an IPG EAR-20K-C-LP-SF 20 W fiber amplifier, operated at maximum output. This light is focused into the PPLN crystal with a 45 nm waist. The crystal is AR coated for 780 and 1560 nm. After the first pass through the crystal, the light is retro-reflected by a Layertec $R = 15$ mm custom mirror designed for high reflectance at both 780 and 1560 nm with $0°$ relative phase shift between the two frequencies. This refocuses it back into the crystal for the second pass. A LaserOptik dichroic with high-reflectance at 780 nm and high transmission at 1560 nm separates the output light from the residual unconverted pump light. The crystal

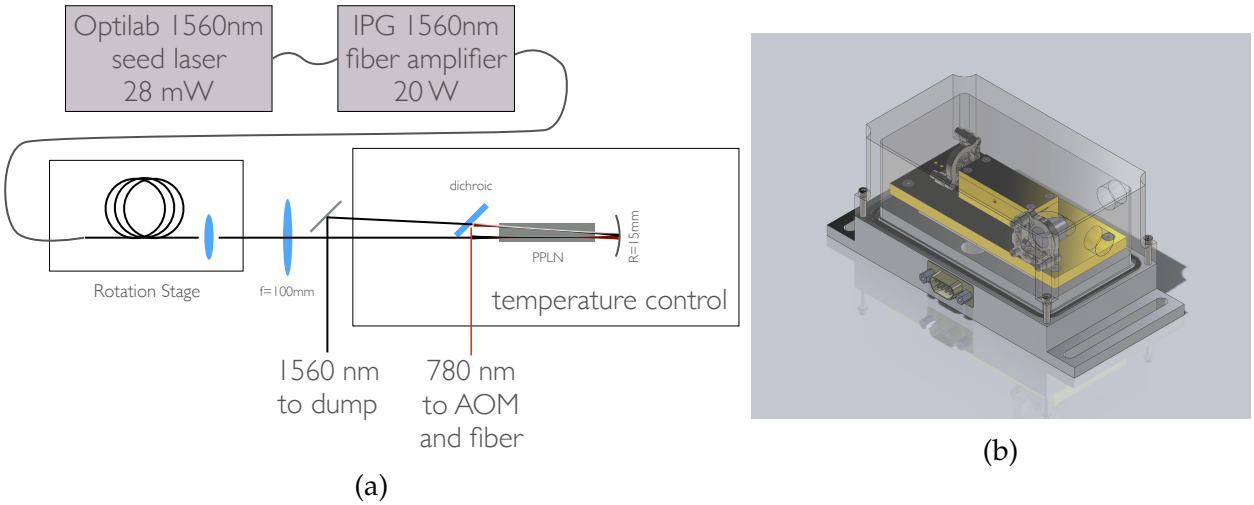


Figure 8.4: (a) Schematic of double-pass second harmonic generation. (b) SolidWorks drawing of temperature controlled SHG crystal housing.

is situated in a custom enclosure (Figure 8.4b) and is temperature controlled by two Marlow TG12-061L thermo-electric coolers (operated as heaters) powered by an Arroyo 5310 10 A servo controller. The optimal crystal temperature was found to be $98.36°C$.

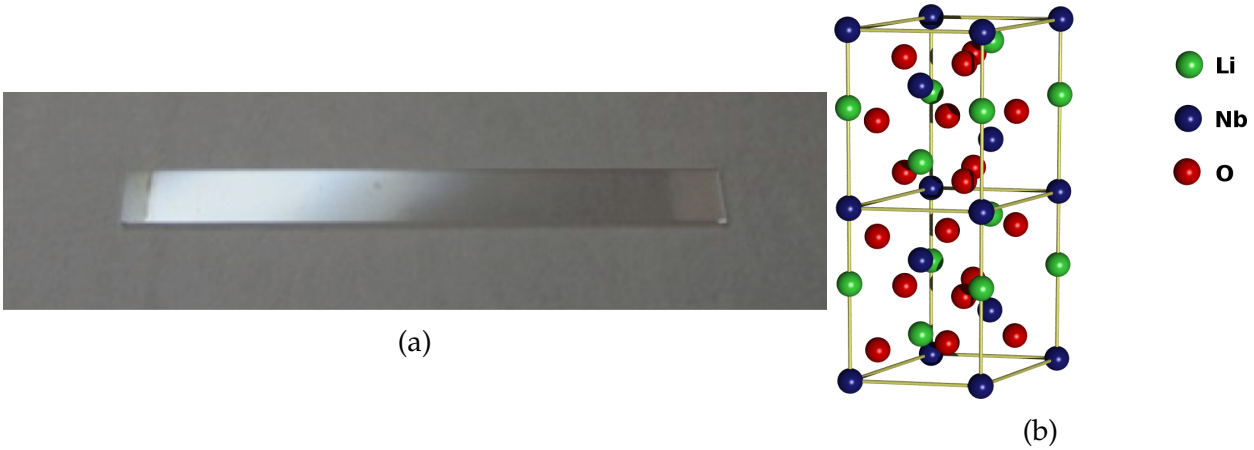


Figure 8.5: (a) Periodically polled lithium niobate crystal used for second harmonic generation of 780 nm light. The crystal is 50 mm long, but the 45 mm periodically polled region in the center can be seen as a grey coloration. (b) The unit cell of a lithium niobate ($LiNbO3$) crystal. Image by Ansgar Hellwig (2005).

A conversion efficiency of 52% was achieved, for a total of 10.4 W of 780 nm light output with 20 W of 1560 nm pump light.

This result compares favorably with the best results for this type of system, which was

11.4 W of 780 nm light using a single pass through a 40 mm long PPLN crystal and 30 W of 1560 nm pump light, as demonstrated by Sané et al. [69].

8.1.1.6 Phase Shift Problem in AR Coating

The single pass results, such as Figure 8.2, show the expected sinc-like shape of power as a function of temperature. However, in the double-pass configuration we found a very different double peak structure. Initially it was assumed that one peak was from the first pass, and the other peak was from the second pass, and that the passes had different optimal temperatures because of their different angles through the crystal. However, the center of the single-pass peak does not correspond to either peak, as shown in Figure 8.6. Also, perfectly retro-reflecting the beam by allowing the pump beam to pass through the dichroic on the input side did not remove the double-peak, but instead exaggerated it. It was found that the best power could be achieved not by perfect retro-reflection, but with a misalignment of $\sim 2°$. This causes the double-peak structure to become asymmetric, as shown in Figure 8.7. The higher peak could be selected, and this is how the maximum output power was achieved.

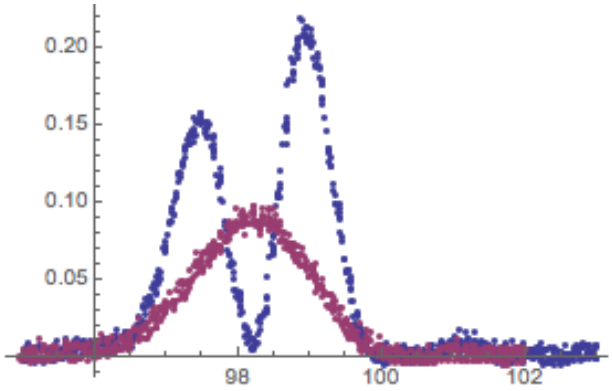


Figure 8.6: Measurements of SHG output power versus temperature for single-pass (red points) and double-pass (blue points) configurations.

The source of this problem is likely a relative phase shift between the 780 nm and 1560 nm light in the AR coating on the PPLN crystal. The crystal itself is designed with periodic polling and is temperature controlled to adjust the phase shift in the crystal. The retro-reflection mirrors were custom designed to have zero relative phase shift. The AR coatings on the crystal ends, however, were not delivered with a phase specification. Simulating the effect of this phase shift recovers the observed behavior. Figure 8.8a shows a

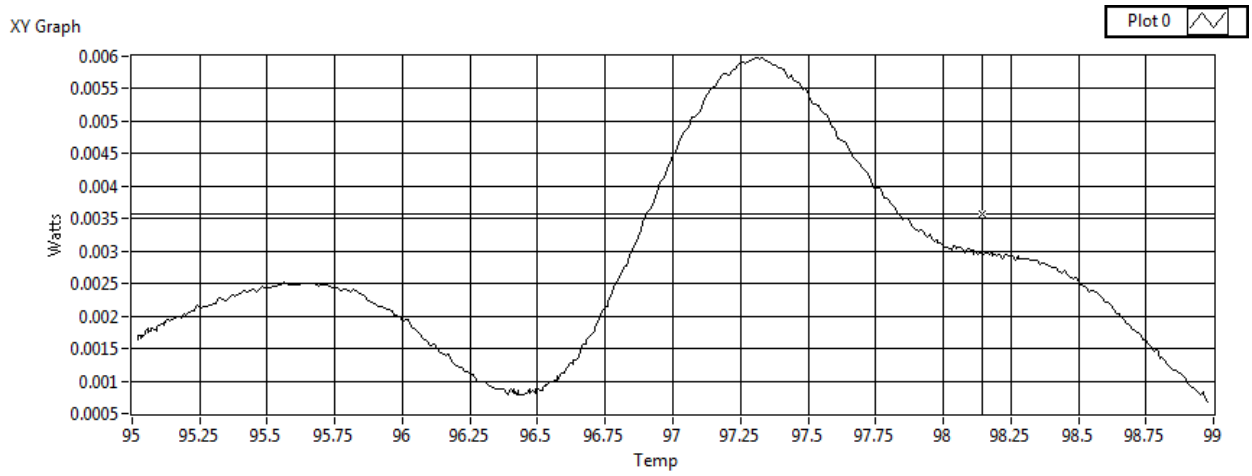
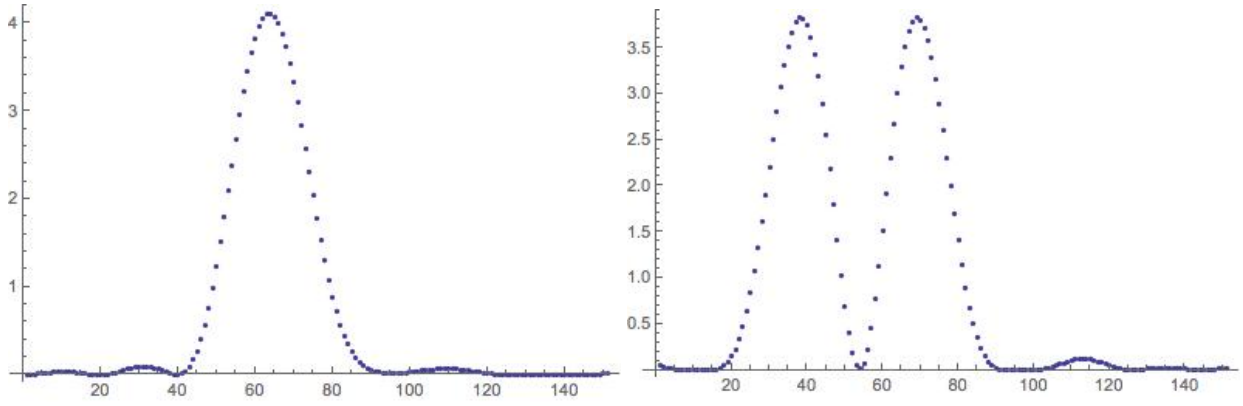


Figure 8.7: SHG output power versus temperature with misalignment of the retro-reflected beam in the double-pass setup to $\sim 2°$. This causes the double peak structure to become asymmetrical, giving higher output power on one of the peaks. Data from 2013-05-11.

simulation of the double-pass SHG output with no phase shift between the first and second passes, and we see a nice single peak. Figure 8.8b shows a simulation of the double-pass SHG output with a π phase shift on the pump light between the first and second passes, which gives the double peak structure that we observe in the experiment.



(a) (b)

Figure 8.8: (a) Simulation of double-pass SHG output with zero phase shift between passes. (b) Simulation of double-pass SHG output with $180°$ phase shift on pump light between first and second passes.

8.1.2 Ti:Sapphire Laser

The 6-site half-incoherent Gaussian beam array (see Section 7.3.1) was implemented using the $1560 \rightarrow 780$nm SHG laser. However, the full-incoherent implementation of the Gaussian beam array requires two source lasers, and so a second laser was required for the 49-site array (see Section 7.3.2). Although the SHG laser system was very successful, we were fortunate to have a Ti:Sapphire laser system available from a decommissioned experiment. The Ti:Sapphire is tunable across a large range (Moulton [70]), unlike the SHG system. This provides the possibility to tune the Ti:S to another wavelength in the future, for example to set the traps to a magic wavelength (Carr and Saffman [71]).

We use a Coherent Verdi V18 pump laser, which provides 18 W of 532 nm green light. This pumps a Ti^{3+} doped Al_2O_3 crystal in an M^2 SolsTiS-PSX-F, which creates a broadband frequency output. The tunable range of a Ti:S laser is typically 650 to 1100 nm, and an etalon is tuned to select the desired output frequency. We operate the Ti:S at 780 nm which is near the peak of the conversion efficiency curve. When most optimally tuned, we are able to get 7.1 W of 780 nm power out of the Ti:S (see Figure 8.10), but during typical operation we get 5.5 W of output.

The output light from the M^2 was highly astigmatic, which made it difficult to couple into an AOM mode for switching. To overcome this, we instead take the 0^{th} order of two AOMs in series (see Figure 8.9), which gives sufficient on/off contrast. The light is then fiber coupled for delivery of 2.5 W to the trap array optics.

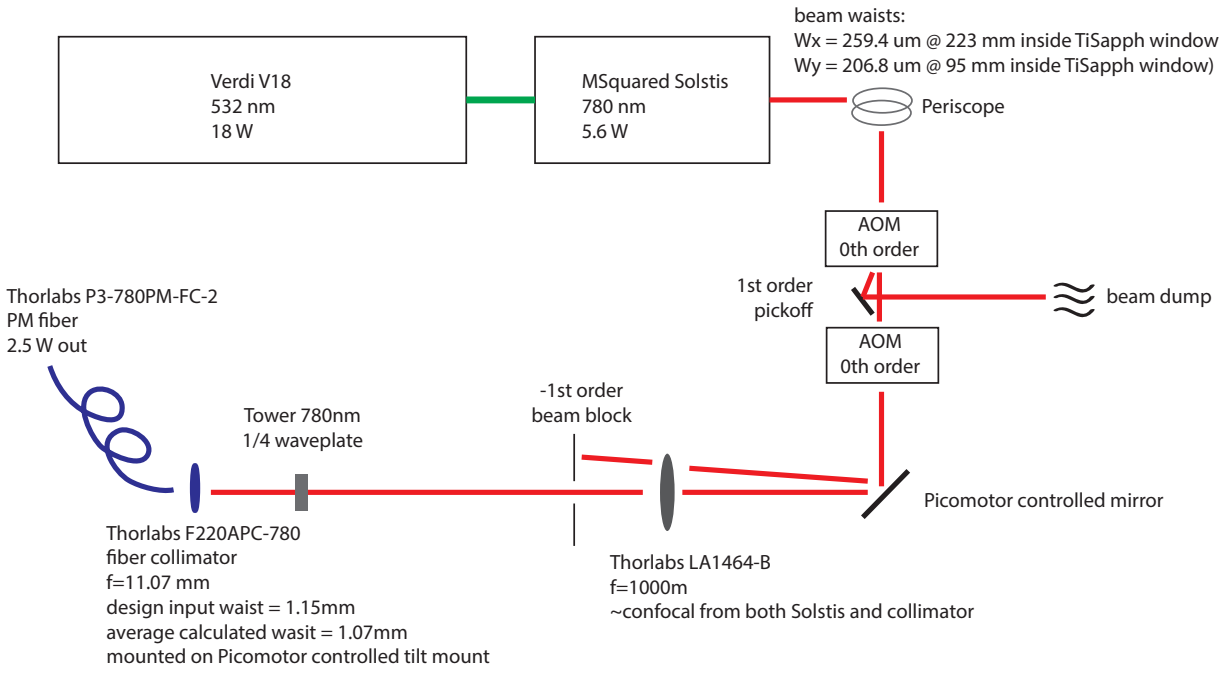


Figure 8.9: Schematic of the Ti:Sappire laser system consisting of a Coherent Verdi V18 pump and MSquared SolsTiS. The two AOMs in series are used to get sufficient shutoff suppression when using the 0^{th} order beams, because not enough power could be coupled into the 1^{st} order of a single AOM.

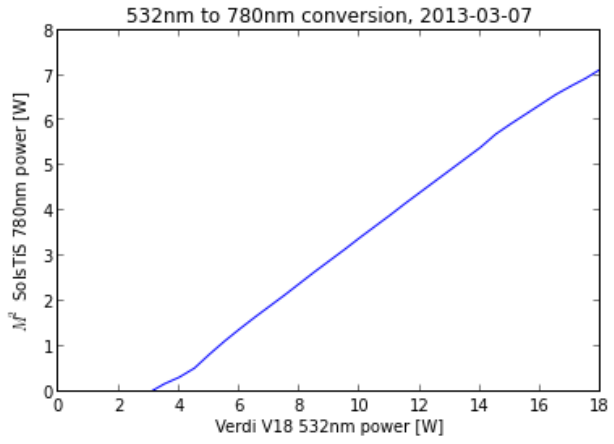


Figure 8.10: 780 nm power output versus 532 nm pump input for the MSquared SolsTiS Ti:S laser system. Data from 2013-03-07.

8.2 $852\,\text{nm}$ Laser Cooling and Readout, $894\,\text{nm}$ Optical Pumping

We use $6s_{1/2} \leftrightarrow 6p_{1/2}$ D1 light and $6s_{1/2} \leftrightarrow 6p_{3/2}$ D2 light (see Steck [72]) for all of the following operations

- laser cooling in the 2D MOT
- laser cooling in the 3D MOT (and single atom traps)
- state selective blowaway
- readout
- repump during: cooling, readout, and optical pumping
- optical pumping

This light is provided by four Vescent Photonics lasers. The lasers are coupled through cesium vapor cells which allow feedback locking of the lasers to atomic resonances via saturated absorption spectroscopy (MacAdam, Steinbach, and Wieman [73]). In most cases the light is switched on and off using acousto-optic modulators (AOM), which will impart a frequency shift of hundreds of MHz to the light. To account for this frequency shift, we make use of locking to various hyperfine levels and their cross-over signals (see Preston [74]) such that after the AOM frequency shift the light is at the desired resonance of our atoms. Tuning of the light to optimize detuning and to account for Stark shifts from the $780\,\text{nm}$ trapping light can also be conveniently performed by adjusting the AOM RF modulation frequency. The laser lock frequencies are detailed in Table 8.3 and Figure 8.11, with saturated absorption spectroscopy shown in Figure 8.12. The purpose and tuning of each laser is discussed below, and summarized in Table 8.4.

8.2.1 2D MOT

The 2D MOT is formed in the lower vacuum chamber using two pairs of large ($\sim w_0 = 2$ cm) σ^+/σ^- retro-reflected orthogonal beams in the horizontal plane, which trap atoms in a vertical line. Atoms emitted from a Cs dispenser running at $2.5\,\text{A}$ and are then collected from the vapor in the 2D MOT. A fifth beam is then applied from below to push atoms up through a small aperture to the 3D MOT in the upper vacuum chamber. The atoms are cooled on the $6s_{1/2}, F = 4 \leftrightarrow 6p_{3/2}, F = 5$ cycling transition. The light for the 2D MOT cooling is provided by a Vescent Photonics D2-100-CECL laser locked to the $6s_{1/2}, F =$

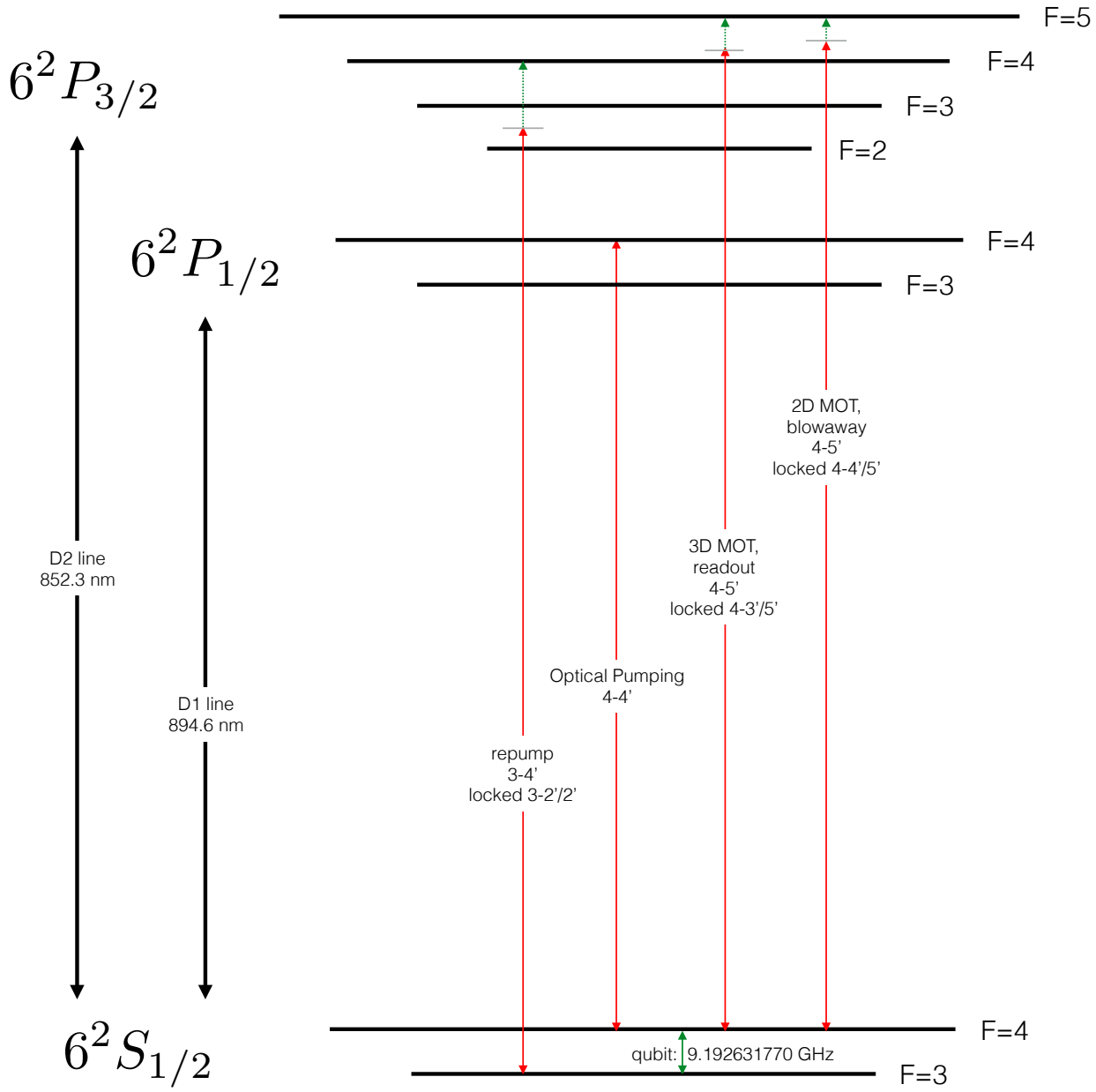


Figure 8.11: Cesium energy levels for the D1 and D2 transitions, which are used the lock the 2D MOT, 3D MOT, repump, and optical pumping lasers. Laser lock transitions are shown in solid red, with AOM shifts in dashed green. Not to scale.

$4 \leftrightarrow 6p_{3/2}, F = 4/5$ crossover, which is 125.5458 MHz below the desired transition. The light is shifted by a double pass AOM at 57.75 MHz bringing it to 10 MHz or -0.3Γ red detuning, where $\Gamma_{D2} = 32.889$ MHz [72]. The small detuning is desirable because the accompanying large scattering rate will give a fast atom loading rate, at the expense of higher atom temperature. In comparison, the 3D MOT will be operated at a larger detuning to decrease light scattering and get to colder temperatures. The AOM is not used to control switching because fast timing is not needed. Instead a shutter provides the complete shutoff necessary to shut down the atom source beam.

8.2.2 3D MOT

The 3D MOT is formed in the upper vacuum chamber with three ($\sim w_0 = 1$ mm) σ^+/σ^- retro-reflected beams. One beam is brought in vertically and the other two are in the "X2/4" and "X3/6" windows at 60° to each other in the horizontal plane. The light is generated using a Vescent Photonics D2-100-DBR laser locked to the $6s_{1/2}, F = 4 \leftrightarrow 6p_{3/2}, F = 3/5$ crossover, which is $226.189\,35$ MHz below the desired $6s_{1/2}, F = 4 \leftrightarrow 6p_{3/2}, F = 5$ cycling transition. The light is amplified by an m2k-TA-0850-2000-CM tapered amplifier from m2k-laser GmbH. Then it is frequency shifted by a double pass AOM. The amount of frequency shift depends on the operation being performed, as listed in Table 8.2. This same light is used for 3D MOT cooling, polarization gradient cooling (PGC), light assisted collisions (to eliminate loading more than one atom per trap), PGC in the trap, and imaging readout. The operations done with the the 780 nm traps on have -3.5Γ extra detuning due to the Stark shift from the trap light.

Atoms are loaded and cooled to 5 to 20 µK in 500 ms as measured by drop-and-recapture experiments using the single-atom traps, and fitting to a kinematic model of atom motion in the modulated traps.

8.2.3 Repump

The 2D and 3D MOT cooling light will only cycle a limited number of times before atoms spontaneously decay from $6p_{3/2}, F = 5$ to $6s_{1/2}, F = 3$. Since this light is not resonant with the cooling beams, it must be "repumped" up to $F = 4$. This is done with light from a Vescent Photonics D2-100-DBR laser locked to the $6s_{1/2}, F = 3 \leftrightarrow 6p_{3/2}, F = 2/3$ crossover, which is $276.899\,45$ MHz below the desired $6s_{1/2}, F = 3 \leftrightarrow 6p_{3/2}, F = 4$ transition. The

	AOM RF frequency (MHz)	Detuning $(2\pi f/\Gamma_{D2})$	AOM RF power (dBm-30)
MOT loading	107.56	-2.114	-0.062
PGC in MOT	91.25	-8.347	-7.084
light assisted collisions	93.63	-7.438	-5.887
PGC in traps	82.08	-11.85	-0.478
readout	93.08	-7.648	-6.292
blowaway	219.99	-0.188	-11.87

Table 8.2: Detuning for the various operations performed by the 3D MOT laser.

light is then frequency shifted in a switch AOM by $268.4\,\text{MHz}$ to -0.3Γ red detuning. This light is mixed into both the 2D MOT and 3D MOT beams using polarizing beam cubes.

8.2.4 Optical Pumping

We prepare our atoms for every experiment by optically pumping into $6s_{1/2}, F = 4, m_F = 0$, which we refer to as the qubit $|1\rangle$ state. This is done using $6s_{1/2}, F = 4 \leftrightarrow 6p_{1/2}, F = 4$ resonant linearly polarized light, applied from the top of the vacuum chamber, in the presence of a $1.5\,\text{G}$ magnetic field perpendicular to the applied light. The magnetic bias field serves to provide a well-defined orientation for the spin and prevents mixing of the m_F sub-levels. Any of the $6s_{1/2}, F = 4 \leftrightarrow 6p_{1/2}, F = 4$ transitions with $\Delta m_f = 0$ are allowed by this light, except for $m_F = 0 \leftrightarrow m'_F = 0$ which is forbidden by the electric dipole selection rules. In fact the Clebsch-Gordon coefficient $\langle F, 0, 1, 0|\ F, 0\rangle = 0$, and so for π polarized light and $F = F'$, any $|F, m_F = 0\rangle \leftrightarrow \left|F', m'_f = 0\right\rangle$ transition is forbidden (to 1^{st} order). This means that the optical pumping light will pump atoms out of every state in $F = 4$ *except* for the qubit $|1\rangle$ state. The other states will be excited to $F' = 4$ and upon spontaneous decay, will have some chance of ending up in $|1\rangle$. If the atoms do end up in $|1\rangle$, they will stay there. The other states will continue to mix until all the atoms are shelved in $|1\rangle$.

The optical pumping light is provided by a Vescent Photonics D2-100-DBR laser locked to the $6s_{1/2}, F = 4 \leftrightarrow 6p_{1/2}, F = 4$ transition. This light needs to be switched, but still stay resonant with this transition. So we use two AOMs. First a double-pass AOM gives a 2×100 MHz frequency shift in the +1 order, followed by a single-pass AOM with a -200 MHz shift in the -1 order. This allows the beam to be turned on and off while having 0Γ detuning from the $6s_{1/2}, F = 4 \leftrightarrow 6p_{1/2}, F = 4$ transition.

The optical pumping light also needs a repumper to prevent atoms from collecting in

$F = 3$. The optical pumping repump light comes from the same laser as the 2D and 3D MOT repump light. The OP repump light is frequency shifted by $278.5\,\mathrm{MHz}$ to $+0.05\Gamma$ detuning.

8.2.5 Blowaway

In order to make a determination of the final state of each qubit after each experiment, we need a state selective operation. The readout imaging could be state selective as the $F = 4 \leftrightarrow F' = 5$ light will only fluoresce the $F = 4$ ($|1\rangle$), and not the $F = 3$ ($|0\rangle$) state. However, the $F = 4 \leftrightarrow F' = 5$ transition will only cycle a limited number of times before spontaneous decay to $F = 3$ occurs, and unfortunately we do not have enough photon collection efficiency to distinguish the atom from the background before this occurs. So, we do the readout with the repump light on, but unfortunately this mixes the $|0\rangle$ and $|1\rangle$ states.

To distinguish $|0\rangle$ and $|1\rangle$, we use a state selective blowaway before the readout. Unlike the balanced readout light, this blowaway light is applied from only one direction, and is tuned closer to resonance. The momentum kick imparted to the atom is

$$p = mv = n\frac{hf}{c} \tag{8.11}$$

where m is the atomic mass, n is the number of photons, f is the photon frequency, h is the Planck constant, and c is the speed of light. The amount of kinetic energy imparted to the atom is

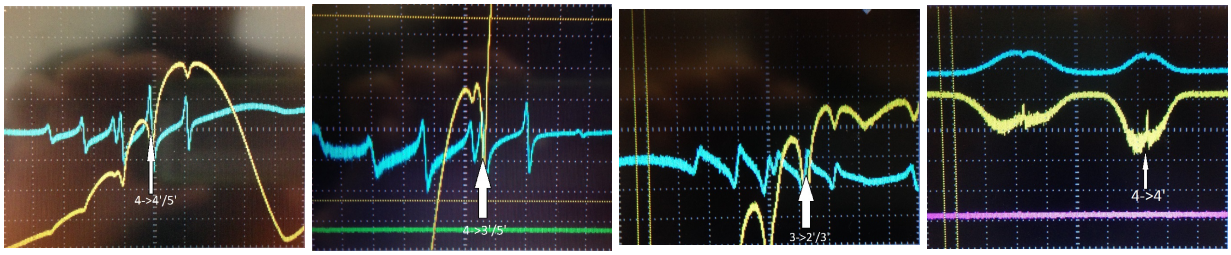
$$E = \frac{1}{2}mv^2 = \frac{p^2}{2m} = \frac{n^2h^2f^2}{2mc^2} \tag{8.12}$$

and the number of photons required to eject the atom from the trap is therefore

$$n = \frac{c}{hf}\sqrt{2mU_t} = \frac{c}{hf}\sqrt{2mk_BT} \tag{8.13}$$

where U_t is the trap depth potential, k_B is the Boltzmann constant, and T is the trap depth equivalent temperature. For our experiment parameters it then takes only 76 photons to eject an atom from the traps.

The blowaway light is provided by the same laser as the 3D MOT cooling and readout light. However it is sent through a different single-pass-only AOM, giving it a frequency shift of $219.99\,\mathrm{MHz}$ which brings it to -0.188Γ red detuning.



(a) (b) (c) (d)

Figure 8.12: Cs saturated absorption spectroscopy used for D1 and D2 laser locks. Yellow curve is transmission and blue curve is error signal. Colors reversed in (d). (a) D2 $F = 4 \leftrightarrow 4'/5'$ crossover lock for 2D cooling. (b) D2 $F = 4 \leftrightarrow 3'/5'$ crossover lock for 3D cooling. (c) D2 $F = 3 \leftrightarrow 2'/3'$ crossover lock for repumper. (d) D1 $F = 4 \leftrightarrow 4'$ lock for optical pumping.

laser	model	power	wavelength (nm)	line	lock transition	frequency (THz)
2D cooling	CECL	73 mW	852	D2	$6s_{1/2}, F = 4 \leftrightarrow 6p_{3/2}, F = 4/5$	351.721835
3D cooling	DBR	43 mW	852	D2	$6s_{1/2}, F = 4 \leftrightarrow 6p_{3/2}, F = 3/5$	351.721936
repump	DBR	34 mW	852	D2	$6s_{1/2}, F = 3 \leftrightarrow 6p_{3/2}, F = 2/3$	351.730625
optical pumping	DBR	42 mW	894	D1	$6s_{1/2}, F = 4 \leftrightarrow 6p_{1/2}, F = 4$	335.112538

Table 8.3: Laser locks using saturated absorption spectroscopy to atomic resonances.

output	line	lock transition	output transition	detuning (Γ)	AOM frequency (MHz)	output frequency (THz)	power into fiber (mW)
2D cooling	D2	$4 \leftrightarrow 4'/5'$	$4 \leftrightarrow 5'$	-0.3	2×58	351.837335	12.2
3D cooling	D2	$4 \leftrightarrow 3'/5'$	$4 \leftrightarrow 5'$	-11.9 to -2.1	$2 \times (82$ to $108)$	~ 351.9	11.1
blowaway	D2	$4 \leftrightarrow 3'/5'$	$4 \leftrightarrow 5'$	0	220	351.941936	0.12
2D repump	D2	$3 \leftrightarrow 2'/3'$	$3 \leftrightarrow 4'$	-0.3	268	352.009125	1.34
3D repump	D2	$3 \leftrightarrow 2'/3'$	$3 \leftrightarrow 4'$	-0.3	268	352.009125	11.2
OP repump	D2	$3 \leftrightarrow 2'/3'$	$3 \leftrightarrow 4'$	0.1	274	352.004625	.09
OP	D1	$4 \leftrightarrow 4'$	$4 \leftrightarrow 4'$	0	$2 \times 100 - 200$	335.112538	0.13

Table 8.4: AOM shifts applied to the D1 and D2 lasers to achieve the desired output frequency for each operation.

8.3 459 nm and 1038 nm Rydberg Lasers

The Rydberg levels are so-called by analogy to the Rydberg Series, which describes the energy of the excited states of hydrogen as being proportional to $-\frac{1}{n^2}$. The alkali elements are well described by Rydberg physics, because being on the left-hand side of the periodic table, like hydrogen, they have only one valence electron. In general an excitation of the atom by the laser will excite only that one valence electron, while the remaining electrons stay in filled shells. The nucleus plus the closed shells presents a net charge of $+1$ and behaves much like the single proton in the hydrogen atom. This idealized model is useful, but imperfect because even the excited state wavefunctions extend inward to the nucleus, and so a "quantum defect" is given to describe the deviation from the Rydberg model.

In cesium, the valence electron begins in the $6s_{1/2}$ ground state, and may be excited up to these Rydberg states. There is no agreed upon definition of how high the principle quantum number must be to consider the atom to be in a Rydberg state, but generally above $n = 25$. As we increase n, the $-\frac{1}{n^2}$ spacing means that the states will get closer and closer together, asymptotically approaching the 6.238×10^{-19} J 1st ionization energy. This is equivalent to a single 941.5 THz photon, or a wavelength of 318.4 nm. This UV wavelength is used in some experiments, such as Hankin et al. [75], to directly excite cesium from the ground state to a Rydberg state. However, working with UV light presents difficulties, such as poor transmission through fiber optics.

Instead, we use a two-photon transition, first on the $6s_{1/2} \leftrightarrow 7p_{1/2}$ transition with a 459 nm laser, and then on $7p_{1/2} \leftrightarrow ns_{1/2}$, $7p_{1/2} \leftrightarrow nd_{3/2}$ or $7p_{1/2} \leftrightarrow nd_{5/2}$ with a 1038 nm laser, as shown in Figure 8.13. The sum of these two photon energies is equal to the 318 nm photon energy (i.e. $\frac{1}{318} = \frac{1}{459} + \frac{1}{1038}$). We detune the light by ~ 360 MHz to the blue of the $6s_{1/2}, F = 4 \leftrightarrow 7p_{1/2}, F = 4$ transition. The particular Rydberg level targeted is determined by the sum of the 459 and 1038 nm photon energies, and can be changed by the choice of 1038 cavity lock peak, and fine tuned with AOM frequency shifts.

The 459 nm and 1038 nm Rydberg laser layouts, described in the rest of this section, are near mirror images of each other, as shown in Figure 8.14.

8.3.1 459 nm Rydberg Laser

The 459 nm photon is generated by a frequency doubled 918 nm external cavity diode laser. A 300 mW Axcel M9-915-0300-D50 laser diode in the Littman-Metcalf configuration (Liu and Littman [76]) is first roughly tuned using temperature and grating angle.

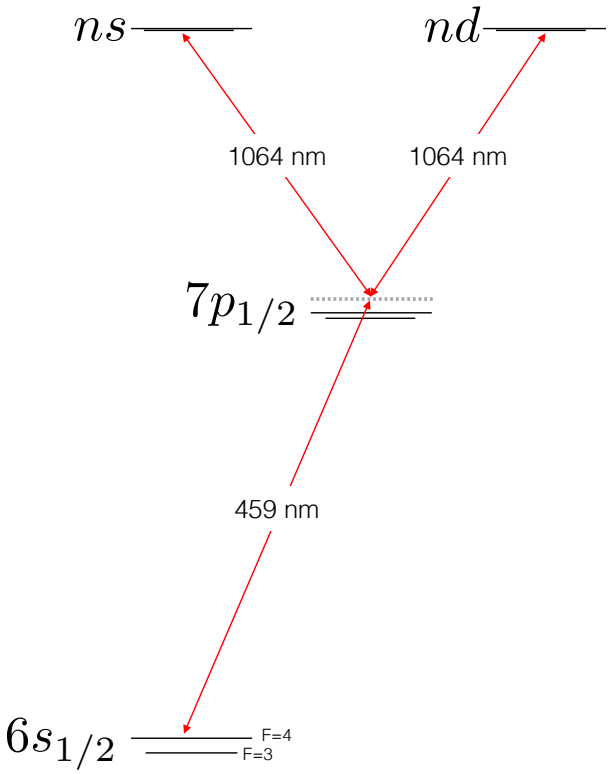


Figure 8.13: The Rydberg states are reached by a two photon 459 nm and 1038 nm transition, via the $7p_{1/2}$ level. This allows access to ns or nd Rydberg states.

The light is then adjusted in frequency by up to 1.5 GHz by a double-pass 750 MHz AOM, whereby the laser can be scanned across the free-spectral range of a high-finesse cavity. This allows us to lock the 918 laser to the cavity using the Pound-Drever Hall technique (Pound [77] and Drever et al. [78]), but still have complete freedom to adjust the laser to target any Rydberg level that we choose.

The cavity, from Advanced Thin Films, has a finesse 160000 at 918 nm. It consists of a 10 cm ultra-low expansion (ULE) glass spacer with a mirror on either end. One mirror is planar and the other has an $R = 50$ cm radius of curvature. The free spectral range is ~ 1.5 GHz, and the high finesse gives a cavity linewidth of 9.4 kHz linewidth. A small amount of the laser light is sampled, passed through an EOM to add 79 MHz sidebands, and coupled into the cavity. The reflected light is measured using a photodiode and then mixed with a heterodyne signal to give a fast-feedback signal that is used to modulate the laser current. The same signal is also used in a slow-feedback loop to a PID servo controller on the piezo-mounted laser grating. The ULE zero-expansion temperature was found by locking the laser to the cavity, and monitoring the true frequency using our optical

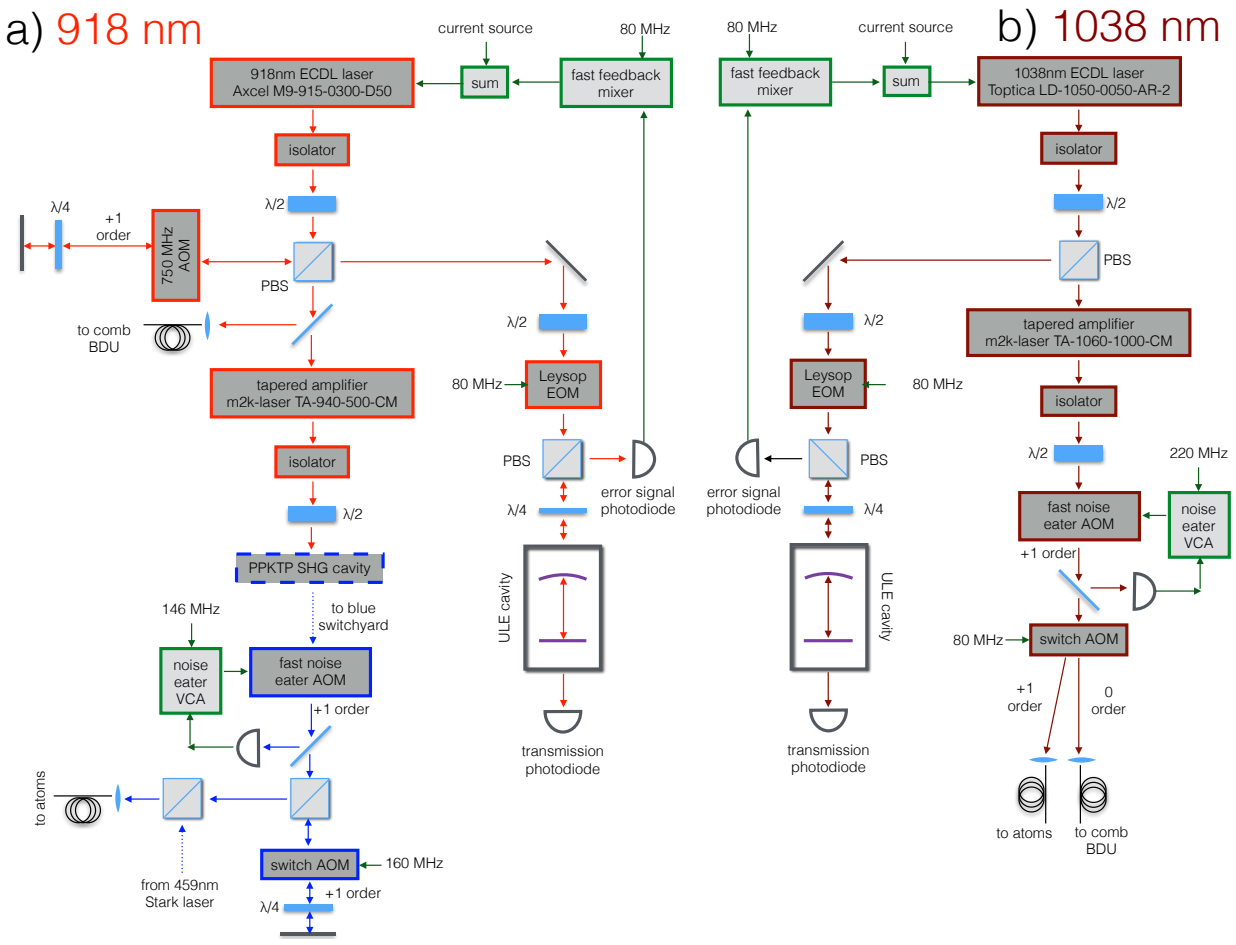


Figure 8.14: The 459 nm and 1038 nm Rydberg laser layouts. Each setup uses an ECDL laser, tapered amplifier, and PDH lock to a ULE cavity. The light is transported to the experiment via fibers, where 2D AOM beam scanners for each color target the atoms. The 2 photon sum excites the atoms to the Rydberg states.

frequency comb (see Section 8.7), while sweeping the cavity temperature. A turning-point in the frequency vs. temperature curve (see Figure 8.15) indicates the condition where the coefficient of thermal expansion changes sign from positive to negative, giving a stable operating point.

The stabilized light is amplified using a 500 mW m2k-laser TA-940-500-CM tapered amplifier. The tapered amplifier chip for this and other lasers is mounted in a custom made three piece mount. The mount can accommodate different thicknesses of TA chip by swapping the middle piece, while reversing the outer pieces to maintain the same footprint, so the same base plate may be used. See Figure 8.16.

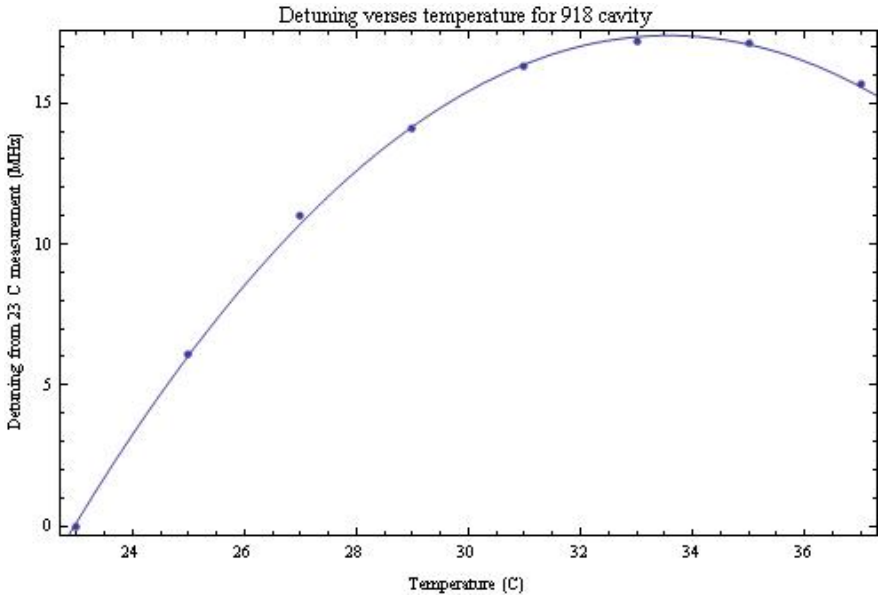


Figure 8.15: Measurement of the frequency of the 918 nm locked to a high-finesse ULE cavity, as the temperature of the cavity is swept using a TEC. The frequency is measured using a beat measurement with an optical frequency comb. The turning point indicates the condition of zero-expansion. The peak temperature was 32.26 °C as measured on an uncalibrated 50 kΩ thermistor, corresponding to 31.0 °C on a type-K thermocouple.

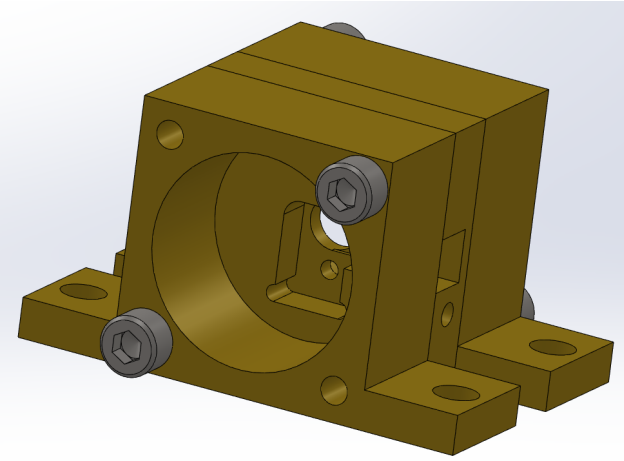


Figure 8.16: Our custom designed three-piece tapered amplifier mount. The mount can accommodate different thicknesses of TA chip by swapping the middle piece, while reversing the outer pieces to maintain the same footprint, so the same base plate may be used.

The amplified light is then coupled into a second harmonic generation cavity. This cavity is a bow-tie ring cavity with a 2 cm periodically poled potassium titanyl phosphate (PPKTP) crystal from Raicol, which doubles the frequency by summing two 918 nm photons into one 459 nm photon. The output coupler of the bow-tie cavity is manufactured by LaserOptik and has $R > 99.5\%$ at 918 nm and$R < 2\%$ at 459 nm. The maximal SHG output has been found to with 45 mW into the tapered amplifier, giving 400 mW into the SHG cavity, and 35 mW of 459 nm light output.

The 459 nm light is then put through a double-pass high-bandwidth AOM to tune the frequency to a specific Rydberg level. This light is then combined with light from the 459 nm Stark shifting laser and fiber coupled. The fiber goes to a 2D AOM beam steering system inside the experiment box, which is used to target the 459 nm light at single atoms.

8.3.2 1038 nm Rydberg laser

The implementation of the 1038 nm laser is very similar to the 459 nm laser, except without the need for frequency doubling. The system was originally seeded by a 16 W Yb fiber amplifier from IPG. Due reliability problems, this system was retired in favor of an external cavity diode laser and tapered amplifier, as in the 459 nm Rydberg system. The diode is a 50 mW Toptica LD-1050-0050-AR-2, and the tapered amplifier is a 500 mW m2k-laser TA-1060-1000-CM. The high-finesse cavity locking scheme is identical to the 459 nm Rydberg system. The output from this laser system is fiber coupled and sent to a 2D AOM beam steering system inside the experiment box. The 1038 nm and 459 nm beam steering systems are situated on opposite sides of the vacuum cell to minimize the momentum transfer to the atoms during Rydberg operations.

8.4 459 nm and 9.2 GHz Ground State Rotations

The energy splitting between the $|0\rangle$ and $|1\rangle$ qubit states is the $9.192\,631\,770$ GHz cesium clock transition frequency. We can cause the atoms to oscillate between these two states by applying microwave radiation at this frequency. However, because the wavelength is 3.3 cm we cannot aim this radiation at a single atom, but instead must do these operations globally. Sometimes this is a desired operation, but in many cases we will want to address this operation to a single site. To do so we must use a laser instead. We have used two methods to achieve these single-site qubit rotations. First, an all optical system using a two-

laser Raman process. Second, using the AC Stark shift of a single laser to tune microwaves in and out of resonance.

8.4.1 9.2 GHz Microwave Horn

Ground state rotations are performed globally on all sites in the atom array using 9.2 GHz microwaves, which are radiated from a horn antenna located externally to the vacuum cell, and aimed at the atom array from a position normal to the trapping/imaging/Rydberg axis, and 45° above the horizontal, as labeled in the picture in Figure 8.17.

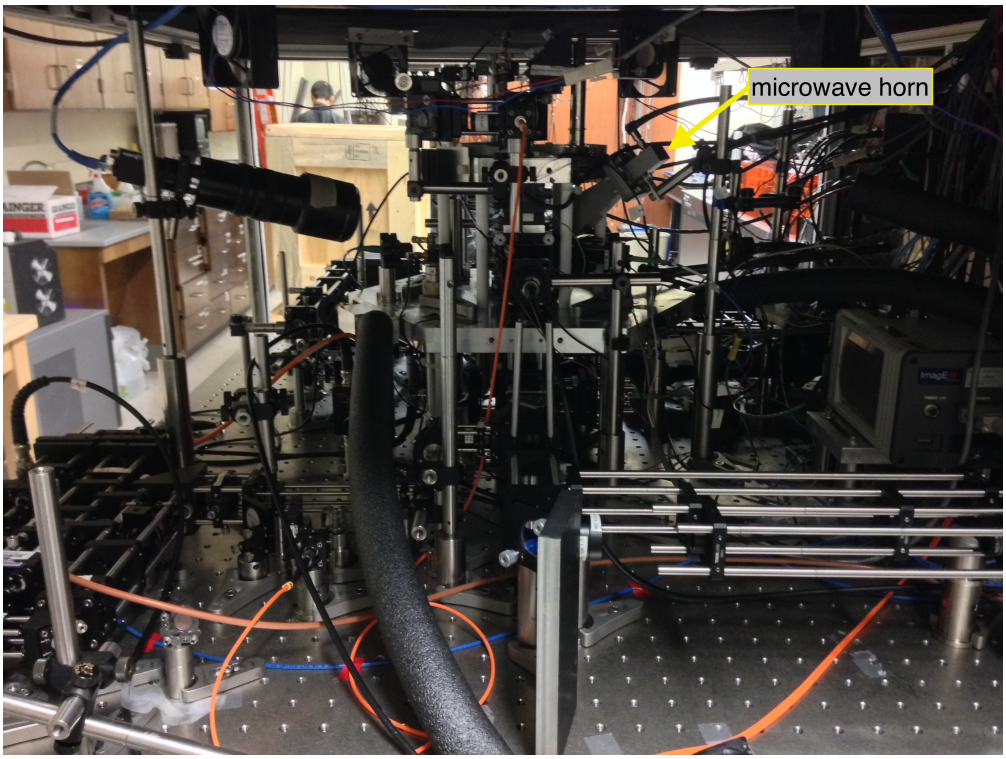


Figure 8.17: The experimental apparatus, showing the microwave horn used for ground state rotations. The horn is 45° from horizontal, and normal to the magnetic bias field.

All the experimental operations are done with reference to these 9.2 GHz microwaves, and so a common reference is important. The microwaves sources are all synched together by reference to a 1 GHz microwave synthesizer, which in turn gets long-term frequency stability from the 10 MHz reference. This reference is derived from the Global Positioning System, whose satellite timing signals are received by an antenna on the roof of Chamberlin Hall. Through this chain the experiment is ultimately referenced with the atomic clocks at the Naval Observatory in Washington, D.C.

To provide adjustability of the microwave source, we tune our qubit frequency RF synthesizer to 200 MHz below the exact cesium clock frequency. This signal is then mixed with a $\sim$ 200 MHz signal from a direct digital synthesis RF generator. These Analog Devices AD9910 DDS generators are computer controlled. Each has eight pre-programmable profiles. We employ two of these DDS generators, and use an RF switch to select between them, giving 16 possible fast-switching choices of frequency, amplitude and phase. These 16 profiles are used to perform rotations on various trapping sites with site-specific RF frequencies, as described in Chapter 13, or phase shifted gates, as described in Chapter 14.

The mixed signal gives $\sim$9.2 GHz, which is then amplified by 30 dB. Some of the signal is split using a directional coupler, and an Agilent 8437B Low-Barrier Schottky Diode Detector is used to sense the RF power. This signal is fed to a homemade noise eater circuit, which provides feedback to a voltage controlled attenuator to keep a constant RF power level.

A fast RF switch gives on/off pulse control, before the signal is amplified by 35 dB and then emitted from the horn antenna at $\sim$10 cm from the atoms. A complete schematic of the microwave system is given in Figure 8.18.

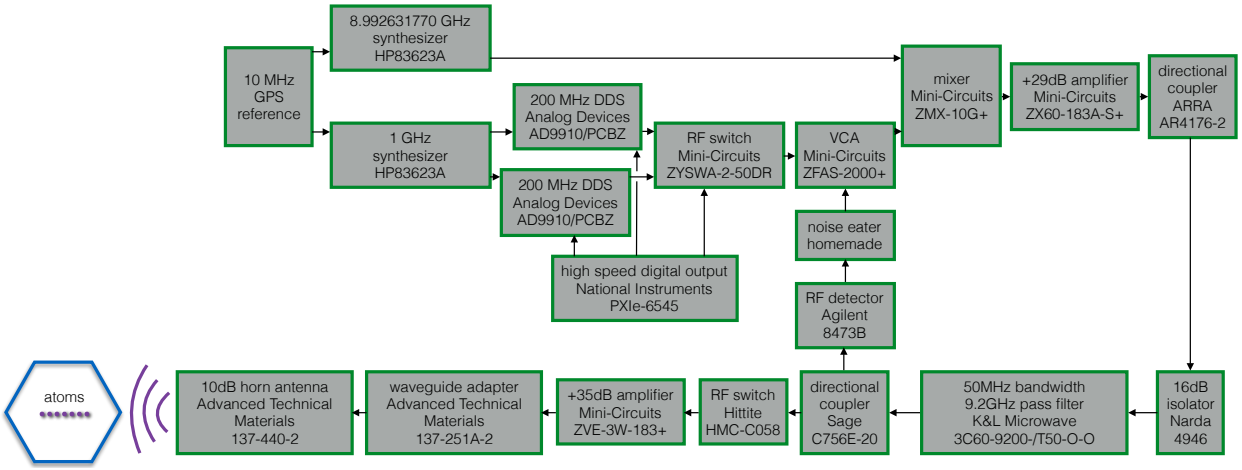


Figure 8.18: A schematic of the RF electronics which provide microwave radiation for performing ground state rotations of the qubit. The microwaves irradiate all the atoms, performing global operations, but can made site-selective with the addition of a Stark shifting site-specific laser beam.

8.5 459 nm Raman Lasers

Two lasers that hit the atoms at the same time can sum in frequency, as with the 459 and 1038 nm Rydberg lasers, or they can excite a transition that is the difference between their frequencies. By employing two 459 nm lasers of nearly the same frequency, but detuned by 9.2 GHz from each other, we can use these lasers to implement all optical qubit rotations. The lasers are detuned by 14 MHz from the $6s_{1/2} \leftrightarrow 7p_{1/2}$ transition. By using a large detuning we ensure that the light scattering from the excited state is minimal, and that the atoms are effectively transferred from one $6s$ hyperfine ground state to the other, without ever populating the $7p$ state. The delta-shaped transition shown in Figure 8.19 is an anti-Stokes Raman process.

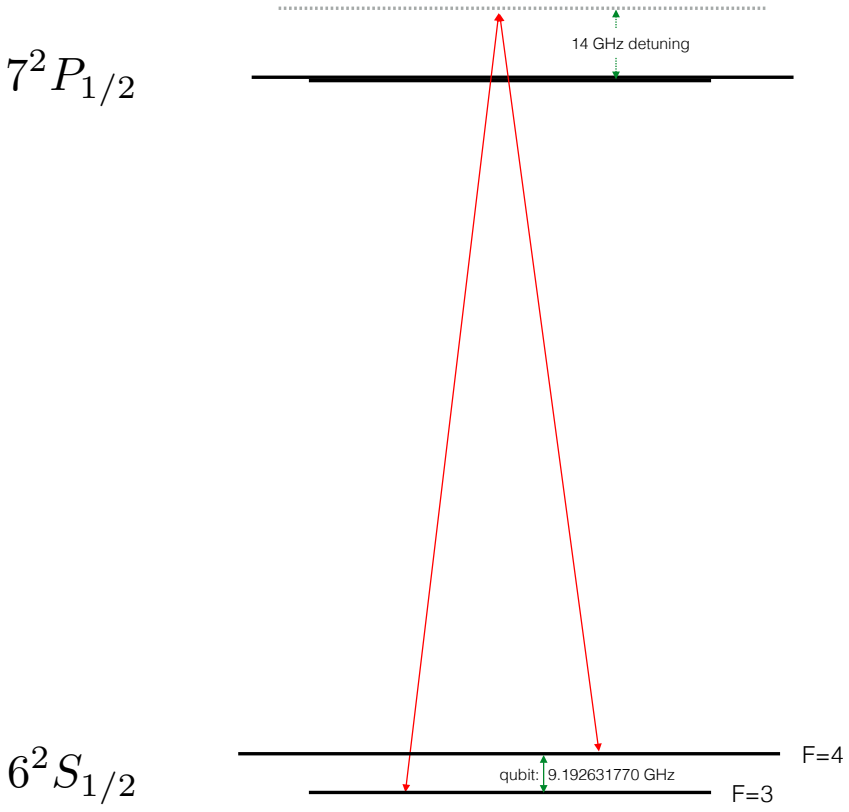


Figure 8.19: A Raman transition that can be used to rotate the ground state qubit using site-addressable lasers. The large detuning prevents the excited state from being populated.

These two lasers are identical in construction to the 459 nm Rydberg laser, except that the cavity used for the Pound-Drever-Hall lock is of lower finesse. Instead of the ULE cavity that gives the stability necessary to excite the Rydberg transitions, the Raman lasers

use a home-built cavity that uses Invar (low-thermal expansion high-nickel stainless steel) to maintain the spacing between two mirrors in a vacuum chamber. The two lasers are then phase locked together (Hall, Long-Sheng, and Kramer [79]) with a line-width of better than 1 Hz. This light is then coupled into the same fiber as the 459 nm Rydberg light, and transported to the blue 2D AOM beam scanner inside the experiment box, so that single atoms may be targeted.

8.6 459 nm Stark Shifting Laser and 9.2 GHz Microwaves

Because of the complexity of the two-laser Raman system leading to poor reliability, it has been retired in favor of a one-laser implementation. One technique that has been pursued, but not fully implemented, was the use of a single-laser Raman system. In this system, one of the 459 nm lasers is passed through an EOM to add sidebands at $\pm\frac{9.2\,\text{GHz}}{2}$. A prism-based Mach-Zender interferometer is then used to selectively remove the carrier peak, leaving light only at the sideband frequencies, with a splitting of 9.2 GHz.

The system that was ultimately employed with much success, however, is to use a single 459 nm laser as a Stark shifting beam, to shift the microwaves into or out of resonance. In the *shift-out* scheme, the microwaves are tuned to resonance, and the 459 light is aimed at one atom to make that atom non-resonant. This then has the effect of performing a ground state rotation on all atoms except the targeted site. This is typically only useful in a two qubit experiment, where we can perform a microwave rotation on one atom by shifting the other atom out of resonance. The other atoms in the grid will also undergo a microwave rotation, but if we are not concerned with them during a given experiment, it is irrelevant. When considering operations on larger numbers of atoms in the array, we must employ a *shift-in* scheme, where the microwaves are tuned out of resonance, but the 459 light shifts it back into resonance for one atom only. This scheme is harder to implement, because it requires the 459 power and detuning to be stable, such that the AC Stark shift due to the laser is stable. However, it is necessary to use this technique when considering multi-qubit operations, because it allows a microwave operation to be performed on one and only one site, while the rest are illuminated with non-resonant microwaves.

For the shift-in technique, as described in Xia et al. [80], we detune the microwave frequency ω by $\delta = \omega - \omega_q$. This suppresses the microwave qubit rotation by a factor scaling as Ω^2/δ^2 where Ω is the resonant microwave Rabi frequency. We have employed a microwave detuning ranging from 33 to 85 kHz depending on the experimental conditions,

as described in Chapter 13. The atom that we wish to perform the single-site operation on is targeted by a tightly focused beam from the 2D beam scanner as described in Section 5.2. The Stark beam is σ_+ polarized and propagates normal to the plane of the atom array. We detune the 459 nm Stark shifting laser by 14 to 20 GHz from the $\left|6s_{1/2}, F = 4\right\rangle \leftrightarrow \left|7p_{1/2}, F = 4\right\rangle$ transition. The intensity of the 459 nm beam was adjusted such that the induced differential Stark shift between states $|0\rangle$ and $|1\rangle$ was set equal to δ to bring the selected site into resonance (see Zhang, Rolston, and Das Sarma [81]). The choice of detuning for δ for single-site gates is a trade off between less than perfect suppression of the microwave field at small δ and excessive photon scattering from the Stark beam at large δ. For a given value of δ the photon scattering can be reduced by working at large optical detuning Δ_S, but not completely eliminated since for large Δ_S the detuning $\delta \sim \omega_q/\Delta_S^2$ and $\lim_{\Delta_S \to \infty} \delta = 0$. An optimized working point which reduces the need for large δ can be found by choosing a detuning for which the off-resonant coupling to non-selected sites gives a pulse area which is a multiple of 4π and therefore does not disturb the qubit states. For a pulse area of θ_R on the targeted qubit the condition for minimal disturbance of non-targeted sites is

$$\Omega_{non-target} t = n \times 4\pi \tag{8.14}$$

$$\sqrt{\Omega^2 + \delta^2}\, t = 4\pi n \tag{8.15}$$

$$\frac{\sqrt{\Omega^2 + \delta^2}}{\Omega} = \frac{4\pi n}{\theta_R} \tag{8.16}$$

$$\frac{\Omega^2 + \delta^2}{\Omega^2} = \frac{16\pi^2 n^2}{\theta_R^2} \tag{8.17}$$

$$1 + \frac{\delta^2}{\Omega^2} = \frac{16\pi^2 n^2}{\theta_R^2} \tag{8.18}$$

$$\frac{\delta^2}{\Omega^2} = \frac{16\pi^2 n^2}{\theta_R^2} - 1 \tag{8.19}$$

$$\frac{\delta}{\Omega} = \sqrt{\frac{16\pi^2 n^2}{\theta_R^2} - 1} \tag{8.20}$$

Thus, the leakage error should have a first local minimum for a π pulse at $\delta/\Omega = \sqrt{15}$. The leakage can be further reduced by going to the second local minimum at $\delta/\Omega = \sqrt{63}$, as described in Chapter 13. For operations that require site-selective $\theta_R = \pi/2$ gates, the first minimum leakage condition is then at $\delta/\Omega = \sqrt{63}$. For some experiments, such as CNOT or 2-qubit Grover, the π phase shift that will be imparted on the non-targeted qubits during

site-selective $\pi/2$ gates at the $\delta/\Omega = \sqrt{15}$ condition does not affect the population results, as discussed in Chapter 14. Therefore, the smaller detuning condition may be used for those experiments. We have employed both the $\sqrt{15}$ and $\sqrt{63}$ conditions as various stages in our experimental work.

The condition given in Equation 8.14 is an approximation that holds true for operations beginning in basis states. To evaluate the cross-talk more generally, we must average over all possible starting states with equal weight. Let the initial state be anywhere on the Bloch sphere, expressed as $|\theta, \phi\rangle = \cos(\theta/2)|0\rangle + e^{i\phi}\sin(\theta/2)|1\rangle$. This state undergoes a unitary transformation $|\theta, \phi\rangle \rightarrow U_j(\theta_R, \delta)|\theta, \phi\rangle$ with $U_j(\theta_R, \delta)$ the operator for a θ_R rotation about axis j detuned by δ. The fidelity of the transformed state with respect to the original state, averaged over the Bloch sphere, is

$$F^2(\theta_R, \delta) = \frac{\int_0^{\pi} d\theta \sin(\theta) \int_0^{2\pi} |\langle\theta, \phi| U_j(\theta_R, \delta)|\theta, \phi\rangle|^2}{4\pi} \tag{8.21}$$

The crosstalk error, defined as $E_{xt} = 1 - F^2(\theta_R, \delta)$, is shown in Figure 8.20 for π and $\pi/2$ rotations about x and z. Because each operation has its error minimized for different δ, the detuning of the 459 nm Stark shifting light should ideally be dynamically adjusted for each operation.

Experimental demonstrations of site-selective single qubit rotations have been performed with a fidelity of $0.9923(7)$ and are detailed in Chapter 13.

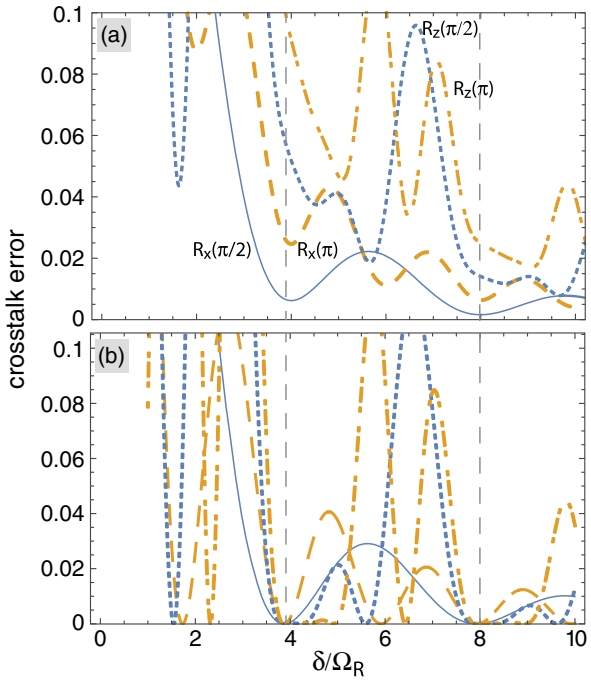


Figure 8.20: Crosstalk error for $R_x\,(\pi/2)$ (solid blue line), $R_x\,(\pi)$ (dashed yellow line), $Rz\,(\pi/2)$ (dotted blue line), and $R_z\,(\pi)$ (dash-dotted yellow line) rotations. The vertical dashed lines mark values of $\sqrt{16n^2-1}$. Panel (a) is the error from Eq. 8.21 averaged over input states, and panel (b) is the error for the initial state $|1\rangle$. Figure from Xia et al. [80].

8.7 Frequency Comb

Tuning the experiment to different Rydberg levels involves precise tuning of the $1038\,\text{nm}$ and $459\,\text{nm}$ lasers over a range, and requires better accuracy than we can achieve with our wavemeters. To facilitate this, we employ a frequency comb. Our unit is a Menlo Systems FC1000 Optical Frequency Synthesizer.

The basic operation of the frequency comb is that of a pulsed mode-locked laser [82]. In this type of laser, a pulse envelope circulates in the laser cavity at a well-defined period. The time-series is that of a delta function pulse train, or comb. The Fourier transform of such a waveform is also a pulse-train in frequency space.

The pulses propagate at velocity v_g, and have period $T = 2L/v_g$ and frequency

$$\omega_r = \frac{v_g}{2L} \tag{8.22}$$

where L is the length of the cavity. Within the pulse envelope, however, the electric field

moves at a phase velocity v_p which is in general not the same as v_g. This leads to an offset in the frequency space representation of the comb light. In general the comb is composed of many teeth, which have frequency

$$\omega_n = n \cdot \omega_r + \omega_0 \tag{8.23}$$

where n is an integer, ω_r is the repetition frequency of the laser, and ω_0 is the offset frequency imposed by the phase evolution of the electric field. The repetition of our comb is $\sim 250\,\mathrm{MHz}$ and is easily measurable by digital electronics. To measure ω_0 we make use of the large bandwidth of the comb, which spans at least one octave. There exist comb teeth near both $1030\,\mathrm{nm}$ and $515\,\mathrm{nm}$. The FC1000 uses second harmonic generation to frequency-double the $1030\,\mathrm{nm}$ light to $515\,\mathrm{nm}$. The original and doubled teeth, both at $515\,\mathrm{nm}$, can then be interfered with each other to find a beat note.

$$\omega_{doubled\,1030} - \omega_{515} = 2\left(n\omega_r + \omega_0\right) - \left(2n\omega_r + \omega_0\right) = \omega_0 \tag{8.24}$$

This isolates the offset frequency which is also easily measurable RF.

Any CW laser within the bandwidth range of the comb can be beat against the nearest tooth. By making this measurement at two different repetition rates, the number of the nearest tooth n can be determined. The frequency of the CW laser is then $\omega_n + \omega_{beat}$ and is now known as an absolute measurement. Despite being hundreds of THz, we can now easily determine laser frequencies with sub kHz accuracy.

The uncertainty in frequency of a given comb tooth is [83]

$$\delta\omega = n\delta\omega_r + \delta\omega_0 \tag{8.25}$$

For our comb we have $\omega_r = 2\pi \cdot 250$ MHz and typical lock uncertainties of $\delta\omega_r = 2\pi \cdot 3$ mHz and $\delta\omega_0 = 5$ Hz. When observing the beat note with $918\,\mathrm{nm}$ light at $326\,\mathrm{THz}$ we use the $N \simeq 1.3 \times 10^6$ tooth. This gives an uncertainty of $\delta\omega = 2\pi \cdot 3.9\,\mathrm{kHz}$.

Each tooth is broadened further by phase noise to $\delta\omega_n \simeq 2\pi \cdot 100\,\mathrm{kHz}$. To reach the lower $\delta\omega$ of the lock uncertainties we must average for time t such that

$$\delta\omega \sim \frac{\delta\omega_n}{\sqrt{2\pi\delta\omega_n t}} \tag{8.26}$$

or

$$t \sim 2\pi \frac{\delta\omega_n}{(\delta\omega)^2} \tag{8.27}$$

For our system $t = 6.6$ ms which is short enough that it is not a concern, because our laser is narrowed using a stable cavity and the comb will only be used to correct long term drifts.

There is also uncertainty in the comb repetition rate due to the $10\,\text{MHz}$ reference signal that we derive from a Novus NR1111 GPS locked frequency reference. This signal is up-converted by 25 times to use as a local oscillator to compare against the $250\,\text{MHz}$ repetition rate. The uncertainty due to this reference is

$$\delta\omega = 25N\delta\omega_{GPS}$$

The Novus NR1111 has $\delta\omega_{GPS}/\omega_{GPS} = 4 \times 10^{-10}$ after $1\,\text{s}$ and $\delta\omega_{GPS}/\omega_{GPS} = 2.5 \times 10^{-11}$ after $10\,\text{s}$, giving $\delta\omega = 2\pi \cdot 130$ kHz and $\delta\omega = 2\pi \cdot 8.1$ kHz, respectively. This oscillator reference is therefore the limiting factor in measurement uncertainty at the experimentally relevant time scale of seconds. However, when used as a correction for long term drift the gains from a better oscillator are negligible.

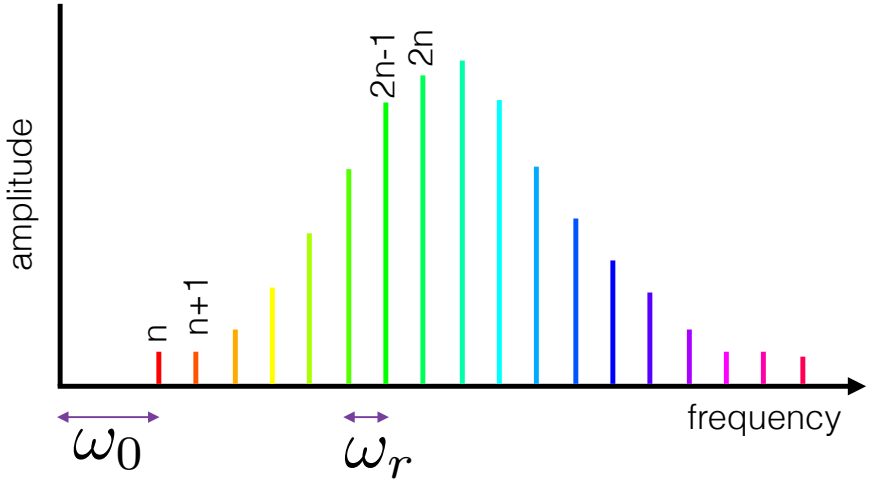


Figure 8.21: The frequency spectrum of an optical frequency comb. The pulsed laser leads to a repetition rate ω_r whereas the phase evolution of the pulses give an offset frequency ω_0. The comb spans an octave, which allows it to be self-referenced by comparing n and $2n$ teeth via second harmonic generation.

9 Experiment Control Software

Our experiments require the ability to create a timed sequence of events from many different pieces of hardware. This includes at the minimum: digital input/output, analog input/output, camera triggers, noise eater triggers, motion control stages, and temperature control. We need to update hardware with particular settings, execute a sequence of events, and then collect data.

This in general is repeated many times to gather statistical results. Furthermore, in any given experiment, we generally want to sweep at least one parameter, to observe the effect on our outcomes. Often changing this one parameter actually requires varying settings on many pieces of hardware. All of this is just for one particular type of experiment. In a given day we run a dozen different experimental sequences, with different goals for what data to collect and how to analyze that data.

All of this means that we require a very flexible experiment control system. We cannot hard-code the experimental sequences in pulse generators because it would be too cumbersome to update. Most, if not all, of our instruments must be computer controlled. One program must be able to set, synchronize and collect data from all these various instruments.

To meet this need, the CsPyController software was written by the author to run experiments and collect data for the AQuA (*Atomic Qubit Array*) project. It was designed with generality in mind, and should be usable for a wide variety of physics experiments. It is the successor to CsLabViewController, also by the author. This was in turn the successor to QCE Suite by Thomas Henage, which was used for VXI hardware control on past rubidium experiments, but was not adaptable to the hardware used on AQuA. CsPyController presents many improvements over those codes, including increased flexibility, programmability, ease of use, maintainability, and in particular a built-in optimizer.

The ability to automatically optimize our experimental parameters to minimize or maximize some cost function has enabled us to reach a much higher level of performance on our system. The optimization function is used to adjust almost every parameter on the experiment, and is used on atom loading, readout fidelity, shot-to-shot retention, optical pumping efficiency, cycle time, single-atom alignment, gate phases, and overall gate performance. Most of these are complex functions of multiple variables. The optimizer can in general find better solutions than the single-variable scans that human operators usually employ, and in many cases can do so in fewer iterations.

The general architecture of the software, as well as results achieved with the optimizer, are described here. For complete detail on using the software, and for extending the software with new instruments and new analyses, see the *CsPyController Users' Manual* and *CsPyController Programmers' Manual*, which are available within the CsPyController git repository. These manuals, along with all the code, is open-source and freely available at `https://github.com/CsPyController/CsPyController`.

Other notable implementations of experiment control software include LabRad (Ansmann [84]), labscript suite (Starkey et al. [85]), and Cicero/Atticus (Keshet and Ketterle [86]). These three packages take a similar approach as CsPyController toward modularity and use of internet protocols for communication between parts of the software. In particular we are thankful to Starkey et al. [85] for bringing the HDF5 data format to our attention. Development on CsPyController began before these alternatives were available, but it is encouraging that a similar direction has been taken by various research groups, leading us to believe that our system is well designed for the task of atomic physics and quantum computing experiments.

9.1 Architecture

CsPyControler uses a central controller written in Python as the high-level **command center**. This **command center** sequences the experiment, sends out commands to instruments, collects data, and runs some analyses. Under normal operation, the user only interacts with the Python **command center**.

Some instruments are controlled by the **command center** directly, however many are controlled by satellite **instrument server** programs. These **servers** may be running on the same computer, or they may run on a different computer. Regardless of location, communication between the **command center** and the **servers** is done using *Transmission Control Protocol/Internet Protocol* (TCP/IP) for messaging. This allows the **servers** to be written in any language for any operating system. The user must manually start any separate **servers**, but once they are running the **command center** acts as a *TCP/IP client* and all user interaction, setup and control is done from there. The main instruments in use on the AQuA project are on a separate PXI system, controlled by a **server** written in *LabView* running on an embedded *Windows* controller running on that system.

The control hierarchy of CsPyController and some of the **instrument servers** we have created in various programming languages is shown in Figure 9.1.

For every experiment, the settings and data are saved into *HDF5* files, which is a standardized and well-supported file format which is ideally suited for scientific data collection. Some analyses are done on-the-fly in the **command center**, but any other analysis desired may always be done on the data saved to the HDF5 file, using your scientific computing software of choice (e.g. *Mathematica*, *Matlab*, or as we generally use: *Python* with the `ipython`, `h5py`, `numpy`, `scipy` and `matplotlib` packages.)

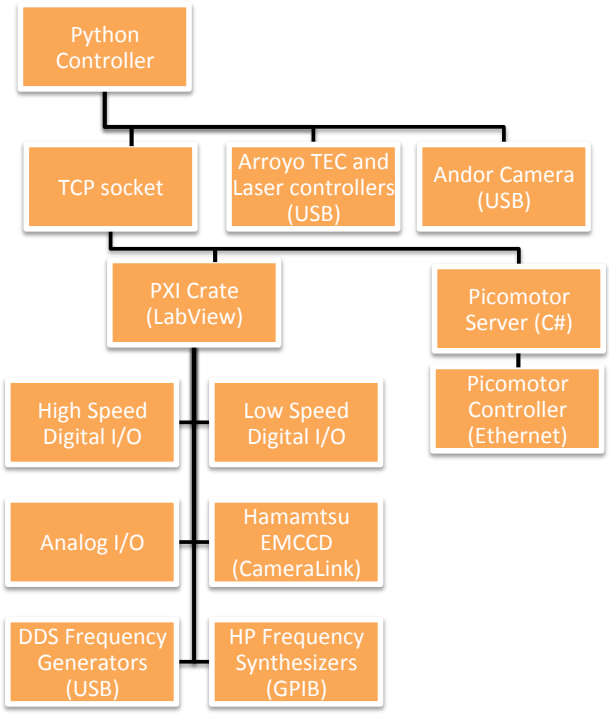


Figure 9.1: The control hierarchy of CsPyController and some of the **instrument servers** we have implemented in various programming languages.

9.2 Experiments, Iterations, Measurements and Shots

Let us establish some nomenclature. There are several levels of repetition performed by the software. From big to small, they are *experiments*, *iterations*, *measurements* and *shots*.

An *experiment* is one round of execution with one set of programmed specifications. Generally there is one new *experiment* and one new results file every time the *Run* button is pressed. Then some changes are made by the user and another *experiment* is run. In the case of using the *optimizer*, covered in Section 9.5, there will be more than one *experiment* per file.

An *iteration* is one set of settings. As an *experiment* runs, it can step through different settings as specified by the *independent variables*. Each of these steps is an *iteration*. The *independent variable* settings define the number of *iterations* per *experiment*.

A *measurement* is one execution of the currently programmed experiment sequence. Generally, the user will specify an *iteration* to have many *measurements* to gather better statistics.

A *shot* is a single camera exposure. Usually there are two or more *shots* per *measurement*, in order to make a before-and-after or time-of-flight comparison. A shot is usually specified in the *functional waveform* sequencing, by triggering a digital output pin. For some cameras, the number of expected shots must be entered on their settings page for the purpose of error checking. Every *measurement* in a given *iteration* should have the same number of *shots*.

Note that in almost all cases, lists and arrays in CsPyController are numbered starting from 0. For example, shot 0 is the 1^{st} shot, and shot 1 is the 2^{nd} shot.

9.3 Modularity, Maintainability, and Extensibility

One of the driving factors behind the development of CsPyController was the lack of maintainability of previous versions. Previous code was difficult to modify for use with new types of experiments because things like the number of free parameters were hard-coded, for example. With CsPyController, we have at every step tried to make the experiment structure as general as possible, at the expense of more work in the development of the code. One example of this is that there are no limits on the number of *independent variables* because the looping structure of the experiment is not hard-coded, but rather is determined dynamically. The number of *iterations* is limited only by hard drive space, as data is flushed to storage files, in fact after every measurement, and is not retained in RAM unless required by a particular graphing analysis.

We allow the user to have a great deal of flexibility by providing text boxes for *constant* and *dependent variable* specifications that can run any python code. Straightforward variable assignment can easily be done with this method of course, but the power of this method is that the user can create functions to make more complicated experiments a reality.

The goal of having the software be robust enough for future use is aided by the modularity. Previous experiment codes have required the existence of certain hardware drivers to be installed, even if that hardware does not exist on a given experiment. In some cases,

installing drivers can be problematic, or even impossible as operating systems are upgraded. By separating the functionality into separate *instrument servers*, we allow for those servers to only be running when needed by a particular piece of hardware, and hence there is no requirement to install unnecessary drivers.

Text based programming languages have the advantage of working well with version control systems (such as *GIT*, which we used extensively), which has allowed CsPyController to be maintained in a modular fashion, with work being done in multiple branches and merged when ready. Text based programming also has a significant advantage over graphical programming languages like LabView in that graphical programming languages tend to be difficult to document sufficiently, because of limited screen real-estate. Furthermore, while they made small tasks easy, graphical programming languages generally result in literal spaghetti code for large software efforts.

The code has been designed always with the idea that future experiments will use new and different hardware, and require new and different analyses. To this end, there is *no* master instrument that controls the whole experiment. In practice we use a National Instruments HSDIO card to define the experiment timing for the rest of our system, but that is not inherent to the code. This flexibility is left to the user. It is expected that communication with new instruments will need to be programmed in the future, and so a general framework is provided which allows new instruments to function in the context of the experiment flow. Similarly, every experiment has different desires for real-time analysis and graphing of data, and so a general framework is provided for analyses as well, and new ones will be automatically be passed the relevant data nodes, and be evaluated at the proper time in the experiment cycles.

9.4 Implementation

9.4.1 High-level Sequencing in Python

The **command center** is written in Python. This choice was made mostly due to the amazing availability of scientific computing packages for Python. One of the main jobs of the **command center** is to handle large numerical data sets, do some analysis, and plot results. Due mostly to the `numpy` package, Python can handle numerical computation on mutli-dimensional rectilinear arrays with great speed. Coupled with the `matplotlib` package, making high quality plots from this data is very simple. Further support for curve fitting, and much more, is in the `scipy` package. Advanced machine learning techniques

are available in the `scikit-learn` package. Python has become the de-facto language of scientific computation, and combining these many available packages makes it greater than the sum of its parts.

Furthermore, writing the high-level flow of the experiment control in Python is a job well suited to the language. Python is known for ability to facilitate clean, well structured high-level code. Python handles memory management through dynamic typing and automatic garbage collection, taking much of the burden of these low-level tasks off the programmer. However, Python is not known for being fast. The low-level operations that need to be fast are then left to compiled packages like `numpy` or for the **instrument servers**.

9.4.2 Functional Waveforms

Initial versions of CsPyController used a table-based entry method to specify the sequencing of digital events, and a separate equation based system for entering analog waveforms. This methods had several problems. It was cumbersome to edit, being a full-table on all channels for what was usually only a sparse amount of events. It made it difficult to synchronize digital and analog events, especially when some section in the middle of the experiment was changed in length.

We have switched to a system that we call *Functional Waveforms*, in which both the digital and analog events are sequenced in the same space, and are done so using the syntax of Python functions. This is one way in which using Python for high-level control can allow us to simplify implementation. Because Python is an interpreted, not compiled, language, the code entered by the user can be evaluated by the Python runtime itself.

This functional waveforms system has many advantages:

- it allows building sequences both in series (time-wise) and in parallel (channel-wise)
- it allows events to be referenced to either absolute or relative times
- many different time references can be created so that the event times refer to the most relevant other event in the sequence
- sequences can be built out of many different nested levels, so that low level functions can be defined once, and high level functions can be mixed and matched to define an experiment
- it eliminates the need to specifically calculate the length of any sequence

- allows implementation of complex behaviors like automatic Gray coding
- waveforms are more compact (a "sparse" implementation), and evaluation is much faster
- repetition is eliminated, so changes can be made across all waveforms sharing some function
- waveforms can be nested to reuse code
- backend code is actually simpler in many ways than with the table implementation, because only transitioning samples are specified
- view a universal graph of HSDIO and AO waveforms, across the entire experiment
- waveforms are readable, commentable, and make a lot more sense to the human user

This users' code has access to the namespace of variables defined by the **constants**, **independent variables**, and **dependent variables**. It is re-evaluated every **iteration**.

Detail on using the functional waveforms is given in the *CsPyController Users' Manual*. The graphical representation provided by CsPyController of the combined digital and analog sequencing is shown in Figures 9.2 and 9.3.

9.4.3 Low-level Execution in Python, LabVIEW and C#

Each **instrument server** is written in the language most well-suited to that hardware. In many cases this is defined by which language sample-code was provided in, thereby making the task easier. One particular sticking point is that some drivers are compiled as *.NET assemblies*. These drivers can only be called from code written in one of the Microsoft .NET languages and compiled into the Common Language Runtime (CLR), and hence cannot be called from the standard distribution of Python which is compiled in standard C. One solution that was tried is to use IronPython, which is Python compiled for .NET, but the lack of availability of almost all 3rd party packages for IronPython defeats much of the point of using Python at all. The *Python.NET* package, which purports to bridge this gap by allowing regular Python to call CLR code, was found to be unreliable. The solution employed in most of these .NET cases was generally to write the **instrument server** in C#, which is largely similar to C and C++ in syntax, and is extremely well supported by Microsoft. For National Instruments hardware, the best solution was to use LabView.

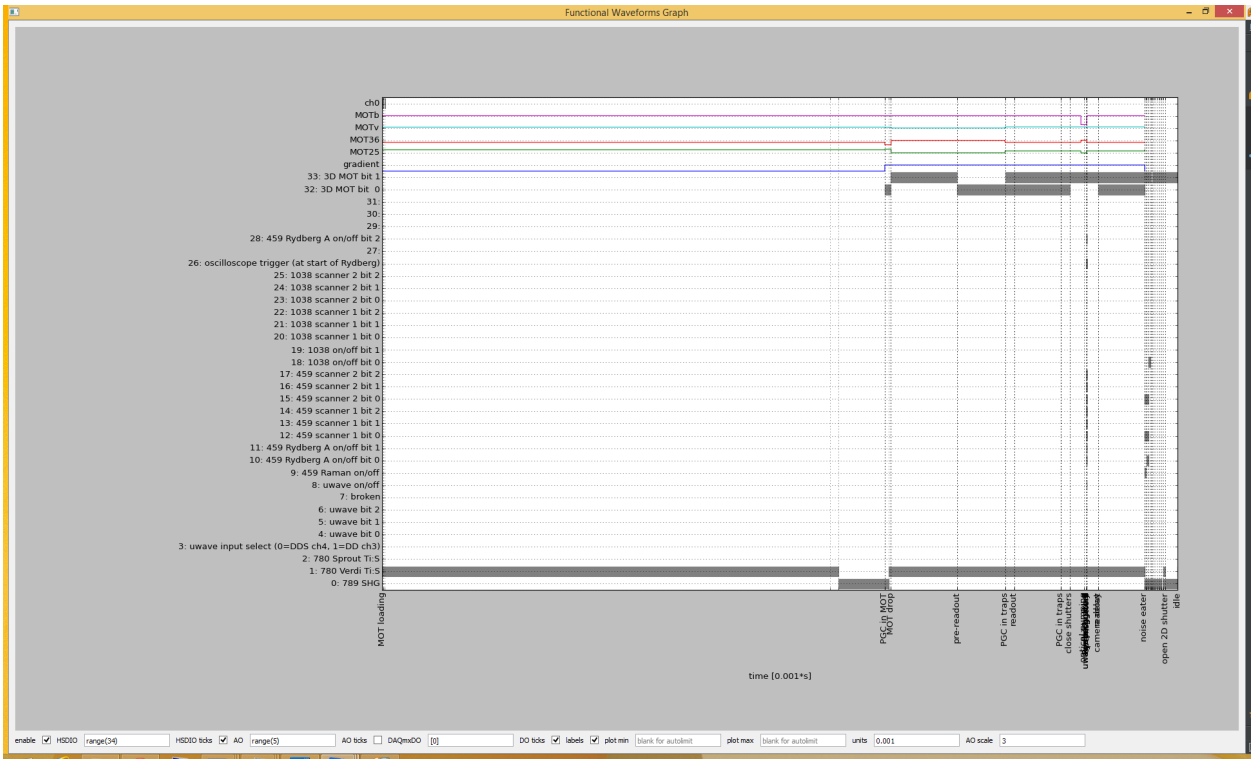


Figure 9.2: The combined graph of both the digital and analog output that is sequenced by the functional waveforms. This is a zoomed-out view of the entire experiment.

Although many National Instruments drivers can be called from C# or C++ or other text based languages, one of our main systems is a PXI chassis with a controller that has the ability to dual-boot into either Windows or a proprietary NI real-time OS based on PharLap. To use the real-time OS, only LabView or LabWindows/CVI can be used. Because the NI support is much better for LabView, we decided to use LabView to program the **instrument server** for these instruments.

The experimental flow between the high-level Python **command center** and the low-level **instrument servers** is shown in Figure 9.4.

9.4.4 Object-Oriented Programming

In order to allow for future upgradability, and in particular adding new hardware instruments, or data analyses, we used the concepts of object-oriented programming whenever possible. Object-oriented programming languages, such as Python, are designed around the idea of abstraction. Classes are created that specify a certain type of behavior, with the expectation that new subclasses will be created that conform to that behavior, while

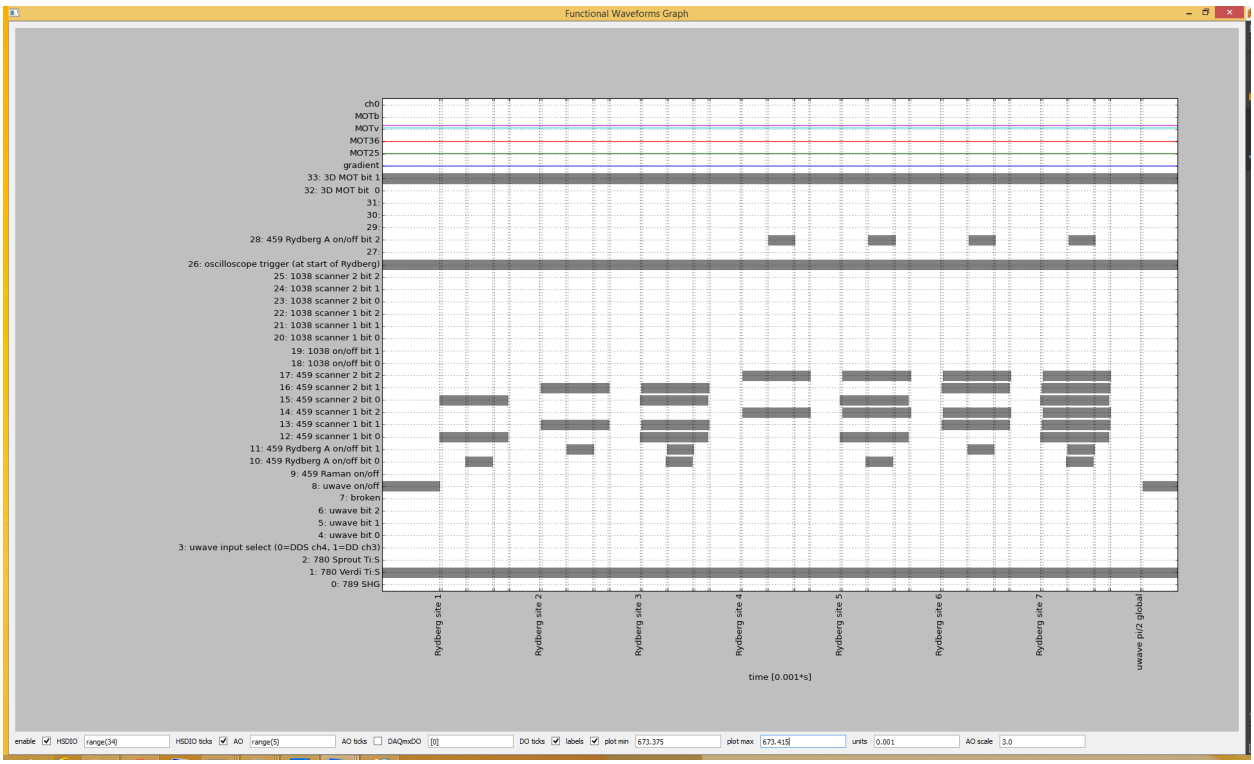


Figure 9.3: The combined graph of both the digital and analog output that is sequenced by the functional waveforms. This is a zoomed-in view of just the fast Rydberg operations in the experiment.

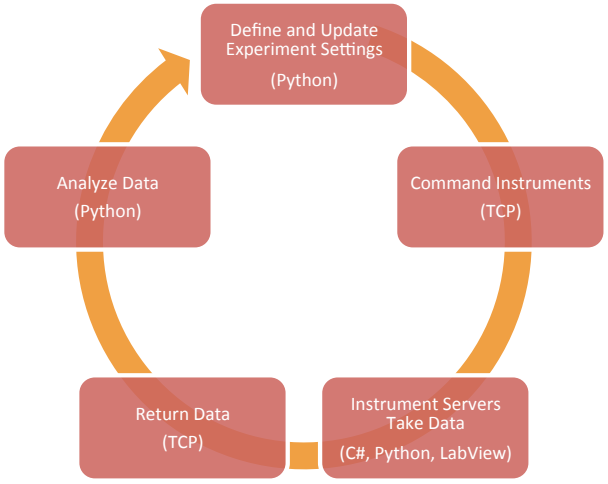


Figure 9.4: The flow of experiment control and data between the CsPyController command center, and the instrument servers. TCP/IP is used as the communication bus between these modular elements of the control software.

adding new more detailed features. The canonical example is that of the hierarchy of vehicle→car→Tesla, for example.

Using this model we have created a general class (`Prop`) that handles all the functionality of evaluation of variables, saving of properties, and synchronization with the GUI. A general `Instrument` class, which is a subclass of `Prop`, defines the framework necessary to update an instrument every *iteration*, to start the hardware every `measurement`, and to collect data from the hardware when the `measurement` is finished. The details of what commands should be sent to a particular piece of hardware are left to implementation in a subclass of `Instrument`.

We also have created a general `Analysis` class, which has the proper structure to be called after each *measurement*, *iteration* or *experiment*. The details of what to run at those times is left to subclasses. Each `Analysis` can also function as a filter, by returning an optional success code that indicates if the data from a particular measurement met certain requirements (such as atom loading). An `AnalysisWithFigure` class is provided to use in the common case of an analysis that plots a `matplotlib` figure to the screen every *measurement* or *iteration*.

9.4.5 GUI

The graphical user interface (GUI) front-end was developed using the *Enaml* package by Colbert [87]. This is a constraints based GUI description package which allows a GUI to be created using an entirely text based, yet simple and easily readable, language. Enaml is backend independent, and works well with either *Qt* or *wx*. The layout is specified hierarchically, using Python indentation rules to govern widget ownership. Layout constraints can be defined to specify the design intent of the the GUI, which allows it to adjust for various window and screen sizes. The text based nature is particularly suited to use with version control systems. See Figure 9.5 for an example of the GUI in use.

9.4.6 TCP/IP Networking

TCP/IP was selected as the messaging protocol to use for communication between the central Python **command center** and the separate **instrument servers**. TCP/IP has the advantage of being available as a core functionality in every operating system and every programming language, which gives us the most flexibility to run the **instrument servers** on the platform most well suited to them. In almost all cases TCP/IP can be used without

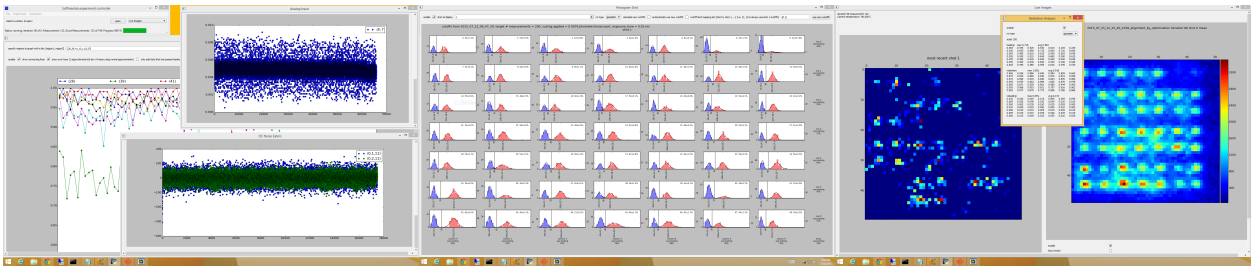


Figure 9.5: The GUI for the command center of the CsPyController software. Many windows with different plots, analyses and settings can be positioned independently to show the information of interest. Shown here across three screens, with analog input graph, DC noise eater error signal graph, retention vs iteration for selected sites, 49-site histograms, live and averaged array images, and loading/retention/reloading analysis results.

installing any extra drivers. Some hardware even comes with a built-in ethernet port that allows us to communicate directly with the hardware, rather than using an **instrument server** as an intermediary to some other communications bus. For security purposes, we have created an intranet, which is not connected to the building ethernet, and which we use for all of the hardware communication on our experiment. This also has the advantage of making sure that all routers involved are 1000 Mbps, and that we have the full bandwidth available to use. We can assign fixed IP addresses to all our hardware from the complete IP space, which is convenient when adding new hardware. The use of TCP/IP in our experiment does not create any slowdown in performance. In fact, we actually see a boost in data rate because our **instrument servers** can begin taking new data while the **command center** is still processing the previous measurement. To ensure that TCP/IP packets are synchronized, complete and uncorrupted, we employ a simple format. All messages must start with 'MESG' followed by 4 bytes of unsigned long (32-bit) integer which denote the length of the rest of the message, followed by the rest of the message. If the received message does not fit this format, the buffer is flushed and an error message is returned. The sender then has the option to resend. Encoding the length of the message greatly simplifies action on the receiving end, because it is not necessary to use any stop characters, and the port is polled for exactly the right amount of data, instead of looping and waiting for those stop characters. Because of the intranet, we are not worried about malicious external messages. However, before the intranet was implemented this simple protocol did on one occasion did stop an unwanted, probably vandalous, external connection.

9.4.7 Data Storage in HDF5

Settings and data are stored in *HDF5* files. *HDF5*, or *Hierarchical Data Format 5* is a standard file format, controlled by the HDF Group [88]. It is ideally suited to use in experimental physics. *HDF5* files store numerical data efficiently in a binary format, but they contain sufficient metadata so that there is never any confusion about what the data type is. They can handle multi-dimensional arrays. The various data saved into the *HDF5* file can be placed in a tree format to keep it well organized.

One can easily see what data are in an *HDF5* file by using the *HDFView* [88] Java program. This program is also useful to edit settings files by deleting parts that you do not want, or to combine settings from two or more files. CsPyController does not have the capability to load partial settings, as CsLabViewController did, because this can be done using *HDFView* in a far more powerful and flexible way.

HDF5 files can be accessed from all major numerical analysis software (*Mathematica*, *Matlab*, *Python*), but one of the best ways to work with them is using the `h5py` package in Python because it allows *HDF5* data to be loaded as `numpy` arrays, and also it is extremely fast.

HDF5 files have internal paths to label the location of each dataset. The experiment settings, including every variable setting, instrument setting, and analysis setting, are stored. The settings are saved automatically into the results file at the start of each experiment, so that there is always a good record of what experiment was run. Any time the settings are saved, either automatically or manually, the default settings, stored in the `CsPyController/python` program directory, are updated.

Every time an experiment is run, a new directory is created, named with the timestamp of the start of the experiment and a user-defined suffix (`yyyy_mm_dd_hh_mm_ss_suffix`). This directory is placed inside a daily directory (created if it does not already exist). Within the *HDF5* file, data for each iteration is stored at `/iterations/0`, `iterations/1`, etc. Every iteration node then has a place for analyses (i.e. `/iterations/0/analysis`) such as loading data. The data for each measurement is then stored at `/iterations/0/measurements/0`, `/iterations/0/measurements/1`, etc. Within these nodes are contained all the raw and processed data for the experiment.

9.4.8 Variables

One of the strengths of this software package is the ability to work with variables in a flexible and powerful way. There are three places that variables can be specified: *Constants*, *Independent Variables*, and *Dependent Variables*. These variables are stored in a namespace that can be used in almost every other setting in the software.

Settings where variables can be used are called a `Prop` (short for *property*) in the code, and are defined by a *name*, *description*, *function*, and *value*. Some settings such as simple enable/disable, hardware clock-rates, etc., are not `Prop`s because it is never necessary for their values to be dynamic. The *function* is where the desired expression is entered. Any valid python syntax is allowed. The expression can reference any defined variable, and even any external package that was imported in the *Constants* and *Dependent Variables*. The entire namespace of `from numpy import *` is made available by default for convenience (so `sin`, `cos`, `pi` and many more are already imported). The value returned by evaluating the *function* must be of the correct type (i.e. `int`, `float`, `str`) for that `Prop`, otherwise an error will be returned. It is useful to keep the **command prompt** window visible to watch for errors, which are very descriptive and can be read to see what the settings error is. The offending `Prop` will also be highlighted in red.

Evaluation of the variables and `Prop`s occurs at the start of every *iteration*. Upon evaluation, the `Prop` values are updated. Evaluation of the `Prop`s can be forced from the main **command center** window menu under *Evaluation→Update variables throughout experiment*.

The order of evaluation is explained below.

9.4.8.1 Constants

Constants are executed first, and only once, at the beginning of the *experiment*. The *constants* are defined in a large multi-line text box on the *Constants and Dependents* page. The *constants* are defined using python code. This could be as simple as, for example:

```
a = 5
readout_time = 7
```

Or it can be more complex, involving function definitions, imports, and much more. The namespace of `from numpy import *` is available, as well as anything else the user chooses to import. The entire namespace that results from the execution of this code is preserved and available in the rest of the variable evaluation process.

9.4.8.2 Independent Variables

Independent Variables are evaluated second, once at the beginning of each *iteration*. The independent variables have a more structured entry format.

Each *independent variable* is defined by a function, which can use anything defined in the *constants* namespace. This function must evaluate to something that can be cast to a 1D *numpy array*. In other words, it must either be a scalar or a 1D list. Useful functions include: `linspace(a, b, n)` to make `n` evenly spaced points between `a` and `b` inclusive, and `arange(a, b, step)` to make points with spacing `step` from `a` to `b`. One could enter just a single value (i.e. `0.271`), or even a list of specific values (i.e. `[3, 0.2, 4.9, 5.0]`).

Every *iteration*, only one scalar value is used for each *independent variable*. The values are iterated through in a series of nested loops, with the inner-most loop being at the top of the list, and the outer-most loop at the bottom of the list. The number of iterations is defined by the product of the length of each *independent variable* evaluation. *Independent variables* of length 1 do not contribute to the number of *iterations*. There do not need to be any *independent variables*, but there is always at least 1 *iteration*.

After this evaluation, the *independent variable* names are in the variable namespace, and they have a single scalar value associated with them. For the purposes of later calculation, they are not lists or arrays, no matter how large a list or array was used to define them.

9.4.8.3 Dependent Variables

Dependent variables are executed third. The *dependent variables* are defined by a large multi-line text box, just like the *constants*. The difference is that *dependent variables* are evaluated at the start of each *iteration* but after the *independent variables*, so they can implement functions that rely on both *constants* and *independent variables*. The *dependent variables* then update as the *iterations* are stepped. Everything defined by the *constants*, *independent variables* and *dependent variables* is then stored in a namespace that is available to all later `Prop` function evaluations.

9.5 Optimization

The **optimizer** allows CsPyController to automate improvements to the experiment settings. The **optimizer** functions by running an **experiment** many times, and making changes to some or all of the **independent variables**, in a way that minimizes a **cost function**.

The need for multi-dimension optimization is demonstrated by Figure 9.6. This figure shows a contrived, but simple, example of an elliptical Gaussian cost function. Such a cost function might easily represent the coupling between the two horizontal knobs of a two-mirror beam alignment to a fiber. The challenge presented by such an alignment is that if only one adjustment is made at a time, we scan across the narrow ridge on axis 1 and find a position at the top of the ridge, but very far from the global maximum. Then we scan axis 2 and find that the position already found by scanning axis 1 is the best we can do. But that is because the direction in which adjustment actually needs to be made is not along either axis.

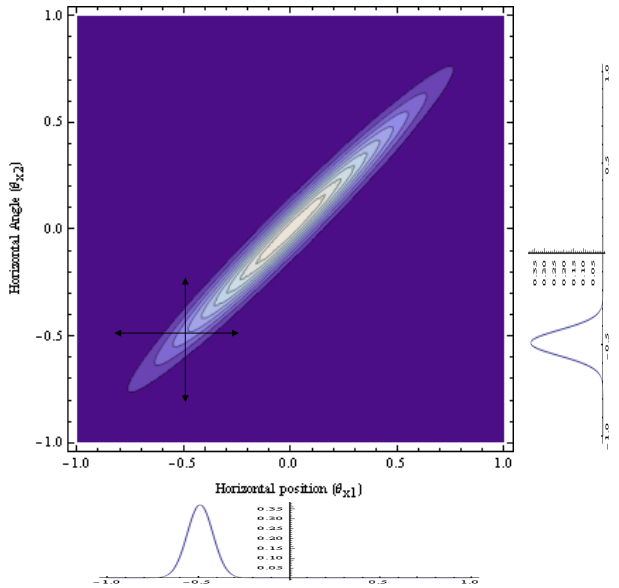


Figure 9.6: An elliptical Gaussian cost function with its principal axes at 45° to the axes of the experimental knobs. Making single axis scans will not reveal the global, or even local maximum.

One solution would be to perform a *brute force* search, by performing a raster scan of both variables as shown in Figure 9.7a. However, this is an extremely inefficient method. In this situation, the human experimentalist would instead *walk the mirrors*. In this process, as shown in Figure 9.7b, a move on axis 1 is made away from the local ridge, and then axis 2 is adjusted. By changing the axis 1 position many times, eventually the best position is found. While far better than brute force, this method is still very inefficient, as the moves are never being made straight toward the global maximum.

These problems are exacerbated when the space has many coupled variables. This is often the case in AMO experiments where alignment, frequencies, and pulse timing

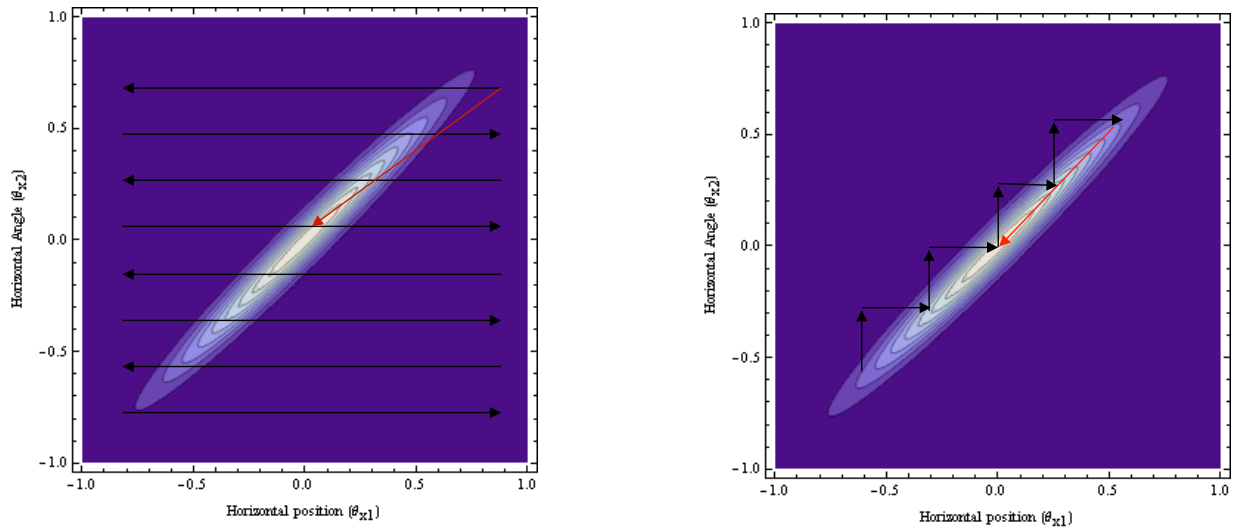


Figure 9.7: (a) A brute force 2D raster scan. (b) *Walking the mirrors* finds the maximum, but is not efficient.

all interact. A better solution is to use the computer to allow us to do multi-dimensional optimization. There are many algorithms for performing multi-dimension optimization, but most share the characteristic that they take some measurements to determine the landscape of the cost function, and then make a move on all axes at the same time.

Details of several optimization algorithms that were implemented as part of CsPyController are given here. Results of optimization experiments are given in Chapter 16. There are many more optimization methods possible than covered here, and recent efforts are taking excellent advantage of developments in artificial intelligence and machine learning (see e.g. Wigley et al. [89]).

9.5.1 Optimizer Methods

9.5.1.1 Gradient Descent

The *gradient descent* method is the most canonical multi-dimensional optimization method. The algorithm consists of the following steps to minimize a cost function:

1. Measure the cost function at the starting point.
2. Take n measurements at small displacements on each of n axes. Use this information to calculate the gradient.

3. Move down the slope in the direction of the fastest decreasing gradient.
    a) If this decreases the cost function, move twice as far.
        i. Repeat (a) until the cost function no longer decreases.
    b) If this increases the cost function, the step is too large. Move half as far.
        i. Repeat (b) until the cost function increases.
4. Repeat (2)-(4) until the step size decreases to the convergence limit.

The gradient descent method is a very powerful tool, with fast convergence. Once the gradient is found, the *line search* process takes the optimizer as far or as short as it can go in that direction, before the gradient needs to be re-evaluated.

The problem with using the gradient descent method is that it requires knowledge of the scale of the gradient. In a computer model, the gradient can be calculated over an arbitrarily small extent to find the local value. However, in a real system, there is noise, and if we measure over too small a distance, we will only see changes due to noise, and not due to the real sensitivities of the system. Because the noise level is unrelated to the distance over which the gradient is measured, a very small distance will give a false measurement of a huge gradient, due only to the noise. However, if we measure the gradient over too large a distance, we will miss the true dynamics of the system. Imagine for example testing a point on one side of a harmonic potential. We must be sure not to measure the gradient using a point on the other side of the potential, which could give entirely the wrong slope.

There are methods to dynamically adjust the scale over which the gradient is measured, but they perform poorly without some knowledge of the proper scale. Because of the complex nature of our experiment, we have often tried to use the optimizer in situations where we do not know the details of the dynamics. This is precisely why we are using the optimizer in the first place, in fact. As such, we have not found the gradient descent method to be the most useful algorithm.

9.5.1.2 Genetic Algorithm

A much more general optimization method is the *genetic algorithm*. This method is biologically inspired, and is meant to mimic the process by which evolution can improve the functionality of a species by repeated mutations. Helpful mutations survive and poor mutations do not survive. The procedure for this method is:

1. Test the cost function at the starting point.
2. Try a random motion.
3. If the change in (2) helps decrease the cost function, keep it. If not, throw it out.
4. Repeat (2)-(4).

Shown conceptually in Figure 9.8 the genetic algorithm is easy to use because it requires no knowledge of the system. In CsPyController we implement the random changes using a normal distribution, and allow the user to specify the width of the distribution on each axis. So in this case some knowledge of scale is helpful, but not required. However, the convergence of the genetic algorithm is simply too slow to be helpful at all. For example, if the cost function is linear and independent on each axis, then to make any progress at all, it is necessary to at least choose the correct sign on each axis. As the number of axes increases, this becomes more difficult as $1/2^n$. We often do 50 variable optimizations, giving the genetic algorithm a chance of improving only one in every $2^{50} \simeq 10^{15}$ tests. This is simply too slow to be useful.

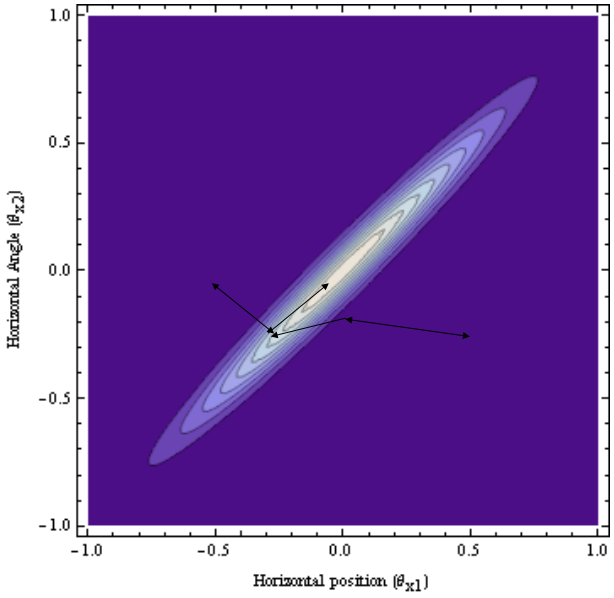


Figure 9.8: The genetic algorithm makes random motions, so it requires no knowledge of the cost function landscape. However, it will converge extremely slowly.

9.5.1.3 Nelder-Mead Simplex

The *Nelder-Mead* algorithm (Nelder and Mead [90]), also known as the *downhill simplex* method, is the optimization algorithm that we have found to be most useful in this research. The Nelder-Mead algorithm is "gradient free," in that it does not rely on measuring a gradient to determine which direction to move at every step. Instead, during an initialization period, it uses a similar process to construct a *simplex*, which is the simplest $n + 1$ sided polyhedron that rests comfortably in n dimensions, where we have n free variables that we are optimizing. In two dimensions, the simplex is a triangle. In three dimensions, the simplex is a tetrahedron. After the initial construction of the simplex, the next move is made by taking the worst of the $n + 1$ points and reflecting it in the remaining n points.

In two dimensions this appears as a triangle that continually flips and flops across the space toward the maximum, as shown in Figure 9.9.

The simplex algorithm benefits from some knowledge of the scale of the problem, to make useful step sizes. However, it does not require this knowledge, because the size and shape of the simplex is adjusted as the algorithm proceeds, growing in directions where more motion is helpful, and shrinking in directions where the scale is smaller. A poor choice of the size of the initial simplex will slow down the time to convergence, but not prevent it.

The full algorithm proceeds as follows:

1. Measure the cost function at $n + 1$ non-collinear points near the starting point. We take the starting point plus motions along each cardinal axis.

2. Order the points to find the worst point.

3. Calculate the centroid of the n points not including the worst one. Reflect the worst point across this point.

    a) If the new point is no longer the worst, but not the best, use it to replace the worst point.

    b) If the new point is the best, expand the simplex by going twice as far in that direction.

        i. If this expanded point is even better than the initial reflection, keep it.

        ii. If the expanded point is not any better than the reflection, use the reflection.

c) If the reflected point is still worse than all other points, try not crossing over the mean, but instead go halfway between the original worst point and the mean.

   i. If the contracted point is better than the original worst point, keep it.

d) If all the above tests fail, the contracted point is the worst of all points considered. So reduce the size of the whole simplex, bringing each point in halfway towards the best point.

4. Repeat step (2)-(4).

The Nelder-Mead algorithm is not the most efficient optimization algorithm available, but we have found for our work that it is the best combination of efficiency and ease-of-use, given the knowledge, and lack-thereof, we have about the space in which we are trying to optimize.

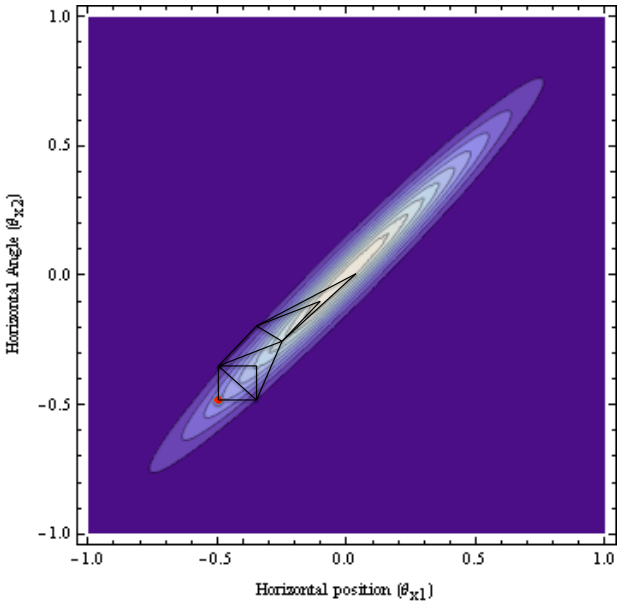


Figure 9.9: The progress of the Nelder-Mead algorithm can be visualized in 2D as a triangle flopping across the space. The triangle also expands and contracts to move more efficiently in the directions that improve the cost function.

9.5.1.4 Weighted Simplex

We designed a modification to the Nelder-Mead algorithm to try to achieve a further possible gain in convergence speed. In the canonical Nelder-Mead algorithm, the *centroid*

of the n best points is calculated, without regard to how good the cost function might be at those points. In the modification we call the *weighted simplex* algorithm, instead of the centroid we compute the center of mass of the n best points, with the mass weighting being the cost function at those points. (The absolute value of the cost function is used to account for the cost function being normally negative during a minimization.) This has the effect of steering the reflections in the direction of the better points, rather than simply away from the worst.

Convergence tests for the canonical Nelder-Mead and weighted simplex algorithms are shown in Figures 9.10 and 9.11. In these tests, the cost function is a simple Gaussian $-e^{-x^2-y^2}$, and the starting point for each is $x = -0.5$, $y = 0.5$. Unfortunately the weighted algorithm was observed to take about 40% longer to converge, and had more oscillation. It seems that the more aggressive action of the weighted algorithm leads to more overshoot. To use this modification, it may be necessary to tune decrease the parameters internal to the Nelder-Mead algorithm that control how far each reflection is taken, and effectively add more dampening to the algorithm.

In the experiments in Chapter 16 we have exclusively used the unweighted canonical Nelder-Mead algorithm.

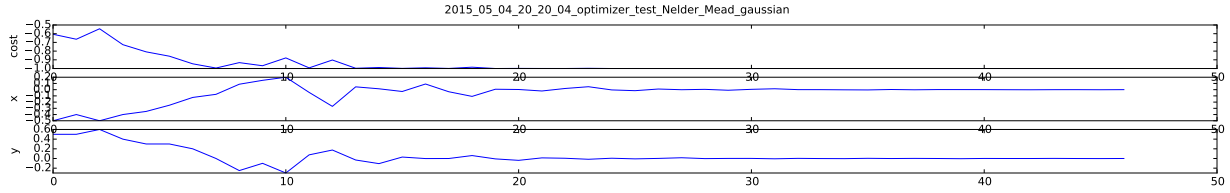


Figure 9.10: A convergence test for the canonical Nelder-Mead simplex algorithm.

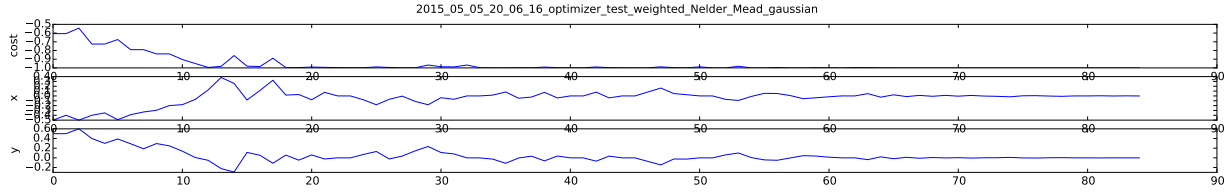


Figure 9.11: A convergence test for the weighted simplex modification to the Nelder-Mead algorithm.

9.5.2 Designing a Cost Function

Using the optimizer, we have learned that there is an art to designing an appropriate cost function. First, it is necessary to take care that while optimizing one aspect of the experiment, another is not sacrificed. One example of this is our initial attempts at loading optimization, in which we made the cost function the summed brightness of the first shot (the one that shows atom loading). One unfortunate result can be that the readout time is increased to the point that retention of the atoms in compromised. Because of this, even when optimizing loading, we will generally look to the second camera shot, to ensure that those atoms survive to throughout the experiment. Second, the relative weighting of different features in the cost function should usually be thought of in terms of their units. For example, when trying to increase loading and retention, but decrease readout time, it is generally not useful to design a cost function such as

```
-(loading + retention - readout_time)
```

While `loading` and `retention` have the same units (% atoms), `readout_time` has units of time. Some scaling could be applied between these functions, but the choice of scaling will always be arbitrary and in no way motivated by physics. Instead, it makes sense to construct the cost function as

```
-(loading+retention)/readout_time
```

In this way, the cost function has units of % atoms/time, which while not necessarily meaningful, can at least be treated consistently as a physics quantity, and it captures how the different quantities interact. Scalings may still be added to this form of cost function if desired.

9.5.3 Machine Learning as a Teacher

We have found that one of the most useful functions of the optimizer is that it teaches us about our experiment. For example, by watching the results of the optimizer, we have learned that our experiment is generally more sensitive to the vertical magnetic field shims than to any other. In this way the unknown dynamics of the system can be explored, this gives the optimizer utility as a physics tool, not just an engineering tool.

10 Analysis

The CsPyController program has a number of useful analyses implemented which have been extremely valuable for the AQuA program. Additionally, the program is designed to be easily extendable to further analyses as described in the *CsPyController Programmers' Manual*.

Here we describe some of the particular calculations, perhaps novel, which have been developed for use on the AQuA project.

10.1 Region of Interest Determination

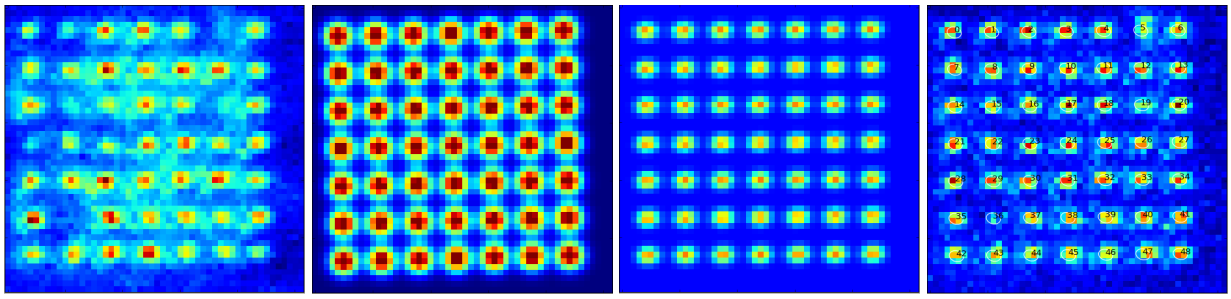
Prior atom trapping work in our lab has employed rectangular regions of interest (ROI) around each trapping site. For example, a 3-by-3 set of pixels was designated manually for each trapping site. This method is not only cumbersome but also does not maximize the signal-to-noise ratio. Each atom trapping site has a bright center where the atom is most likely to be found and decreases outward. The point spread function of the optics dominates over spreading due to atomic motion. The central pixel has the highest signal-to-noise ratio, while outer pixels have lower-signal-to-noise ratios.

Using only the central pixel is not the ideal solution because it throws away valuable information in the outer pixels. To use this information properly, all the pixels should be weighted according to their signal-to-noise ratio.

10.1.1 Grid of Gaussian Regions

We implement this method by fitting each atom trapping site to a 2D Gaussian. This Gaussian is then used as an ROI mask. Every incoming image is multiplied by this mask, and the result is summed to find the ROI value for that shot. This is performed 49 times, once for each different mask for the 49 ROIs.

Because finding these ROI masks for each trapping site would be cumbersome for our large array, we automate this task by fitting the entire grid to a grid of Gaussians. A guess is made by providing only the approximate upper-left and lower-right coordinates of the grid. Then the Gaussian grid is allowed to vary the grid angle, site spacing, Gaussian width in x and y, Gaussian rotation, background level, and Gaussian amplitude. Each Gaussian is restricted to have the same widths and amplitude. Results of this fitting routine are shown in Figure 10.1.



(a) (b) (c) (d)

Figure 10.1: Automatic fit of a Gaussian regions of interest to the atom trapping sites. (a) raw summation image (b) guess for grid of Gaussians (c) fit to grid of Gaussians (d) ROI numbers, and 1 sigma contours of the 2D Gaussian regions shown on top of atom data (cleaned up with ICA). Data from 2015-07-27.

10.1.2 Independent Component Analysis

A more sophisticated way to identify region of interest masks is to use *principle component analysis* or *independent component analysis*. These techniques are explored in Segal et al. [91].

Principle component analysis (PCA) is the process of taking a set of images, concatenating them into one array, and finding the eigenvalues and eigenvectors of the array. The eigenvectors are each of the same size as an image, and if visualized can show the various components that make up the set of images. Taking the eigenvectors with the 49 largest eigenvalues gives 49 sets of the most correlated pixels, which corresponds closely to the atom trapping sites.

PCA analysis is not sufficiently useful for identifying our ROIs, however. One issue is the PCA components are strictly orthogonal, such that they form a complete set that spans the space of images, and any image can be decomposed into a sum of PCA components. However, there is no reason to require that our ROIs be orthogonal. Secondly, our high loading rate means that sets of sites will often load together, and this leads to PCA components that contain strong signals from multiple sites. This problem is heralded by the fact that the largest PCA component in unreduced data is always the mean image. This is worked around by either skipping the first component or subtracting the mean from the data set beforehand. However, it is indicative that the PCA regions will not give exactly what we want for individual ROIs.

A better technique is independent component analysis (ICA). The ICA algorithm typically starts with PCA, but then uses a cost function to optimize the regions found to be as statistically independent as possible. To evaluate this, the contribution of each component

to each image is evaluated, and a histogram is made for each component. Typically the cost used is the kurtosis of the histogram, or 4th standardized moment, defined as:

$$\frac{E\left[(X-\mu)^4\right]}{\left(E\left[(X-\mu)^2\right]\right)^2} \tag{10.1}$$

where μ is the mean. This is one way to define how *non*-Gaussian a distribution is. By enhancing the kurtosis of each component as much as possible, the ICA algorithm leads to components that are as statistically independent as possible. This is exactly what we want for ROI identification. An example of 49 regions that were automatically identified using ICA, and then automatically sorted based on centroid position, is shown in Figure 10.2.

ICA has also proven to be a useful image filtering tool. It allows us to take a dataset of atom images, pull out the 49 most independent components, and composite those components to show the locations of the trapping sites without background noise. An example of this filtering is shown in Figure 10.3.

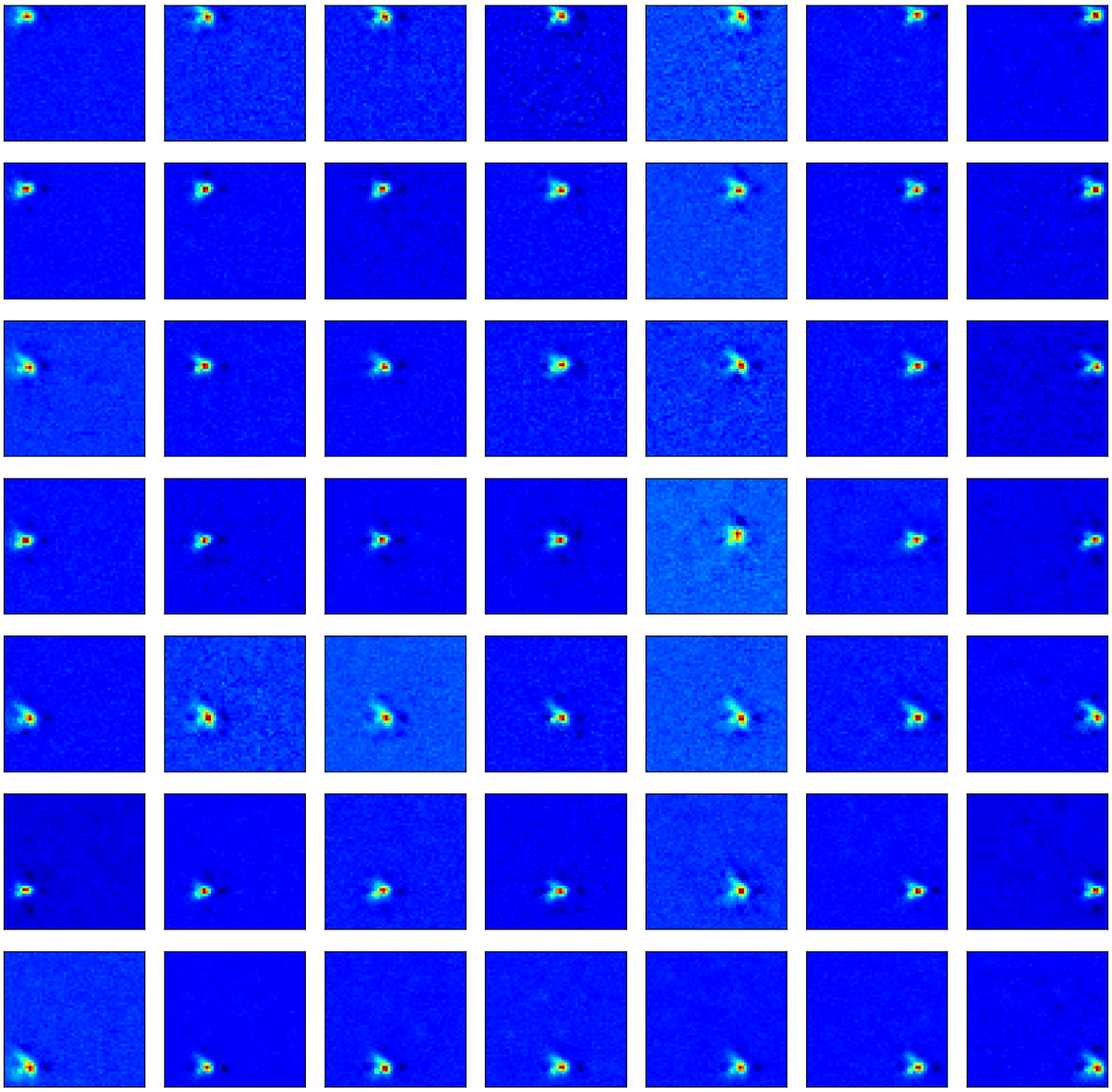
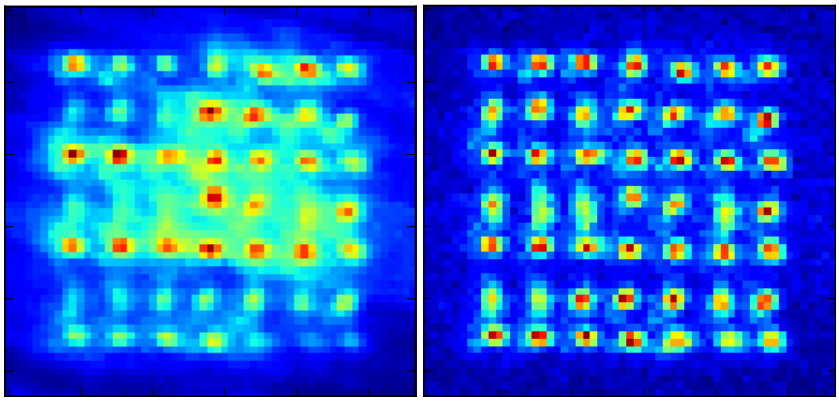


Figure 10.2: Independent component analysis is used to automatically separate the trapping site regions of interest for a 500 shot run of atom loading data. The sites are automatically sorted based on their centroid. The ROI images will be used as masks on each future image taken, to find the integrated brightness of each site. Data from 2015-02-26-10-42-33.



(a) (b)

Figure 10.3: Independent component analysis can be used as a filtering tool. By taking the 49 most statistically independent components from a data set and discarding the rest, we can create a composite image that highlights the regions of interest and eliminates background noise. Compare (a) raw image to (b) ICA filtered image. Data from 2014-10-13-06-41-09.

10.2 Analytical Threshold of Two Gaussians

To distinguish between one atom and two atoms, it is necessary to define a cutoff intensity between the two peaks. This threshold can be defined separately for each region of interest. Images with regions of interest with total brightness below the cutoff are tagged as 0 atoms, and those with higher brightness are tagged as 1 atom. Upper and lower cutoffs may also be used to exclude shots with 2 or more atoms, and optionally those with erroneously low brightness. Once the 0 and 1 atom peaks have been fit to Gaussians, the cutoff can either be found numerically or analytically.

An example of these cutoffs is shown as the vertical lines in histograms of our 49 site array in Figure 7.36.

To find the cutoff numerically, an algorithm can simply scan between the two peaks, with some arbitrary step size, looking for the location with the lowest sum.

The cutoff can also be found analytically, as follows. Let us say you have two Gaussians:

$$f_1 = a_1 e^{-2(x-x_1)^2/w_1^2} \qquad f_2 = a_2 e^{-2(x-x_2)^2/w_2^2} \tag{10.2}$$

We would like to find the point where they intersect:

$$a_1 e^{-2(x-x_1)^2/w_1^2} = a_2 e^{-2(x-x_2)^2/w_2^2} \tag{10.3}$$

This point may not be unique, we will show how to select the correct point below. First we solve this equation for x. To do so, start by taking the natural log of both sides:

$$\ln(a_1 e^{-2(x-x_1)^2/w_1^2}) = \ln(a_2 e^{-2(x-x_2)^2/w_2^2}) \tag{10.4}$$

$$\ln(a_1) + \ln(e^{-2(x-x_1)^2/w_1^2}) = \ln(a_2) + \ln(e^{-2(x-x_2)^2/w_2^2}) \tag{10.5}$$

$$\ln a_1 - 2(x-x_1)^2/w_1^2 = \ln a_2 - 2(x-x_2)^2/w_2^2 \tag{10.6}$$

$$\ln \frac{a_1}{a_2} = 2\left(\frac{(x-x_1)^2}{w_1^2} - \frac{(x-x_2)^2}{w_2^2}\right) \tag{10.7}$$

$$\frac{w_1^2 w_2^2}{2} \ln \frac{a_1}{a_2} = 2\left(w_2^2(x-x_1)^2 - w_1^2(x-x_2)^2\right) \tag{10.8}$$

$$\tag{10.9}$$

This can be rearranged into a quadratic equation:

$$0 = (w_2^2 - w_1^2)x^2 + 2(x_2 w_1^2 - x_1 w_2^2)x + \left(x_1^2 w_2^2 - x_2^2 w_1^2 - \frac{w_1^2 w_2^2}{2} \ln \frac{a_1}{a_2}\right) \tag{10.10}$$

If $w_2 = w_1$ then $a = (w_2^2 - w_1^2) = 0$. In this case using the quadratic formula would result in a divide by zero, but instead we may simplify to:

$$0 = 2(x_2 w^2 - x_1 w^2)x + \left(x_1^2 w^2 - x_2^2 w^2 - \frac{w^2 w^2}{2} \ln \frac{a_1}{a_2}\right) \tag{10.11}$$

$$0 = 2(x_2 - x_1)x + \left(x_1^2 - x_2^2 - \frac{w^2}{2} \ln \frac{a_1}{a_2}\right) \tag{10.12}$$

$$x = \frac{-x_1^2 + x_2^2 + \frac{w^2}{2} \ln \frac{a_1}{a_2}}{2(x_2 - x_1)} \tag{10.13}$$

In the case where $w_2 = w_1$ and $a_1 = a_2$ this reduces even further:

$$x = \frac{-x_1^2 + x_2^2}{2(x_2 - x_1)} x \qquad = \frac{(x_2 + x_1)(x_2 - x_1)}{2(x_2 - x_1)} x = \frac{(x_2 + x_1)}{2} \tag{10.14}$$

This is just the average of the two peaks, as expected.

Returning to the general case of $w_1 \neq w_2$ we can use the quadratic formula to solve for

x:

$$0 = (w_2^2 - w_1^2)x^2 + 2(x_2 w_1^2 - x_1 w_2^2)x + \left(x_1^2 w_2^2 - x_2^2 w_1^2 - \frac{w_1^2 w_2^2}{2} \ln \frac{a_1}{a_2}\right) \tag{10.15}$$

$$x = \frac{-2(x_2 w_1^2 - x_1 w_2^2) \pm \sqrt{(2(x_2 w_1^2 - x_1 w_2^2))^2 - 4(w_2^2 - w_1^2)\left(x_1^2 w_2^2 - x_2^2 w_1^2 - \frac{w_1^2 w_2^2}{2} \ln \frac{a_1}{a_2}\right)}}{2(w_2^2 - w_1^2)} \tag{10.16}$$

$$x = \frac{x_1 w_2^2 - x_2 w_1^2 \pm \sqrt{(x_2 w_1^2 - x_1 w_2^2)^2 - (w_2^2 - w_1^2)\left(x_1^2 w_2^2 - x_2^2 w_1^2 - \frac{w_1^2 w_2^2}{2} \ln \frac{a_1}{a_2}\right)}}{w_2^2 - w_1^2} \tag{10.17}$$

$$x = \frac{x_1 w_2^2 - x_2 w_1^2}{w_2^2 - w_1^2} \tag{10.18}$$

$$\pm \frac{\sqrt{(w_2^4 - w_2^4 + w_1^2 w_2^2)x_1^2 - 2w_1^2 w_2^2 x_1 x_2 + (w_1^4 + w_1^2 w_2^2 - w_1^4)x_2^2 + (w_2^2 - w_1^2)\left(\frac{w_1^2 w_2^2}{2} \ln \frac{a_1}{a_2}\right)}}{w_2^2 - w_1^2} \tag{10.19}$$

$$x = \frac{x_1 w_2^2 - x_2 w_1^2 \pm \sqrt{w_1^2 w_2^2 x_1^2 - 2w_1^2 w_2^2 x_1 x_2 + w_1^2 w_2^2 x_2^2 + (w_2^2 - w_1^2)\left(\frac{w_1^2 w_2^2}{2} \ln \frac{a_1}{a_2}\right)}}{w_2^2 - w_1^2} \tag{10.20}$$

$$x = \frac{x_1 w_2^2 - x_2 w_1^2 \pm w_1 w_2 \sqrt{(x_1 - x_2)^2 + \frac{1}{2}(w_2^2 - w_1^2) \ln \frac{a_1}{a_2}}}{w_2^2 - w_1^2} \tag{10.21}$$

We must determine which of the two roots to choose. To analyze this, without loss of generality let $x_2 > x_1$. These equations are linear under a uniform shift to both x_1 and x_2, so we can shift one of them to zero without loss of generality. Do this by taking $x_1 \to 0$ and $x_2 \to x_2 - x_1$

$$x = \frac{-(x_2 - x_1)w_1^2 \pm w_1 w_2 \sqrt{(x_1 - x_2)^2 + \frac{1}{2}(w_2^2 - w_1^2) \ln \frac{a_1}{a_2}}}{w_2^2 - w_1^2} \tag{10.22}$$

The desired solution is at $0 < x < x_2 - x_1$. We can see that if $w_2 > w_1$ then the *minus* solution has $x < 0$, and so is outside the desired bounds. The positive solution is therefore the correct choice when $w_2 > w_1$.

To analyze the case where $w_1 > w_2$, it is easier to shift again so $x_1 \to x_1 - x_2$ and $x_2 \to 0$.

The desired solution is now at $x_1 - x_2 < x < 0$.

$$x = \frac{(x_1 - x_2)w_2^2 \pm w_1 w_2 \sqrt{(x_1 - x_2)^2 + \frac{1}{2}(w_2^2 - w_1^2)\ln\frac{a_1}{a_2}}}{w_2^2 - w_1^2} \tag{10.23}$$

We can see that if $w_1 > w_2$ then the *minus* solution has $x > 0$, and so is outside the desired bounds. The positive solution is therefore also the correct choice when $w_1 > w_2$.

For our experiment analyses, the x values will in all cases have $x_1 < x_2$. So we want to always choose the positive solution, and the position of the crossover is given by:

$$x = \frac{x_1 w_2^2 - x_2 w_1^2 + w_1 w_2 \sqrt{(x_1 - x_2)^2 + \frac{1}{2}(w_2^2 - w_1^2)\ln\frac{a_1}{a_2}}}{w_2^2 - w_1^2} \tag{10.24}$$

10.3 Analytical Overlap of Two Gaussians

We define the quality of the readout by how well separated the zero and one atom peaks are in the histograms. In Figure 7.36 we can see that the sites are all well separated. We qualitatively measure this separation by a quantity we call *overlap*, defined as

$$\text{overlap} = \frac{\text{area of intersection of Gaussians}}{\text{area of union of Gaussians}} \tag{10.25}$$

An alternative to this metric is the T-test, which measures the separation divided by the peak width. However, we find that the *overlap* is a more useful metric for our system. When running an optimization on readout, we would like the readout time to be as long as necessary to fully separate the peaks, but no longer because it could increase atom loss. While the T-test would continue increasing as the separation increases, the *overlap* increases until the peaks are fully separated, dropping to zero, and then stays there for any larger amount of separation. This frees up the optimizer to prioritize other variables after this point, and does not make the readout needlessly long.

We calculate the *overlap* analytically. We use the erf error function to find the integrated

area under a Gaussian (the cumulative normal distribution function):

$$\text{overlap}_1 = \frac{1}{2}\left(1 + \text{erf}\left(\frac{x_1 - \text{cutoff}}{\sigma_1\sqrt{2}}\right)\right) \tag{10.26}$$

$$\text{overlap}_2 = \frac{1}{2}\left(1 + \text{erf}\left(\frac{\text{cutoff} - x_2}{\sigma_2\sqrt{2}}\right)\right) \tag{10.27}$$

$$\text{overlap} = \frac{a_1\text{overlap}_1 + a_2\text{overlap}_2}{\min(a_1, a_2)} \tag{10.28}$$

where x_1 and x_2 are the peak locations, σ_1 and σ_2 are the widths of the two Gaussians. a_1 and a_2 are the integrated areas of two Gaussians, where we typically normalize the equations so that the amplitude gives the integrated area. cutoff is the cutoff threshold between the two peaks, as found in the previous section.

10.4 Optimal Selection of Test Points

In most of our experiments we take data while varying some parameter, and fit the resulting data to some curve motivated by theory. For example, we might sweep a frequency and fit the resulting resonance peak to a Gaussian, Lorentzian or sinc function, depending on the specific situation. One very common situation is to observe the sinusoidal oscillation from a Rabi or Ramsey experiment. In most of our day-to-day operations, we already have a good guess for what the results will look like, and we need only to get the curve fit to fine tune an experimental parameter. For example the half-period of a Rabi oscillation can be used to tune our laser pulse length for a π pulse.

Typically this data is collected by taking m identical measurements at n distinct settings over some range. The values for m and n have typically been decided as a hunch, based on the prior experience of the user. This is an imprecise way to conduct experiments. It also leads to a great deal of wasted time because often a) the number of measurements taken is insufficient to yield statistically significant results, b) imprecise results lead to poor experiment settings being propagated forward, or c) more data is taken than necessary.

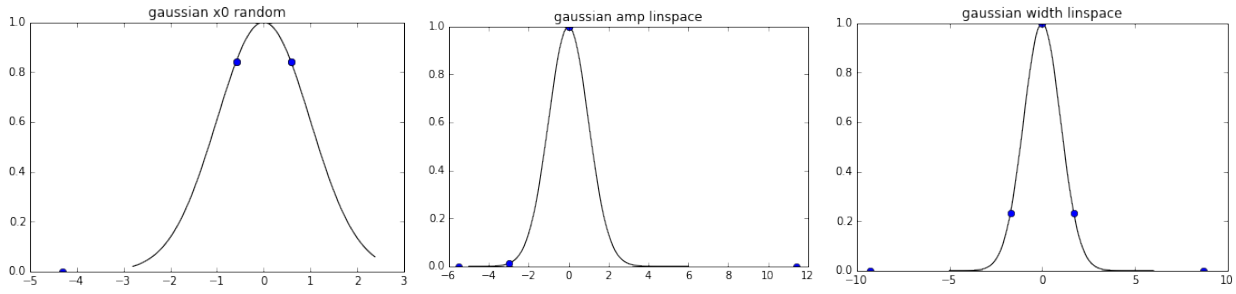
To address these concerns, we have developed software tools to guide the user to choosing the minimum values of m and n necessary. The figure of merit is the uncertainty of the curve fit. So we want the smallest values of m and n that will yield some desired level of uncertainty in the curve fit parameters. Typically this is not a unique solution, and so we can introduce the further constraint that we would like to reach this uncertainty level in the minimum time. Because changing to a new set of settings has a time cost associated

with it (typically 30 seconds for our apparatus), it is faster to take more measurements, rather than to extend to more iterations of settings. For n_0 free parameters we need to take data at least at n_0 different settings. This generally constrains the fit exactly, and so we need more than n_0 data-points if we are to evaluate a fit uncertainty.

A further consideration is exactly where should the data be taken? Typically users have done linear steps over the experimental range. However, this often not the most efficient strategy. For our experiment, almost all of our results come in the form of binomial data, where the presence or absence of an atom at the end of the experimental sequence is our signal. To form curves we repeat the experiment many times to get an average retention value p somewhere between 0 and 1. The variance in binomial data is $mp(1-p)$. Because of this, data that is always 0 or always 1 has a very low uncertainty. However, data near 0.5 has a large uncertainty. This in general makes taking data near the peaks and troughs of a curve more advantageous. However, there is an opposing cost to this, which is that because the peaks and troughs represent places where the curves are flat, the fit parameters have the lowest sensitivity to data taken at these points. For example, if one desires to determine the period of a cosine curve, the peaks and troughs do not constrain longitudinal shifts in the curve, while the highly sloped regions halfway in-between give very good constraints on the period.

The algorithms we have developed in Python take in a function that represents the presumed equation that the data will fit, the fit variable of concern (i.e. the one that we want to determine in this experiment), and a range over which data may be taken, an initial guess for the best n, and a required uncertainty level. The algorithm then proceeds as follows:

1. Make a linearly spaced guess for the n test points over the allowed range.
2. Optimize the location of the test points to minimize the uncertainty in the fit variable of concern. If more than one variable is given we sum the uncertainties in quadrature.
3. For the optimized test locations, determine how many measurements m must be taken to reach the uncertainty requirement.
4. Calculate the time for this experiment based on m, n and the known time-per-measurement and added-time-per-iteration.
5. Increase or decease n and repeat steps (1)-(5) to find a local minimum in the experimental time-to-reach-uncertainty-level.



(a) (b) (c)

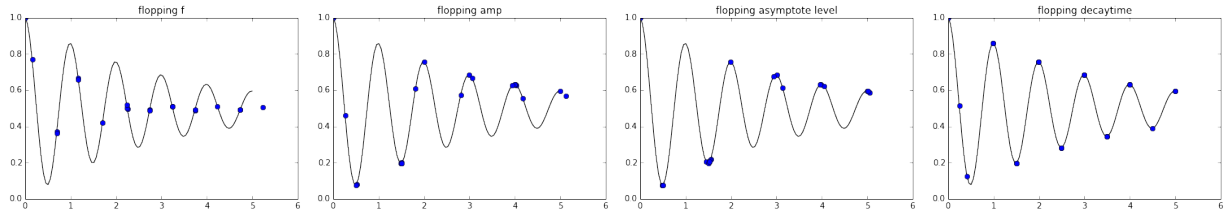
Figure 10.4: The suggested test points for the minimum uncertainty fit to Gaussian data. The optimal points vary depending on whether we want to minimize the uncertainty in (a) peak location (b) amplitude (c) width.

The results of this algorithm of course represent only a useful guide to how to set up the experiment, and do not predict with exactitude the uncertainty of the experiment. A lucky or unlucky streak of measurements can increase or decrease the actual fit uncertainty given by the experiment.

The optimal locations at which to take data are interesting and often surprising. Let us consider some illustrative examples.

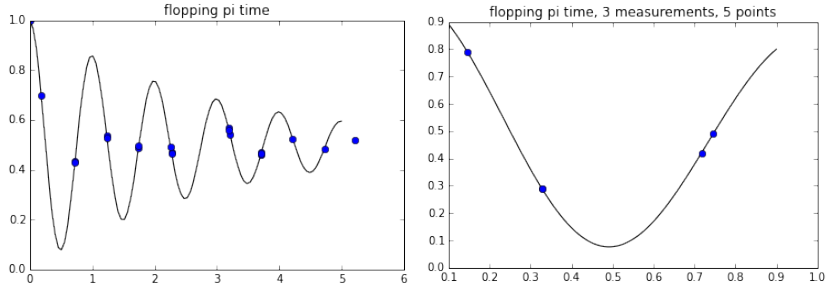
First, consider a Gaussian function of the form $y_0 + a * e^{-0.5(x-x_0)^2/w^2}$, where we wish to determine the location x_0 of the peak. As described above, the highest and lowest points give the best uncertainty, but the peak itself is too flat to be useful. The suggested points to test are shown in Figure 10.4a. The best places to sample depend on which fit parameter we are concerned with, however. As shown in Figure 10.4b, if we want to determine the amplitude of the Gaussian, then the peak and the base are the only points that we should concern ourselves with. It is interesting to contrast the optimal points for x_0, with the optimal points for the width, shown in Figure 10.4c. Both suggest points on the steep edge, but the width measurement is better taken lower down where the shape is wider.

A similar analysis yields interesting results for Rabi flopping data, which we fit to $y_\infty + a\cos\left(\pi + 2\pi f\left(t - t_\pi\right)\right)e^{-t/\tau}$, where y_∞ is asymptote level, a is the amplitude, f is the frequency, t_π is the half-period, and τ is the decay time constant. $a = 0.5$ and $y_\infty = 0.5$ represents a maximal contrast signal. Suggested locations for 20 points distributed over 5π are shown in Figure 10.5. It is interesting that the frequency fit suggests intermediate points, which converge to 0.5 as we move through the scan range. The amplitude, asymptote level, and decay time fits, all suggest testing points at the peaks and troughs, but the amplitude and decay time share the interesting feature of suggesting a point on the edge at $\pi/2$.



(a) (b) (c) (d)

Figure 10.5: The suggested test points for the minimum uncertainty fit to Rabi flopping data. The optimal points vary depending on whether we want to minimize the uncertainty in (a) frequency (b) amplitude (c) asymptote level (d) decay time.



(a) (b)

Figure 10.6: Optimal points for measuring the π time for Rabi flopping. (a) 20 points over 5π (b) 5 points over 2π.

The π time is the most interesting of these, shown in Figure 10.6a, as it suggests intermediate values that grow closer, but do not converge the way that the suggested frequency points do. Compare this also to Figure 10.6b, which shows suggested points for determining π time with 5 measurements over 2π. This is a very common measurement that we do. Note in particular that none of the suggested points are near the actual π time.

Part III

Experiment

11 Experimental Sequence

All of our experiments follow the same basic sequence with regards to atom loading and data acquisition. What varies from experiment to experiment is a short sequence in the middle where some specific operation is performed on the atoms. Here we detail the features of the sequence common to all the experiments.

11.1 Before Gate Operation

phase	duration [ms]	description
MOT Loading	480	The 3D MOT is loaded by D2 cooling light at -2.1Γ detuning. An atom beam pushed from the 2D MOT is on for the first 430 ms, after which it is shut to make sure the beam is not on when we later try to load the single atom traps. The trapping light is on for the first 435 ms, which will prevent atoms from collecting in the trap area, but is needed to maintain a steady state temperature for stable alignment in the trap array optics. The last 45 ms allows cold atoms to collect in the trap area.
Polarization Gradient Cooling in MOT	5	Atoms are cooled by D2 light at -8.3Γ detuning. The larger detuning allows us to reach colder temperatures, at the expense of MOT density, but a sufficient density has already been loaded during the previous phase. The single atom trapping light is still off during this time.
Trap Loading	1	$780\,$nm trapping light is turned on for the final 1 ms of PGC cooling. These single atom traps are superimposed on the MOT so that a small number of atoms are now confined in the trap array.
MOT Drop	68	Once the single atom traps are filled, the D2 light is turned off and the majority of the atom cloud is allowed to fall away.

phase	duration [ms]	description
Light Assisted Collisions	44	Because more than one atom may be in each trap array site to begin with, we use near-resonant D2 light to impart forces on the atoms to encourage collisions. If two atoms collide, there is a chance of a spin-flip that will release a $9.2\,\mathrm{GHz}$ photon and eject both atoms from the trap. An even number of atoms will pair-collide down to zero, while an odd number of atoms will pair-collide down to one. It is due to this phase of the experiment that we never see more than one atom in our traps.
Polarization Gradient Cooling in Traps 1	9	PGC cooling is repeated again, but at -11.9Γ to account for the Stark shift induced by the trapping light.
Loading Image Readout	30	The array is fluoresced with D2 light, and an image is acquired on the EMCCD camera. This first image, before the gate operation, gives information about which sites have loaded.
Polarization Gradient Cooling in Traps 2	9	PGC cooling is repeated once more at -11.9Γ to counter act any heating during the readout. A final temperature of 5 to 20 μK is reached, as measured by drop-and-recapture experiments.
Close D2 Shutters	11	Piezo shutters in the path of the 3D MOT beams are closed to ensure that no D2 light, which could decohere the qubit states, is present during the gate operations.
Optical Pumping	5	Atoms are pumped into $\|F = 4, m_F = 0\rangle$ using D1 light and repumper.

11.2 Gate Operation

The length of the gate operation varies, depending on the individual experiments, which will be detailed in Chapters 13, 14, 15, and 16. In general this experiment-specific portion of the experiment takes 1 to 10 ms.

11.3 After Gate Operation

phase	duration [ms]	description
Blowaway	0.2	Because the readout is done with repump light on to scatter enough photons, both $\|0\rangle$ and $\|1\rangle$ will fluoresce. Therefore most experiments use a blowaway of atoms in $\|1\rangle$ by a beam tuned to resonance with $F = 4$ before the readout, to allow us to distinguish between states. This step is skipped in some experiments that use atom loss as a signal (such as Rydberg spectroscopy and trap lifetime measurements).
Open D2 Shutters	11	The D2 shutters are reopened in preparation for readout.
Retention Image Readout	30	Another 30 ms camera exposure is taken while fluorescing the atoms with D2 light. A comparison of the first image, with this image, shows the changes due to the gate operation.
Laser Level Measurements	32	We turn off all the lasers, then cycle them on one-by-one, and observe the power incident on photodiodes. This allows the DC noise eaters to read the power levels on the 459 nm and 1038 nm lasers and adjust for fluctuations. Other laser levels are recorded by the ADC card, and checked against preset limits. Data is automatically discarded and an alarm sounded in case of laser failure.
Idle at MOT Settings	10	All lasers and magnetic fields are set back to MOT loading settings, so that the MOT can begin loading during the time between measurements. Our system begins taking new data immediately, while still analyzing the previous measurement, and so the gap time is only ~ 10ms.

11.4 Magnetic Fields

The magnetic fields for the 2D MOT coils are always on at a constant amperage. The magnetic fields for the 3D MOT coils are cycled through 6 phases during the experiment.

The anti-Helmholtz gradient coils produce 25.96 G/cm during MOT loading, and are off for the rest of the time. One set of Helmholtz coils (X1/4, along the Rydberg laser axis) are reserved as "bias" coils to create a well-defined magnetic field direction to remove degeneracy from the m_F Zeeman sub-levels. Those coils produce 1.31 G during the optical pumping and are off otherwise.

The remaining coils (vertical, X2/5 and X3/6) coils are used to zero the Earth's magnetic

field. We have optimized the field values in each experiment phase. The PGC shim field levels are used through both PGC and Trap Loading. The MOT Drop does not require specific shim settings so we switch to the values for Light-Assisted Collisions during this phase. Readout values are also used for PGC in Traps, and Blowaway.

Some variation in the optimized fields are expected, for the following reasons: The MOT Loading values are slightly different to pull the MOT cloud closer to the point of the 6-beam laser crossing, to increase loading. The PGC levels are expected to be the closest to perfect cancellation of Earth's field, to achieve the coldest temperatures. The values during light-assisted collisions have optimized to purposefully unbalanced levels to induce forces on the atoms. The readout levels need to zero the field at the trap array, which is not perfectly centered on the 6-beam crossing point. The optical pumping values are optimized to align the magnetic field with the polarization vector of the optical pumping beam. The gate values, which are matched to the optical pumping values here, can in practice vary if the Rydberg beam propagation direction is not well-aligned with the optical pumping polarization vector. Values for the shim magnetic fields, and their vector sum, are given in Table 11.1.

	MOT loading	PGC	light-assisted collisions	readout	optical pumping	gate
bias (X1/4)	0.00	0.00	0.00	0.00	1.31	1.31
vertical shim	-0.46	-0.38	-0.02	-0.47	-0.49	-0.49
horizontal shim (X2/5)	-0.44	-0.51	0.01	-0.27	-0.02	-0.02
horizontal shim (X3/6)	0.25	0.63	-0.02	0.27	-0.01	-0.01
shim vector sum	0.64	0.80	0.03	0.58	0.49	0.49

Table 11.1: Magnetic field shim values for various experiment phases, in gauss. The vector sums do not include the bias field.

12 Catalysis Loading

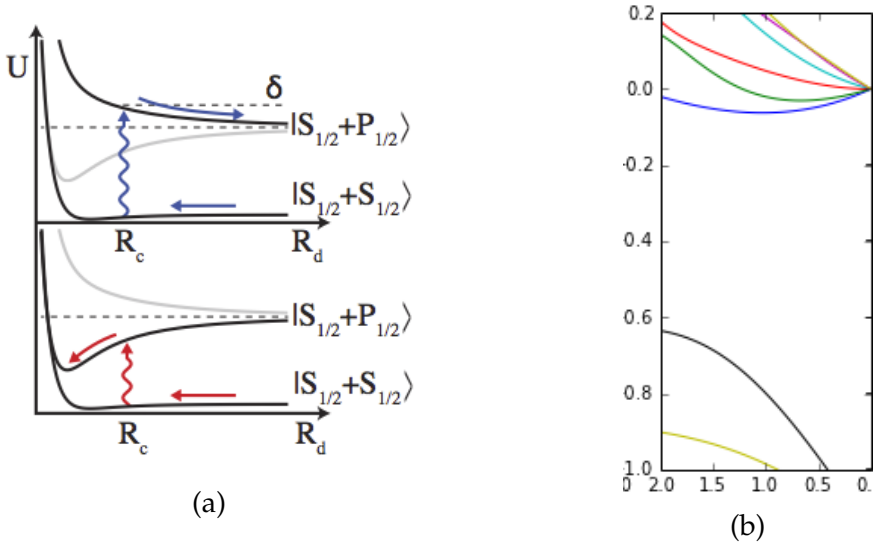
As discussed in Chapter 7, we have achieved array averaged loading results of 60.9%. Optimization of this result via the MOT and timing parameters will be discussed in Chapter 16, whereas here we will discuss attempts to improve this result by modifying the atom collision kinematics. Our loading results are sub-Poissonian, as we do not observe 2 atom events. Our small traps give a high likelihood that if multiple atoms are present in the traps, they will undergo collisions. When two atoms collide in the traps there is a chance of a spin-flip, which will release $h{\cdot}9.2$ GHz of energy, which is much larger than our trap depth, thereby kicking both atoms out of the trap. Without deeper analysis, one would expect to start with even or odd numbers of atoms with equal probability. An even number will pair collide down to zero, while an odd number will pair collide down to one, leaving a 50% overall loading rate. The fact that we see a better loading rate than this was serendipitous.

We employ light-assisted collisions, in the form of D2 light near the readout parameters, to encourage collisions further, and ensure that there is never more than 1 atom remaining in a trap.

One can, however, use light-assisted collisions to enhance the loading rate even further. The theory behind this technique has been developed by Walker and Pritchard [92] and Lett et al. [93]. Experimentally, Grunzweig et al. [94] demonstrated 82.7% loading, and Carpentier et al. [95] improved that to 91% loading. However, more analogous to our experiment are results in the *tight micro-trap regime*, which encourages collisions and generally prevents more than 1 atom from remaining in the trap. In this regime Fung and Andersen [96] achieved 80% loading, and Lester et al. [97] achieved 90% loading in a 2×2 array of red detuned traps. These results are all either in ^{85}Rb and ^{87}Rb.

The general process behind this technique is shown in 12.1a. During a collision, two atoms approach in the molecular ground state $\left|S_{1/2} + S_{1/2}\right\rangle$. A *catalysis* beam can be used to excite one atom, putting the two atom system into a $\left|S_{1/2} + P_j\right\rangle$ excited state. Both attractive and repulsive potentials exist for the excited two atom system, which merge as the distances goes to infinity and the interaction between the atoms vanishes. A red detuned catalysis beam will preferentially excite attractive potentials, where the atoms will continue to accelerate as they approach, usually adding sufficient energy to eject both atoms from the traps. A blue detuned catalysis beam will preferentially excite the atoms to repulsive potentials, and the energy added to the system as the atoms separate will be equal to the detuning (in units of h). The detuning can be adjusted to be equal to one trap

depth and thereby eject only one atom from the trap. It is assumed that after excitation, atoms will continue adiabatically along these potentials.



(a) (b)

Figure 12.1: (a) As two atoms approach during a collision, a catalysis beam can be used to excite one atom. Red detuned light (bottom) will excite the atom to an attractive potential, usually adding sufficient energy to eject both atoms from the traps. Blue detuned light (top) will excite the atoms to repulsive potentials, and the energy added will be equal to the detuning (units of h). The detuning can be adjusted to be equal to one trap depth and eject only one atom from the trap. Figure from Lester et al. [97]. (b) Molecular potential curves of ^{133}Cs (see Figure 12.3 caption for axes and units). Shown here zoomed in on large inter-atomic distance for the 3g molecular state. Note how some potentials that are repulsive at small-interatomic spacing become attractive as the atoms separate. This detail due to hyperfine structure complicates the dynamics of trap-loss and catalysis loading.

12.1 Calculation of Molecular Potentials

To asses whether or not it might be possible to improve the loading rate in ^{133}Cs by these techniques we have done detailed simulations of the 2 atom molecular potentials. We do so taking into account hyperfine effects following the method of Walker and Pritchard [92]. For these simulations we consider all possible angular momentum combinations for collisions of one atom in $6s_{1/2}$ and the other in $6p_{1/2}$. We evaluate the potentials for these $\left|6s_{1/2}+6p_{1/2}\right\rangle$ molecular states over a range of distances where the dipole-dipole interaction between the atoms is much weaker than the spin-orbit interaction within each atom, out to infinity where the potentials are simply those of two free atoms. The dipole-

dipole interaction for the ground state has no first order effect and so those potentials are flat at the distances simulated here. We consider only $6p_{1/2}$ and not $6p_{3/2}$ because we will be using the D1 light (from the optical pumping laser) for catalysis loading experiments, while the D2 lasers are simultaneously used to cool the atoms back into the traps.

The Hamiltonian of the system is [92]

$$H = H_1\left(\vec{r}_1\right) + H_2\left(\vec{r}_2\right) + V_{DD}\left(\vec{r}_1, \vec{r}_2, \vec{R}\right) \tag{12.1}$$

where H_1 and H_2 are the Hamiltonians of the individual atoms, $\vec{r}_1$ and $\vec{r}_2$ denote the position of the electron in each atom (hence the excitation state), and

$$V_{DD} = -e^2\left(2z_1z_2 - x_1x_2 - y_1y_2\right)/R^3 \tag{12.2}$$

is the dipole-dipole interaction between the two atoms with separation $\vec{R}$. The free atom Hamiltonians are diagonal matrices with the entries filled by the published [72] relative energies of the transition to each state under consideration, taking into account fine and hyperfine structure. The states can be labeled as

$$\left|\phi^{\pm}GJFm_F\right\rangle = \left(\left|Gm_G; JFm_F\right\rangle \pm \left|JFm_F; Gm_G\right\rangle\right)/\sqrt{2} \tag{12.3}$$

where F and m_F denote the sub-levels of the atom in $6s_{1/2}$, G and m_G denote the sub-levels of the atom in $6p_{1/2}$, $\phi = m_F + m_G$, and $\pm$ denotes symmetric and antisymmetric two atom states. The dipole-dipole matrix elements are given by [92]

$$\begin{aligned}
&\left\langle \phi^{\pm}G'JF'm'_F\right| V_{DD}\left|\phi^{\pm}GJFm_F\right\rangle \\
&= \pm\frac{C_3}{R^3}\left(-1\right)^{2I+G+G'+F+F'+m_F+m'_F}\left(J+\frac{1}{2}\right) \\
&\sqrt{\left(2G+1\right)\left(2G'+1\right)\left(2F+1\right)\left(2F'+1\right)}\begin{Bmatrix} F' & 1 & G \\ 1/2 & I & J \end{Bmatrix}\begin{Bmatrix} F & 1 & G' \\ 1/2 & I & J \end{Bmatrix} \\
&\times\left[2\begin{pmatrix} F' & G & 1 \\ -m'_F & \phi - m_F & 0 \end{pmatrix}\begin{pmatrix} F & G' & 1 \\ -m_F & \phi - m'_F & 0 \end{pmatrix}\right. \\
&\qquad -\begin{pmatrix} F' & G & 1 \\ -m'_F & \phi - m_F & 1 \end{pmatrix}\begin{pmatrix} F & G' & 1 \\ -m_F & \phi - m'_F & 1 \end{pmatrix} \\
&\qquad \left. -\begin{pmatrix} F' & G & 1 \\ -m'_F & \phi - m_F & -1 \end{pmatrix}\begin{pmatrix} F & G' & 1 \\ -m_F & \phi - m'_F & -1 \end{pmatrix}\right]
\end{aligned} \tag{12.4}$$

where the $C_3 = \frac{e^2\langle 3/2\|r\|1/2\rangle^2}{2R^3}$ is defined in terms of the reduced matrix element, $\begin{pmatrix} \square & \square & \square \\ \square & \square & \square \end{pmatrix}$ is the Wigner-3j symbol and $\begin{Bmatrix} \square & \square & \square \\ \square & \square & \square \end{Bmatrix}$ is the Wigner-6j symbol.

We solve this system numerically in Python. First we iterate over inter-atomic distances in units of $\frac{C_3}{R^3}$ and evaluate H at every distance. We then solve for the eigenvalues of H to find the potential for each state at this given distance. Ordering the eigenvalues allows us to plot continuous potential curves.

The results of these calculations are shown in Figure 12.3. As described above, we see that blue detuning from the excited state will tend to transfer population to repulsive potentials, while red detuning will tend to transfer population to attractive potentials. Closer inspection of the potentials reveals detailed structure that complicates this picture. For example in Figure 12.1b which shows a zoomed view at large inter-atomic spacing of the potentials for $\phi = 3$ symmetric states, we see potentials that are repulsive at small distances and attractive at large distances, due to avoided crossings. Conversely, in other states there exist potentials which are attractive at small distances and repulsive at large distances.

12.2 Detuning Scan

The calculation of these molecular potentials shows that repulsive potentials exist and that catalysis loading will be possible. It also reveals that the hyperfine effects complicate the prediction of the best detuning to use for this procedure. We have made some very preliminary attempts at implementing catalysis loading. In these experiments, we use the D1 optical pumping laser during the light-assisted collisions phase, and we eliminate the MOT drop phase to ensure that we will begin the catalysis loading with the possibility of multiple atoms. The laser intensity used at the atoms is 0.34 I_{sat}. This is, however, very low compared to that reported by Lester et al. [97], because this laser was set up for optical pumping, and upgrades will be required before more D1 light is available at the atoms.

In our exploration of the catalysis effect, the detuning of the D1 light was scanned from -50 to $+50$ MHz. The results are shown in Figure 12.2. The desired increase in loading rate was not seen. However, we did find a very sharp feature where the loading was decreased, and even went to zero on some sites. This dip is at -6.8 MHz red detuning from the $\left|6s_{1/2}, F = 4\right\rangle \leftrightarrow \left|6p_{1/2}, F = 4\right\rangle$ transition, accounting for ac Stark shift from the traps, and so it is not a resonant blowaway effect. It is notable that the feature creates 100% loss on

some sites and no loss on other sites. On all sites where the feature is visible it occurs at the same detuning. We believe this feature is a trap-loss catalysis effect, but the subject requires further investigation to increase our understanding.

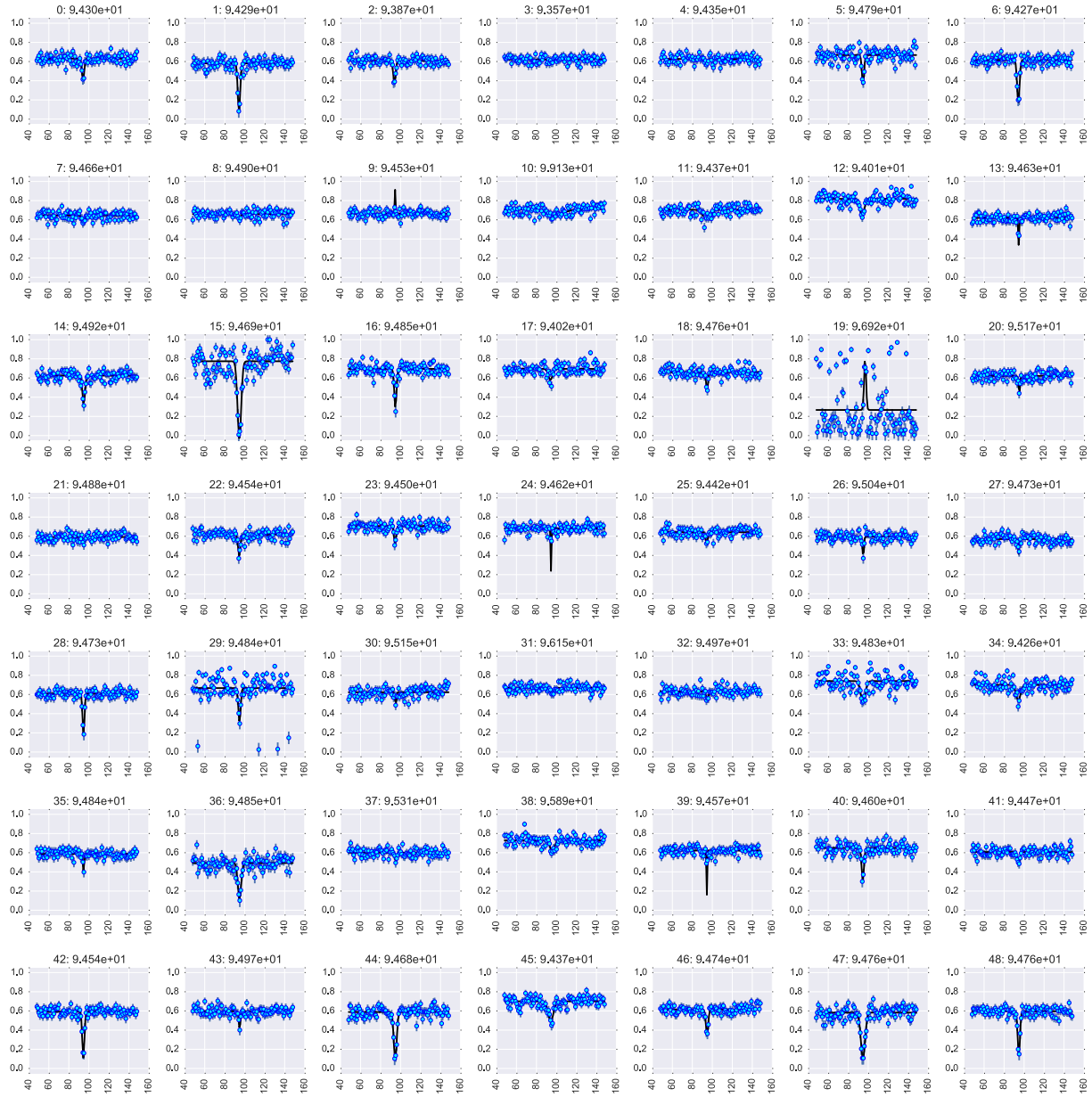


Figure 12.2: Detuning scan of the D1 catalysis beam. Loading rate is shown versus detuning in MHz for each site. The expected increase in loading rate was not seen. However a narrow resonance causing a sharp drop in loading rate is present at -6.8 MHz red detuning from the $\left|6s_{1/2}, F = 4\right\rangle \leftrightarrow \left|6p_{1/2}, F = 4\right\rangle$ transition. Array averaged dip location 94.62 ± 0.08 MHz. Data from 2015-08-08-10-46-26.

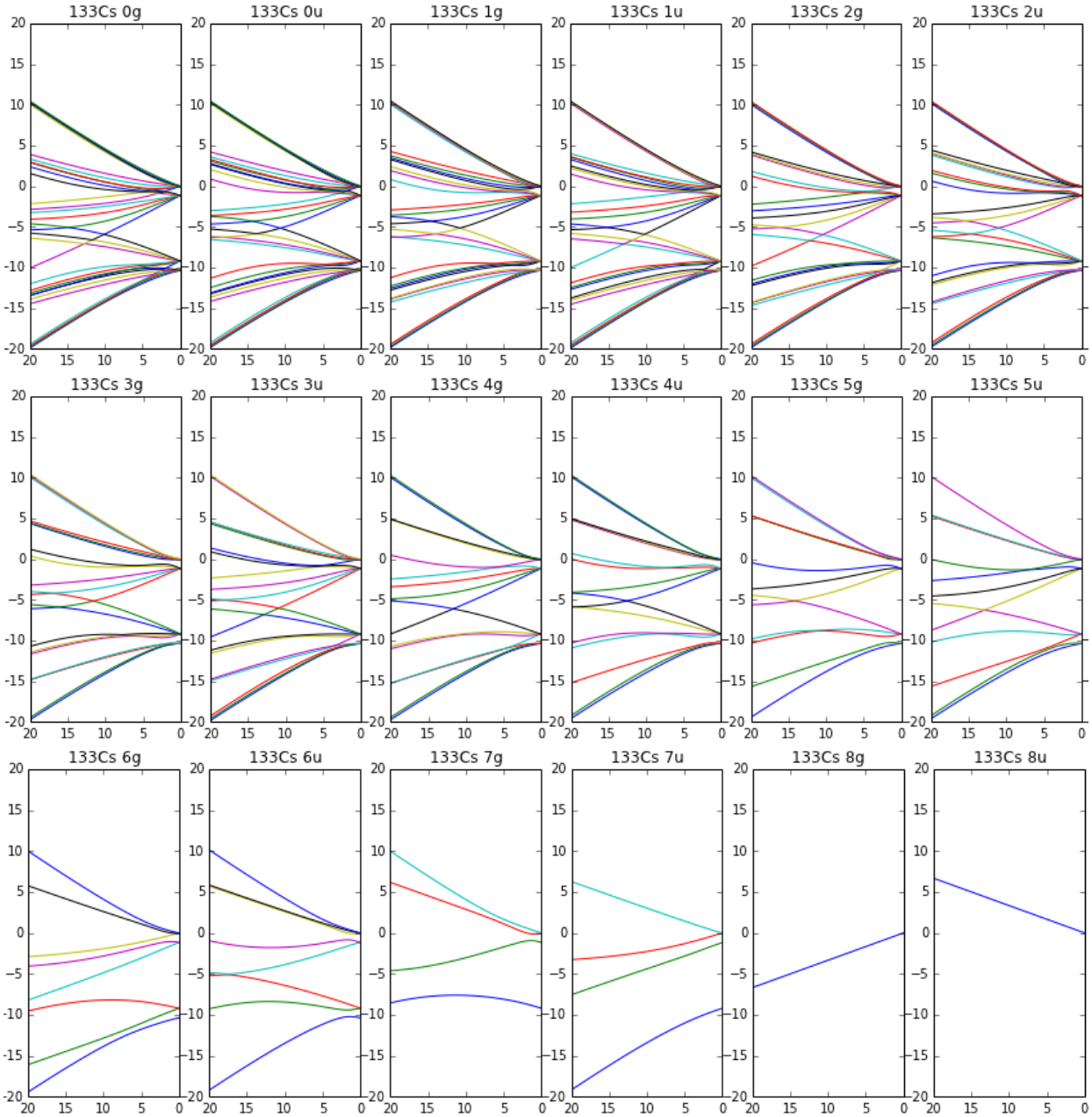


Figure 12.3: Molecular potential curves of ^{133}Cs for $\left|6s_{1/2}+6p_{1/2}\right\rangle$ excited states. The x-axis denotes inter-atomic spacing in units of C_3/R^3, with infinite inter-atomic distance on the right. The y-axis denotes energy in units of h·GHz relative to the $\left|6s_{1/2}, F=4\right\rangle$ and $\left|6p_{1/2}, F=4\right\rangle$ hyperfine levels in free atoms. Subfigure titles give $\phi = m_F + m_G$ and g for symmetric and u for anti-symmetric states. States with $\phi < 0$ have been omitted because their potentials are identical to those shown.

13 Single Qubit Operations

In this chapter we present demonstrations of single qubit operations in our 49 atom array. We have performed these operations both globally (the same operation on every site), and on single sites using site-specific addressing.

13.1 Optical Pumping and Depumping

The first step in performing any quantum computation is to prepare the qubits into a known state. We do this by optically pumping into the logical $|1\rangle$, $\left|6s_{1/2}, F = 4, m_F = 0\right\rangle$ state as described in Section 8.2.4. During this operation, the $|F = 4, m_F = 0\rangle$ state is dark to the optical pumping laser, while the repump laser ensures that we always bring any atoms that have decayed into $F = 3$ back into the $F = 4$ manifold. A scan of the optical pumping time can be fit to the equation:

$$\text{retention} * (1 - e^{-t/\tau}) \tag{13.1}$$

where τ represents the $1/e$ time constant for population transfer into $|F = 4, m_F = 0\rangle$. After optical pumping we can then perform a *depumping* operation, which is identical to the optical pumping operation, but with the repumper off. Because of the imperfect setup of the optical pumping, the depumping operation slowly moves population out of $|F = 4, m_F = 0\rangle$. It will eventually decay to the $F = 3$ manifold, but without the repumper it stays there and cannot be restored to $F = 4$. If the optical pumping is set up well, with the magnetic bias field well parallel to the polarization vector of the optical pumping light, then the depumping operation will take a long time. A depumping time scan can be fit to find the $1/e$ time in the same way as an optical pumping time scan. In particular, we would like the ratio $\frac{\text{depumping time}}{\text{optical pumping time}}$ to be large. We find that a ratio of at least 40 is necessary for good performance. We have seen ratios as high as 100 by optimizing for specific sites in the array, although the array averaged performance is lower. The actual optical pumping used in the experiments is significantly longer than the $1/e$ optical pumping time constant, and our observed state preparation fidelity exceeds 99%, indicating that this is sufficient.

In Figure 13.1a we show an optical pumping time scan, averaged across the array, and in Figure 13.1b we show the corresponding depumping time scan. In this data, you can see that the array averaged ratio is only 10. However, in Figures 13.1c and 13.1d, we show data for only one particular site (in this case site 17) and we see the requisite time ratio of 40

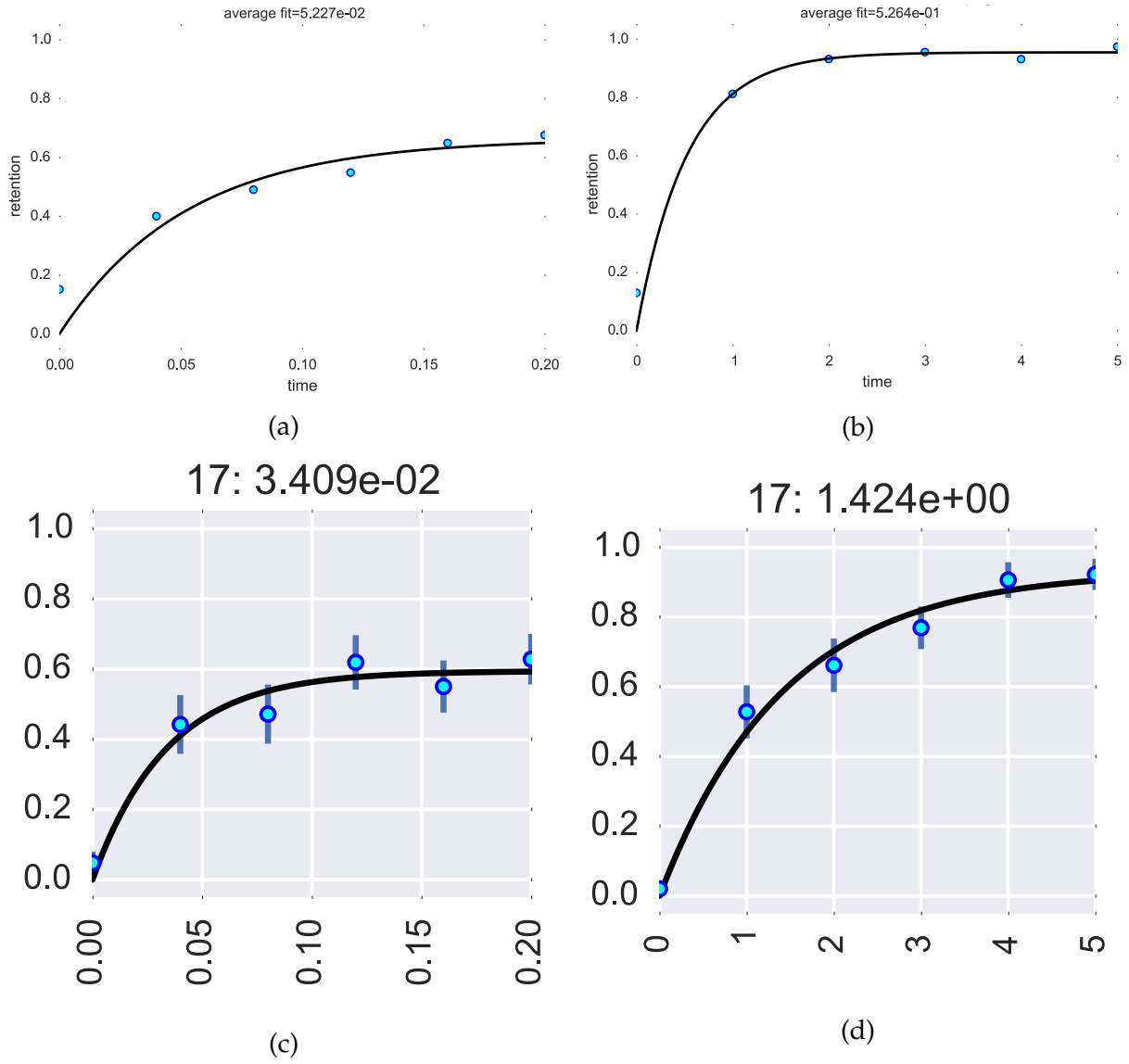


Figure 13.1: Scans of optical pumping time (a,c) and depumping time (b,c) shown as an array average (a,b) and for one particular site with above average performance (c,d). Data from 2015-04-30-10-29-00 and 2015-04-30-11-04-39.

is exceeded. For much of our work we focus on achieving results in particular sites, and select the sites that are performing better. In Section 16.4 we discuss the optimization of optical pumping to improve values across the entire array.

13.2 Microwave Rabi Flopping Experiments

By optically pumping the atoms into one state and then irradiating the array with microwave energy that is resonant with the $9.192\,631\,770\,\mathrm{GHz}$ qubit transition frequency, we can perform a Rabi experiment where the population will "flop" back and forth between $|1\rangle$ and $|0\rangle$. The effective Rabi frequency is

$$\Omega_1 = \sqrt{\Omega^2 + \delta^2} \tag{13.2}$$

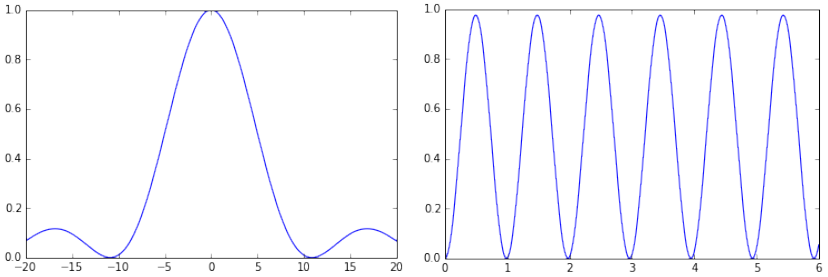
where Ω is the on-resonance flopping frequency and δ is the detuning from resonance. If we express the initial state in vector form as $\begin{bmatrix} 0 \\ 1 \end{bmatrix}$ then the state transforms in time according to the unitary operator [98]

$$\begin{bmatrix} e^{i\delta t/2}\left(\cos\left(\Omega_1\frac{t}{2}\right) - i\frac{\delta}{\Omega_1}\sin\left(\Omega_1\frac{t}{2}\right)\right) & ie^{i\delta t/2}\left(\frac{\Omega^*}{\Omega_1}\sin\left(\Omega_1\frac{t}{2}\right)\right) \\ ie^{-i\delta t/2}\left(\frac{\Omega}{\Omega_1}\sin\left(\Omega_1\frac{t}{2}\right)\right) & e^{-i\delta t/2}\left(\cos\left(\Omega_1\frac{t}{2}\right) + i\frac{\delta}{\Omega_1}\sin\left(\Omega_1\frac{t}{2}\right)\right) \end{bmatrix} \tag{13.3}$$

We can scan the length of the microwave pulse, followed by a state-selective blowaway, to get sinusoidal flopping as simulated in Figure 13.2b. We identify the 2π time as the time for one complete oscillation of this retention, and the more useful π time as the time between peak and trough where $\Omega_1 t_\pi = \pi$. If we hold the time fixed at t_π and scan the microwave frequency, we get a sinc function with a peak at the resonance, as simulated in Figure 13.2a. The frequency and amplitude of the Rabi flopping will change if the microwaves are off resonance. However, while the height of the spectroscopy peak will suffer if the time is not exactly t_π, the position of the peak is still exactly at the resonance frequency. For this reason, when using these two measurements, microwave spectroscopy and microwave Rabi flopping, to tune the microwave interactions, it is imperative to always perform the spectroscopy operation first.

13.2.1 Global Operations

We can perform these operations globally on all sites at the same time. In fact, this is the simplest scenario, because the wavelength of the microwaves is larger than our array. A typical microwave spectroscopy is shown in Figure 13.3 and a typical microwave flopping is shown in Figure 13.4 for all sites. We find from spectroscopy that our qubit frequency in the traps is detuned by $\sim\ 40$ Hz from the exact cesium clock frequency. In Figure 13.5 we



(a) (b)

Figure 13.2: Simulation of (a) Rabi spectroscopy (population vs. detuning, arbitrary units) and (b) Rabi flopping (population vs. time, arbitrary units).

show the entire array coherently flopping out to 10π.



Figure 13.3: Microwave spectroscopy globally on all sites at the same time. Frequency is expressed as MHz change from resonance. Number above each site is the fitted frequency shift in MHz relative to the previous tuning point. Array averaged $-5.8(4) \times 10^{-4}$ MHz. Data from 2015-04-23-08-00-03 and 2015˙04˙23˙08˙38˙48.

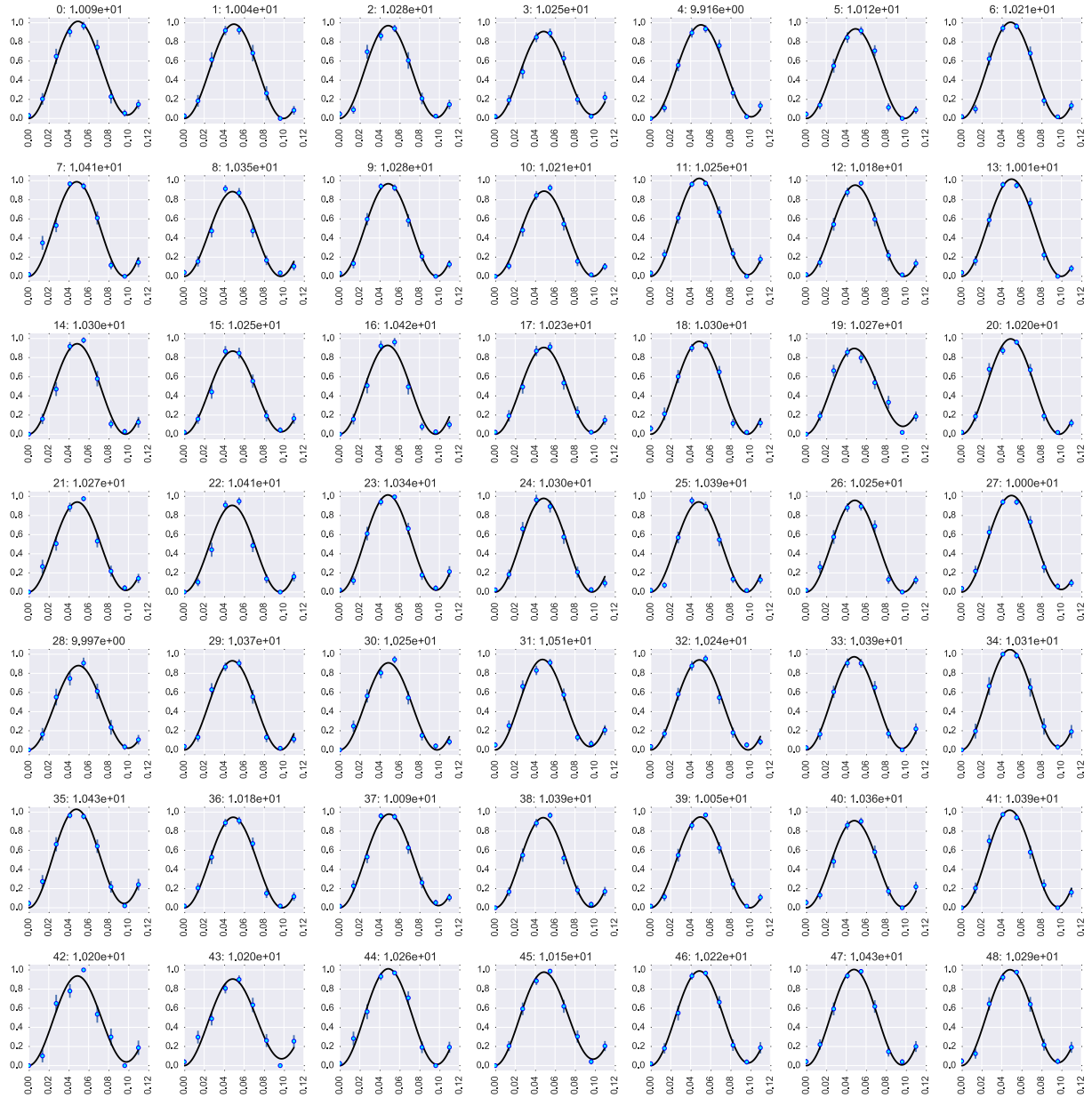


Figure 13.4: Microwave Rabi flopping, shown here to just past 2π. Number above each site is the fitted flopping frequency in MHz. Array average $10.25(3)$ MHz. Data from 2015-04-23-09-50-50.

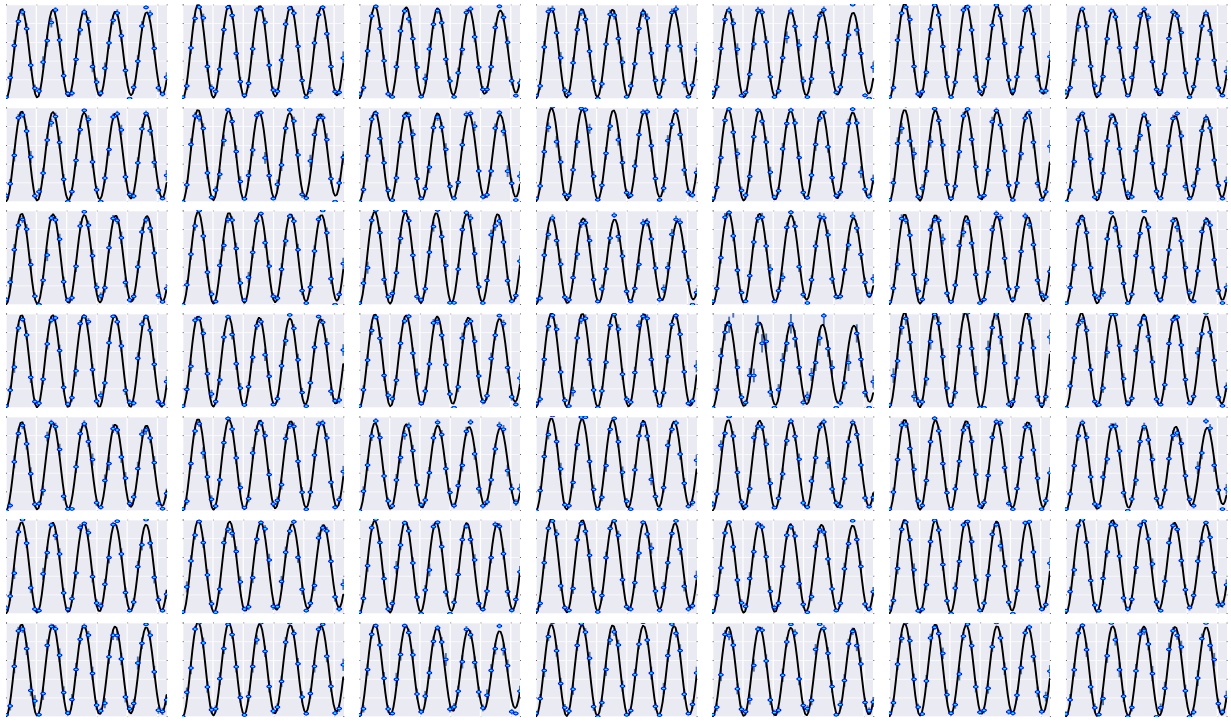


Figure 13.5: Microwave Rabi flopping, globally on the whole array, out to 10π. Data from 2015-02-26-11-35-15.

13.3 Site-selective Operations

For universal quantum computing, it is of course insufficient to perform only global operations, as we need to be able to freely manipulate individual qubits. We can perform ground state rotations and Rabi flopping on individual sites by using a $459\,$nm laser beam focused on a single atom to Stark shift the microwaves either into or out of resonance. The technique is described in Section 8.6 and Xia et al. [80]. We can either tune the microwaves to resonance and use the Stark laser to "shift-out" for a single site, or detune the microwaves and use the Stark laser to "shift-in" for a single site. The shift-out technique is generally more immune to errors because the detuning of the laser is not as critical (it affects the cross-talk as described previously, but does not affect the targeted site). However, the shift-out technique only works when considering two qubits, and for larger systems the shift-in technique must be used.

In Figure 13.6 we show site-specific operation, using the shift-in method with $\delta/\Omega = \sqrt{15}$. The site-specific operation is seen to have a lower flopping amplitude. The cross-talk on surrounding sites is minimal, but however it is seen to be anisotropic, indicating an

imperfect shape to the Stark beam. The cross-talk is quantified in Section 13.4.

In Figure 13.7 we demonstrate the full power of this method by selectively doing Rabi flopping on 7 sites throughout the array, using the shift-in method with $\delta/\Omega = \sqrt{63}$. The larger detuning suppresses cross-talk further. All 7 sites are targeted sequentially in the every measurement, and so the cross-talk seen on non-targeted sites is actually at 7 times the nominal level. The $459\,\text{nm}$ Stark laser is capable of targeting any site in the array, but the 7 sites used in this data were selected based on having long T2 times.

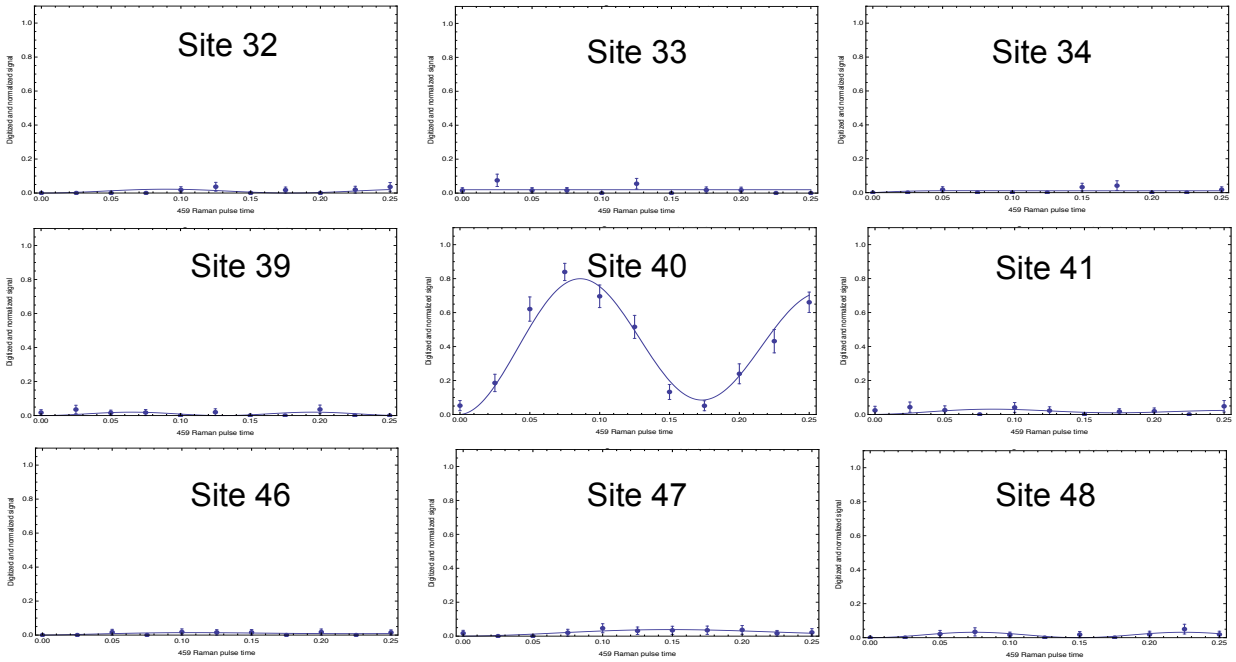


Figure 13.6: Oscillations on site 40 using Stark addressing. Amplitude of the oscillation is lower than for global operations. The surrounding sites show low cross talk.

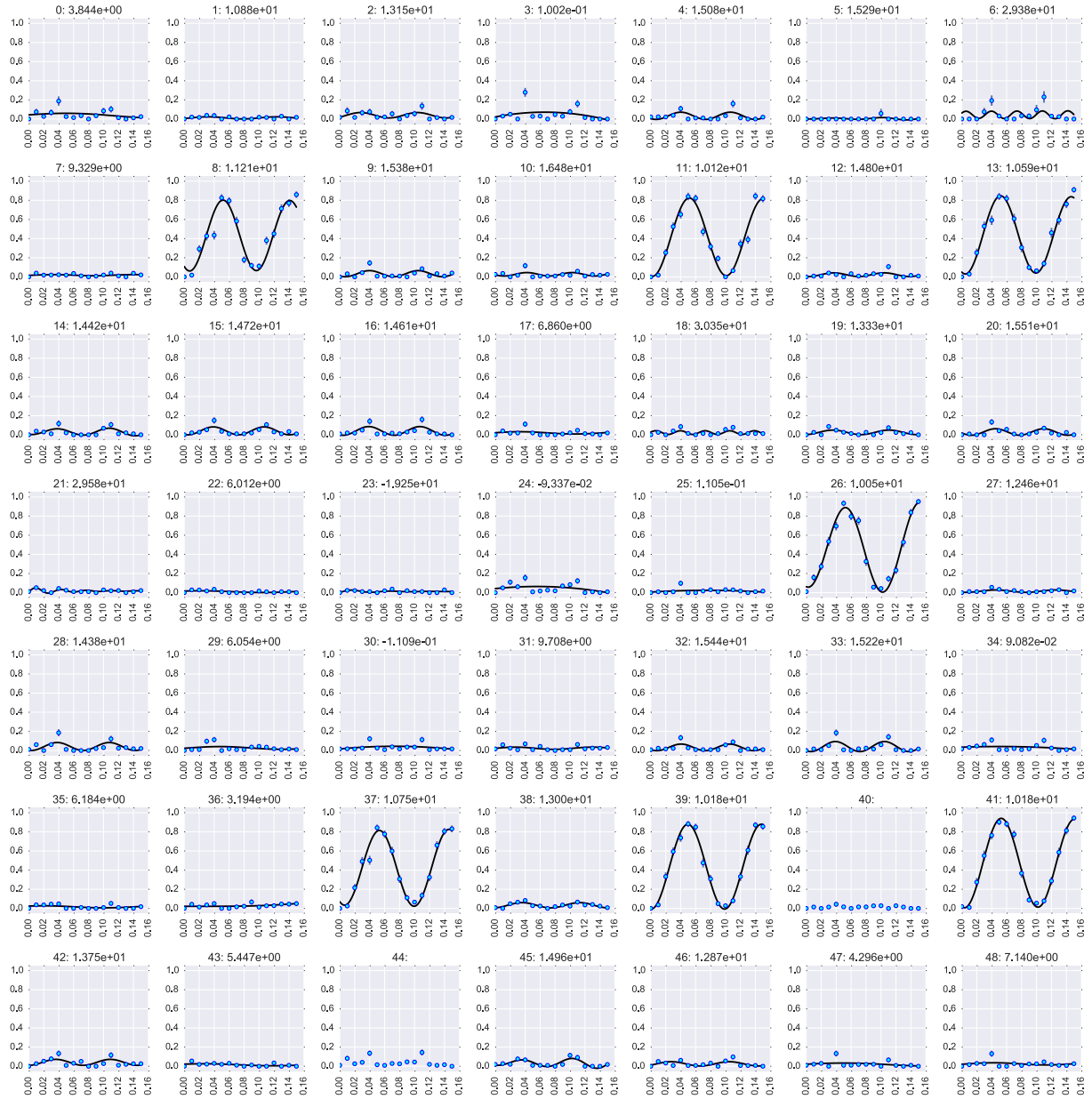


Figure 13.7: Single-site addressing performed on 7 separate sites during the same measurement sequence. This demonstrates our ability to target arbitrary sites in the array without any manual realignment. The sites were targeted using the *shift-in* method of microwave detuning, at $\delta/\Omega = \sqrt{63}$. All seven operations were performed in every measurement, and so the cross-talk on non-targeted sites is seven times the nominal level. Data from 2015-07-21-21-13-55.

13.4 Randomized Benchmarking

We have used randomized benchmarking to characterize the performance of our single qubit rotations, both global and site-addressed. We use the complete set of 24 Clifford gates ($\mathcal{C}_1$). These gates are generated from the set $\{I, R_j(\pm\pi/2), R_j(\pi)\}$ where $R_j(\theta) = e^{-i\theta\sigma_j/2}$ are rotations about the axes $j = x, y, z$. σ_j are the Pauli matrices, and I is the identity. We use square microwave pulses, and nominal pulses are defined as R_x rotations. We can phase shift the pulses using the DDS frequency generators which are summed into the RF signal, and a 90° phase shift gives R_y rotations. R_z rotations are performed by compositing R_x and R_y operations.

Random Clifford sequences of length ℓ are generated with each gate chosen uniformly from $\mathcal{C}_1$. We start with all qubits optically pumped into $|1\rangle$, and at the end of each sequence we add a final gate which, in the absence of errors, would transfer the qubits to $|0\rangle$, such that there should be a high signal after blowaway. In the presence of depolarizing errors the probability of measuring $|0\rangle$ is

$$P_{|0\rangle} = \frac{1}{2} + \frac{1}{2}(1 - d_{if})(1 - d)^{\ell} \tag{13.4}$$

Here d_{if} (if for initial, final) is the depolarization probability associated with state preparation, the final transfer gate, and state measurement. d is the average depolarization of a Clifford gate for ℓ gates. The fidelity for a transformation between two density matrices ρ and ρ' is defined as $F(\rho, \rho') = \mathrm{Tr}\left[\sqrt{\sqrt{\rho}\rho'\sqrt{\rho}}\right]$ (see Nielsen and Chuang [27]), and the square of the average gate fidelity is then

$$F^2 = 1 - \frac{d}{2} \tag{13.5}$$

We applied seven randomized Clifford gate sequences globally to all the trapping sites at ten different truncation lengths of $\{1, 12, 23, 34, 45, 56, 67, 78, 89, 100\}$ gates. Each sequence was repeated 50 times. The decay of $P_{|0\rangle}$ versus number of gates was fit to Equation 13.4 to find d_{if} and d. Figure 13.8 shows the results of this experiment on one site, with an inset histogram for F^2 across the array. We find an average fidelity of 0.9983(14), with a maximum of 0.9999(3). These results are comparable with the best achieved single-site neutral atom gates reported to date of 0.99986(1) (Olmschenk et al. [99]). The results are summarized in Table 13.1.

We also performed randomized benchmarking for a single site (site 31) that was ad-

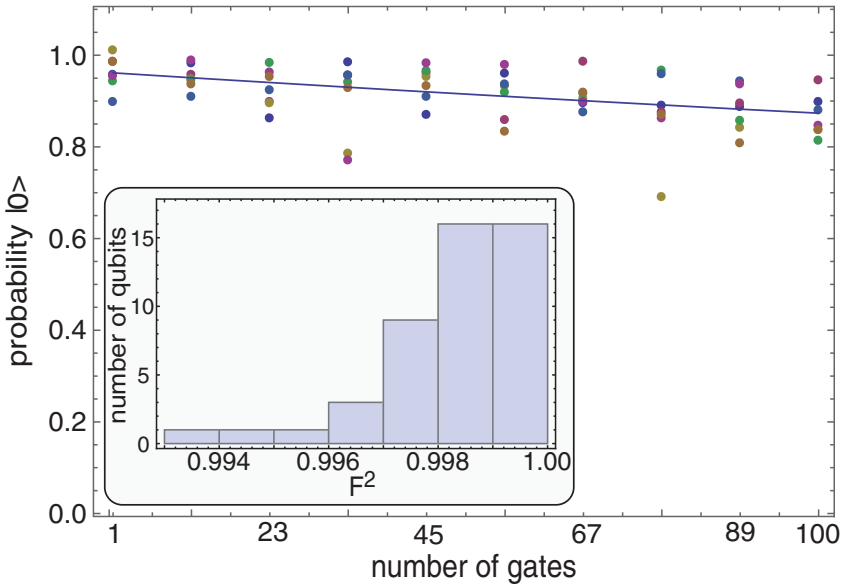


Figure 13.8: Probability of measuring the correct output state on one particular site (27) during global operations during randomized benchmarking. Colored dots represent the seven different randomized sequences used. Data is plotted against the ten truncation lengths of the sequences. Inset shows a histogram of the F^2 fidelity for the whole array (excluding two sites that had poor loading). Figure from Xia et al. [80].

dressed using the $459\,\text{nm}$ Stark shifting beam using the shift-in method. We used ten randomized sequences and eight truncation lengths of $\{1, 8, 15, 22, 29, 36, 43, 50\}$. Results of the singly-addressed measurement are shown in Figure 13.9. Fitting again to Equation 13.4 and averaging across the ten sequences we find an F^2 fidelity of 0.9923(7). The error per gate, d is 4.5 larger than for the global operations, likely due to fluctuations in the intensity and alignment of the Stark beam. We define the crosstalk on non-target sites as $E_{\text{xt}} = 1 - F^2$, where again we use the definition of F in terms of the probability of measuring $|0\rangle$, but for all non-targeted sites the ideal result is that they stay in $|1\rangle$ as prepared. The array averaged cross-talk was $\langle E_{\text{xt}} \rangle = 0.002(9)$, but the results for nearest neighbor sites is higher, as summarized in Table 13.1.

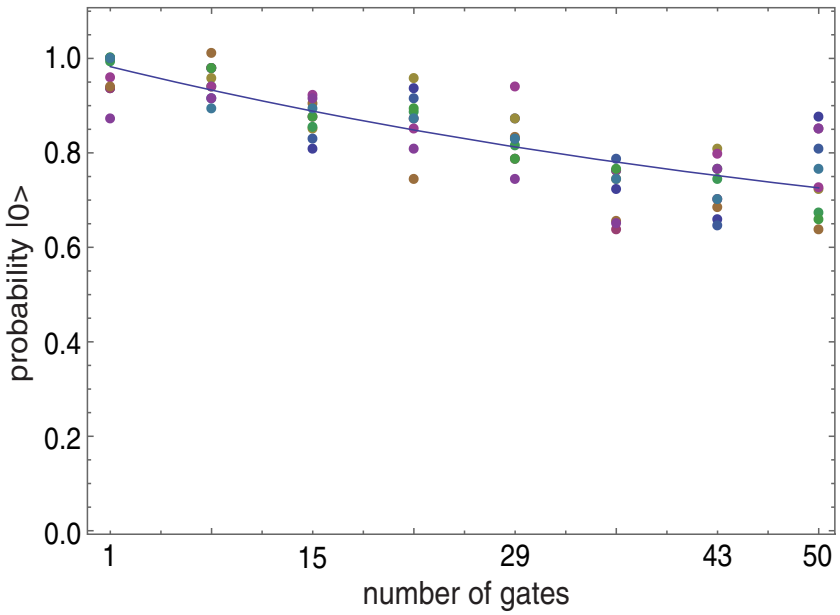


Figure 13.9: Probability of measuring the correct output state on a singly-addressed site (31), using the Stark beam *shift-in* method at $\delta/\Omega = \sqrt{15}$. Colored dots represent the ten different randomized sequences used. Data is plotted versus the eight truncation lengths for each sequence. Figure from Xia et al. [80].

$\langle d_{if} \rangle_{47 \text{ sites}}$	0.092 ± 0.066
$\langle d \rangle_{47 \text{ sites}}$	0.0035 ± 0.0027
$F^2_{47 \text{ sites}}$	0.9983 ± 0.0014
F^2_{min}	0.9939 ± 0.0007
F^2_{max}	0.9999 ± 0.0003
$F^2_{\text{single site}}$	0.9923 ± 0.0007
$\langle d_{if} \rangle_{\text{xt}}$	0.037 ± 0.027
$\langle E_{\text{xt}} \rangle$	0.002 ± 0.009
$\langle E_{\text{xt}} \rangle_{\text{NN}}$	0.014 ± 0.02
$\langle E_{\text{xt}} \rangle_{\text{!NN}}$	0.0005 ± 0.001

Table 13.1: Results of randomized benchmarking fidelity measurements for global (rows 1-5) and single site addressed (rows 6-10) operations. The global operations are given over 47 sites because two sites were loading poorly during the experiment. $\langle E_{\text{xt}} \rangle$ is the average crosstalk error over the array, $\langle E_{\text{xt}} \rangle_{\text{NN}}$ is the crosstalk error for nearest-neighbor sites, and $\langle E_{\text{xt}} \rangle_{\text{!NN}}$ is the crosstalk for all sites except nearest neighbors.

13.5 Coherence Measures

We have characterized our atomic qubits by the T_1 and T_2 coherence times. T_1, representing the amplitude error of the qubit states, is measured by observing the time for a population prepared in $|1\rangle$ to decay, and we find an array averaged value of $590\,\text{ms}$. This is significantly longer than any of our gate operations, and so does not pose a limitation on gate performance.

T_2 represents the dephasing error of the qubit states. T_2 excludes the effects of any predictable dephasing, and is therefore a best-case-scenario including only truly random effects. Generally, however, we do not measure T_2, but rather T_2^*, which includes all dephasing effects. This is a more realistic measure of the noise on our gates, and is also easier to measure. To take a T_2^* measurement, we prepare the qubits in $|1\rangle$, perform a global $R_x\,(\pi/2)$ rotation, wait some delay time, and then perform another $R_x\ pi/2$, blowaway and measure the resulting population. If this was performed on fine enough time scales, this is a Ramsey type measurement and we would expect to see oscillations at $9.2\,\text{GHz}$. The oscillations would decay, and a fit to the decay envelope would give T_2^*. However, this is too fast for our experimental setup, as we cannot perform microwave $\pi/2$ pulses that are short compared to $1/(9.2\,\text{GHz})$ and if we could it would require an unreasonable number of iterations for our data rate. Instead we use an alternate technique. We take larger steps in the delay time, and because we then do not have information about what phase the oscillation is at after this delay, we scan the phase of the second microwave pulse over a 2π range. We have tuned our microwaves into resonance with the atoms, effectively putting our experiment in the rotating frame. The variation of the maximal phase represents the deviation of the RF generator frequency from the true qubit clock. By scanning the phase at each delay time, we get an oscillation. The amplitude of that oscillation represents the remaining coherence of the qubit, and we fit an exponential decay to those reduced amplitudes to find T_2^*. The results of such a T_2^* measurement are shown in Figure 13.10. When properly tuned we have measured an array averaged T_2^* of $14\,\text{ms}$, with individual sites as high as $50\,\text{ms}$ which we attribute to site-to-site variations in the atom temperature.

The T_2^* time is limited primarily by magnetic noise and finite temperature motional effects of the atoms. There are two sources of magnetic noise that we can eliminate. The first is the effect of $60\,\text{Hz}$ noise from the AC lines. We eliminate this noise by creating a TTL signal synced with the AC line signal, and then triggering our experiment off that signal. Waiting for this signal gives only a minor delay in the experiment, and ensures that every

measurement is taken at the same condition with respect to the AC line phase. The second source of magnetic noise we have addressed is due to the Madison Symmetric Torus, a plasma experiment in the same building as our apparatus. When operating, this experiment runs very high currents that create large magnetic field spikes approximately every 100 seconds, and which last for ~ 10 seconds. We monitor the magnetic field environment just outside our vacuum cell, and the results are shown in Figure 13.11. We filter our data based on the magnetic field measurements, and drop any data during which MST was active, resulting in an effective 10% reduction in data rate.

13.5.1 Spin-Echo Techniques

Some of the *systematic* dephasing of the qubits can be eliminated with a spin-echo technique. In a spin echo measurement we use a microwave π pulse between the two $\pi/2$ pulses, halfway through the delay period. This reverses the precession of the qubit phases, and so whatever systematic phase accumulates during the first half of the delay will be removed during the second half. That phase accumulation varies from site-to-site, but if it is repeatable then a spin-echo can remove its effect. Increasing the number of echo pulses can remove higher frequency fluctuations, but also adds noise due to the π pulses themselves.

By trying various numbers of echo pulses and measuring T_2^* with each sequence, the best measurement reveals T_2, which is the best-case-scenario time scale for qubit dephasing. We have tried up to 6 spin echo pulses, and seen an improvement of array averaged T_2 to $22.7\,\text{ms}$, and up to $75.4\,\text{ms}$ for an individual site.

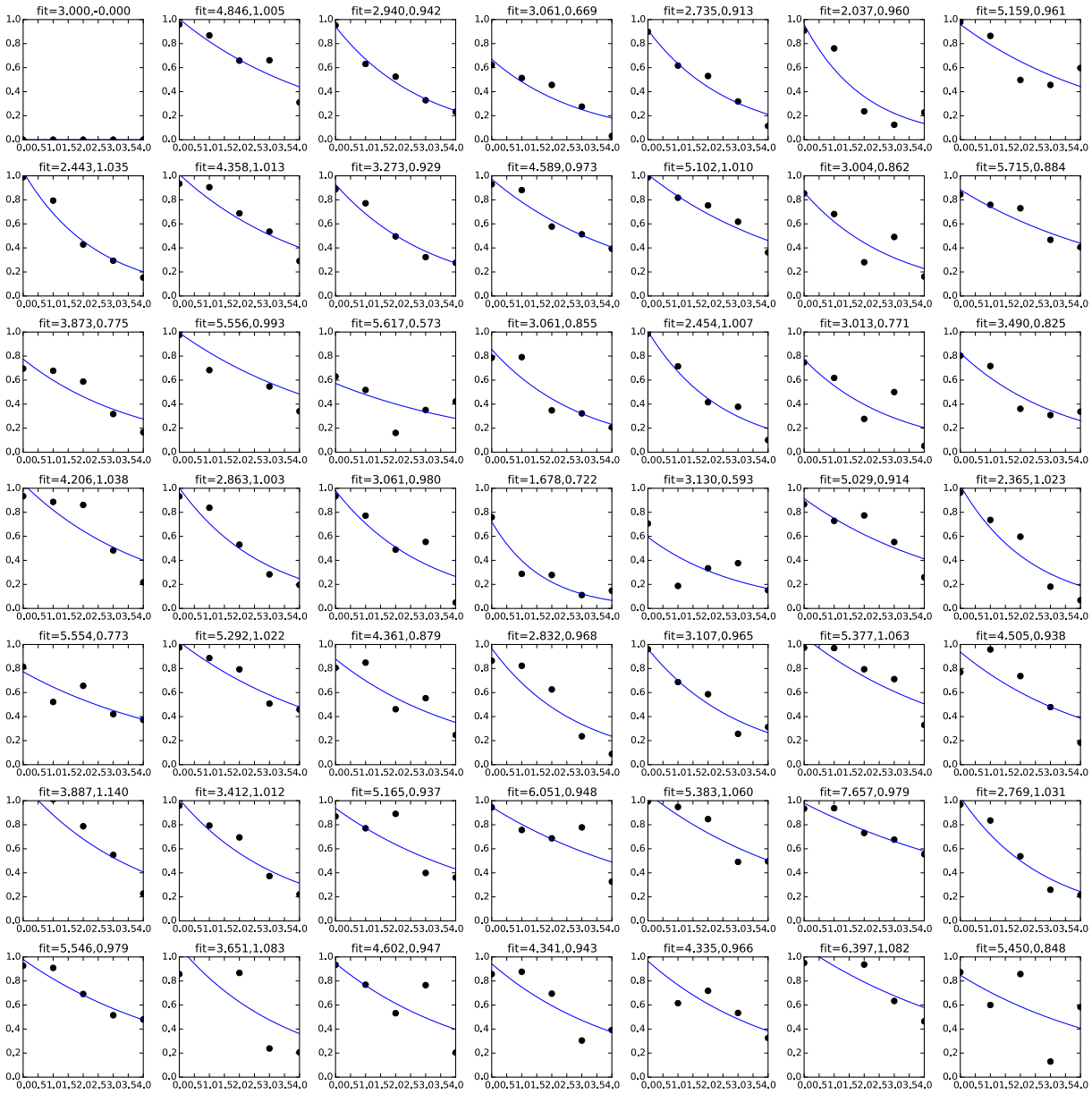


Figure 13.10: T_2^* decay. Each data point represents the reduction of 4 iterations of scanning the phase of the second microwave $\pi/2$ pulse. The data is plotted versus time in ms, and the numbers above each site gives the fit to T_2^* and initial retention. Data from 2015-02-09-10-24-00.

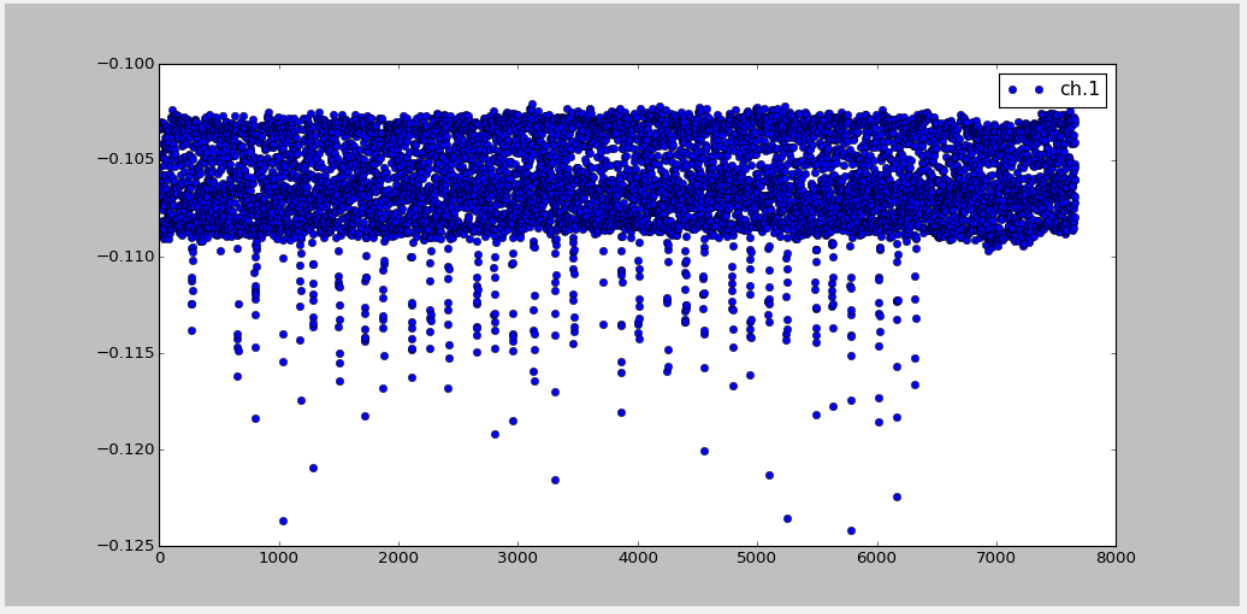


Figure 13.11: A measurement of the magnetic field near our apparatus, showing large spikes due to the operation of the Madison Symmetric Torus in the same building. We filter the data based on the magnetic field, and drop any measurements during which MST was active. Scale is $2\,G/V$. Data from 2015-03-09.

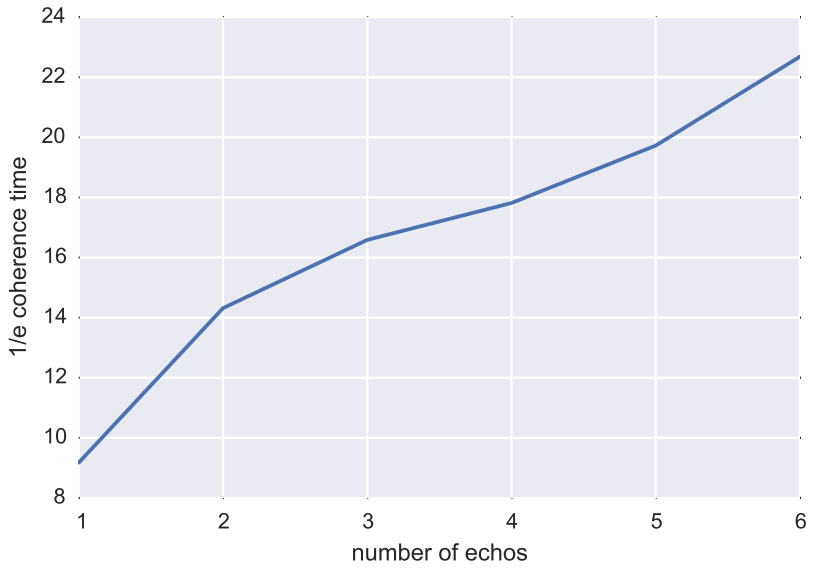


Figure 13.12: Results of spin-echo experiments to extend T_2, plotted versus number of echo pulses. We tried up to 6 echo pulses, and further improvement may be possible. Data from 2015-02-26-21-06-23.

13.6 459 Alignment and Ground Ramsey

We use a Ramsey experiment on the ground state in the presence of 459 nm light from the Rydberg laser as the basis of our alignment of the 459 scanner, and as a key diagnostic of the 459 nm intensity for tuning the Rydberg gates. For this measurement, we perform a microwave $\pi/2$ pulse, followed by a delay time during which the 459 nm Rydberg laser is on, followed by a second microwave $\pi/2$ pulse. Because the 459 nm light is detuned from the $7p_{1/2}$ level, we do not significantly populate that level. Instead, the qubit stays in the ground state manifold and acquires a phase at the rate of the differential Stark shift of the $|0\rangle$ and $|1\rangle$ states due to the 459 nm light. The frequency of the oscillation is proportional to intensity, and so we can use this signal to align the 459 nm beam scanners to each atom trapping site. If an approximate Ramsey frequency is known, we can set the length of the 459 pulse to about 10% under the π time (to prevent a double-peak if the intensity on-alignment drives the oscillation faster than expected) and then sweep each axis of the beam scanner. This technique allows us to establish the positioning of the 459 nm scanner independently of the 1038 nm scanner, and so it is always done first. Typical 459 ground Ramsey frequencies for our system are 0.8 to 1.1 kHz.

13.7 Rydberg spectroscopy

We measure the transition to the Rydberg states on a single site using two-photon spectroscopy. As described in Section 8.3, we use a 459 nm and 1038 nm photon to transfer atoms to some specific Rydberg state via $7p_{1/2}$. After aligning the 459 nm beam scanner using the ground Ramsey measurement, we can align the 1038 nm beam scanner using the Rydberg signal. Because the Rydberg atoms are not as well trapped as the ground state, we can use an atom *loss* signal as a measure of successful transition to the Rydberg state. The 459 nm and 1038 nm light are both on simultaneously for a length of time that maximally transfers population to the Rydberg level (a Rydberg π pulse), therefore leaving the atoms in the Rydberg state until many of them are lost. No microwave pulses or blowaway are used.

There are four measurements that must be tuned using this signal, and to find the properly adjusted settings they must usually be iterated. These four measurements are adjustment of the two axes of the 1038 nm beam scanner, spectroscopy of the Rydberg state, and Rabi measurement of flopping to the Rydberg state. As with the 459 nm alignment, it is best to set the pulse time to 10% under the π time, if known, to prevent a double peak

during 1038 nm alignment. A sweep of the 1038 beam scanner will show a dip in retention as seen in Figure 13.13.

Once aligned, we perform a two-photon spectroscopy scan by sweeping the frequency of the 459 nm on/off switch AOM. We automatically adjust the switch AOM frequency due to the scanner alignments using the formula:

$$\begin{aligned} \text{RydA_switch_AOM_frequency} = .5 * (&\text{RydA_frequency_offset} \\ &- (\text{scanner_1_459} - \text{scanner_2_459}) \\ &- (\text{scanner_1_1038} - \text{scanner_2_1038})) \end{aligned} \tag{13.6}$$

where the factor of 0.5 accounts for the double-pass setup of the 459 switch AOM, and RydA_frequency_offset is whatever value is necessary to put the lasers in resonance with the Rydberg state. By employing this formula we do not need to worry about corrections due to alignment changes, and we only need to fine-tune RydA_frequency_offset to account for changes in trap-induced Stark shifts and offset drifts in the laser-lock electronics

The signal for the two-photon spectroscopy is an atom loss signal, just as with the alignment, and looks very similar, but with a linewidth of 700 kHz. Although we have done some work with Rydberg signal with the 780 nm traps always on, typically we turn off the traps during the Rydberg pulses, as we find it actually increases the atom retention. If the 780 nm traps are left on it causes a -3 MHz shift in the Rydberg spectroscopy.

Once the alignment and two-photon spectroscopy are complete, we can find the π time by performing Rabi flopping to the Rydberg state. This is done by simply varying the length of time of the Rydberg pulse, with both lasers on for the same amount of time. If the experiment is being performed on more than one site per measurement, we must wait 5 ms between pulses to insure that the Rydberg blockade does not degrade the signal on the second site. Rydberg Rabi flopping is shown in Figure 13.14. Typical Rydberg Rabi frequencies for our system are 400 to 750 kHz. In addition to tuning of the Rydberg pulse length, this diagnostic is used to tune the 459 and 1038 nm beam power as described in the next chapter.

13.8 Rydberg Ramsey

Finally, we can also perform a Rydberg Ramsey measurement. In this measurement we again use the atom loss signal with no blowaway. The experiment sequence consists of a Rydberg $\pi/2$ pulse at the beginning and end, with a variable gap time in between.

Phase accumulates for the portion of the qubit wavefunction in the Rydberg state, and this experiment gives us a direct measurement of the differential ac Stark shift on the $|0\rangle$ and $|1\rangle$ states due to the Rydberg pulse. We would like to completely cancel this ac Stark shift to ensure our gates have the proper phase output. We are typically able to null Rydberg Ramsey frequencies in our system to below $250\,\mathrm{kHz}$.

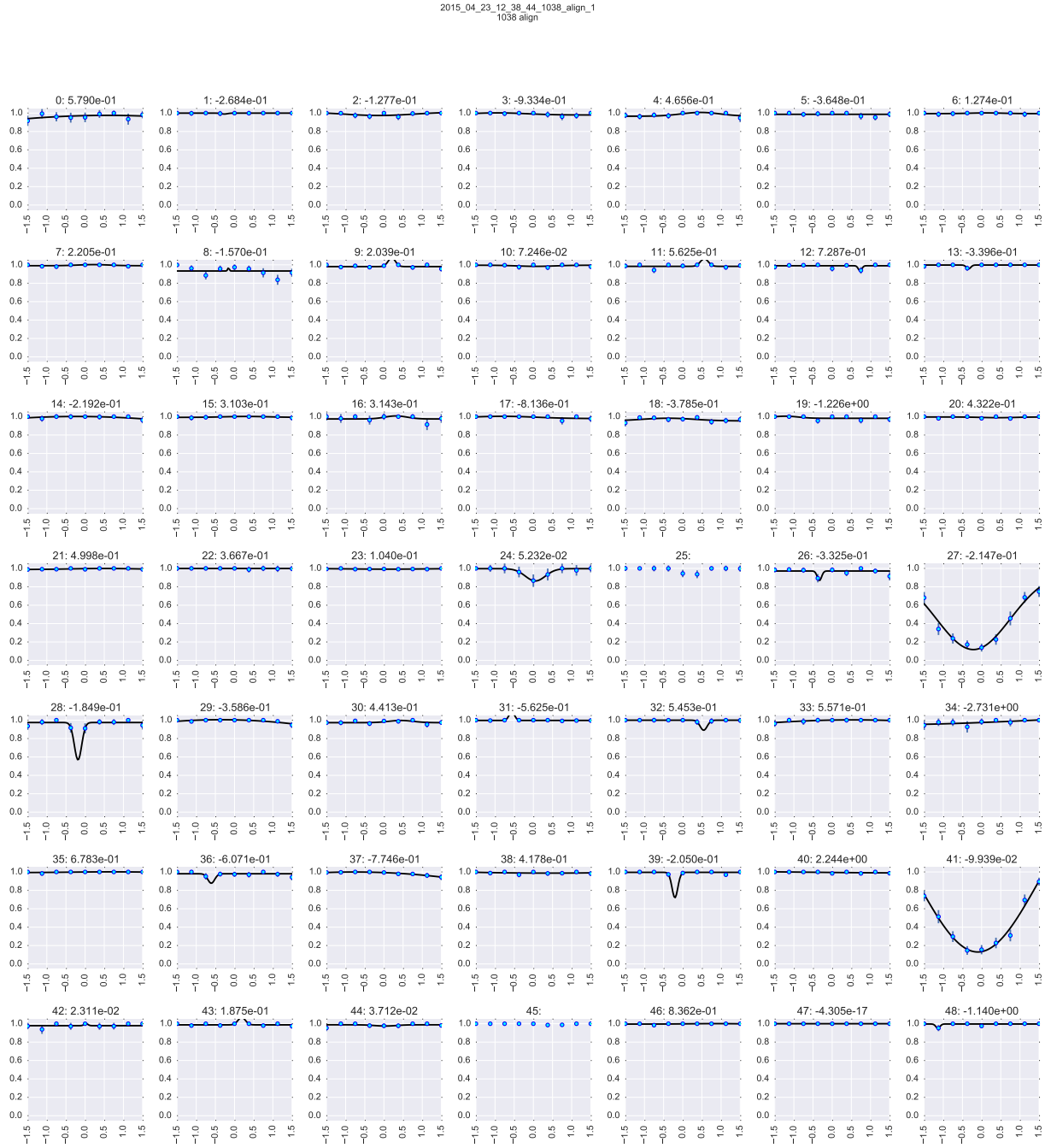


Figure 13.13: Alignment scan of 1038 nm scanner on sites 27 and 41. The dip corresponds to atom loss from population transferred into the less-well-trapped Rydberg state. The x-axis is given in MHz of scanner AOM frequency shift, and the number above each site represents the fitted shift from the previous alignment. Data from 2015-04-23-12-38-44.

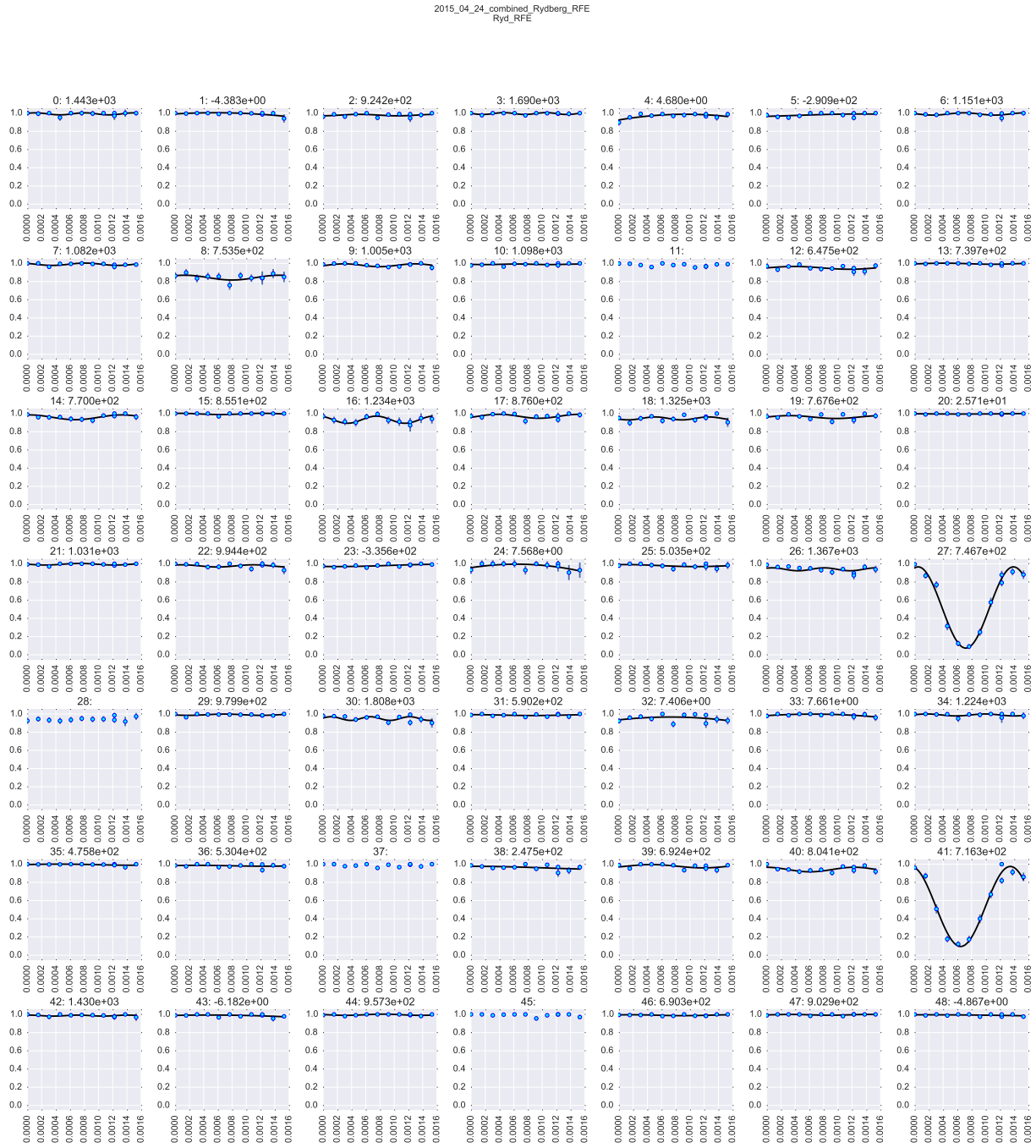


Figure 13.14: Rydberg Rabi flopping on sites 27 and 41, by scanning the length of a Rydberg pulse. The x-axis is given in ms and the value above each site gives the fitted Rydberg Rabi frequency. Data from 2015˙04˙24˙12˙37˙39 and 2015˙04˙24˙13˙33˙43.

14 Two Qubit Experiments

In this chapter we describe experiments demonstrating two qubit entangling gates. The preparation for these experiments begins with tuning and alignment in the one qubit experiments described in the previous chapter. The results of these experiments have been published in [100].

We refer to the two atoms participating in these experiments as the *control* and *target*. The fundamental gate implemented in our system is a C_z gate, as described in Section 2.6. This is implemented with a Rydberg π pulse on the control, followed by a Rydberg 2π pulse on the target, followed by a final Rydberg π pulse on the control (Figure 2.3a). To convert this C_z gate to a C_{NOT} gate we sandwich the C_z between two site-addressed microwave $\pi/2$ ground rotations on the target. We will allow for a variable phase on the second microwave pulse, which will be used to tune the gate, as described below.

The experiments described in this chapter were performed using the $82s_{1/2}$ Rydberg state, and have been demonstrated both on neighboring atoms, and beyond nearest-neighbors up to 2 sites away.

14.1 State Preparation

Demonstration of our two qubit gates requires that we show the output of the gate for every basis state, not just for all qubits prepared in $|1\rangle$. A minimal state tomography on the output of the gate requires that we check the transfer of population from each of the input basis states $|00\rangle, |01\rangle, |10\rangle, |11\rangle$ to each of the output basis states.

As a prelude to this, we must be able to prepare each of the input states with good fidelity. After optical pumping, preparing $|11\rangle$ requires no operation, $|01\rangle$ and $|10\rangle$ require a single site addressed $R_x(\pi)$ rotation, and $|00\rangle$ requires a global $R_x(\pi)$ rotation.

We perform each of these operations, and then measure the population in $F = 3$ for both atoms. This gives us a direct measurement of $|00\rangle$, and because the atom retention during microwave operations is nearly unity, allows us to infer the population in the other three states (we will not make this assumption after the lossy Rydberg operations). The result of such a state preparation is shown in Figure 14.1.

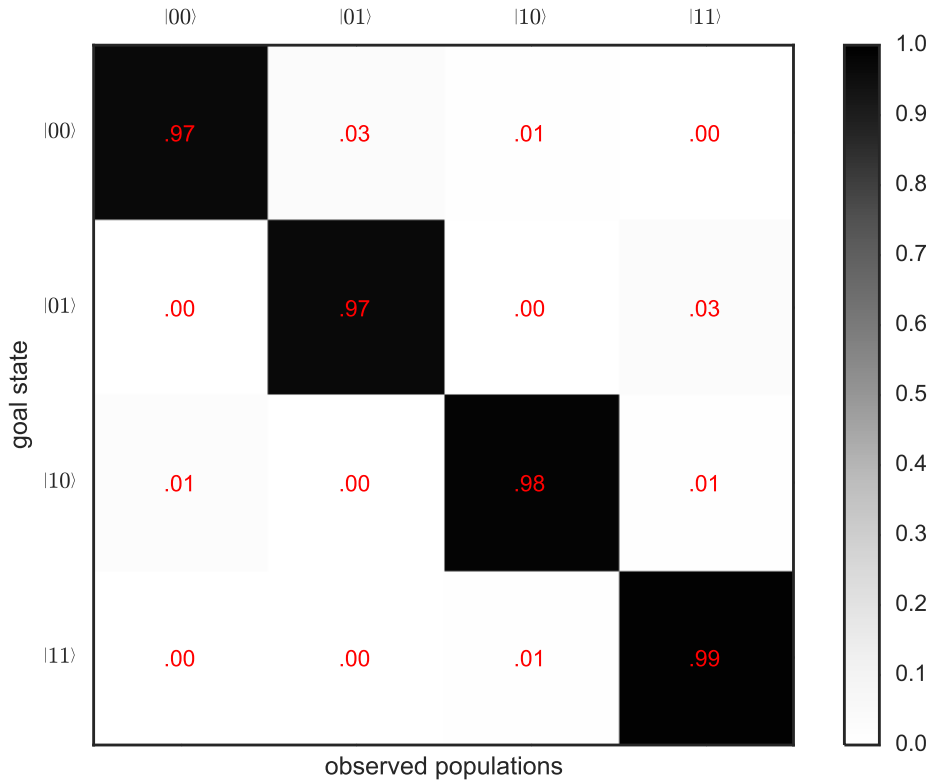


Figure 14.1: Results of state preparation. Four iterations are performed for the input states, and the output populations are inferred from measurements of $F = 3$ on each atom. The ideal matrix is the identity. Data from 2015-08-11-01-19-28.

14.2 Eye Diagram

To determine the correct phase to use for the second microwave $\pi/2$ pulse, we use the $|11\rangle$ input state and scan the phase. We desire to have the C_{NOT} gate maximally transfer $|11\rangle$ into $|10\rangle$, while $|01\rangle$ stays at $|01\rangle$. We take a shortcut to measuring this, by cutting the data on whether or not the control atom has loaded. If the control atom loads, we know the state is prepared to $|11\rangle$, but if the control atom does load, we call that $|01\rangle$ because there will be no possible blockade. This gives us a doubling of our data rate, because we only require the target atom to load, not both atoms. We perform a final global microwave π before readout to give us the population in $F = 4$.

Separating the data based on the presence or absence of the control atom, and plotting versus the the phase of the second microwave $\pi/2$ pulse, we get a curve such as that in

Figure 14.2. This is referred to as an *eye diagram* due to its lenticular shape. We see a π phase shift between the blockaded and unblockaded signals, which is exactly as desired. We choose the phase that gives the maximum contrast between the signals. Because of the asymmetry between the curves, this leads us to choose the phase that will give us the compliment of a C_{NOT} gate. This is a different but equally entangling gate.

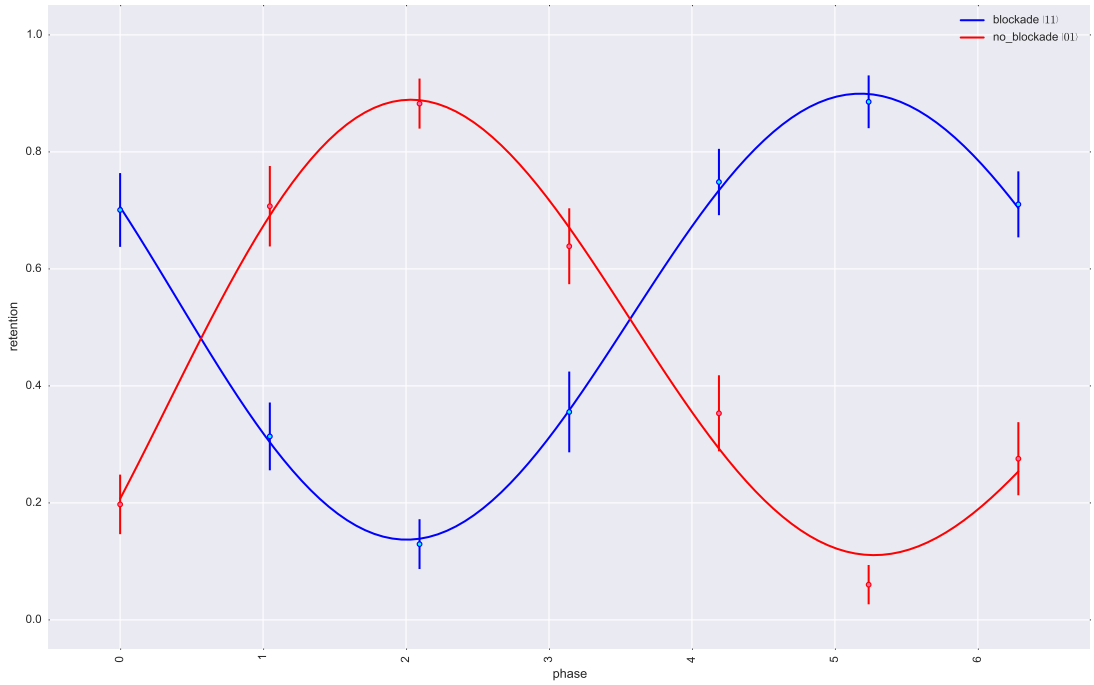


Figure 14.2: Results of scanning the C_{NOT} phase. The blockaded and unblockaded signals are defined by the presence or absence of a control atom. Note the π phase shift between the two curves. We choose the phase that gives maximal transfer of $|00\rangle \rightarrow |01\rangle$, which is the complement of the canonical C_{NOT}. Data from 2015-04-24-14-35-43.

14.3 C_{NOT} Population

Because of atom loss during the Rydberg operations, we cannot measure the output of the C_{NOT} gate as easily as we measured the state preparation matrix. Instead, we must have positive confirmation of the population in each output state by rotating that state into $|00\rangle$ where we get a bright signal for both atoms (if they are there). This means that we need 4 output rotations for each of 4 input states, or 16 total iterations.

This is performed once the gate phase has been tuned using the eye diagram, and it gives us a measure of state tomography on the output of the gate. It does not satisfy

full process tomography, and indeed doing these measurements only on basis states is insufficient to establish that we have an entangling gate as it does not demonstrate phase coherence between input and output states. Demonstrating entanglement will be covered in the next section. However, showing the population that results as an output of the gate is an important metric.

Figure 14.3 shows the resulting C_{NOT} population matrix for our system. We find a trace-averaged population of 82%. The major cause of error is generally atom loss during the Rydberg operations. However in this particular case we have actually better atom retention for the $|01\rangle$ input than for the $|11\rangle$ input which undergoes only global microwave operations. So it is clear that there are several aspects of the gate which can be improved.

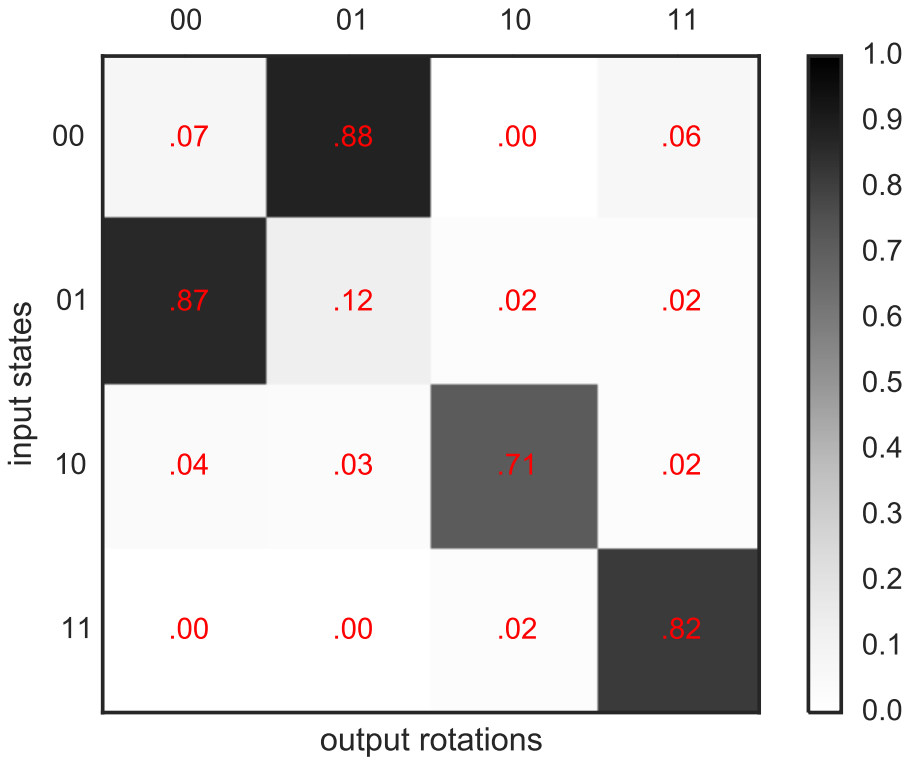


Figure 14.3: The C_{NOT} population matrix demonstrated. The gate implemented has the complementary phase to a traditional C_{NOT}. The highly populated states are in the locations desired, but atom loss and other errors leads to an imperfect 82% population. Data from 2015-04-24-15-24-01.

14.4 Bell State Preparation

The first step in establishing entanglement is to create an maximally entangled Bell state. We do this by preceding the C_{NOT} gate with a microwave $\pi/2$ rotation on the control atom, giving the sequence

$$|11\rangle \rightarrow \frac{1}{\sqrt{2}}\left(|01\rangle + |11\rangle\right) \rightarrow \frac{1}{\sqrt{2}}\left(|00\rangle + |11\rangle\right) \tag{14.1}$$

We can combine the initial $\pi/2$ on the control with the $\pi/2$ on the target to make it a more efficient global operation. For this one input case, we measure all 4 output rotations to fully account for atom loss. The resulting population matrix is shown in Figure 14.4. Here we report the fraction of the output that resides in each basis state to give a complete picture of where the population ends up. The population of the canonical Bell state should be read out the the rightmost column. The populations and uncertainties are $|00\rangle : 0.54 \pm 0.06, |01\rangle : 0.03 \pm 0.02, |10\rangle : 0.05 \pm 0.03, |11\rangle : 0.38 \pm 0.06$. The trace-averaged population fidelity is 0.93.

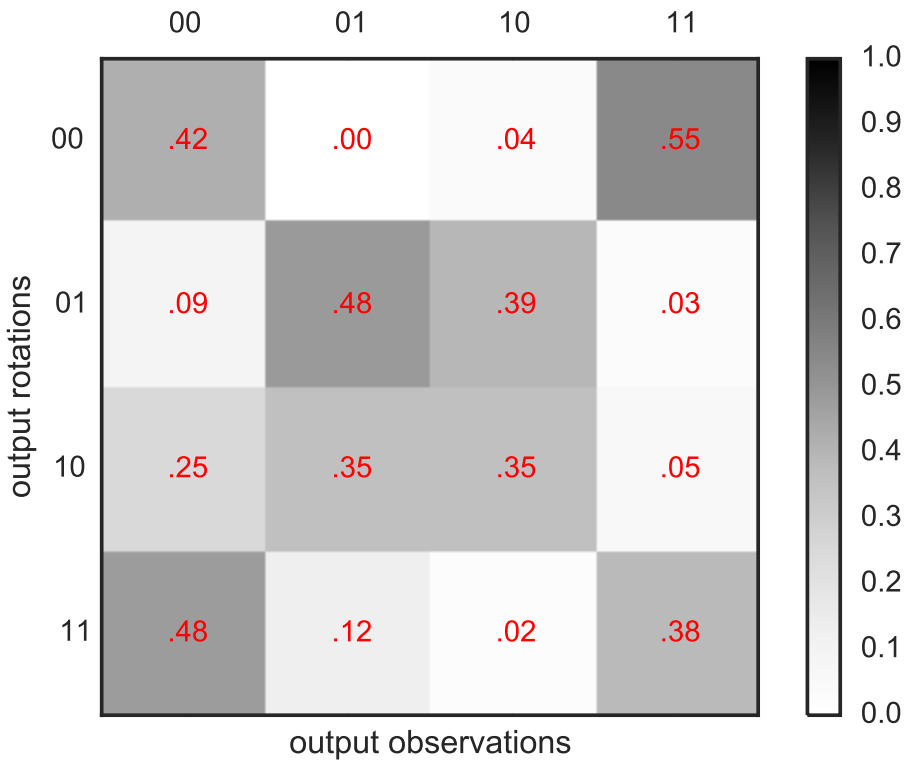


Figure 14.4: The Bell state population matrix. The population of the canonical Bell state can be read in the rightmost column, while the rest of the matrix gives observations for where the rest of the remaining population ended up. Data from 2015-04-24-17-13-35.

14.5 Parity Measurement

To test entanglement, we must show that the state we have created is not factorable in any basis. To do this, we perform the same Bell state preparation as above, but before the final output rotation, we perform a global microwave $\pi/2$ rotation with a variable phase. At every phase rotation, we calculate the parity from the four measured states, which is

$$\text{parity} = \left(P_{|00\rangle} + P_{|11\rangle}\right) - \left(P_{|01\rangle} + P_{|10\rangle}\right) \tag{14.2}$$

As the output phase is varied, population should shift from the even to odd states, as

$$P = 2\,\mathrm{Re}\left(C_2\right) - 2\left|C_1\right|\cos\left(2\phi + \xi\right) \tag{14.3}$$

where $C_1 = |C_1| e^{i\xi}$ is the coherence between states $|00\rangle$ and $|11\rangle$, and is C_2 is the coherence between states $|01\rangle$ and $|10\rangle$ (see Zhang et al. [4]). We fit the parity oscillation to this equation to find C_1. Finally, we evaluate the entanglement fidelity as

$$F = \frac{1}{2}\left(P_{|00\rangle} + P_{|11\rangle}\right) + |C_1| \tag{14.4}$$

Here $P_{|00\rangle}$ and $P_{|00\rangle}$ can be taken from any point along the parity curve, but we use the initial Bell state preparation measurement where they are maximal. By this fidelity metric, any result with $F > 0.5$ demonstrates entanglement and non-classical behavior.

Our results for the parity measurement are given in Figure 14.5, and the fitted parameters are $|C_1| = 0.27 \pm 0.02$ and $|C_2| = 0.006$. Combined with the Bell state populations given in the previous section, we find an entanglement fidelity of

$$F = 0.73 \pm 0.05 \tag{14.5}$$

This demonstrates that we have achieved a non-classical result well beyond the threshold for entanglement. There is still of course room for improvement, and to scale to longer algorithms we will require an entanglement fidelity closer to the limit of 1.0. However, our work represents the best result thus far for a neutral atom entangling gate. This result is presented entirely without any correction for atom loss. Previous works have achieved Bell state or entanglement fidelities of 0.58 [1], 0.71 [4], 0.75 [2] and 0.81 [101] if atom post-selection is allowed to correct for atom loss. However, if post-selection is necessary the time resources required to perform a computation grow exponentially. Without post-selection previous results have achieved entanglement fidelity of 0.58 [4] and 0.60 [101]. Our result therefore stands as a the current state-of-the-art, and a significant improvement in the field.

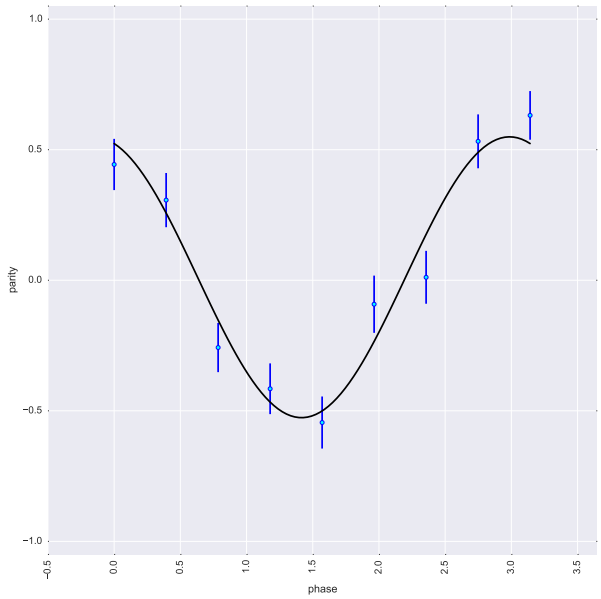


Figure 14.5: The Bell state parity oscillation. Each point represents $P_{|00\rangle} + P_{|00\rangle} - P_{|01\rangle} - P_{|10\rangle}$ calculated for four output rotations. The resulting $|C_1| = 0.27 \pm 0.02$ oscillation amplitude, combined with measurements of the Bell state population, gives an entanglement fidelity of $F = 0.73 \pm 0.05$. Data from 2015-04-24-17-35-38.

15 Grover Quantum Search

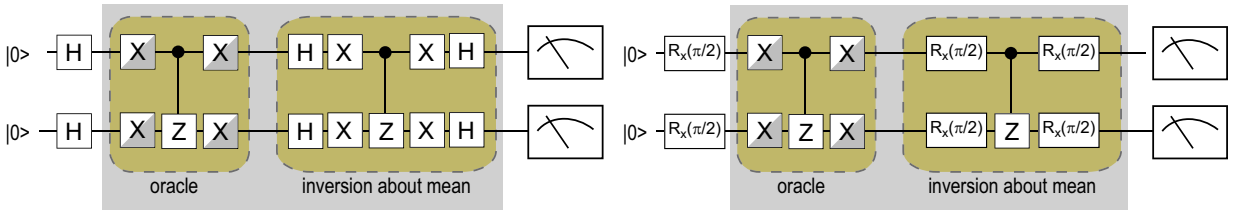
In this chapter we present progress toward implementing Grover's quantum search algorithm (Grover [20] and Grover [24]) in the atomic qubit array.

As presented in the previous chapter, although we have made large advances in the fidelity of neutral atom entangling gates, there is still much improvement needed before we reach a fault tolerant implementation. Despite this, it is not premature to begin investigating the implementation of algorithms in the atomic qubit array. Our main source of gate error is atom loss, and Rao and Mølmer [102] present a technique to implement quantum search in the presence of atom loss. Furthermore, the implementation of the quantum search algorithm is in itself a test of non-classical behavior, which is a useful diagnostic to explore the physics of our system.

The multi-qubit gates based on the Rydberg blockade interaction present a particularly useful system for implementing quantum search, because the blockade is not limited to a two-qubit interaction, or even to nearest neighbors. Therefore we can implement a fundamental multi-qubit gate (Isenhower, Saffman, and Mølmer [103]) rather than composing it out of many one and two-qubit gates. This provides an order of magnitude speedup for the Grover algorithm (Mølmer, Isenhower, and Saffman [29]).

For this research, we have chosen to attempt quantum search on a two qubit system, over a database with 4 entries, and only 1 right answer. The circuit diagram for the canonical two qubit Grover algorithm is shown in Figure 15.1a, where the slashed X gates in the oracle indicate that gate may either be X or I depending on what the "correct" answer to the search is. The same choice of rotation is made on site 1 before and after the oracle C_z gate. For site 2 a different choice of I or X may be made, but the same operation is done on site 2 before and after the oracle C_z gate. This method of specifying the correct answer in the oracle by a choice of 4 possible gate sequences seems somewhat contrived, since the computer must already know the correct answer. However any 2 qubit demonstration will be equally simplistic, and the purpose of this experiment is to demonstrate a scalable implementation of Grover quantum search that would be useful when more qubits are used.

We employ a simplification which makes better use of the native gates on our system by compiling some of the one-qubit H and $R_x(\pi)$ gates into $R_x(\pi/2)$ gates, as shown in Figure 15.1b. This gives the same result and does not skip any of the hard two-qubit operations, and so does not diminish the scalability of this demonstration.



(a) (b)

Figure 15.1: (a) The circuit diagram for the canonical 2 qubit Grover algorithm. (b) The compiled 2 qubit Grover algorithm for our system. Images from [104].

15.1 Measurement of Gate Phases

For the Grover algorithm, we require a C_z gate, which is ideally:

$$C_{z_{\text{canonical}}} = \begin{pmatrix} 1 & 0 & 0 & 0 \\ 0 & 1 & 0 & 0 \\ 0 & 0 & 1 & 0 \\ 0 & 0 & 0 & -1 \end{pmatrix} \tag{15.1}$$

or its compliment which is the fundamental C_z using the Rydberg blockade

$$C_{z_{\text{Rydberg}}} = \begin{pmatrix} 1 & 0 & 0 & 0 \\ 0 & -1 & 0 & 0 \\ 0 & 0 & -1 & 0 \\ 0 & 0 & 0 & -1 \end{pmatrix} \tag{15.2}$$

However due to phases induced by the two-photon transition and the time spent in the Rydberg states (see Maller et al. [100]) what we likely have is

$$C_{z_{\text{actual}}} = \begin{pmatrix} 1 & 0 & 0 & 0 \\ 0 & e^{i\theta_2} & 0 & 0 \\ 0 & 0 & e^{i\theta_3} & 0 \\ 0 & 0 & 0 & e^{i\theta_4} \end{pmatrix} \tag{15.3}$$

where we have removed any irrelevant overall phase to normalize the first diagonal element, but otherwise independent phases have been allowed on each state. We assume no undesired population transfer is induced during the C_z gate, and so the off-diagonal

elements are zero.

In Section 14.2 we introduced the $C_{\rm NOT}$ phase measurement that produces an eye diagram. In this measurement we perform the sequence $R_x(\pi/2)$ on site 2, C_z, $R_\phi(\pi/2)$ on site 2. Here R_ϕ denotes a microwave rotation about an axis in the xy plane with phase ϕ. For our C_z with imperfect phases this operator is

$$\begin{pmatrix} \sin^2\left(\frac{\phi-\theta_2}{2}\right) & \cos^2\left(\frac{\phi-\theta_2}{2}\right) & 0 & 0 \\ \cos^2\left(\frac{\phi-\theta_2}{2}\right) & \sin^2\left(\frac{\phi-\theta_2}{2}\right) & 0 & 0 \\ 0 & 0 & \sin^2\left(\frac{1}{2}(\phi+\theta_3-\theta_4)\right) & \cos^2\left(\frac{1}{2}(\phi+\theta_3-\theta_4)\right) \\ 0 & 0 & \cos^2\left(\frac{1}{2}(\phi+\theta_3-\theta_4)\right) & \sin^2\left(\frac{1}{2}(\phi+\theta_3-\theta_4)\right) \end{pmatrix} \tag{15.4}$$

This operator acts on the prepared state $|1_{\text{site 1}}1_{\text{site 2}}\rangle$, and if we cut on the presence of the site 1 atom then the blockade signal observed on fluorescence of $F = 3$ is

$$\cos^2\left(\frac{1}{2}(\theta_3-\theta_4+\phi)\right) \tag{15.5}$$

where we have summed over the probability to find the atoms in $|00\rangle$ or $|10\rangle$ because the state of the site 1 atom is irrelevant to the measurement. If the site 1 atom is absent the effective input state is $|01\rangle$ and the no-blockade signal is

$$\cos^2\left(\frac{1}{2}(\theta_2-\phi)\right) \tag{15.6}$$

where again we have summed over the probability to find the atom in $|00\rangle$ or $|10\rangle$. If we take the canonical values of $\theta_3 = 0$ and $\theta_4 = \pi$ then the eye diagram is as shown in Figure 15.2.

It is clear from Equations 15.5 and 15.6 that the C_z phase measurement on site 2 alone is insufficient to determine all the gate phases. However, we can perform a similar measurement with the single qubit rotations on the control instead of the target. The sequence $R_x(\pi/2)$ on site 1, C_z, $R_\phi(\pi/2)$ on site 1, gives us the operator

$$\begin{pmatrix} 0 & \cos^2\left(\frac{1}{2}(\phi+\theta_2-\theta_4)\right) & 0 & \sin^2\left(\frac{1}{2}(\phi+\theta_2-\theta_4)\right) \\ \cos^2\left(\frac{\phi-\theta_3}{2}\right) & 0 & \sin^2\left(\frac{\phi-\theta_3}{2}\right) & 0 \\ 0 & \sin^2\left(\frac{1}{2}(\phi+\theta_2-\theta_4)\right) & 0 & \cos^2\left(\frac{1}{2}(\phi+\theta_2-\theta_4)\right) \\ \sin^2\left(\frac{\phi-\theta_3}{2}\right) & 0 & \cos^2\left(\frac{\phi-\theta_3}{2}\right) & 0 \end{pmatrix} \tag{15.7}$$

We can now cut on the presence ($|11\rangle$) or absence ($|01\rangle$) of the site 1 atom, and sum the

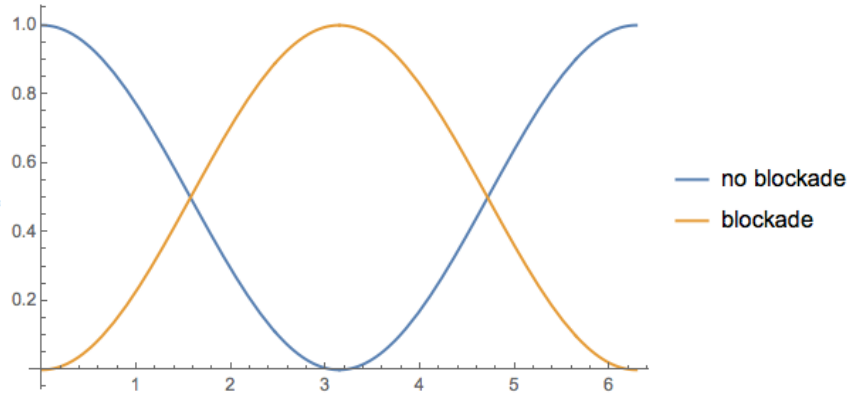


Figure 15.2: The eye diagram for the C_{NOT} target phase measurement, with canonical gate phases.

$|00\rangle$ and $|01\rangle$ output state to get the blockade signal:

$$\cos^2\left(\frac{1}{2}(\theta_2 - \theta_4 + \phi)\right) \tag{15.8}$$

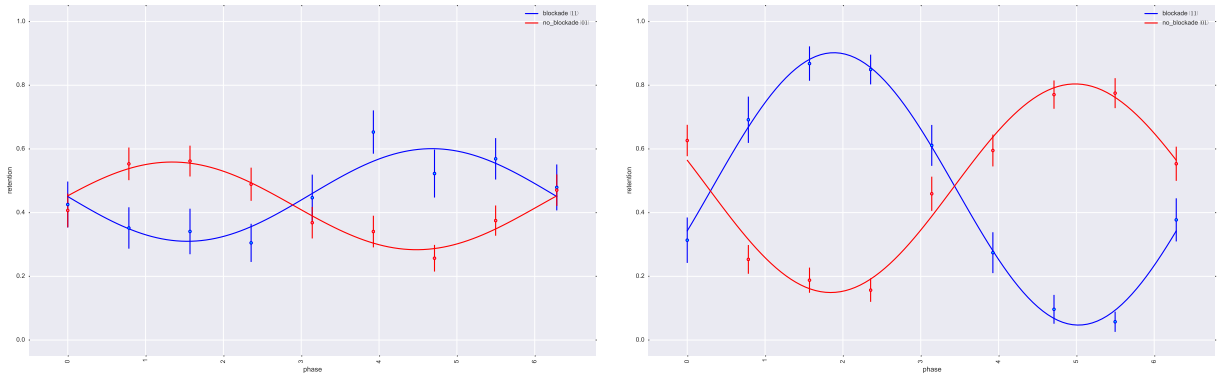
and the no-blockade signal:

$$\cos^2\left(\frac{1}{2}(\theta_3 - \phi)\right) \tag{15.9}$$

Between the C_z phase measurements on site 1 and site 2 we can then determine all the gate phases. Figure 15.3 shows results of both the site 1 and site 2 phase measurements.

Using this technique we have determined that our actual C_z gate is

$$C_{z_{\text{implemented}}} = \begin{pmatrix} 1 & 0 & 0 & 0 \\ 0 & e^{-1.3i} & 0 & 0 \\ 0 & 0 & e^{4.5i} & 0 \\ 0 & 0 & 0 & e^{0.1i} \end{pmatrix} \tag{15.10}$$



(a) (b)

Figure 15.3: (a) C_z gate phase measurement on site 1. Data from 2015-06-23-21-06-50. (b) C_z gate phase measurement on site 2. Data from 2015-06-22-23-54-11. The signal in (a) is inverted by a final global $R_x(\pi)$ rotation to increase signal in the face of Rydberg atom loss, while the signal in (b) is not. The atom loss on site 1 is worse, even with this inversion, because it persists in the Rydberg state for a longer time during the gate while site 2 undergoes a quicker 2π Rydberg pulse.

15.2 Correcting Gate Phases

We can use single site rotations to correct some of the phase errors, as was done using the phase on the second microwave $\pi/2$ rotation in the C_{NOT} experiments. It is not possible to correct arbitrary phases on all the states using this technique. If it were, we would not need a 2 qubit interaction to perform a C_z gate. However, we can fix at least two of the phases. By following the C_z gate by a single site $R_z(\phi_3)$ rotation on site 1 and $R_z(\phi_2)$ on site 2, and factoring out the overall phase on the 1^{st} diagonal element, we have a corrected gate

$$C_{z_{\mathrm{phase}}} = \begin{pmatrix} 1 & 0 & 0 & 0 \\ 0 & e^{i(\theta_2+\phi_2)} & 0 & 0 \\ 0 & 0 & e^{i(\theta_3+\phi_3)} & 0 \\ 0 & 0 & 0 & e^{i(\theta_4+\phi_2+\phi_3)} \end{pmatrix} \tag{15.11}$$

By setting $\phi_2 = -\theta_2$ and $\phi_3 = -\theta_3$ we get

$$C_{z_{\text{corrected}}} = \begin{pmatrix} 1 & 0 & 0 & 0 \\ 0 & 1 & 0 & 0 \\ 0 & 0 & 1 & 0 \\ 0 & 0 & 0 & e^{i(\theta_4-\theta_2-\theta_3)} \end{pmatrix} \tag{15.12}$$

And finally for our implementation by correcting the measured phases we happily get a phase on the last diagonal element of 1.01336π, where π is ideal. Hence we have the nearly canonical gate:

$$C_{z_{\text{corrected,implemented}}} = \begin{pmatrix} 1 & 0 & 0 & 0 \\ 0 & 1 & 0 & 0 \\ 0 & 0 & 1 & 0 \\ 0 & 0 & 0 & e^{i1.01\pi} \end{pmatrix} \tag{15.13}$$

The nearly perfect correction is not merely lucky, as it is the result of the properly functioning blockade giving a π phase difference as desired. This corrected gate can now be used in the Grover algorithm.

15.3 Two Qubit Grover Search

We have attempted the Grover algorithm on two qubits, using the compiled circuit model given above, and the R_z phase corrections given in the previous section via $459\,$nm site-addressed Stark pulses. For this experiment we do all four possible oracle settings, and four output rotations to make a positive measurement of the population in each resulting state. The resulting output matrix is shown in Figure 15.4. The expected result for an ideal execution of the algorithm would be ones on the anti-diagonal. Any result with greater than 0.25 in the correct states would represent a better-than-classical result. Unfortunately, the measured results show no correlation with the desired outcome. As usual, we suspect atom loss during the Rydberg sequence to be our biggest source of error. Improving this result is a subject for immediate future work.

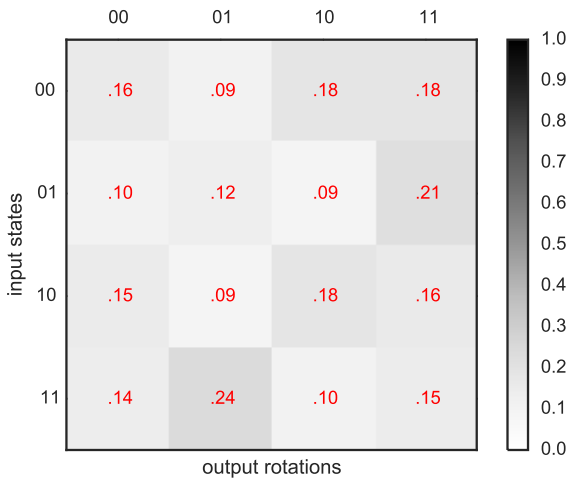


Figure 15.4: Results for the two qubit Grover search algorithm. The desired result is 1 on the anti-diagonal with 0 elsewhere. Data from 2015-06-24-11-16-07.

16 Optimization

We have used the optimization capabilities of CsPyController to greatly improve our experiment performance. The optimizer was described previously in Section 9.5. All optimizations presented in this section were done with the Nelder-Mead algorithm. Here we describe specific performance improvements that we have targeted with the optimizer.

16.1 Readout

We have two goals in the optimization of readout. The first is to improve the contrast between the zero and one atom signal. The second is to decrease the readout time, which is a step towards the larger goal of non-destructive readout (i.e. readout without blowaway or repumper).

The readout results of our system are always reduced to binary data denoting the presence or absence of an atom. The raw images however provide a continuum of intensity levels. To reduce the data, regions of interest (ROI) are identified as described in Section 10.1, and a threshold brightness is set to distinguish between zero or one atom. The two signals each represent a peak in a histogram of the ROI results, as shown in Figure 7.35. To optimize the contrast, or signal-to-noise ratio, between these two signals, we need to either narrow the peaks or move them farther apart. A simple solution is to increase the readout time. However, this comes are the cost of higher atom loss as light forces are placed on the atom for longer times, and trapping is required for longer times.

To prevent the optimizer from simply going to readout times that are too long and cause too much atom loss, we usually combine the readout optimization with a loading and retention optimization, where the cost function includes the atom count in the second shot. The quantified measure of signal-to-noise ratio that we use is the overlap of the zero and one atom peaks, defined as the area of the intersection over the area of the union. Details of determining the overlap are given in Section 10.3.

As calculated, the overlap is unitless fraction. To balance the effects of atom count and histogram overlap in the cost function, we normalize into units of "useful atoms" by multiplying by the number of measurements per iteration. The cost function to be minimized is then:

$$-\left(\text{atoms in shot 1} + \left(\text{measurements per iteration} \times \text{overlap}\right)\right) \tag{16.1}$$

We have found that this is a powerful method to increase the signal-to-noise ratio. Figure 16.1 shows results of this type of optimization, where at the beginning the zero and one atom signals are hardly distinguishable, and by the end a clearly bimodal distribution emerges. In this particular example, the optimizer was allow to vary the (AOM controlled) readout frequency and power, as well as the readout exposure time. It is important to note that the optimizer, while it does increase readout time, does not increase it without bound. It accelerates toward a longer readout time at first, but then finds convergence at a finite value, presumably because of the leash of atom retention. Furthermore, the readout frequency and power track simultaneously with the readout time. Increasing the readout power will also increase the signal-to-noise, but because it also imposes more impulse on the atoms, it must be accompanied by moving to a larger detuning, which is precisely what this particular optimization example achieves.

Through readout optimization we have been able to reduce the overlap, averaged across the whole array, to only 0.0004, indicating that we expect only 1 out of every 2500 shots to be mischaracterized.

We have also explored the second goal of going to shorter readout time, to work toward non-destructive readout. To approach this, we had to iteratively reduce the readout time and then optimize at the shorter readout, then reduce the readout time and optimize again.

We began with a single variable scan of readout time, from the standard 30 ms down to 1 ms, and found that we had resolvable, but poor, readout down to 11 ms, as shown in Figure 16.2a. Next, by allowing all readout variables except time (frequency, power, and magnetic shims) to vary during an optimization, we tuned in the settings for the 11 ms readout, resulting in well separated peaks, as shown in Figure 16.2b.

Taking the optimized 11 ms readout as a starting point, we reduced the readout time again, finding that we had resolvable, but poor, readout down to 5 ms (Figure 16.3a). Optimizing the readout settings again at a fixed 5 ms readout time lead to a readout histogram that was sufficiently separated on some sites, but not sufficiently good on most sites (Figure 16.3b). The signal-to-noise at this short readout time is inherently limited, and the optimizer was not able to make enough improvement to make such a short readout usable. In general other advancements, such as larger numerical aperture lenses, will be necessary to achieve non-destructive readout.

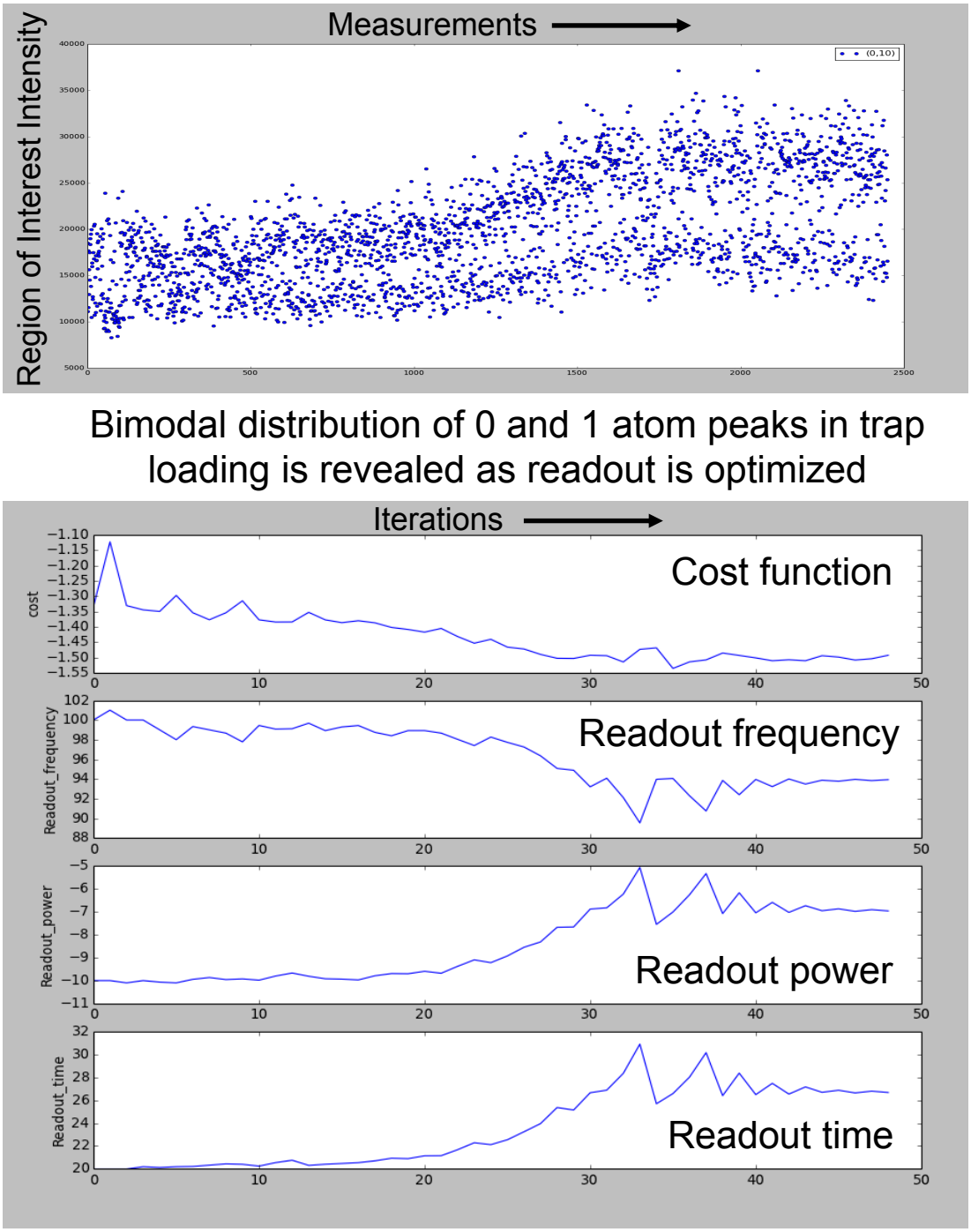
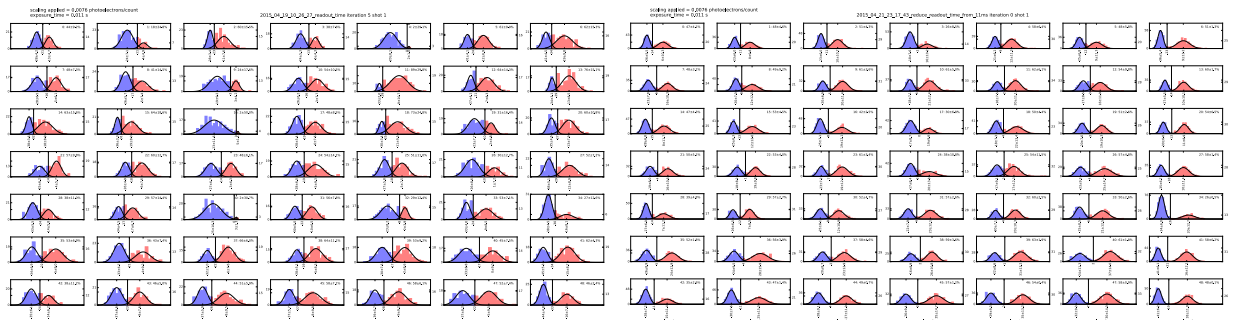
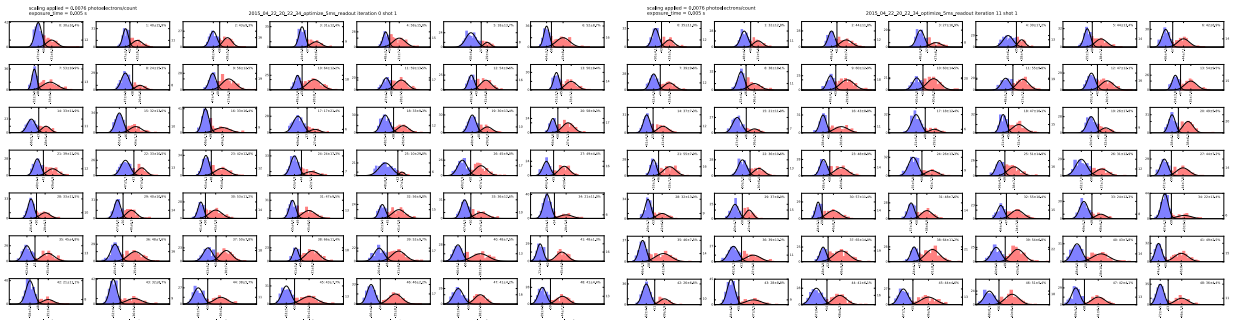


Figure 16.1: Nelder-Mead optimization of readout frequency, power and time. The cost function minimizes the overlap of the zero and one atom peaks. At top is shown the ROI brightness for one atom trapping site, for every measurement as this optimization proceeds. What begins as a low signal-to-noise ratio becomes a clearly separated bimodal distribution of zero and one atom loading. At bottom is shown the cost function, a function of zero and one atom peak overlap, which decreases as the optimization proceeds. Below the cost function are traces for each free variable.



(a) (b)

Figure 16.2: 11 ms readout (a) before and (b) after optimization, showing excellent improvement in the separation of the zero and one atom peaks. Data from 2015-04-19-10-26-27 and 2015-04-21-23-17-43.



(a) (b)

Figure 16.3: 5 ms readout (a) before and (b) after optimization, showing only marginal improvement in the separation of the zero and one atom peaks. Data from 2015˙04˙22˙20˙22˙34.

16.2 Loading and Retention

We desire to have as many of the 49 sites load as possible. This increases our data rate for single site operations in proportion to the loading rate. For two qubit operations, if we require two specific sites to load, then the data rate goes as the square of loading rate. Therefore, for operations involving large numbers of qubits, increasing the loading rate is of paramount importance to the usability of a large qubit array.

The loading optimization can be quite powerful. For example in Figure 16.4 we show how the loading of the entire array can be improved by varying even just a few variables, for example the magnetic field shims during the MOT loading stage.

Retaining the atoms throughout the gate operations is equally important, and with similar scaling. Because our readout scheme works on the presence or absence of an atom

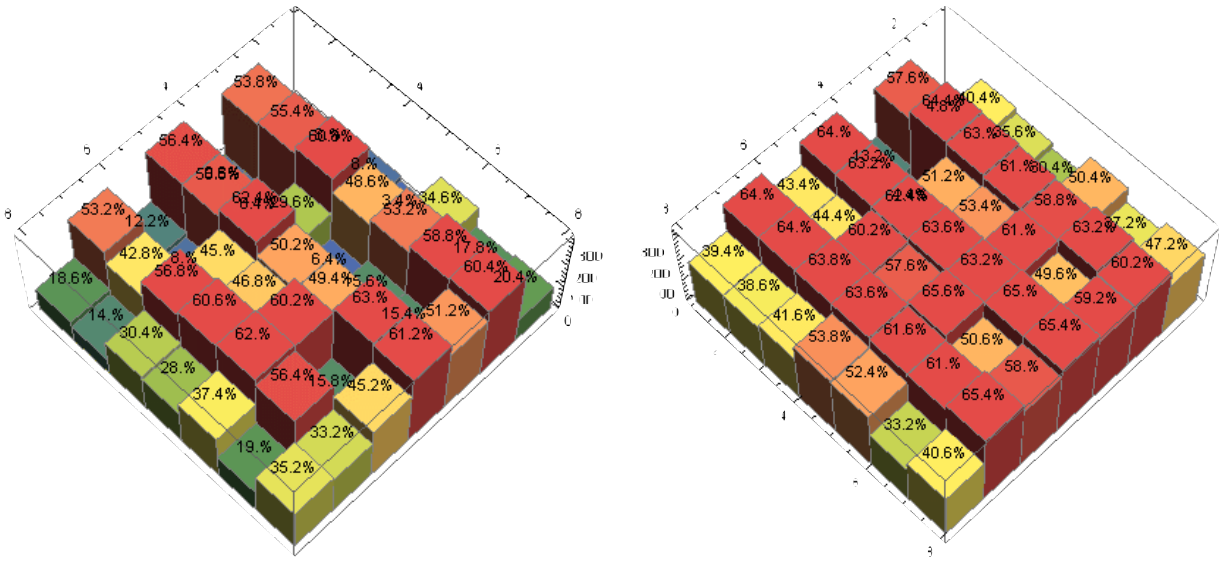


Figure 16.4: A loading optimization showing an excellent improvement in loading rate by varying only the magnetic field shims during the MOT loading stage. The loading bar chart on left shows the loading fraction for each site before optimization, and on the right is the loading fraction for each site after optimization. The residual pattern is the result of imperfections in the trapping light, and interference patterns in the MOT light.

after the gate, then atom loss due solely to poor trapping or hot atoms will degrade our signal.

For these reasons we optimize loading and retention together. In these operations we perform no blowaway operations between the camera shots, and then readout both $F = 3$ and $F = 4$, so that any atom loss signal is due solely to retention. Taking as the cost function the number of atoms in the second shot (negative because the optimizer is a minimizer), we can then simultaneously optimize loading and retention.

There are a large number of variables that go into a loading/retention optimization, because of the many experiment phases that take place (see Chapter 11). Most phases have distinct settings for the magnetic field shims, and each phase has power, frequency, and timing variables. The nature of multi-variate optimization is that it becomes more powerful as we optimize over more variables. In the worst case scenario if the variables are all independent, there is no improvement over doing single variable scans, but it does not take any longer. When variables are coupled however, the multi-dimensional optimization can give a great advantage by finding maxima not possible with single variable scans. In Figure 16.6 we show a very successful loading/retention optimization that took the array

from 19% average loading to 48% average loading. This particular optimization was done with 28 free variables, and typically we now include 50 variables in a loading/retention optimization.

Thermal drifts typically begin to cause loading to drop over the course of a couple of weeks. By running the optimizer overnight we have been able to keep the array loading well. Array averaged loading values of 57% are typical, with a best of 60.9%. Some individual sites load above 70%. We have achieved retention averaged across the array of 99%, with some sites retaining 100% (measured over 500 shots). A typical example of a 49 site loading histogram after being optimized to 57% loading is shown in Figure 16.5.

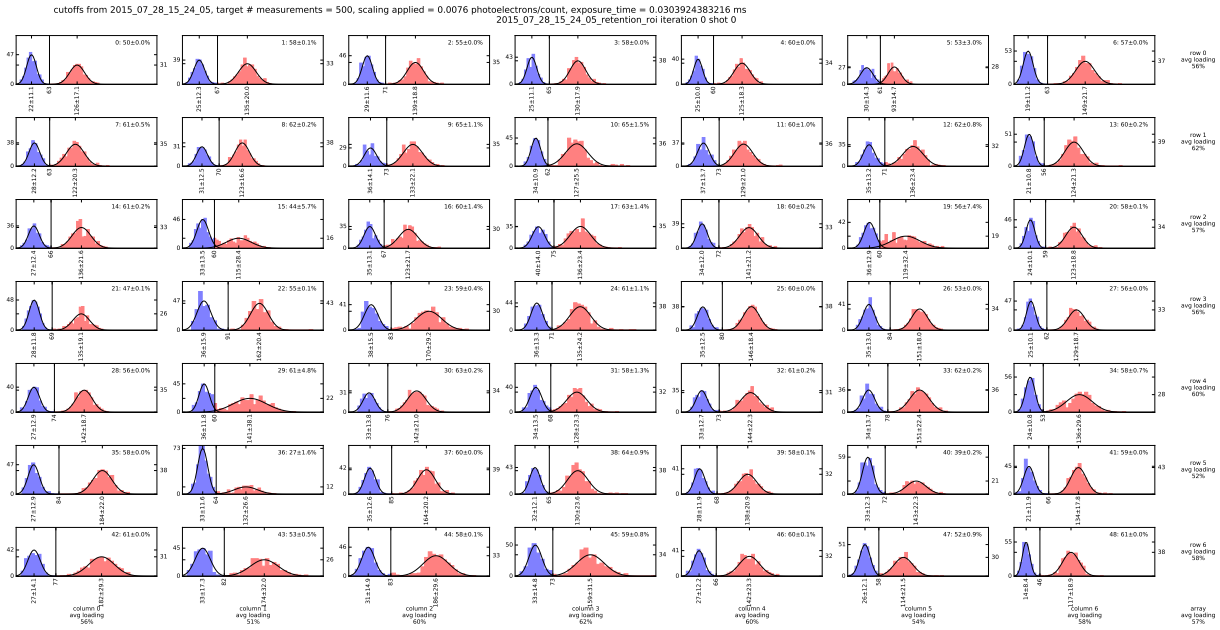


Figure 16.5: Loading histograms for the 49 site array, after being optimized to 57% array averaged loading. Data from 2015-07-28-15-24-05.

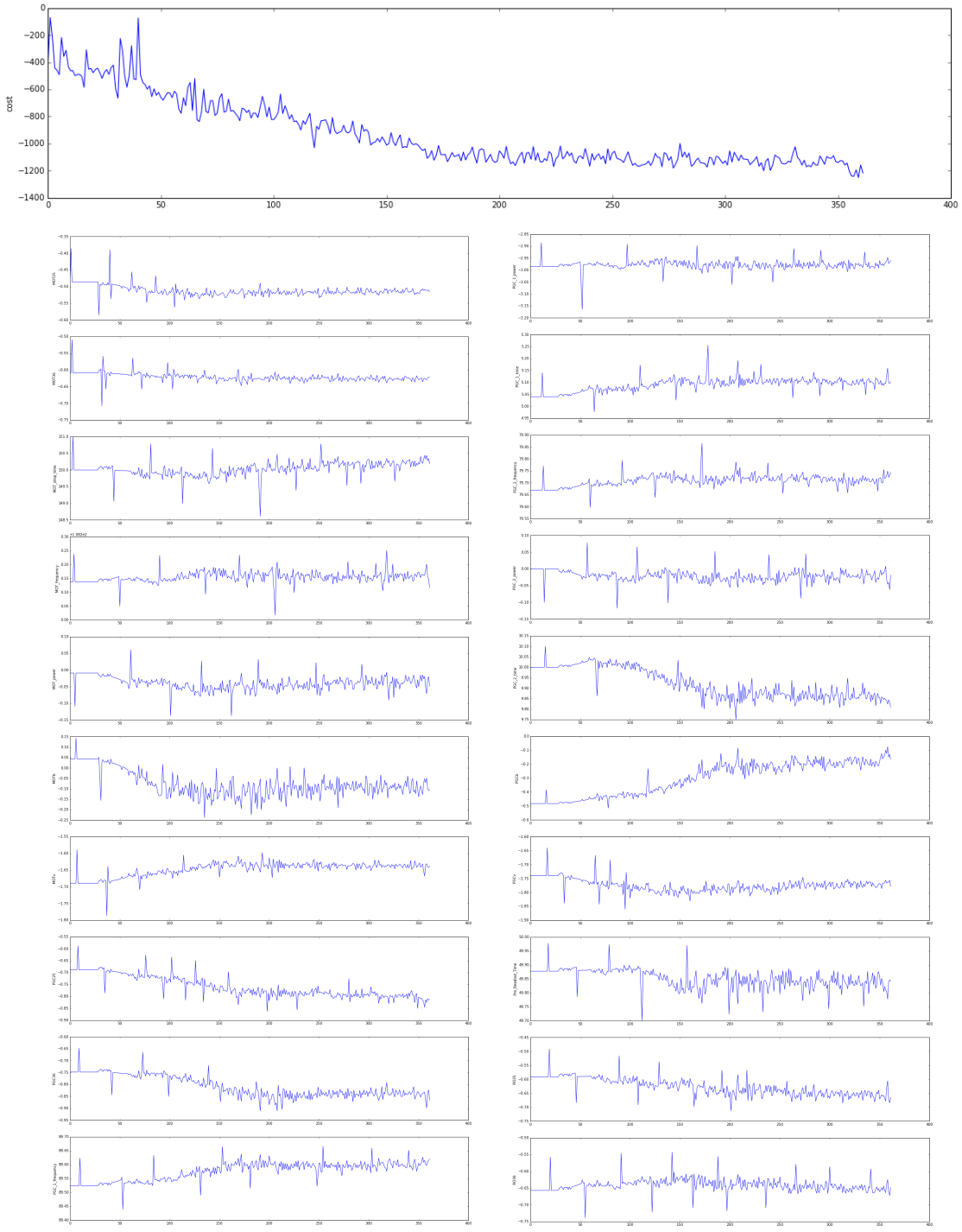


Figure 16.6: Optimization of loading and retention with many free variables. Shown at the top is the cost function, given as total atoms retained per 50 shots. At the bottom are the traces for 20 variables (out of 28 free variables used here), including magnetic fields, laser frequencies, and timing. Data from 2014-10-08.

16.3 Atom Temperature

To measure atom temperature, we include a short trap drop in the experiment sequence. As the duration of the trap drop increases, the atom retention goes down. This relationship is compared to theoretical curves that we find by Monte Carlo numerical simulation of the dynamics of a trapped atom. By comparing to simulations of different temperature atoms, we can determine the actual temperature of the real atoms in the traps.

The retention after a trap drop then provides a signal that we can use to optimize the cooling of the atoms. By including a fixed duration trap drop in the sequence, the retention becomes a signal of atom temperature. We optimize the PGC cooling by allowing the optimizer to vary laser frequency, amplitude, pulse time, and magnetic shim settings.

A sample result of this optimization in shown in Figure 16.7. Before the optimization, a scan of the trap drop time shows the retention starts to drop after $10\,\mu s$. We then optimize by maximizing retention with a $30\,\mu s$ trap drop in the experiment sequence. After the optimization, the temperature curve is flat to $20\,\mu s$. The data is plotted on top of curves for the Monte Carlo temperature simulations. Although the data does not follow the simulation curves well, we can identify that the atom temperature is > 10 µK before optimization, and < 10 µK after optimization.

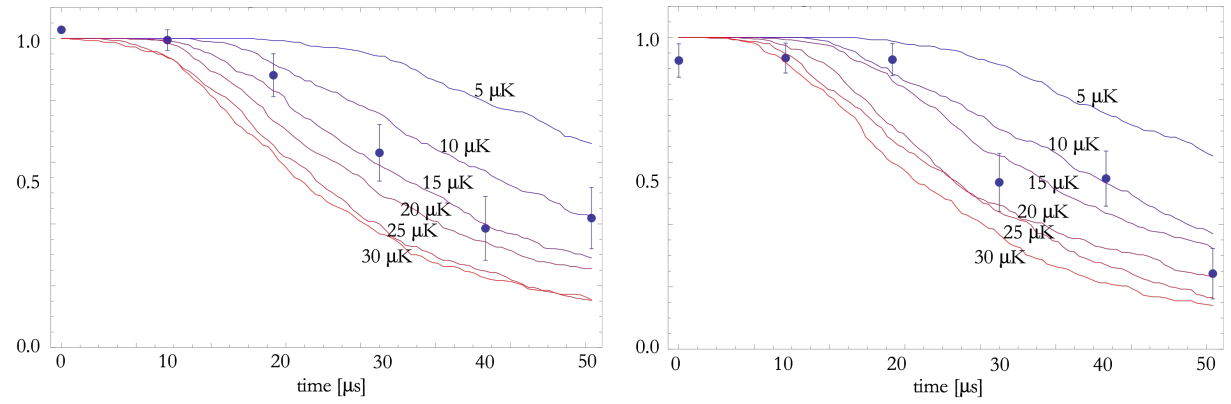


Figure 16.7: Optimization of atom temperature using retention during a fixed trap drop. Shown here is a scan of trap drop time (a) before optimization and (b) after optimization. Data from 2014-10-16-08-16-50 and 2014-10-15-17-43-55.

16.4 Optical Pumping

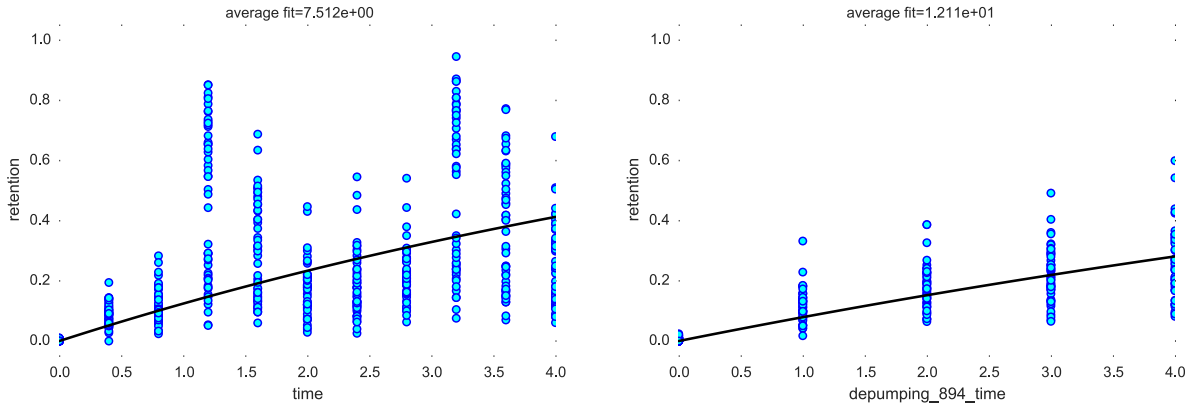
The ability to prepare our qubits to a known state is an important first step in any quantum computation. Without good state preparation, none of the calculations will produce the expected results. We optically pump into the logical $|1\rangle$, $\left|6s_{1/2}, F = 4, m_F = 0\right\rangle$ state as described in Section 8.2.4. During this operation, the $|F = 4, m_F = 0\rangle$ state is dark to the optical pumping laser, while the repump laser ensures that we always bring any atoms that have decayed into $F = 3$ back into the $F = 4$ manifold.

This gives us a good way to check the fidelity of the optical pumping, whereby we define a "depumping" operation as using the optical pumping light without any repumper. If the optical pumping is imperfect, then atoms will be pumped out of $|F = 4, m_F = 0\rangle$ and collect in $F = 3$. The depumping operation then gives us a signal that is highly sensitive to the quality of the optical pumping.

The optical pumping is very sensitive to the orientation of the magnetic fields, which must have a strong bias field aligned with the polarization vector of the optical pumping light. The level of optical pumping light is important as the forbidden $4 \leftrightarrow 4'$ transition will be excited if the polarization is imperfect, and so we do not want too much light. Also important is the ratio of optical pumping to repump light.

To optimize the optical pumping, we run a sequence that has optical pumping followed by a $2\,\text{ms}$ depump operation, and then blowaway. We wish to see as few atoms in $F = 3$ as possible, and so by minimizing the retention during this operation we can maximize optical pumping quality.

One example of this improvement is shown in Figure 16.8, which shows a before-and-after of array-averaged results for a depumping time scan. Scanning the depumping time gives one metric to characterize the quality of the optical pumping by fitting an exponential curve (comparing the ratio of optical pumping time to depumping time provides a complete picture). We see that the optical pumping optimization, which includes the magnetic fields during the optical pumping operation as well as frequency, power and timing, gives an increase in depumping time, as well as suppresses unwanted oscillatory behavior.



(a) (b)

Figure 16.8: A scan of depumping time a) before and b) after optimization. We see that not only is the $1/e$ depumping time in this example improved from 7.5 to 12.1 ms, but some large oscillations due to mixing of m_F states are suppressed. Data from 2015-07-28-17-13-51 and 2015-07-29-09-58-51.

16.5 Two-level Optimization

One of the challenges of designing a cost function for use with the optimizer is to ensure that one aspect of performance is not penalized while improving another. To this end, we have found it very helpful to be able to run several different settings iterations during each optimizer cycle. This was first conceived of as the *two-level optimization* because we have an inner level of looping over a fixed sequence of settings iterations, and an outer level of looping over optimizer-controlled settings updates.

With the implementation of the two-level optimizer, we allow the user to specify which independent variables should be optimized, and which should be allowed to iterate according to the normal rules of experiment sequencing.

The original application of this was to perform a Rabi flopping experiment, with enough iterations to calculate the Rabi frequency, and then optimize to maximize that frequency. Such an optimization generally has too slow an update rate to be useful, however the two-level optimization has proven to be a very useful feature in other scenarios.

For example, if we wish to simultaneously optimize optical pumping microwave performance and blowaway, this is could be done by doing optical pumping into $F = 4$, followed by a microwave π pulse into $F = 3$, followed by blowaway of $F = 4$. A good signal is then high retention. However, we run the risk of simply optimizing into a situation where none of the operations are working, which has the same signal.

To make sure our signal is truly representative of what we want, we can instead look at the contrast between doing these sequences without and with the microwave π pulse. Without the π pulse we expect a low signal, and with the π pulse we expect a high signal. We test both of these sequences at the same optimizer settings, and so there can be no confusion as to whether those settings are truly optimizing to the desired condition.

In Figure 16.9 we show a trace of retention vs. iteration for a two-level optimization of optical pumping. We see that the signal alternates between low and high. The optimizer however is not evaluated for every iteration, but rather for each pair of iterations, taking the difference between the low and high signals. In this optimization there are only three free variables: the magnetic shim settings during optical pumping. While the contrast is initially 18% array averaged, and below 60% for all sites, the optimizer soon increases it to 61% array averaged, and nearly 100% for some sites.

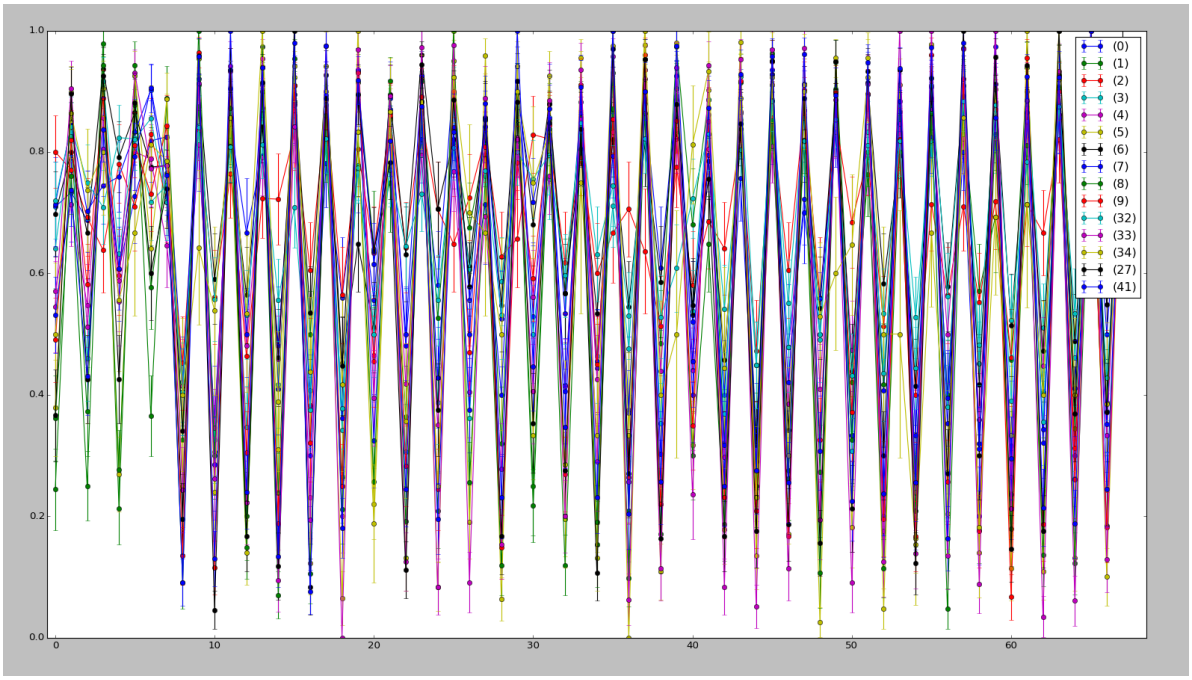


Figure 16.9: Two-level optimization of magnetic field shims during optical pumping. Shown here is the retention vs. iteration, where every low-high pair of iterations is a set performed without and with a microwave π pulse, respectively. The cost function is calculated by combining each pair to evaluate the contrast, which is maximized. Data from 2015-05-05.

The idea behind using the optimizer to improve performance metrics like retention and optical pumping, is that this will ultimately give an improvement in gate fidelity. The ultimate use of the optimizer is then to directly optimize the gate fidelity, using the blockade signal between two sites. This has been thus far prohibitively difficult because the Rydberg lasers are sensitive and do not stay locked long enough to endure a long multi-variate optimization run.

We have however made some progress toward that goal, first of all by using optimization to align the Rydberg beams to the atoms. This is an excellent use of the multi-variate optimization, because the alignment to each atom has two 459 nm and two 1038 nm beam scanners, all of which are coupled. Using the optimizer to perform the task is not only easier, but also has the potential to find a better alignment, and can help combat the slow thermal drift of the beam scanners. Much of this alignment can be done in parallel on multiple atoms by using multiple Rydberg pulses per measurement.

Furthermore, we have used the optimizer to tune the Rydberg pulse sequence itself. We measure the Rydberg iteration on a single site by performing a Rydberg π pulse, which leaves the atom in the less-well-trapped Rydberg state, and leads to large atom loss. By minimizing the retention after this operation, we can then optimize the Rydberg interaction. The problem with this sort of optimization, is that there is no way to distinguish large loss due to a good Rydberg interaction, from simply poor settings like an overly long trap-off time.

To combat this we use the two-level optimization. We have performed this optimization in two ways. The first is to look at the contrast between a Rydberg π pulse, and a Rydberg 2π pulse. We expect large atom loss after π, but desire high retention after 2π. This technique prevents parasitic optimization of the atom loss. The second method employed is meant to have increased verisimilitude to an entangling gate, wherein we optimize the contrast between a Rydberg π pulse, and a sequence of two Rydberg π pulses separated by a delay. The π-gap-π is the sequence that the control atom undergoes during the C_z and C_{NOT} gate. We recognize that simply increasing atom loss after a π pulse might increase the atom loss after π-gap-π as well, and so by looking at the contrast signal we prevent the optimizer from making changes which might be parasitic to the goal of a high fidelity gate.

Using these techniques we have obtained a modest 2% improvement in the Rydberg signal, and we hope to continue to employ optimization to directly improve Rydberg gate

fidelity in the future.

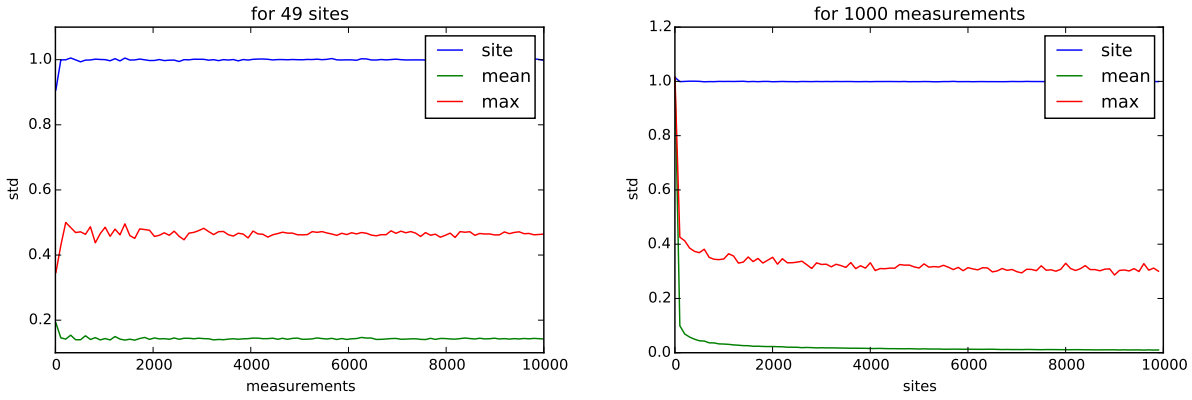
16.7 Single Site vs. Mean vs. Max Statistics

Although we are often concerned with optimizing only one or two sites, we will usually use the entire array in our cost functions to improve the data rate. Good convergence relies on having a noise level lower than the fluctuations being induced by settings changes made by the optimizer. When taking the average of N sites, we get a $\sqrt{N}$ improvement in sampling statistics, and so averaging our cost function over the whole array gives a $\sqrt{49} = 7$ times improvement in effective data rate.

Averaging over the whole array has the disadvantage of not fully optimizing any one site to the best it could possibly be. Even when optimizing to improve the performance of one particular site that we will be using, we rarely care *which* particular site that actually is. So instead, we can program the cost function to take the values for the best performing site, whichever one that may be. As the optimizer progresses, it is okay if this switches from one site to another, as at the end we will simply use whichever site was optimized to the highest level of performance.

This technique of taking the max value gives an improvement in data rate, although not as large as using the mean. In Figure 16.10 we compare these methods, using simulated data. We use virtual sites that return data with normally distributed noise, and a standard deviation of 1 for any single measurement on one site. Figure 16.10a shows the comparison of these methods for a fixed $N = 49$ sites, and a varying number of measurements. Steady-state levels are quickly reached after 100 measurements. Single site operations have a standard deviation of 1 as specified, and the mean has a standard deviation of $1/\sqrt{49} = 0.14$. Taking the maximum site on each measurement gives a standard deviation of 0.45. This technique therefore gives almost half the data rate of taking the mean, while having the potential to increase some particular site to a much higher level of performance.

In Figure 16.10b we fix the number of measurements at 1000 and increase the number of sites. As before, single site measurements have a standard deviation of 1. Taking the mean cost function asymptotes to a standard deviation of 0 as $\lim_{N\to\infty} \frac{1}{\sqrt{N}} = 0$. Taking the max cost function, we see the standard deviation continue to decrease to 0.3 as the number of sites increases to 10000, but it is unclear if this will continue to decrease to zero or if it has some asymptote at a larger value.



(a) (b)

Figure 16.10: A comparison of the standard deviation of single site measurements vs. array-averaged measurements vs. array-maximum measurements. Data is simulated, with single sites having normally distributed noise with a standard deviation of 1. (a) For a fixed number of sites. (b) For a fixed number of measurements.

Part IV

Coda

17 Summary and Future Directions

We have created a stable, inherently 2D array of neutral cesium atom qubits. The novel Gaussian beam array trapping scheme has been implemented to create single atom traps with 49 trapping sites and a 60% loading fraction, and progress has been made toward implementing an 121 site trap array with the new line array grid design.

The qubits are well characterized. Single atom qubits in this array are individually addressable, and we have demonstrated 99.83% fidelity for global operations and 99.2% fidelity for site-selective operations with low cross-talk. Two-qubit entangling gates using the Rydberg blockade have been demonstrated with a non-classical result of 73% fidelity as measured using Bell state parity. These results are reported without any post-selection for atom loss, and have been demonstrated beyond nearest-neighbors.

These systems are controlled using original software with the ability to perform multi-dimensional optimization on all experiment parameters. This has been an important tool in tuning the experiment to a high level of performance.

Our system satisfies all the elementary criteria for scalable universal quantum computing. We have begun efforts to demonstrate Grover's quantum search algorithm in the system. These efforts have not yet shown non-classical behavior, and our near future work includes improving this result. The biggest source of error in this computation is atom loss, which is compounded over two C_z gates. Attempts to reduce atom loss will include modifying the experiment sequence to leave the trapping lasers on during Rydberg operations, eliminating DC electric fields using electrodes inside the vacuum cell, and tuning pulse timing and laser intensity to reduce the gate time. Switching from square pulses to Gaussian or optimally controlled shaped pulses will give several orders of magnitude reduction in gate time and will further reduce atom loss.

Other near future work centers around the increase of our experiment data rate. This will allow more thorough optimization of the system, collection of more sample data for better statistics, and will reduce the environmental drift that occurs in the time between system tune-up and experiments. Techniques for improving the data rate include implementing a more sensitive readout, such that no repump light is necessary, and hence readout can be done without atom blowaway. This will eliminate the need to reload the traps every experiment and provide an order of magnitude speedup in data rate. Further work will include implementing techniques for deterministic loading of the trapping sites, such as catalysis loading, which will nearly double our data rate for single-site work, and for

n-qubit work scales as the loading rate to the n^{th} power. Implementation of an FPGA based control system will allow fast decisions on site-selective operations, and so can be used to do operations on whichever sites in the array have loaded qubits, further increasing the data rate.

The long term goals of this work are to pave the road toward fault-tolerant error-corrected logical qubits, in demonstrably scalable arrays large enough to implement computations that are not currently possible on classical computers. We have shown first steps along this road and look forward to the future journey ahead.

References

[1] L. Isenhower, E. Urban, X. L. Zhang, A. T. Gill, T. Henage, T. A. Johnson, T. G. Walker, and M. Saffman. "Demonstration of a Neutral Atom Controlled-NOT Quantum Gate". In: *Phys. Rev. Lett.* 104 (1 2010), p. 010503. DOI: 10.1103/PhysRevLett.104.010503.

[2] T. Wilk, A. Gaëtan, C. Evellin, J. Wolters, Y. Miroshnychenko, P. Grangier, and A. Browaeys. "Entanglement of Two Individual Neutral Atoms Using Rydberg Blockade". In: *Phys. Rev. Lett.* 104 (1 2010), p. 010502. DOI: 10.1103/PhysRevLett.104.010502.

[3] C. Knoernschild, X. L. Zhang, L. Isenhower, A. T. Gill, F. P. Lu, M. Saffman, and J. Kim. "Independent individual addressing of multiple neutral atom qubits with a micromirror-based beam steering system". In: *Applied Physics Letters* 97.13, 134101 (2010). DOI: 10.1063/1.3494526.

[4] X. L. Zhang, L. Isenhower, A. T. Gill, T. G. Walker, and M. Saffman. "Deterministic entanglement of two neutral atoms via Rydberg blockade". In: *Phys. Rev. A* 82 (3 2010), p. 030306. DOI: 10.1103/PhysRevA.82.030306.

[5] Dieter Meschede and Arno Rauschenbeutel. "Manipulating Single Atoms". In: ed. by G. Rempe and M.O. Scully. Vol. 53. Advances In Atomic, Molecular, and Optical Physics. Academic Press, 2006, pp. 75 –104. DOI: 10.1016/S1049-250X(06)53003-4.

[6] M. Saffman, T. G. Walker, and K. Mølmer. "Quantum information with Rydberg atoms". In: *Rev. Mod. Phys.* 82 (3 2010), pp. 2313–2363. DOI: 10.1103/RevModPhys.82.2313.

[7] C.S. Adams and E. Riis. "Laser cooling and trapping of neutral atoms". In: *Progress in Quantum Electronics* 21.1 (1997), pp. 1 –79. ISSN: 0079-6727. DOI: 10.1016/S0079-6727(96)00006-7.

[8] Thomas F Gallagher. *Rydberg Atoms*. Cambridge University Press, 1994.

[9] M. Saffman and T. G. Walker. "Analysis of a quantum logic device based on dipole-dipole interactions of optically trapped Rydberg atoms". In: *Phys. Rev. A* 72 (2 2005), p. 022347. DOI: 10.1103/PhysRevA.72.022347.

[10] David P DiVincenzo. "The Physical Implementation of Quantum Computation". In: (2000). arXiv: 0002077 [quant-ph].

[11] Charles H. Bennett, David P. DiVincenzo, John A. Smolin, and William K. Wootters. "Mixed-state entanglement and quantum error correction". In: *Phys. Rev. A* 54 (5 1996), pp. 3824–3851. DOI: 10.1103/PhysRevA.54.3824.

[12] Emanuel Knill and Raymond Laflamme. "Theory of quantum error-correcting codes". In: *Phys. Rev. A* 55 (2 1997), pp. 900–911. DOI: 10.1103/PhysRevA.55.900.

[13] Daniel Gottesman. "Theory of fault-tolerant quantum computation". In: *Phys. Rev. A* 57 (1 1998), pp. 127–137. DOI: 10.1103/PhysRevA.57.127.

[14] E. Knill, R. Laflamme, A. Ashikhmin, H. Barnum, L. Viola, and W. H. Zurek. "Introduction to Quantum Error Correction". In: (2002). arXiv: 0207170 [quant-ph].

[15] Daniel Gottesman. "An Introduction to Quantum Error Correction and Fault-Tolerant Quantum Computation". In: (2009). arXiv: 0904.2557 [quant-ph].

[16] Peter W. Shor. "Scheme for reducing decoherence in quantum computer memory". In: *Phys. Rev. A* 52 (4 1995), R2493–R2496. DOI: 10.1103/PhysRevA.52.R2493.

[17] Emanuel Knill, Raymond Laflamme, and Wojciech Zurek. *Accuracy Threshold for Quantum Computation*. 1996.

[18] A. M. Steane. "Error Correcting Codes in Quantum Theory". In: *Phys. Rev. Lett.* 77 (5 1996), pp. 793–797. DOI: 10.1103/PhysRevLett.77.793.

[19] Raymond Laflamme, Cesar Miquel, Juan Pablo Paz, and Wojciech Hubert Zurek. "Perfect Quantum Error Correcting Code". In: *Phys. Rev. Lett.* 77 (1 1996), pp. 198–201. DOI: 10.1103/PhysRevLett.77.198.

[20] Lov K. Grover. "A Fast Quantum Mechanical Algorithm for Database Search". In: *Proceedings of the Twenty-eighth Annual ACM Symposium on Theory of Computing*. STOC '96. Philadelphia, Pennsylvania, USA: ACM, 1996, pp. 212–219. ISBN: 0-89791-785-5. DOI: 10.1145/237814.237866.

[21] P. W. Shor. "Algorithms for quantum computation: Discrete logarithms and factoring". In: *Proc. 35nd Annual Symposium on Foundations of Computer Science (Shafi Goldwasser, ed.), IEEE Computer Society Press* (1994), pp. 124–134.

[22] Thorsten Kleinjung, Kazumaro Aoki, Jens Franke, Arjen Lenstra, Emmanuel Thomé, Joppe Bos, Pierrick Gaudry, Alexander Kruppa, Peter Montgomery, Dag Arne Osvik, Herman te Riele, Andrey Timofeev, and Paul Zimmermann. *Factorization of a 768-bit RSA modulus*. Cryptology ePrint Archive, Report 2010/006. 2010. URL: http://eprint.iacr.org/.

[23] John A. Smolin, Graeme Smith, and Alexander Vargo. "Oversimplifying quantum factoring". In: *Nature* 499.7457 (July 2013), pp. 163–165. DOI: 10.1038/nature12290.

[24] Lov K. Grover. "Quantum Mechanics Helps in Searching for a Needle in a Haystack". In: *Phys. Rev. Lett.* 79 (2 1997), pp. 325–328. DOI: 10.1103/PhysRevLett.79.325.

[25] Peter W. Shor. "Polynomial-Time Algorithms for Prime Factorization and Discrete Logarithms on a Quantum Computer". In: *SIAM Review* 41.2 (1999), pp. 303–332. DOI: 10.1137/S0036144598347011.

[26] Christof Zalka. "Grover's quantum searching algorithm is optimal". In: *Phys. Rev. A* 60 (4 1999), pp. 2746–2751. DOI: 10.1103/PhysRevA.60.2746.

[27] M. A. Nielsen and I. L. Chuang. *Quantum Computation and Quantum Information*. Cambridge, England: Cambridge University Press, 2000.

[28] G. L. Long. "Grover algorithm with zero theoretical failure rate". In: *Phys. Rev. A* 64 (2 2001), p. 022307. DOI: 10.1103/PhysRevA.64.022307.

[29] Klaus Mølmer, Larry Isenhower, and Mark Saffman. "Efficient Grover search with Rydberg blockade". In: *Journal of Physics B: Atomic, Molecular and Optical Physics* 44.18 (2011), p. 184016. URL: http://stacks.iop.org/0953-4075/44/i=18/a=184016.

[30] D. Deutsch. "Quantum Theory, the Church-Turing Principle and the Universal Quantum Computer". In: *Proceedings of the Royal Society of London A: Mathematical, Physical and Engineering Sciences* 400.1818 (1985), pp. 97–117. ISSN: 0080-4630. DOI: 10.1098/rspa.1985.0070.

[31] Kurt Gödel. *On Formally Undecidable Propositions of Principia Mathematica and Related Systems, I.* 1992nd ed. Dover, 1930.

[32] Alfred North Whitehead and Bertrand Russell. *Principia Mathematica*. Cambridge University Press, 1910.

[33] Douglas R. Hofstadter. *Gödel, Escher, Bach: an Eternal Golden Braid*. Basic Books, 1999.

[34] Vladan Panković and Milan Predojević. "A Quantum Gate as a Physical Model of an Universal Arithmetical Algorithm without Church's Undecidability and Gödel's Incompleteness". In: (2006). arXiv: 0602009 [quant-ph].

[35] Roman Kossak. "What are infinitesimals and why they cannot be seen". In: *Amer. Math. Monthly* 103.10 (1996), pp. 846–853.

[36] Richard Kaye. *Models of Peano arithmetic*. Vol. 15. Oxford Logic Guides. New York: The Clarendon Press, Oxford University Press, 1991.

[37] S. Tennenbaum. "Non-Archimedean Models for Arithmetic". In: *Notices Am. Math. Soc.* 6 (1959), p. 270.

[38] E. L. Raab, M. Prentiss, Alex Cable, Steven Chu, and D. E. Pritchard. "Trapping of Neutral Sodium Atoms with Radiation Pressure". In: *Phys. Rev. Lett.* 59 (23 1987), pp. 2631–2634. DOI: 10.1103/PhysRevLett.59.2631.

[39] William D. Phillips, Phillip L. Gould, and Paul D. Lett. "Cooling, Stopping, and Trapping Atoms". In: *Science* 239.4842 (1988), pp. 877–883. DOI: 10.1126/science.239.4842.877.

[40] C. Monroe, W. Swann, H. Robinson, and C. Wieman. "Very cold trapped atoms in a vapor cell". In: *Phys. Rev. Lett.* 65 (13 1990), pp. 1571–1574. DOI: 10.1103/PhysRevLett.65.1571.

[41] Steven Chu. "Laser Manipulation of Atoms and Particles". In: *Science* 253.5022 (1991), pp. 861–866. DOI: 10.1126/science.253.5022.861.

[42] C. G. Townsend, N. H. Edwards, C. J. Cooper, K. P. Zetie, C. J. Foot, A. M. Steane, P. Szriftgiser, H. Perrin, and J. Dalibard. "Phase-space density in the magneto-optical trap". In: *Phys. Rev. A* 52 (2 1995), pp. 1423–1440. DOI: 10.1103/PhysRevA.52.1423.

[43] Karl D. Nelson, Xiao Li, and David S. Weiss. "Imaging single atoms in a three-dimensional array". In: *Nat Phys* 3.8 (Aug. 2007), pp. 556–560. DOI: 10.1038/nphys645.

[44] P.S. Jessen and I.H. Deutsch. "Optical Lattices". In: ed. by Benjamin Bederson and Herbert Walther. Vol. 37. Advances In Atomic, Molecular, and Optical Physics. Academic Press, 1996, pp. 95 –138. DOI: 10.1016/S1049-250X(08)60099-3.

[45] J. I. Gillen, W. S. Bakr, A. Peng, P. Unterwaditzer, S. Fölling, and M. Greiner. "Two-dimensional quantum gas in a hybrid surface trap". In: *Phys. Rev. A* 80 (2 2009), p. 021602. DOI: 10.1103/PhysRevA.80.021602.

[46] Jacob F. Sherson, Christof Weitenberg, Manuel Endres, Marc Cheneau, Immanuel Bloch, and Stefan Kuhr. "Single-atom-resolved fluorescence imaging of an atomic Mott insulator". In: *Nature* 467.7311 (Sept. 2010), pp. 68–72. DOI: 10.1038/nature09378.

[47] D. Schrader, I. Dotsenko, M. Khudaverdyan, Y. Miroshnychenko, A. Rauschenbeutel, and D. Meschede. "Neutral Atom Quantum Register". In: *Phys. Rev. Lett.* 93 (15 2004), p. 150501. DOI: 10.1103/PhysRevLett.93.150501.

[48] Rudolf Grimm, Matthias Weidemüller, and Yurii B. Ovchinnikov. "Optical Dipole Traps for Neutral Atoms". In: Advances In Atomic, Molecular, and Optical Physics 42 (2000). Ed. by Benjamin Bederson and Herbert Walther, pp. 95 –170. ISSN: 1049-250X. DOI: 10.1016/S1049-250X(08)60186-X.

[49] Nicolas Schlosser, Georges Reymond, Igor Protsenko, and Philippe Grangier. "Sub-poissonian loading of single atoms in a microscopic dipole trap". In: *Nature* 411.6841 (June 2001), pp. 1024–1027. DOI: 10.1038/35082512.

[50] Renée C. Nesnidal and Thad G. Walker. "Light-induced ultracold spin-exchange collisions". In: *Phys. Rev. A* 62 (3 2000), p. 030701. DOI: 10.1103/PhysRevA.62.030701.

[51] S. D. Gensemer, P. L. Gould, P. J. Leo, E. Tiesinga, and C. J. Williams. "Ultracold $^{87}\mathrm{Rb}$ ground-state hyperfine-changing collisions in the presence and absence of laser light". In: *Phys. Rev. A* 62 (3 2000), p. 030702. DOI: 10.1103/PhysRevA.62.030702.

[52] E. Urban, T. A. Johnson, T. Henage, L. Isenhower, D. D. Yavuz, T. G. Walker, and M. Saffman. "Observation of Rydberg blockade between two atoms". In: *Nat Phys* 5.2 (Feb. 2009), pp. 110–114. DOI: 10.1038/nphys1178.

[53] Nir Davidson, Heun Jin Lee, Charles S. Adams, Mark Kasevich, and Steven Chu. "Long Atomic Coherence Times in an Optical Dipole Trap". In: *Phys. Rev. Lett.* 74 (8 1995), pp. 1311–1314. DOI: 10.1103/PhysRevLett.74.1311.

[54] H. J. Lee, C. S. Adams, M. Kasevich, and S. Chu. "Raman Cooling of Atoms in an Optical Dipole Trap". In: *Phys. Rev. Lett.* 76 (15 1996), pp. 2658–2661. DOI: 10.1103/PhysRevLett.76.2658.

[55] Takahiro Kuga, Yoshio Torii, Noritsugu Shiokawa, Takuya Hirano, Yukiko Shimizu, and Hiroyuki Sasada. "Novel Optical Trap of Atoms with a Doughnut Beam". In: *Phys. Rev. Lett.* 78 (25 1997), pp. 4713–4716. DOI: 10.1103/PhysRevLett.78.4713.

[56] Roee Ozeri, Lev Khaykovich, and Nir Davidson. "Long spin relaxation times in a single-beam blue-detuned optical trap". In: *Phys. Rev. A* 59 (3 1999), R1750–R1753. DOI: 10.1103/PhysRevA.59.R1750.

[57] S. Zhang, F. Robicheaux, and M. Saffman. "Magic-wavelength optical traps for Rydberg atoms". In: *Phys. Rev. A* 84 (4 2011), p. 043408. DOI: 10.1103/PhysRevA.84.043408.

[58] G. Li, S. Zhang, L. Isenhower, K. Maller, and M. Saffman. "Crossed vortex bottle beam trap for single-atom qubits". In: *Opt. Lett.* 37.5 (2012), pp. 851–853. DOI: 10.1364/OL.37.000851.

[59] M. J. Piotrowicz, M. Lichtman, K. Maller, G. Li, S. Zhang, L. Isenhower, and M. Saffman. "Two-dimensional lattice of blue-detuned atom traps using a projected Gaussian beam array". In: *Phys. Rev. A* 88 (1 2013), p. 013420. DOI: 10.1103/PhysRevA.88.013420.

[60] M. Saffman and M. Lichtman. *System and Method for Optical Confinement of Atomic Particles*. USPTO Patent Application. Applied for 2014.

[61] P. A. Franken, A. E. Hill, C. W. Peters, and G. Weinreich. "Generation of Optical Harmonics". In: *Phys. Rev. Lett.* 7 (4 1961), pp. 118–119. DOI: 10.1103/PhysRevLett.7.118.

[62] G. D. Boyd, W. L. Bond, and H. L. Carter. "Refractive Index as a Function of Temperature in LiNbO3". In: *Journal of Applied Physics* 38.4 (1967), pp. 1941–1943. DOI: 10.1063/1.1709786.

[63] O. Gayer, Z. Sacks, E. Galun, and A. Arie. "Temperature and wavelength dependent refractive index equations for MgO-doped congruent and stoichiometric LiNbO3". English. In: *Applied Physics B* 91.2 (2008), pp. 343–348. ISSN: 0946-2171. DOI: 10.1007/s00340-008-2998-2.

[64] Dieter H. Jundt. "Temperature-dependent Sellmeier equation for the index of refraction, ne, in congruent lithium niobate". In: *Opt. Lett.* 22.20 (1997), pp. 1553–1555. DOI: 10.1364/OL.22.001553.

[65] D. A. Kleinman, A. Ashkin, and G. D. Boyd. "Second-Harmonic Generation of Light by Focused Laser Beams". In: *Phys. Rev.* 145 (1 1966), pp. 338–379. DOI: 10.1103/PhysRev.145.338.

[66] G. D. Boyd and D. A. Kleinman. "Parametric Interaction of Focused Gaussian Light Beams". In: *Journal of Applied Physics* 39.8 (1968), pp. 3597–3639. DOI: 10.1063/1.1656831.

[67] G. D. Boyd, Robert C. Miller, K. Nassau, W. L. Bond, and A. Savage. "LiNbO3: An efficient phase matchable nonlinear optical material". In: *Applied Physics Letters* 5.11 (1964), pp. 234–236. DOI: 10.1063/1.1723604.

[68] Ichiro Shoji, Takashi Kondo, Ayako Kitamoto, Masayuki Shirane, and Ryoichi Ito. "Absolute scale of second-order nonlinear-optical coefficients". In: *J. Opt. Soc. Am. B* 14.9 (1997), pp. 2268–2294. DOI: 10.1364/JOSAB.14.002268.

[69] S. S. Sané, S. Bennetts, J. E. Debs, C. C. N. Kuhn, G. D. McDonald, P. A. Altin, J. D. Close, and N. P. Robins. "11 W narrow linewidth laser source at 780nm for laser cooling and manipulation of Rubidium". In: *Opt. Express* 20.8 (2012), pp. 8915–8919. DOI: 10.1364/OE.20.008915.

[70] P. F. Moulton. "Spectroscopic and laser characteristics of Ti:Al2O3". In: *J. Opt. Soc. Am. B* 3.1 (1986), pp. 125–133. DOI: 10.1364/JOSAB.3.000125. URL: http://josab.osa.org/abstract.cfm?URI=josab-3-1-125.

[71] A. W. Carr and M. Saffman. "Doubly magic trapping for Cs atom hyperfine clock transitions". In: (2014). arXiv: 1406.3560 [atom-ph].

[72] Daniel A. Steck. *Cesium D Line Data*. available online. 2010. URL: http://steck.us/alkalidata.

[73] K. B. MacAdam, A. Steinbach, and C. Wieman. "A narrow-band tunable diode laser system with grating feedback, and a saturated absorption spectrometer for Cs and Rb". In: *American Journal of Physics* 60.12 (1992), pp. 1098–1111. DOI: 10.1119/1.16955.

[74] Daryl W. Preston. "Doppler-free saturated absorption: Laser spectroscopy". In: *American Journal of Physics* 64.11 (1996), pp. 1432–1436. DOI: 10.1119/1.18457.

[75] A. M. Hankin, Y.-Y. Jau, L. P. Parazzoli, C. W. Chou, D. J. Armstrong, A. J. Landahl, and G. W. Biedermann. "Two-atom Rydberg blockade using direct $6S$ to nP excitation". In: *Phys. Rev. A* 89 (3 2014), p. 033416. DOI: 10.1103/PhysRevA.89.033416.

[76] Karen Liu and Michael G. Littman. "Novel geometry for single-mode scanning of tunable lasers". In: *Opt. Lett.* 6.3 (1981), pp. 117–118. DOI: 10.1364/OL.6.000117.

[77] R. V. Pound. "Electronic Frequency Stabilization of Microwave Oscillators". In: *Review of Scientific Instruments* 17.11 (1946), pp. 490–505. DOI: 10.1063/1.1770414.

[78] R.W.P. Drever, J.L. Hall, F.V. Kowalski, J. Hough, G.M. Ford, A.J. Munley, and H. Ward. "Laser phase and frequency stabilization using an optical resonator". English. In: *Applied Physics B* 31.2 (1983), pp. 97–105. ISSN: 0946-2171. DOI: 10.1007/BF00702605.

[79] J.L. Hall, Ma Long-Sheng, and G. Kramer. "Principles of optical phase-locking: Application to internal mirror He-Ne lasers phase-locked via fast control of the discharge current". In: *Quantum Electronics, IEEE Journal of* 23.4 (1987), pp. 427–437. ISSN: 0018-9197. DOI: 10.1109/JQE.1987.1073354.

[80] T. Xia, M. Lichtman, K. Maller, A. W. Carr, M. J. Piotrowicz, L. Isenhower, and M. Saffman. "Randomized Benchmarking of Single-Qubit Gates in a 2D Array of Neutral-Atom Qubits". In: *Phys. Rev. Lett.* 114 (10 2015), p. 100503. DOI: 10.1103/PhysRevLett.114.100503.

[81] Chuanwei Zhang, S. L. Rolston, and S. Das Sarma. "Manipulation of single neutral atoms in optical lattices". In: *Phys. Rev. A* 74 (4 2006), p. 042316. DOI: 10.1103/PhysRevA.74.042316. URL: http://link.aps.org/doi/10.1103/PhysRevA.74.042316.

[82] *FC1000 Optical Frequency Synthesizer Manual*. MenloSystems GmbH. Munich, Germany, 2011.

[83] Mark Saffman. "Optics for Physicists". Unpublished. 2015.

[84] Marcus Ansmann. "Benchmarking the Superconducting Josephson Phase Qubit: The Violation of Bell's Inequality." PhD thesis. University of California, Santa Barbara, 2009.

[85] P. T. Starkey, C. J. Billington, S. P. Johnstone, M. Jasperse, K. Helmerson, L. D. Turner, and R. P. Anderson. "A scripted control system for autonomous hardware-timed experiments". In: *Review of Scientific Instruments* 84.8, 085111 (2013), pp. –. DOI: 10.1063/1.4817213.

[86] Aviv Keshet and Wolfgang Ketterle. "A distributed, graphical user interface based, computer control system for atomic physics experiments". In: *Review of Scientific Instruments* 84.1, 015105 (2013), pp. –. DOI: 10.1063/1.4773536.

[87] S. Chris Colbert. *Enaml declarative GUI language*. Nucleic Development Team. 2013. URL: http://nucleic.github.io/enaml/docs/.

[88] HDF Group. *Hierarchical Data Format, Version 5*. URL: https://www.hdfgroup.org/HDF5/.

[89] P. B. Wigley, P. J. Everitt, A. van den Hengel, J. W. Bastian, M. A. Sooriyabandara, G. D. McDonald, K. S. Hardman, C. D. Quinlivan, M. Perumbil, C. C. N. Kuhn, I. R. Petersen, A. Luiten, J. J. Hope, N. P. Robins, and M. R. Hush. "Fast machine-learning online optimization of ultra-cold-atom experiments". In: (2015). arXiv: 1507.04964 [quant-ph].

[90] J. A. Nelder and R. Mead. "A Simplex Method for Function Minimization". In: *The Computer Journal* 7.4 (1965), pp. 308–313. DOI: 10.1093/comjnl/7.4.308.

[91] Stephen R. Segal, Quentin Diot, Eric A. Cornell, Alex A. Zozulya, and Dana Z. Anderson. "Revealing buried information: Statistical processing techniques for ultracold-gas image analysis". In: *Phys. Rev. A* 81 (5 2010), p. 053601. DOI: 10.1103/PhysRevA.81.053601.

[92] T. Walker and D. Pritchard. "Effects of Hyperfine Structure on Alkali Trap-Loss Collisions". In: *Laser Physics* 4.5 (1994), pp. 1085–1092.

[93] P D Lett, K Molmer, S D Gensemer, K Y N Tan, A Kumarakrishnan, C D Wallace, and P L Gould. "Hyperfine structure modifications of collisional losses from light-force atom traps". In: *Journal of Physics B: Atomic, Molecular and Optical Physics* 28.1 (1995), p. 65. URL: http://stacks.iop.org/0953-4075/28/i=1/a=009.

[94] T. Grunzweig, A. Hilliard, M. McGovern, and M. F. Andersen. "Near-deterministic preparation of a single atom in an optical microtrap". In: *Nat Phys* 6.12 (Dec. 2010), pp. 951–954. DOI: 10.1038/nphys1778.

[95] Alicia V Carpentier, Yin H Fung, Pimonpan Sompet, Andrew J Hilliard, Thad G Walker, and Mikkel F Andersen. "Preparation of a single atom in an optical microtrap". In: *Laser Physics Letters* 10.12 (2013), p. 125501. URL: http://stacks.iop.org/1612-202X/10/i=12/a=125501.

[96] Y H Fung and M F Andersen. "Efficient collisional blockade loading of a single atom into a tight microtrap". In: *New Journal of Physics* 17.7 (2015), p. 073011. URL: http://stacks.iop.org/1367-2630/17/i=7/a=073011.

[97] Brian J Lester, Niclas Luick, Adam M Kaufman, Collin M Reynolds, and Cindy A Regal. "Rapid production of uniformly-filled arrays of neutral atoms". In: (2015). arXiv: 1506.04419 [quant-ph].

[98] Mark Saffman. “Coherent interaction of atoms and light”. Unpublished. 2014.

[99] S Olmschenk, R Chicireanu, K D Nelson, and J V Porto. “Randomized benchmarking of atomic qubits in an optical lattice”. In: *New Journal of Physics* 12.11 (2010), p. 113007. URL: http://stacks.iop.org/1367-2630/12/i=11/a=113007.

[100] K. M. Maller, M. T. Lichtman, T. Xia, Y. Sun, M. J. Piotrowicz, A. W. Carr, L. Isenhower, and M. Saffman. “Rydberg-blockade controlled-not gate and entanglement in a two-dimensional array of neutral-atom qubits”. In: *Phys. Rev. A* 92 (2 2015), p. 022336. DOI: 10.1103/PhysRevA.92.022336.

[101] Y.-Y. Jau, A. M. Hankin, Tyler Keating, I. H. Deutsch, and G. W. Biedermann. “Entangling Atomic Spins with a Strong Rydberg-Dressed Interaction”. In: (2015). arXiv: 1506.06416 [quant-ph].

[102] D. D. Bhaktavatsala Rao and Klaus Mølmer. “Effect of qubit losses on Grover’s quantum search algorithm”. In: *Phys. Rev. A* 86 (4 2012), p. 042321. DOI: 10.1103/PhysRevA.86.042321.

[103] L. Isenhower, M. Saffman, and K. Mølmer. “Multibit C k NOT quantum gates via Rydberg blockade”. English. In: *Quantum Information Processing* 10.6 (2011), pp. 755–770. ISSN: 1570-0755. DOI: 10.1007/s11128-011-0292-4.

[104] Mark Saffman. “A little bit of quantum information”. Unpublished. 2015.